Dissertation zur Erlangung des Doktorgrades

der Fakultät für Chemie und Pharmazie

der Ludwig-Maximilians-Universität München

Mesoporous Metal Phosphate-Citrate Nanoparticles as Anti-Cancer Agents

Constantin Heinz Nepomuk Freiherr Schirndinger von Schirnding

aus

München, Deutschland

2017

Erklärung

Diese Dissertation wurde im Sinne von § 7 der Promotionsordnung vom 28. November 2011 von Herrn Prof. Dr. Thomas Bein betreut.

Eidesstattliche Versicherung

Diese Dissertation wurde eigenständig und ohne unerlaubte Hilfe erarbeitet.

München,

Constantin Frhr. von Schirnding

Dissertation eingereicht am 12.06.2017

1. Gutachter: Prof. Dr. Thomas Bein
2. Gutachter: Prof. Dr. Christoph Bräuchle

Mündliche Prüfung am 10.07.2017

DANKSAGUNG

Mein aufrichtigster Dank gilt zuerst meinem Doktorvater Professor Thomas Bein. Ohne deine Unterstützung und dein Vertrauen hätte die vorliegende Arbeit nicht entstehen können. Dein langer Atem und deine ausdauernde Geduld bis zu den ersten aussagekräftigen Resultaten haben mich über die ersten eineinhalb Jahre nicht aufgeben lassen, die Entwicklung von biokompatiblen Nanopartikeln voranzutreiben. Mit einer unerwarteten Entdeckung zahlten sich die intensiven Forschungen letztlich aus. Ich danke dir für deine stete Unterstützung bei der Anmeldung des Patentes, welche mir nun viele Wege eröffnet. Für dein entgegengebrachtes Vertrauen und die daraus resultierenden Freiheiten während meiner Promotionszeit spreche ich dir meinen herzlichsten Dank aus. Sehr lehrreich waren für mich die vielfältigen Möglichkeiten, auf mehreren internationalen und nationalen Konferenzen meine Daten auszugsweise zu präsentieren. Die Gelegenheit, der Öffentlichkeit Drug Delivery Systeme durch die Teilnahme am NIM NanoDay vorzustellen, hat dem Team und mir viel Freude gebracht. Vor allem aber danke ich dir für die familiäre Atmosphäre, die du in der Gruppe etabliert hast. Das hat eine sehr harmonische Arbeitsatmosphäre ermöglicht.

Dir, liebe Hanna, möchte ich für die unzähligen Ideen, Gedanken, Vorschläge, Diskussionen, Ratschläge und die Durchführung von Millionen Zellexperimenten während meiner und für meine Promotion danken. Dein offenes Ohr und deine Antworten haben mich auch in schwierigen Phasen immer wieder nach vorne gebracht. Deine Unterstützung durch Suchen nach Kooperationspartnern und durch stundenlange Meetings hat zum Erfolg meiner Promotion einen riesigen Anteil geleistet. Dass die Zellexperimente und die Mikroskopaufnahmen mit dir möglich waren, ist ein wesentlicher Bestandteil meiner Arbeit geworden. Die Aufklärung des

Mechanismus hat viele Wochenenden gekostet, die du immer wieder geopfert hast. Auch vielen herzlichen Dank für die Unterstützung bei unseren Vorhaben mit der Firmengründung, den Anträgen, den Ratschlägen und deinen Kontakten. Unsere Zusammenarbeit und unseren Zusammenhalt sowie unser Vertrauen in allen Bereichen schätze ich außerordentlich und freue mich auf die weiteren Jahre mit dir.

Prof. Dr. Christoph Bräuchle möchte ich sehr herzlich danken für die Erstellung des Zweitgutachtens zu dieser Arbeit und auch die Unterstützung von Hanna, die die Labore und Ausstattung weiternutzen konnte, wodurch meine Arbeit sehr profitierte.

Prof. Dr. Ernst Wagner, Dr. Andreas Roidl, Dr. Adam Hermawan und Ann-Kathrin Sommer danke ich vielmals für die fruchtbare Kooperation zu den Zellversuchen, die zum Verständnis des Wirkmechanismus beigetragen haben und die auch das Potential der Entwicklung gezeigt haben. Außerdem danke ich euch für die vielen Diskussionen und Vorschläge für weitere zielführende Versuche, die das Ergebnis meiner Promotion maßgeblich vorantrugen.

Meinen griechischen Freunden, Dr. Georgios Stathopoulos, Malamati Vreka und Maria Papageorgopoulou möchte ich meinen Dank für die unkomplizierte und sofortige Durchführung der ersten Mausexperimente aussprechen. Ich freue mich auf viele weitere Versuche im Rahmen unserer Zusammenarbeit.

Meinen Bürokollegen sage ich „Moinsn“ und „Tschausn“: Danke, dass ihr die Zeit im Office so kurz wirken habt lassen! Ohne euch wäre es niemals so eine schöne Zeit geworden. Es wäre nicht so einfach gewesen, jeden Morgen unbeschwert in die Arbeit zu kommen. Danke für eure vielfältige Unterstützung im beruflichen und privaten Bereich. Danke, dass es so lustig mit euch war.

Dr. Christian Argyo sage ich herzlichen Dank für die durchgängige Unterstützung beginnend mit der Betreuung meines F-Praktikums und der Empfehlung bei Thomas mich in die Gruppe aufzunehmen bis hin zur Planung der Firmengründung. Der gesamten MesoBio-Subgroup danke ich für die guten Diskussionen, Ratschläge und Ideen. Dr. Markus Döblinger und Steffen Schmidt danke ich für die exzellenten TEM und REM Bilder. Dr. Alesja Ivanova, Dr. Bastian Rühle und Michael Beetz danke ich für die vielen hervorragenden REM-Bilder und dafür, dass ihr mir immer das gezeigt habt, was ich sehen wollte. Tina Reuther danke ich dafür, dass sie alles am Laufen gehalten hat, sie mir meine vielen Proben gemessen hat und sie mich so viele Jahre als Büromitglied aufgenommen hat. Dr. Bastian Rühle danke ich für die Einführung und die vielen Nachhilfestunden in das Programm PovRay.

Herzlich bedanke ich mich auch bei meinen vielen F-Praktikanten und NIM Studenten für die gute und zuverlässige Arbeit: Markus Siegert, Florian Fink, Jonathan Sappl, Marie Bayer, Ahmed Hassaan, Durbis Pazas, und Marina Carmona. Ich weiß, ich bin kein einfacher Betreuer gewesen.

Regina Huber, der Seele des Arbeitskreises Bein, möchte ich für die großartige Unterstützung und Beratung bei allem Organisatorischen danken. Du hast so manches Schlupfloch gefunden, um Dinge zu beschleunigen oder gar erst zu ermöglichen!

Zuletzt gilt mein Dank meiner lieben Familie. Ich habe durchaus mitbekommen, dass ich wohl nicht so ein einfaches Kind war. Vielleicht bin ich auch jetzt noch nicht so einfach. Und daher danke ich euch, Mutt und Vat, unendlich, dass ihr mich unterstützt habt und ihr mich immer habt ausprobieren lassen, was ich mir in den Kopf gesetzt hatte. Dies hat meinen Forschungs- und Erfindergeist sicherlich entwickelt und letztlich zu meinem Abschluss geführt. Meinen Geschwistern, Jobst,

Felicitas und Leopold, möchte ich für die vielen aufmunternden Ratschläge und tatkräftigen Unterstützungen danken und euch sagen, dass ich mich sehr glücklich schätze, dass ihr immer zu mir haltet. Meiner Britta danke ich für den seelischen und moralischen Beistand. Ich danke dir, für das Mut machen mit der Promotion zu beginnen. Deine Gabe, mich immer wieder auf den Boden der Tatsachen zurückzuholen, hat zum erfolgreichen Abschluss dieser Arbeit beigetragen. Dein offenes Ohr für meine Gedanken und Ideen haben mich dazu geführt, diese zu strukturieren und zu fokussieren. Ich danke dir aus tiefstem Herzen für alles.

Danke.

ABSTRACT

The development of efficient and effective anti-cancer therapies is one of the leading goals in pharmaceutical sciences. Well-established anti-cancer chemotherapeutics (such as cisplatin, doxorubicin, fluorouracil) are injected into the bloodstream or administered as tablets by swallowing. These chemotherapeutics are highly toxic and often classified as carcinogenic as well. During cancer treatment the patient receives high doses of chemotherapeutics. Because the conventional chemotherapeutics are not able to distinguish well between cancerous or healthy tissue, the patient usually suffers from very strong side effects. Recent strategies in chemotherapy employ specific targeting methods to enhance the selectivity of the drugs and attack cancer cells only. So-called antibody-drug conjugates rely on the modified protein composition exhibited by the membrane of cancer cells that is recognized by the antibody. With this strategy one active chemotherapeutic molecule at a time can be transported into cancer cells. To enhance the efficiency of the targeted transport, nanoparticles have attracted increasing attention, since they can deliver many active molecules per particle. For example, polymer conjugates, polymeric nanoparticles, micelles, lipid-based carriers, dendrimers, carbon tubes, nanoshells, and nanocages have been investigated in this context. Nanoparticles can be transported to cancer cells either passively (e.g. through the enhanced permeability and retention effect) or they can interact more specifically with certain cell types through targeting. Nanoparticles can be taken up by cancer cells through endocytosis. The internalized particles or their cargo must then escape from the endosome to release the encapsulated drug and to kill the cancer cell. Thus, the endosomal escape is a crucial part in the effectiveness of drug delivery systems and remains a challenge in the field. Generally, in case of anti-cancer drug transport through nanoparticles, the

delivery system remains in the cell and must be degraded or removed from the body as extrinsic material. Therefore, a major goal in the development of drug delivery systems is to increase the biocompatibility of the carrier material.

Since drug delivery system based anti-cancer treatments are promising therapy approaches, we wish to contribute to this field. Therefore, the development of stimuli-responsive nano-agents for anti-cancer therapy has been a goal of my PhD thesis. The following chapters summarize the results of the research, concerning the synthesis of mesoporous (alkaline earth) metal phosphate-citrate nanoparticles. Thereby, these chapters address the progression from calcium phosphate-citrate nanoparticles to magnesium phosphate-citrate nanoparticles as promising nano-agents for anti-cancer therapy.

Firstly, a novel synthesis strategy for amorphous mesoporous calcium phosphate-citrate nanoparticles (CPCs) is reported. The influence of the complexing agent, citric acid, on the development of the mesopores was investigated. A high degree of mesoporosity is a recognized need for applicable drug delivery systems. For systems based on calcium phosphate backbones this could not be achieved until today. Here, a solution is presented for this need. Characterization and visualization of the mesoporous framework was performed by nitrogen sorption analysis and transmission and scanning electron microscopy. By optimizing the reaction conditions, CPCs were synthesized with diameters of around 200 nm measured with dynamic light scattering. Nitrogen sorption analysis revealed a BET surface area of about 575 m^2/g. The pore size is about 5 nm with a corresponding pore volume of 0.6 cm^3/g. The incorporation of citrate into the structure of CPCs was verified with IR spectroscopy. Also, thermogravimetric analysis data were acquired. Additionally, CPCs are of amorphous nature with the ability to crystallize over time in aqueous

media. The transition of the amorphous phase into the crystalline phase was followed by X-ray diffraction.

Secondly, synthetic approaches for the functionalization of mesoporous CPCs were examined. Via co-precipitation methods, the incorporation of strontium and manganese ions into the framework of CPCs was achieved. Strontium and manganese ions possess high radiopacity and paramagnetic properties, respectively. These additional physical characteristics were investigated using computer aided tomography measurements and magnetic resonance imaging to confirm possible applications as diagnostic tool or for detection in living matter. Via co-precipitation of CPCs with fluorescent calcein, also acting as chelating agent, self-fluorescent CPCs were obtained. These particles were incubated with HeLa cells to visualize particle uptake by cells. Due to the negative zeta potential of CPCs, the particle uptake by cells could only be achieved after coating the nanoparticles with a supported lipid membrane. Overall, the different functionalizations did not have any negative influence on the BET surface area, pore volume, and pore size compared to the unfunctionalized CPCs. Characterization was performed with nitrogen sorption analysis, IR spectroscopy, dynamic light scattering, thermogravimetric analysis, transmission and scanning electron microscopy, X-ray diffraction, and fluorescence confocal microscopy.

Thirdly, a further improvement of the reaction conditions for the synthesis of CPCs led to an increase of porosity. This was achieved by adding an additional surfactant template and by reducing the precipitation kinetics. The particles feature an extraordinary BET surface area of 900 m^2/g, a very narrow pore size distribution with a maximum at 4.8 nm, and a cumulative pore volume of 1.0 cm^3/g obtained with nitrogen sorption analysis. IR spectroscopy reveals two strong vibrations at

1414 cm^{-1} and 1590 cm^{-1} that are attributed to citrate incorporated into the structure. The incorporation of citrate into the CPCs´ structure was additionally demonstrated with solid-state nuclear magnetic resonance spectroscopy. Further physical characterization was performed with dynamic light scattering, zeta potential measurements, thermogravimetric analysis, transmission and scanning electron microscopy, and X-ray diffraction. The loading capacity and release kinetics of CPCs were investigated with calcein as model drug and ibuprofen and confirmed with fluorescence and UV-Vis measurements. For lipid-coated CPCs there was no significant premature release detectable. Cell experiments were carried out on fourteen different cell lines. For this purpose seven mesenchymal cancer cell lines (HeLa, H1299, MDA-MB-231, LLC, Neuro 2A, AE17, B16), six epithelial cancer cell lines (BT-474, MCF7, HuH7, 293T, A549, MC38), and one epithelial cell line derived from non-tumorigenic tissue (MCF 10A) were investigated. The cellular uptake is dependent on the lipid-coating of CPCs, while uncoated CPCs are not taken up by cells. Importantly, internalized CPCs dissolve once the endosomal pH turns acidic. However, a rapid release of Ca^{2+} ions into the cytosol (producing a calcium shock) is only induced if small amounts of the amphiphile cetyltrimethylammonium chloride are incorporated in the CPCs. Remarkably, mesenchymal cancer cell lines are much more strongly affected by the Ca^{2+} shock and induce apoptosis at lower IC_{50} values than epithelial cancer cells. And strikingly, the non-cancerous cell line MCF 10A was not affected significantly by the particles up to concentrations of 100 µg/mL. To determine cell viability, the established MTT-assays were conducted. The correlation of the Ca^{2+} shock induced by the dissolved particles with cellular response was demonstrated with time-resolved cell experiments. After several hours of particle uptake the activation of caspase-3/7 was recorded, which was followed by a decrease in NADH and ATP depletion, and finally leading to apoptosis.

Additionally, a first mouse study on an intrapleural tumor model revealed a decrease in tumor mass of 40 wt% after one single injection of CPCs as well as a good biocompatibility of the treatment. These results suggest a strong selectivity in the toxic effect of CPCs, thus demonstrating their great potential as low-toxicity chemotherapeutic nano-agents.

Fourthly, a systematic study on the exchange of calcium ions against magnesium ions in calcium phosphate-citrate nanoparticles was performed. For this purpose, the amount of magnesium was gradually increased with respect to the calcium content of CPCs. At 60 mol% of magnesium ions in magnesium-calcium phosphate-citrate, a drastic increase in size led to objects with 5 µm in length. A strong pH-dependency on the formation of colloidal mesoporous magnesium-calcium phosphate-citrate nanoparticles during the precipitation was observed. Accordingly, the synthesis of magnesium phosphate-citrate nanoparticles (MPCs) was demonstrated. These particles feature diameters of around 255 nm measured with dynamic light scattering. Nitrogen sorption analysis revealed a large BET surface area of 560 m^2/g for MPCs. The pore size is calculated to about 6.3 nm with a corresponding pore volume of 0.8 cm^3/g. The incorporation of citrate into the structure of MPCs was proven with IR spectroscopy. Further characterization methods were thermogravimetric analysis, transmission and scanning electron microscopy, and X-ray diffraction. Additionally, the insights into the pH-dependency of the nanoparticle formation were adapted to the synthesis of colloidal mesoporous manganese phosphate-citrate nanoparticles. Therefore, a general method for the synthesis of mesoporous bivalent cationic phosphate-citrate nanoparticles was proposed.

At last, mesoporous magnesium phosphate-citrate nanoparticles (MPCs) were synthesized as biocompatible drug delivery systems. To this end, the impact of the

complexing agent, citric acid, was investigated with respect to the formation of mesoporous MPCs. A maximum BET surface area of 560 m^2/g and a pore size of about 6.3 nm with a corresponding pore volume of 0.8 cm^3/g could be obtained with nitrogen sorption analysis. The amount of incorporated citrate into the structure was verified with IR spectroscopic methods and thermogravimetric analysis. Characterization techniques including dynamic light scattering, transmission and scanning electron microscopy, and X-ray diffraction were applied. Furthermore, MPCs were coated with a lipid membrane to encapsulate fluorescent calcein as model drug and the anti-cancer drug methotrexate (MTX). The lipid membrane encapsulating MPCs prevented the drugs from premature release, which was confirmed by fluorescence measurements and UV-Vis spectroscopy. Cell viability assays (MTT-assay) on HeLa cells revealed low toxicity of unloaded MPCs with an IC_{50} value of 77 µg/mL compared to MTX loaded MPCs with a drastically lower IC_{50} value of 1.1 µg/mL (MPCs mass). Therefore, with mesoporous magnesium phosphate-citrate nanoparticles an advanced biodegradable platform was designed that can potentially reduce the side effects of current chemotherapies.

In summary, we have developed a novel method for the synthesis of colloidal mesoporous (alkaline earth) metal phosphate-citrate nanoparticles as stimuli-responsive agents against cancer. Citric acid plays a key role as complexing agent for the cations, presumably by slowing down the precipitation kinetics and inhibiting crystallization. The newly obtained materials can either be applied directly as chemotherapeutic agent in the case of calcium phosphate-citrate nanoparticles or in the case of magnesium phosphate-citrate nanoparticles as advanced biocompatible drug delivery system. Additionally, the nanoparticles can be flexibly functionalized for special detection or diagnostic reasons. Moreover, the newly developed synthesis

strategy opens up many additional possibilities regarding the design of new materials such as manganese phosphate-citrate nanoparticles that could enable novel applications in the future.

TABLE OF CONTENTS

CHAPTER 1

INTRODUCTION

1.1 The Challenge of Cancer

Cancer is known to be the second most common cause for morbidity worldwide, affecting about 14 million new patients in 2012.[1] In the same year, 8 million cancer related deaths were counted from populations in all countries and all regions.[2] The five most common cancer sites for men are the lung (16.7%), prostate (15.0%), colorectum (10.0%), stomach (8.5%), and liver (7.5%), whereas women suffer from breast (25.5%), colorectum (9.2%), lung (8.7%), cervix (7.8%), and stomach (4.8%) as main cancer sites.[2] Therefore, cancer can arise in nearly any part of the body. Cancer emerges from the transformation of normal cells into cancerous cells in a multistage process.[3,4] This process includes failures in the control mechanisms of cell cycle, apoptosis, genome integrity, morphogenetic reactions, and cell differentiation.[3,5,6] Cancerous cells proliferate at a much faster rate than strongly regulated normal cells constrained within the boundaries of a proper cell cycle.[7,8] This eventually leads to an alteration of correctly functioning biological cell processes, to an accumulation of mutations and to the development of cancer.[5]

Fighting cancer has been a challenge and a goal for researchers since decades. Knowing that cancer is fundamentally a cellular dysfunction,[3] the cancerous cells need to be eliminated from the body with therapeutic agents. The first linkage of the development, progression, and treatment of cancer to apoptosis has started an emerging field in fighting cancer.[9,10] Therefore, one major mode of action for chemotherapeutic agents is the activation of the apoptotic pathway.[11,12,13] Apoptosis is the programmed and, as a result, regulated death of a cell.[10,14,15] Apoptosis can be characterized with morphological changes and biochemical hallmarks, like cell shrinkage, nuclear DNA fragmentation, and membrane blebbing.[12,16] The morphological changes described by Kerr *et al.*[9] are caused by caspases that are

activated during apoptotic cell death.[16,17] Therefore, the activation of caspases can be crucial in attacking cancerous cells. There are different mechanisms to initiate the production of caspases in cells, namely the receptor or the mitochondrial pathway.[12,16] In general, if any of the two pathways is initiated, a cascade of signaling steps is triggered and leads to apoptosis. For example, the initiator caspases-2, -8, -9, and -10 are activated upon an apoptotic stimulus, which in turn, proteolytically activate the effector caspases-3, -6, and -7.[18] Their activation leads to the cleavage of various substrates, eventually ending in cell death.[19]

After understanding the underlying mechanism for inducing apoptosis in cancer cells, mankind has invented and developed many chemotherapeutic agents addressing the apoptotic pathway.[20] However, patients receiving chemotherapeutic agents are burdened by severe side effects due to the non-selectivity of the anti-cancer drugs. Every cell is affected by a chemotherapeutic molecule - cancerous and non-tumorigenic cells as well. For instance, doxorubicin, a well-established chemotherapeutic agent, exhibits an IC_{50} value (half maximal inhibitory concentration) for the cancerous breast cell line MCF7 of 0.41 µM and for the non-tumorigenic breast cell line MCF 10A of 0.31 µM.[21] Therefore, the effectiveness of a treatment is directly linked to the ability of the therapeutic agent to selectively destroy only cancer cells while the healthy cells survive.[22] Consequently, a growing field has emerged aimed at reducing side effects by enhancing the selectivity of the anti-cancer drugs. Two pathways have evolved for achieving that goal: either a more specific anti-cancer drug or methods for targeted delivery.[22] Nowadays conventional anti-cancer drugs still face problems such as limited stability, poor solubility, rapid metabolization, fast excretion of the drug, undesired side effects, and the lack of selectivity.[23,24,25] Thus, the development of drug delivery systems has emerged. Typically, these drug delivery systems are based on nanotechnology and employ

nanoconstructs in the size range of 1-1000 nm.[24] The delivery of therapeutics with nanoconstructs potentially improves their stability and solubility, reduces the rapid metabolization and fast excretion of the nanoconstruct, and limits undesired side effects. Additionally, drug delivery systems can potentially enhance the selectivity due to the functionalization of the nanoconstruct with targeting agents.[26,27] The first nanoconstruct for therapeutic applications was developed in 1955, a polymer-drug conjugate.[24,28] From that time on, the path for the development of more precise and personalized anti-cancer therapies was initialized.

Until today, however, patients suffer strongly form the diagnosis cancer. In most cases this means that they are likely to die from this disease and that they know their cause of death the day they were diagnosed. Therefore, scientists all over the world still address the challenge of curing cancer but at this point it has not yet been fully solved.

1.2 Introduction to Nanotechnology

Nanostructured materials were used by mankind since many centuries without having an idea what nanomaterials are. This is based on the fact that nature developed nanotechnology throughout evolution long before humans were alive. Nowadays, there are many known nanomaterials that were initially created by evolution. Therefore, nanomaterials were often based on biological systems. For example DNA, proteins, viruses, and many more biological systems belong in a sense to the category of nanomaterials due to their small dimensions. With the implementation or combination of nanomaterials into larger scale domains, nature developed certain effects with various outcomes. One could also argue that a living cell is a combination of nanomaterials influencing each other and acting together.

Nanomaterials or nanostructures were implemented even in larger domains: the leaves of *Nelumbo nucifera* feature the so-called "Lotus effect" based on nanometer sized domains causing a hydrophobic effect, which repels water from them. Spiders can produce spider silk, a material with very high tensile strength and at the same time being very thin.[29] Many more biological materials are built from objects at the nanoscale that in the end create larger domains, like insect wings, opals, cotton, feathers, horns, hair, bone, shells, etc.

First, nanomaterials were defined by the logical application of the SI unit. Therefore, materials with characteristic sizes in the 10^{-9} m range belong to the class of nanomaterials.[30] But this definition became unclear and ambiguous as nanotechnology continued to evolve. During the last few decades numerous nanomaterials definitions have been specified by industry, governments, and standard organizations. Naturally, this led to variable definitions how to classify nanomaterials.[31] As an example: the European Commission defined nanomaterials as follows:

"A natural, incidental or manufactured material containing particles, in an unbound state or as an aggregate or as an agglomerate and where, for 50 % or more of the particles in the number size distribution, one or more external dimensions is in the size range 1 nm-100 nm."[32]

By convention, 1-100 nm is the size range most institutions use in reference to nanomaterials. The lower end of this scale is for all institutions identical, because the properties of the material are mainly characterized by the chemistry of the molecules and not by the physical nature of the material. The upper "end" still needs to be interpreted as vague, because a nanomaterial does not abruptly change its properties at a 100 nm size. Therefore, some authorities expanded the upper limit as possibly

being larger than 100 nm.[31,33] The definition of what nanomaterials are is thus still a matter of interpretation.

In former times, one of the better known nano-application was colloidal gold and other metals as an additive in stained glass to decorate church windows. For example, colloidal gold colored church windows in ruby red.[34,35] In 1856, Faraday was the first who suggested that the color results from small gold particles which were suspended in a medium. He was also the first who formed a suspension of gold particles in water and discovered that the color of such solutions is related to the particles´ size.[35,36] Later, in the first decades of the 20th century, the interest in systems on the nano-scale increased strongly. It was Richard Feynman who first summarized in 1959 the great opportunities of such systems in his famous speech "There's plenty of room at the bottom".[37] Then, scientists began the search for synthesis procedures to create defined nanomaterials. Fullerenes, which are carbon-based nanomaterials, were prepared in 1985 and helped to push the field of nanoscience.[38] Five years later, the first carbon based "needle-like tubes" were published.[39,40] In the following years synthesis procedures for many more nanomaterials were published and investigated. Titanium dioxide nanoparticles, for example, were developed and are used today as whitening pigments in paints and in textile industry, as well as blocker of harmful UVA and UVB radiation in sunscreens.[41] Additionally, TiO_2 nanoparticles, especially in the anatase modification, are applied as photo catalyst for the dissociation of water molecules.[42,43] Therefore, the development of new nanomaterials results in different, novel and potentially unexpected properties. Notably, materials at the nanometer scale often offer very different physical properties and behavior than the corresponding bulk material. One reason for this is that with decreasing size the number of surface atoms increases compared to the overall total number of atoms in

the material.[44] Ongoing research and development of new nanomaterials may lead to new application fields and will open up other that will be explored in the future.

Already, due to the pioneering spirit of today's industry, nanotechnologies and nanomaterials have reached high relevance. Nanomaterials can be found in electronics, information and communication technologies, energy production and storage, environmental control, textile industry, and healthcare.[45] In 2004 almost 160 billion $ were assigned to nanotechnology in the global product revenue.[46,47]

1.3 Mesoporous Nanomaterials as Drug Delivery Systems

It has been a major goal to enhance the efficacy of a therapeutic anti-cancer drug. One approach has been the development of drug delivery systems. The potential advantages of drug delivery systems are that drug resistance can be overcome, the circulation time can be enhanced, the poor solubility of anti-cancer drugs can be enhanced, and large amounts of drug can target the tumorous site.[48] Additionally, drug delivery systems could either target cancerous cells and tissue actively or passively.[23] Active targeting of the drug delivery system is potentially achieved by linking the nanocarriers with molecules that bind to overexpressed antigens or receptors on the cancerous cell.[49,50,51] Passive targeting of drug delivery systems is based on the enhanced permeability and retention (EPR) effect of cancer tissue, which sometimes allows for the accumulation of nanocarriers at the diseased site.[52,53,54]

In order to ensure targeted drug delivery to the specified location within the body and to precisely control the release of drugs, many requirements need to be adressed.[55,56,57] The nanocarriers have to fulfil the following characteristics: [55,56]

1. high loading/encapsulation capacity of desired drug molecules,
2. no premature release and no leaking of loaded drug molecules,
3. controlled release of drug molecules with a proper rate of release to achieve an effective local concentration,
4. cell type or tissue specificity and site directing ability,
5. good biocompatibility of nanocarriers.

Although the application of nanomaterials for medical reasons may seem to be a recent trend, the first approaches were already explored in the 1950´s.[24,28,58] The history of drug delivery systems began with the development of polymer-drug conjugates.[24,28,59] Jatzkewitz *et al.* coupled poly(vinylpyrrolidone) to mescaline as drug depot for primary amines. Then, lipid vesicles, namely liposomes, were published in 1965. The authors described the diffusion of univalent cations and anions through the liposomal membrane.[60,61] Some date the development of drug delivery systems back to these two investigations. Eleven years later a non-inflammatory polymer construct showed the first sustained release of proteins.[62] Then in 1994, Gref *et al.* presented a biodegradable polymer coated with polyethylene that prolonged the circulation time. They were able to entrap already 45 wt% of drug in the dense core.[63] All together, these developed systems feature the possibility to encapsulate anti-cancer drugs and to deliver them to a specific site in the body. Nevertheless, these systems had drawbacks regarding flexibility: the exchangeability of the anti-cancer drug is difficult. This is caused by the fact that the anti-cancer drug is added, encapsulated, and strongly bound to the nanocarrier during the synthesis. This defines the entire construct as being the anti-cancer drug. But the potential advantage of drug delivery systems lies in the possibility to easily exchange and personalize the anti-cancer drug during treatment. Thus, these systems were not yet satisfactory as a platform for advanced drug delivery applications. Therefore,

scientists were also searching for other approaches for advanced drug delivery systems - mesoporous nanoparticles.

In a classical sense, porous materials are considered as materials traversed by voids.[64] A recurrence in three-dimensional space is exhibited by the pores, whereas no regularity is required for a substance to be designated as "porous".[64] In accordance with the recommendations of the International Union of Pure and Applied Chemistry porous materials are classified according to their pore diameters: micro- (< 2 nm), meso- (2-50 nm) and macro-porous (> 50 nm) solids.[65] Zeolites and mesoporous silica can be seen as two major classes of (periodic) porous materials.

Zeolites[66,67] were developed in 1956 as adsorbents for industrial separations and purifications.[68] By now more than 200 zeolite-types are known, of which about 40 are naturally occurring.[69,70] Zeolites are used, e.g., as molecular sieves or as catalysts in the cracking process of crude oil.[71,72] Tens of thousands of publications and more than 10.000 patents[68] refer to the zeolite materials. Zeolites are porous crystalline aluminosilicate materials consisting of corner-sharing MO_4 tetrahedra (M = Na, Si, Al, etc.). Most importantly, for the first time crystalline, internal porosity was presented. Their typical pore size is less than 1.5 nm for molecularly templated aluminosilicates.[73,74] Recently, there have been reports on the use of zeolites as drug delivery systems.[75,76,77] But the limiting factor for zeolites as drug delivery system can be explained with the maximal reachable pore size.[78] The pore size was too small for internal adsorption of larger anti-cancer drug molecules. This restrains the possible range of loadable anti-cancer drugs as cargo due to their larger size.

Things changed dramatically when researchers of the Mobil Oil Company discovered a synthesis route for mesoporous silica with a highly ordered pore system in 1992. With pore sizes of 2-10 nm these materials presented pore sizes far beyond

the limits of zeolites.[74,79,80] The first acid-catalyzed sol-gel process for mesoporous silica was introduced. The porous structure was obtained by the addition of a surfactant template yielding very regular pore structures. From now on, large anti-cancer drug molecules as well as proteins could be loaded into a mesoporous framework.

The development from bulk mesoporous silica to mesoporous silica nanoparticles (MSNs)[81], opened the way for novel applications. MSNs have attracted high interest for catalytic applications, chemical sensing, biosensing, and especially as containers for targeted drug delivery.[82,83,84,85,86] The group of Vallet-Regi *et al.* proposed the use of mesoporous silica for drug delivery applications.[87] This was achieved with a base-catalyzed sol-gel process, which has produced colloidal MSNs with around 100 nm in size.[81,88] By means of hydrolysis and condensation of organosilane precursors (TMOS, TEOS, etc.), the formation of a new phase was initiated, the sol-phase. The small colloidal particles within the sol then condensed into the gel-phase.[89] To yield porosity, a cationic surfactant template was added that formed micelles around which the silicate source can be directed. The surfactant template forms either lamellar (g = 1), cylindrical (g = 0.5), or spherical (g = 0.33) micellar structures described with equation (1.1). This depends on reaction parameters such as temperature, pH value, and surfactant to solution ratio. Thereby, the characteristic parameter g defines the surfactant packing parameter.[90]

$$g = \frac{2V}{ad} \tag{1.1}$$

g: Surfactant packing parameter, V: Volume of the micelles, a: Surface interface of micelles, d: Diameter of micelles.

The colloidal stability of MSNs can be a major advantage allowing for intravenous application routes. Colloidal materials were already classified and defined in 1972 by the International Union of Pure and Applied Chemistry as objects with a size between 1 nm and 1000 nm in at least one dimension, if dispersed in a medium.[91] Additionally, MSNs offer high loading capacity due to their internal surface area and pore volume, can specifically be functionalized at the inner pore system and/or at the particle´s surface, and are biocompatible.[92] For example, MSNs feature BET surface areas of around 1150 m^2/g, which offer the pore volume for high loading capacity.[93] The introduction of a core-shell synthesis via a delayed co-condensation process provided access to very flexible and tunable nanoparticles for advanced drug delivery applications.[94] With that approach, different functionalizations were introduced that control drug uptake and release kinetics[95], enable the addition of pore blockers[96,97,98,99,100], allow attachment of endosomal escape agents[101,102,103], enhance the blood circulation time[104,105], and furnish the surface with targeting ligands[95,102]. Additionally, specific MSNs were incubated with HeLa cells and showed no toxic effects up to concentrations of 500 µg/mL.[106]

Today thousands of publications concerning mesoporous silica nanoparticles and drug delivery are listed in established search engines. This underlines the huge relevance of MSNs in the field for advanced drug delivery applications, despite the fact that at the same time many other nanosized materials were introduced as nanocarriers for drug delivery applications. These materials include polymer conjugates, polymeric nanoparticles, micelles, lipid-based carriers, dendrimers, carbon tubes, nanoshells, and nanocages.[23] Figure 1.1 depicts schematically several of the constructs used as drug delivery systems for targeting cancer.

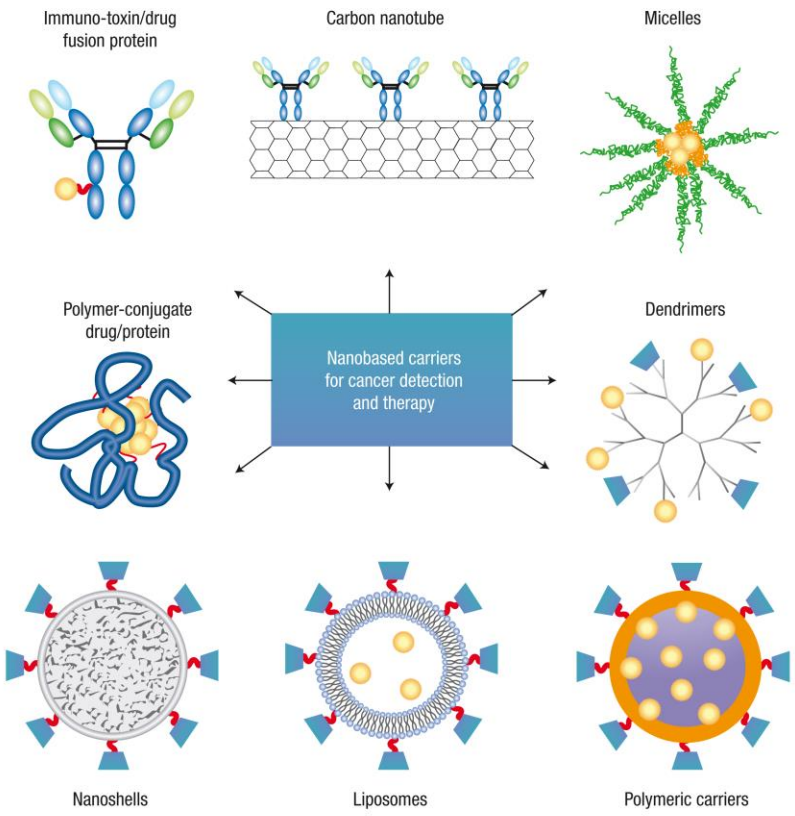

Figure 1.1: Examples of nanocarriers for drug delivery applications. Modified from reference [23].

Polymer conjugates are constructs that entrap drugs in a bundle of biocompatible polymers.[107,108] Polymeric nanocarriers were synthesized from poly(lactic acid), poly(lactic co-glycolic acid), and poly(ε-caprolactone) and therein therapeutic compounds have been encapsulated.[109,110] Micellar drug delivery platforms can be formed through a multimolecular assembly of block copolymers under certain conditions that hold therapeutic drugs in their core.[111,112] Lipid-based nanocarriers, so-called liposomes, have attracted great attention due to their structural variety, biocompatible composition, surface charge, ability to incorporate almost any drug regardless of solubility and to carry cell-specific ligands on their surface.[113,114] Dendrimers are strongly branched three-dimensional macromolecules with very controllable structures. Dendrimers can be obtained from poly(amidoamine) and many other building blocks and find application due to their biomimetic

properties.[115,116] Carbon nanotubes have also emerged as a new alternative as efficient transporter for therapeutic drugs. Additionally, functionalization of the outer surface was published for these materials.[117,118] Antibody-drug conjugates link chemotherapeutic agents with antibodies that can target the cancer cell.[119] And a large class of drug delivery systems is summarized with the term "nanoshell and nanocages", that includes zeolites and porous silica nanoparticles, which already have been discussed, and furthermore special cases like periodic mesoporous organosilica[120], metal organic frameworks[121,122] and quantum dots[123].

All these nanocarrier constructs have many advantages but still face some challenges. Therefore, the development of new and efficient drug delivery systems is of fundamental importance and offers the potential to improve the therapeutic efficacy of many therapeutic molecules.

1.4 Advanced Biodegradable Drug Delivery System

Calcium phosphate materials make up the main inorganic mass in a human body.[124,125] In nature, different forms of calcium phosphates exist, which mainly depend on impurities with other ions and the physiological conditions.[126] For example, in the form of carbonated hydroxyapatite, this material is found in bone, teeth, and tendons as biological hard tissue.[124] Thus, calcium phosphate materials are remarkably biocompatible and have great medical and biological relevance.[124,127] Therefore, the research on synthetic calcium phosphate materials has been gaining increasing interest since the last third of the 20th century.[128,129] The calcium phosphate materials used for medical applications encompass crystalline hydroxyapatite, tricalcium phosphate, biphasic calcium phosphate, monocalcium phosphate monohydrate, and amorphous calcium phosphate.[130,131] For example,

crystalline hydroxyapatite materials find use as coatings for implants, dental filler material or as bone cements for repair due to their high stability.[132,133] However, the success of these materials is limited to the repair of only small bone defects. And until today, the osteogenic and osteoinductive properties of synthetic bone does not resemble the one from bone autografts.[134]

Amorphous calcium phosphate materials have often been encountered as transient phase during the formation of hydroxyapatite.[135,136] That is the reason why amorphous calcium phosphate materials have been investigated as initializing material for bone growth. As a result, the better osteoconductivity and biodegradability compared to crystalline hydroxyapatite was addressed.[137,138,139] However, the high solubility in biological environments leads to poor strength and limits the use of amorphous calcium phosphates as bone cements.[140] Therefore, functionalization of amorphous calcium phosphates was investigated. Stabilization was accomplished with casein phosphopeptides[141,142], or magnesium and adenosine triphosphate[143] which slowed down the transition into crystalline hydroxyapatite.

Furthermore, calcium phosphate-based materials have been applied in research. Transfection of cells with amorphous calcium phosphates in the form of dense co-precipitates with DNA or siRNA has become an established method.[144,145,146,147,148] With a size of approximately 100 nm, these co-precipitates can enter the cell via endocytosis.[128] Then, the constructs dissolve in the acidic lysosomes, which leads to a proton sponge effect.[149] Thereby, the endosome gets ruptured and causes the transfection of the cell.[150] It has been reported that an increase in the intracellular calcium level may become harmful to cells and induce apoptosis.[151,152,153] However, for transfection purposes the Ca^{2+}-induced cell death has not been observed.[154,155,156]

Therefore, considering the use of calcium phosphate nanoparticles in advanced drug delivery systems seems to be very attractive. The backbone of the delivery system consists of biomimetic material and does not have to be degraded and removed from the body as extrinsic material. Additionally, the particles could potentially get dissolved in the lysosome while delivering the drug. In view of these attractive potential features, calcium phosphate-based materials have already been investigated for biological applications and as drug delivery systems.[129,157] Problems have arisen to reproducibly prepare stable nanoparticles. Accordingly, many attempts have been made to reliably prepare nano-sized calcium phosphate particles.[158] The very fast crystallization of amorphous calcium phosphate normally leads to large aggregates. But nano-sized calcium phosphate particles are mandatory for drug delivery applications, because particle uptake by cells is size dependent.[159,160] A crucial factor during nanoparticle synthesis is the time point of precipitation of the calcium phosphate material.[158,161] The precipitation kinetics of calcium phosphates can be controlled with organic complexing agents, such as ethylenediamine tetraacetic acid or citric acid.[162,163] Citrate ions are known to play a fundamental role in bone formation by not only stabilizing existing apatite nanocrystals, but also in crystal nucleation during biomineralization in bone.[164,165] The complexation of metal ions with hydroxycarboxylic acids to slow down kinetics was initially employed by Pechini *et al.* for the preparation of nanocrystalline metal niobates and titanates.[166] In a different approach, Eufinger *et al.* precipitated calcium phosphate nanoparticles and immediately adsorbed DNA or siRNA at the surface, which stabilized the nanoparticles.[167] Bisht *et al.* employed a reverse micro-emulsion process to slowly grow calcium phosphate nanoparticles and simultaneously encapsulated pDNA.[150] Another approach is the control of particle size by using capping agents.

Triethanolamine, ethylene glycol, and ethylenediamine tetraacetic acid have been investigated yielding calcium phosphate nanoparticles with sizes below 150 nm.[168]

Besides the size of the calcium phosphate nanoparticles, the surface charge is crucial for cellular uptake. The zeta potential of calcium phosphate nanoparticles is negative at physiological pH value.[169] Therefore, the shielding of the calcium phosphate nanoparticles comprising DNA in bovine serum albumin turned the zeta potential into positive values. Then, efficient uptake by cells was demonstrated.[170] Reports have also been published about co-precipitation of gemcitabine, siRNA and proteins with calcium phosphate to yield nanoparticles that were taken up by the cells.[171,172] Li *et al.* noted, however, that these calcium phosphate particles were not tested via systemic administration, which may have been due to strong agglomeration problems in body fluid.[158] This led them to encapsulate the calcium phosphate constructs with a lipid layer to prolong circulation time in the blood stream and to enhance particle uptake by cells. In summary, these systems rely on very specific synthesis procedures and do not allow many variations of the loadable drug, DNA, protein or siRNA. Thus, if an exchange of the drug is desired, the reaction conditions need to be adjusted because all molecules take part in the reaction. This may influence the required synthesis conditions and the properties of the entire particle construct. Therefore, these systems possess difficulties if used as a drug delivery platform in that sense.

For advanced drug delivery applications, internal mesoporosity is desirable to enable the facile exchange of drugs depending on therapeutic needs. Yao *et al.* claimed the first synthesis of mesoporous calcium phosphate nanoparticles using the surfactant template cetyltrimethylammonium bromide but with very little mesoporosity and a corresponding pore volume of only 0.0113 cm^3/g, which also could be considered as

being textural porosity.[173] The maximum known surface area for calcium phosphate-based nanoparticles was published with 315 m^2/g. Here, the authors used a microwave assisted synthesis and adenosine triphosphate as phosphate source.[174] In comparison with the established mesoporous silica based nanoparticles, the surface areas of calcium phosphate-based materials obtained so far are rather small, which strongly limits the loading capacity. Nevertheless, porous calcium phosphate-based materials have been loaded with docetaxel, silybin, ibuprofen, and doxorubicin.[174,175,176,177,178]

In this context, an effective pore blocking system was missing, which led to uncontrolled release of the loaded cargo. Therefore, Li *et al.* described mesoporous calcium phosphates (BET surface area = 75 m^2/g) and added a redox-responsive closure mechanism. The premature release of a loaded fluorescent model drug added up to 20 % of the total loading amount.[179] In another approach aptamers were decorated at the surface of rod-shaped mesoporous calcium phosphate nanoparticles (BET surface area = 99 m^2/g) with only 15 wt% of premature drug release.[180] However, access to an advanced and controlled release mechanism for intracellular drug delivery systems remains a big challenge in this field.[180]

Concluding, the development of mesoporous calcium phosphate-based materials for utilization as drug delivery vehicles has been a goal for researchers. Until today, the requirements for drug delivery systems could not be fulfilled satisfactorily with the use of calcium phosphate-based materials. Research needs to gain insights into the control of the precipitation kinetics in order to reproducibly obtain nanoparticles. Additionally, the nanoparticles need to stay colloidally stable over a certain time period. Furthermore, the degree of mesoporosity needs to be enhanced for efficient drug loading. In addition, the drug delivery system can only serve as a flexible

platform if the loaded drugs are exchangeable without influencing the synthesis conditions. Finally, an appropriate closure mechanism needs to be established to prevent premature release.

The following work describes in detail the synthesis and applications of mesoporous calcium phosphate-citrate, magnesium-calcium phosphate-citrate, and magnesium phosphate-citrate nanoparticles. Briefly, the combination of the Pechini process with soft templating methods and the addition of capping agents leads to the desired colloidal mesoporous calcium phosphate-citrate nanoparticles for advanced drug delivery applications. By coating the calcium phosphate-citrate nanoparticles with a lipid membrane, premature release of drugs is prevented. The tunable properties of calcium phosphate-citrate nanoparticles can induce a Ca^{2+} shock in cells, which specifically induces apoptosis. Modifying the developed synthesis approach for Ca^{2+}-based phosphate nanoparticles, an adaptation to other bivalent metal ions, for example magnesium, is achieved. Therefore, mesoporous magnesium phosphate-citrate nanoparticles were additionally utilized as biocompatible advanced drug delivery applications. This work is partially based on a publication with the World Intellectual Property Organization.[181]

1.5 References

1 J. Ferlay *et al.* Cancer incidence and mortality worldwide: sources, methods and major patterns in Globocan 2012. *International Journal of Cancer* **136,** E359-E386, (2015).

2 B. Stewart & C. P. Wild. World cancer report 2014. (2014).

3 A. Chow. Cell cycle control by oncogenes and tumor suppressors: driving the transformation of normal cells into cancerous cells. *Nature Education* **3**, (2010).

4 S. Pathak *et al.* Can cancer cells transform normal host cells into malignant cells? *British Journal of Cancer* **76,** 1134-1138, (1997).

5 B. Kopnin. Targets of oncogenes and tumor suppressors: key for understanding basic mechanisms of carcinogenesis. *Biochemistry C/C of Biokhimiia* **65,** 2-27, (2000).

6 C. J. Sherr. G1 phase progression: cycling on cue. *Cell* **79,** 551-555, (1994).

7 C. J. Sherr. Cancer cell cycles. *Science* **274,** 1672-1677, (1996).

8 A. Pardee. G1 events and regulation of cell proliferation. *Science* **246,** 603-608, (1989).

9 J. F. Kerr, A. H. Wyllie & A. R. Currie. Apoptosis: a basic biological phenomenon with wide-ranging implications in tissue kinetics. *British Journal of Cancer* **26,** 239, (1972).

10 T. G. Cotter. Apoptosis and cancer: the genesis of a research field. *Nature Reviews: Cancer* **9,** 501-507, (2009).

11 G. Makin & J. A. Hickman. Apoptosis and cancer chemotherapy. *Cell and Tissue Research* **301,** 143-152, (2000).

12 S. Fulda & K. M. Debatin. Extrinsic versus intrinsic apoptosis pathways in anticancer chemotherapy. *Oncogene* **25,** 4798-4811, (0000).

13 S. H. Kaufmann & W. C. Earnshaw. Induction of apoptosis by cancer chemotherapy. *Experimental Cell Research* **256,** 42-49, (2000).

14 M. Hassan, H. Watari, A. AbuAlmaaty, Y. Ohba & N. Sakuragi. Apoptosis and molecular targeting therapy in cancer. *BioMed Research International* **2014,** 23, (2014).

15 Y. A. Hannun. Apoptosis and the dilemma of cancer chemotherapy. *Blood* **89,** 1845-1853, (1997).

16 M. O. Hengartner. The biochemistry of apoptosis. *Nature* **407,** 770-776, (2000).

17 E. S. Alnemri *et al.* Human ICE/CED-3 protease nomenclature. *Cell* **87,** 171, (1996).

18 M. Kurokawa & S. Kornbluth. Caspases and kinases in a death grip. *Cell* **138,** 838-854, (2009).

19 U. Fischer, R. U. Janicke & K. Schulze-Osthoff. Many cuts to ruin: a comprehensive update of caspase substrates. *Cell Death and Differentiation* **10,** 76-100, (0000).

20 R. Gerl & D. L. Vaux. Apoptosis in the development and treatment of cancer. *Carcinogenesis* **26,** 263-270, (2005).

21 N. Abu, M. Akhtar, W. Ho, S. Yeap & N. Alitheen. 3-Bromo-1-Hydroxy-9,10-Anthraquinone (BHAQ) Inhibits Growth and Migration of the Human Breast Cancer Cell Lines MCF-7 and MDA-MB231. *Molecules* **18,** 10367, (2013).

22 L. Brannon-Peppas & J. O. Blanchette. Nanoparticle and targeted systems for cancer therapy. *Advanced Drug Delivery Reviews* **64,** 206-212, (2012).
23 D. Peer *et al.* Nanocarriers as an emerging platform for cancer therapy. *Nature Nanotechnology* **2,** 751-760, (2007).
24 R. A. Petros & J. M. DeSimone. Strategies in the design of nanoparticles for therapeutic applications. *Nature Reviews: Drug Discovery* **9,** 615-627, (2010).
25 V. Wagner, A. Dullaart, A.-K. Bock & A. Zweck. The emerging nanomedicine landscape. *Nature Biotechnology* **24,** 1211-1217, (2006).
26 L. Zhang *et al.* Nanoparticles in medicine: therapeutic applications and developments. *Clinical Pharmacology and Therapeutics* **83,** 761-769, (2008).
27 M. E. Davis, Z. Chen & D. M. Shin. Nanoparticle therapeutics: an emerging treatment modality for cancer. *Nature Reviews: Drug Discovery* **7,** 771-782, (2008).
28 H. Jatzkewitz. An ein kolloidales blutplasma-ersatzmittel (polyvinylpyrrolidon) gebundenes peptamin (glycyl-L-leucyl-mezcalin) als neuartige depotform für biologisch aktive primare amine (mezcalin). *Zeitschrift für Naturforschung B* **10,** 27–31 (1955).
29 J. R. Benton. Strength and elasticity of spider thread. *American Journal of Science* **24,** 75-78, (1907).
30 International Organization for Standardization. *Nanotechnologies - Vocabulary - Part 1: Core terms*. Edition ISO/TS 80004-1, (2015).
31 D. R. Boverhof *et al.* Comparative assessment of nanomaterial definitions and safety evaluation considerations. *Regulatory Toxicology and Pharmacology* **73,** 137-150, (2015).
32 Official Journal of the European Union. *Commission Recommendation of 18 October 2011 on the Definition of Nanomaterial*. Edition L275, (2011).
33 FDA. Considering whether an FDA-regulated product involves the application of nanotechnology. *U.S. Food and Drug Administration*, (2014).
34 P. Mulvaney. Not all that's gold does glitter. *MRS bulletin* **26,** 1009-1014, (2001).
35 K. Tseng, J. Huang, C. Liao, D. Tien & T. Tsung. Preparation of gold ethanol colloid by the arc discharge method. *Journal of Alloys and Compounds* **472,** 446-450, (2009).
36 M. Faraday. The bakerian lecture: experimental relations of gold (and other metals) to light. *Philosophical Transactions of the Royal Society of London* **147,** 145-181, (1857).
37 R. Feynman. There's plenty of room at the bottom. *Engineering and Science* **23,** 22-36, (1960).
38 H. W. Kroto, J. R. Heath, S. C. O'Brien, R. F. Curl & R. E. Smalley. C60: Buckminsterfullerene. *Nature* **318,** 162-163, (1985).
39 S. Iijima. Helical microtubules of graphitic carbon. *Nature* **354,** 56-58, (1991).
40 S. Iijima & T. Ichihashi. Single-shell carbon nanotubes of 1-nm diameter. *Nature* **363,** 603-605, (1993).
41 H. Hidaka, S. Horikoshi, N. Serpone & J. Knowland. *In vitro* photochemical damage to DNA, RNA and their bases by an inorganic sunscreen agent on exposure to UVA and UVB radiation. *Journal of Photochemistry and Photobiology A: Chemistry* **111,** 205-213, (1997).
42 A. Sclafani & J. Herrmann. Comparison of the photoelectronic and photocatalytic activities of various anatase and rutile forms of titania in pure

liquid organic phases and in aqueous solutions. *The Journal of Physical Chemistry* **100,** 13655-13661, (1996).

43 Y. Li, N. Lee, E. Lee, J. Song & S. Kim. The characterization and photocatalytic properties of mesoporous rutile TiO_2 powder synthesized through self-assembly of nano crystals. *Chemical Physics Letters* **389,** 124-128, (2004).

44 C. N. R. Rao, A. Müller & A. K. Cheetham. *The Chemistry of Nanomaterials: Synthesis, Properties and Applications*. (John Wiley & Sons, 2006).

45 European Commision. *Nanotechnology: the Invisible Giant Tackling Europe's Future Challenges*. (European Union, 2013).

46 National Research Council, Division on Engineering and Physical Sciences, National Materials Advisory Board & Committee to Review the National Nanotechnology Initiative. *A Matter of Size: Triennial Review of the National Nanotechnology Initiative*. (National Academies Press, 2006).

47 Lux Research Inc. *Sizing Nanotechnology´s Value Chain*. (Lux Research Inc., 2004).

48 K. Cho, X. Wang, S. Nie, Z. Chen & D. M. Shin. Therapeutic nanoparticles for drug delivery in cancer. *Clinical Cancer Research* **14,** 1310-1316, (2008).

49 T. M. Allen. Ligand-targeted therapeutics in anticancer therapy. *Nature Reviews: Cancer* **2,** 750-763, (2002).

50 R. Duncan. Polymer conjugates as anticancer nanomedicines. *Nature Reviews: Cancer* **6,** 688-701, (2006).

51 M. Ferrari. Cancer nanotechnology: opportunities and challenges. *Nature Reviews: Cancer* **5,** 161-171, (2005).

52 G. Sledge & K. Miller. Exploiting the hallmarks of cancer: the future conquest of breast cancer. *European Journal of Cancer* **39,** 1668-1675, (2003).

53 Y. Matsumura & H. Maeda. A new concept for macromolecular therapeutics in cancer chemotherapy: mechanism of tumoritropic accumulation of proteins and the antitumor agent smancs. *Cancer Research* **46,** 6387-6392, (1986).

54 T. Tanaka, S. Shiramoto, M. Miyashita, Y. Fujishima & Y. Kaneo. Tumor targeting based on the effect of enhanced permeability and retention (EPR) and the mechanism of receptor-mediated endocytosis (RME). *International Journal of Pharmaceutics* **277,** 39-61, (2004).

55 Y. H. Bae & K. Park. Targeted drug delivery to tumors: myths, reality and possibility. *Journal of Controlled Release* **153,** 198-205, (2011).

56 I. I. Slowing, J. L. Vivero-Escoto, C.-W. Wu & V. S.-Y. Lin. Mesoporous silica nanoparticles as controlled release drug delivery and gene transfection carriers. *Advanced Drug Delivery Reviews* **60,** 1278-1288, (2008).

57 T. M. Allen & P. R. Cullis. Drug delivery systems: entering the mainstream. *Science* **303,** 1818-1822, (2004).

58 O. C. Farokhzad & R. Langer. Nanomedicine: developing smarter therapeutic and diagnostic modalities. *Advanced Drug Delivery Reviews* **58,** 1456-1459, (2006).

59 H. Jatzkewitz. Incorporation of physiologically-active substances into a colloidal blood plasma substitute. I. Incorporation of mescaline peptide into polyvinylpyrrolidone. *Zeitschrift für Physiologische Chemie* **297,** 149-156, (1954).

60 A. Bangham, M. M. Standish & J. Watkins. Diffusion of univalent ions across the lamellae of swollen phospholipids. *Journal of Molecular Biology* **13,** 238-IN227, (1965).

61 H. Ringsdorf. *Structure and Properties of Pharmacologically Active Polymers* at *Journal of Polymer Science: Polymer Symposia.* 135-153 (Wiley Online Library, **1975**).

62 R. Langer & J. Folkman. Polymers for the sustained release of proteins and other macromolecules. (1976).

63 R. Gref *et al.* Biodegradable long-circulating polymeric nanospheres. *Science* **263,** 1600-1603, (1994).

64 S. Polarz & B. Smarsly. Nanoporous materials. *Journal of Nanoscience and Nanotechnology* **2,** 581-612, (2002).

65 J. Rouquerol *et al.* Recommendations for the characterization of porous solids (Technical Report). *Pure and Applied Chemistry* **66,** 1739-1758, (1994).

66 D. Breck, W. Eversole, R. Milton, T. Reed & T. Thomas. Crystalline zeolites. I. The properties of a new synthetic zeolite, type A. *Journal of the American Chemical Society* **78,** 5963-5972, (1956).

67 T. B. Reed & D. Breck. Crystalline zeolites. II. Crystal structure of synthetic zeolite, type A. *Journal of the American Chemical Society* **78,** 5972-5977, (1956).

68 F. R. Ribeiro. *Zeolites: Science and Technology*. Volume 80 (Springer Science & Business Media, 2012).

69 P. M. Visakh & M. J. M. Morlanes. *Nanomaterials and Nanocomposites: Zero- to Three-Dimensional Materials and Their Composites*. (Wiley, 2016).

70 P. A. Jacobs, E. M. Flanigen, J. C. Jansen & H. van Bekkum. *Introduction to Zeolite Science and Practice*. (Elsevier Science, 2001).

71 D. Breck. *Zeolite Molecular Sieves: Structure, Chemistry, and Use*. (Wiley New York, 1973).

72 H. Owen & E. Demmel. Method and system for controlling the activity of a crystalline zeolite cracking catalyst. *US Patent 3,926,778*, (1975).

73 G. Ozin, A. Arsenault & L. Cademartiri. *Nanochemistry: a Chemical Approach to Nanomaterials*. (Royal Society of Chemistry, 2009).

74 L. Bonifacio, B. Lotsch & G. Ozin. *Periodic Mesoporous Materials: Holes Filled with Opportunities* in *Comprehensive Nanoscience and Technology*, Chapter 5.04, 69-125 (Academic Press, 2011).

75 M. G. Rimoli *et al.* Synthetic zeolites as a new tool for drug delivery. *Journal of Biomedical Materials Research Part A* **87A,** 156-164, (2008).

76 E. Khodaverdi, H. A. Soleimani, F. Mohammadpour & F. Hadizadeh. Synthetic zeolites as controlled-release delivery systems for anti-inflammatory drugs. *Chemical Biology & Drug Design* **87,** 849-857, (2016).

77 R. Marega, E. A. Prasetyanto, C. Michiels, L. De Cola & D. Bonifazi. Fast targeting and cancer cell uptake of luminescent antibody-nanozeolite bioconjugates. *Small* **12,** 5431-5441, (2016).

78 P. Horcajada *et al.* Influence of pore size of MCM-41 matrices on drug delivery rate. *Microporous and Mesoporous Materials* **68,** 105-109, (2004).

79 C. Kresge, M. Leonowicz, W. Roth, J. Vartuli & J. Beck. Ordered mesoporous molecular sieves synthesized by a liquid-crystal template mechanism. *Nature* **359,** 710-712, (1992).

80 F. Hoffmann, M. Cornelius, J. Morell & M. Fröba. Silica-based mesoporous organic–inorganic hybrid materials. *Angewandte Chemie International Edition* **45,** 3216-3251, (2006).

81 Q. Cai *et al.* Dilute solution routes to various controllable morphologies of MCM-41 silica with a basic medium. *Chemistry of Materials* **13,** 258-263, (2001).

82 I. I. Slowing, B. G. Trewyn, S. Giri & V. Y. Lin. Mesoporous silica nanoparticles for drug delivery and biosensing applications. *Advanced Functional Materials* **17,** 1225-1236, (2007).

83 D. Shephard *et al.* Bimetallic nanoparticle catalysts anchored inside mesoporous silica. *Angewandte Chemie International Edition in English* **36,** 2242-2245, (1997).

84 I. Slowing, B. Trewyn, S. Giri & V. Lin. Mesoporous silica nanoparticles for drug delivery and biosensing applications. *Advanced Functional Materials* **17,** 1225-1236, (2007).

85 I. Slowing, J. Vivero-Escoto, C. Wu & V. Lin. Mesoporous silica nanoparticles as controlled release drug delivery and gene transfection carriers. *Advanced Drug Delivery Reviews* **60,** 1278-1288, (2008).

86 H. Lee, D. Sung, M. Veerapandian, K. Yun & S. Seo. PEGylated polyethyleneimine grafted silica nanoparticles: enhanced cellular uptake and efficient siRNA delivery. *Analytical and Bioanalytical Chemistry* **400,** 535-545, (2011).

87 M. Vallet-Regi, A. Ramila, R. Del Real & J. Pérez-Pariente. A new property of MCM-41: drug delivery system. *Chemistry of Materials* **13,** 308-311, (2001).

88 C. J. Brinker & G. W. Scherer. *Sol-Gel Science*. (Academic Press, Inc., 1990).

89 Z. Li, J. C. Barnes, A. Bosoy, J. F. Stoddart & J. I. Zink. Mesoporous silica nanoparticles in biomedical applications. *Chemical Society Reviews* **41,** 2590-2605, (2012).

90 J. Israelachvili. *Intermolecular and Surface Forces*. Edition 2, (Harcourt Brace & Company, 1998).

91 K. Sing *et al.* IUPAC Manual of symbols and terminology appendix 2, Pt. 1. *Colloid and Surface Chemistry, Pure Appl. Chem* **31,** 578, (1972).

92 C. Argyo, V. Weiss, C. Bräuchle & T. Bein. Multifunctional mesoporous silica nanoparticles as a universal platform for drug delivery. *Chemistry of Materials* **26,** 435-451, (2014).

93 J. Kecht, A. Schlossbauer & T. Bein. Selective functionalization of the outer and inner surfaces in mesoporous silica nanoparticles. *Chemistry of Materials* **20,** 7207-7214, (2008).

94 V. Cauda, A. Schlossbauer, J. Kecht, A. Zürner & T. Bein. Multiple core−shell functionalized colloidal mesoporous silica nanoparticles. *Journal of the American Chemical Society* **131,** 11361-11370, (2009).

95 K. Möller *et al.* Highly efficient siRNA delivery from core–shell mesoporous silica nanoparticles with multifunctional polymer caps. *Nanoscale* **8,** 4007-4019, (2016).

96 Y.-Z. You, K. K. Kalebaila, S. L. Brock & D. Oupický. Temperature-controlled uptake and release in PNIPAM-modified porous silica nanoparticles. *Chemistry of Materials* **20,** 3354-3359, (2008).

97 A. Schlossbauer *et al.* A programmable DNA-based molecular valve for colloidal mesoporous silica. *Angewandte Chemie International Edition* **49,** 4734-4737, (2010).

98 A. Schlossbauer, J. Kecht & T. Bein. Biotin–avidin as a protease-responsive cap system for controlled guest release from colloidal mesoporous silica. *Angewandte Chemie International Edition* **48,** 3092-3095, (2009).
99 V. Cauda, C. Argyo, A. Schlossbauer & T. Bein. Controlling the delivery kinetics from colloidal mesoporous silica nanoparticles with pH-sensitive gates. *Journal of Materials Chemistry* **20,** 4305-4311, (2010).
100 S. Datz *et al.* Genetically designed biomolecular capping system for mesoporous silica nanoparticles enables receptor-mediated cell uptake and controlled drug release. *Nanoscale* **8,** 8101-8110, (2016).
101 S. Niedermayer *et al.* Multifunctional polymer-capped mesoporous silica nanoparticles for pH-responsive targeted drug delivery. *Nanoscale* **7,** 7953-7964, (2015).
102 S. A. Mackowiak *et al.* Targeted drug delivery in cancer cells with red-light photoactivated mesoporous silica nanoparticles. *Nano Letters* **13,** 2576-2583, (2013).
103 V. Weiss *et al.* Dendronized mesoporous silica nanoparticles provide an internal endosomal escape mechanism for successful cytosolic drug release. *Microporous and Mesoporous Materials* **227,** 242-251, (2016).
104 V. Cauda, C. Argyo & T. Bein. Impact of different PEGylation patterns on the long-term bio-stability of colloidal mesoporous silica nanoparticles. *Journal of Materials Chemistry* **20,** 8693-8699, (2010).
105 T. Xia *et al.* Polyethyleneimine coating enhances the cellular uptake of mesoporous silica nanoparticles and allows safe delivery of siRNA and DNA constructs. *ACS Nano* **3,** 3273-3286, (2009).
106 S. H. van Rijt *et al.* Protease-mediated release of chemotherapeutics from mesoporous silica nanoparticles to ex vivo human and mouse lung tumors. *ACS Nano* **9,** 2377-2389, (2015).
107 R. Duncan. The dawning era of polymer therapeutics. *Nature Reviews: Drug Discovery* **2,** 347-360, (2003).
108 R. Duncan. Drug-polymer conjugates: potential for improved chemotherapy. *Anti-Cancer Drugs* **3,** 175-210, (1992).
109 J. M. Chan, P. M. Valencia, L. Zhang, R. Langer & O. C. Farokhzad. Polymeric nanoparticles for drug delivery. *Cancer Nanotechnology: Methods and Protocols***,** 163-175, (2010).
110 K. S. Soppimath, T. M. Aminabhavi, A. R. Kulkarni & W. E. Rudzinski. Biodegradable polymeric nanoparticles as drug delivery devices. *Journal of Controlled Release* **70,** 1-20, (2001).
111 K. Kataoka, A. Harada & Y. Nagasaki. Block copolymer micelles for drug delivery: design, characterization and biological significance. *Advanced Drug Delivery Reviews* **47,** 113-131, (2001).
112 A. Lavasanifar, J. Samuel & G. S. Kwon. Poly (ethylene oxide)-block-poly (L-amino acid) micelles for drug delivery. *Advanced Drug Delivery Reviews* **54,** 169-190, (2002).
113 A. Sharma & U. S. Sharma. Liposomes in drug delivery: progress and limitations. *International Journal of Pharmaceutics* **154,** 123-140, (1997).
114 G. Gregoriadis & A. T. Florence. Liposomes in drug delivery. *Drugs* **45,** 15-28, (1993).
115 M. Liu & J. M. Fréchet. Designing dendrimers for drug delivery. *Pharmaceutical Science & Technology Today* **2,** 393-401, (1999).

116 R. Esfand & D. A. Tomalia. Poly (amidoamine)(PAMAM) dendrimers: from biomimicry to drug delivery and biomedical applications. *Drug Discovery Today* **6,** 427-436, (2001).

117 A. Bianco, K. Kostarelos & M. Prato. Applications of carbon nanotubes in drug delivery. *Current Opinion in Chemical Biology* **9,** 674-679, (2005).

118 Z. Liu *et al.* Drug delivery with carbon nanotubes for *in vivo* cancer treatment. *Cancer Research* **68,** 6652-6660, (2008).

119 S. C. Alley, N. M. Okeley & P. D. Senter. Antibody–drug conjugates: targeted drug delivery for cancer. *Current Opinion in Chemical Biology* **14,** 529-537, (2010).

120 S. Datz, H. Engelke, C. v. Schirnding, L. Nguyen & T. Bein. Lipid bilayer-coated curcumin-based mesoporous organosilica nanoparticles for cellular delivery. *Microporous and Mesoporous Materials* **225,** 371-377, (2016).

121 P. Horcajada *et al.* Porous metal-organic-framework nanoscale carriers as a potential platform for drug delivery and imaging. *Nature Materials* **9,** 172-178, (2010).

122 P. Horcajada *et al.* Metal–organic frameworks as efficient materials for drug delivery. *Angewandte Chemie* **118,** 6120-6124, (2006).

123 S. Ghaderi, B. Ramesh & A. M. Seifalian. Fluorescence nanoparticles "quantum dots" as drug delivery system and their toxicity: a review. *Journal of Drug Targeting* **19,** 475-486, (2011).

124 S. V. Dorozhkin & M. Epple. Biological and medical significance of calcium phosphates. *Angewandte Chemie-International Edition* **41,** 3130-3146, (2002).

125 L. C. Palmer, C. J. Newcomb, S. R. Kaltz, E. D. Spoerke & S. I. Stupp. Biomimetic systems for hydroxyapatite mineralization inspired by bone and enamel. *Chemical Reviews* **108,** 4754-4783, (2008).

126 L. L. Hench. Bioceramics. *Journal of the American Ceramic Society* **81,** 1705-1728, (1998).

127 S. V. Dorozhkin. Calcium orthophosphates in nature, biology and medicine. *Materials* **2,** 399-498, (2009).

128 M. Epple *et al.* Application of calcium phosphate nanoparticles in biomedicine. *Journal of Materials Chemistry* **20,** 18-23, (2010).

129 M. Vallet-Regi. Revisiting ceramics for medical applications. *Dalton Transactions***,** 5211-5220, (2006).

130 L. H. Wong, B. Tio & X. Miao. Functionally graded tricalcium phosphate/fluoroapatite composites. *Materials Science and Engineering: C* **20,** 111-115, (2002).

131 Q. Hu *et al.* Effect of crystallinity of calcium phosphate nanoparticles on adhesion, proliferation, and differentiation of bone marrow mesenchymal stem cells. *Journal of Materials Chemistry* **17,** 4690-4698, (2007).

132 M. JARCHO. Calcium phosphate ceramics as hard tissue prosthetics. *Clinical Orthopaedics and Related Research* **157,** 259-278, (1981).

133 G. Daculsi. Biphasic calcium phosphate concept applied to artificial bone, implant coating and injectable bone substitute. *Biomaterials* **19,** 1473-1478, (1998).

134 H. Petite *et al.* Tissue-engineered bone regeneration. *Nature Biotechnology* **18,** 959-963, (2000).

135 P. Layrolle, A. Ito & T. Tateishi. Sol-gel synthesis of amorphous calcium phosphate and sintering into microporous hydroxyapatite bioceramics. *Journal of the American Ceramic Society* **81,** 1421-1428, (1998).

136 J. Mahamid, A. Sharir, L. Addadi & S. Weiner. Amorphous calcium phosphate is a major component of the forming fin bones of zebrafish: indications for an amorphous precursor phase. *Proceedings of the National Academy of Sciences* **105,** 12748-12753, (2008).
137 C. Combes & C. Rey. Amorphous calcium phosphates: synthesis, properties and uses in biomaterials. *Acta Biomaterialia* **6,** 3362-3378, (2010).
138 J. Mahamid *et al.* Mapping amorphous calcium phosphate transformation into crystalline mineral from the cell to the bone in zebrafish fin rays. *Proceedings of the National Academy of Sciences* **107,** 6316-6321, (2010).
139 J. Tao, H. Pan, Y. Zeng, X. Xu & R. Tang. Roles of amorphous calcium phosphate and biological additives in the assembly of hydroxyapatite nanoparticles. *The Journal of Physical Chemistry B* **111,** 13410-13418, (2007).
140 S. Takagi, L. C. Chow & K. Ishikawa. Formation of hydroxyapatite in new calcium phosphate cements. *Biomaterials* **19,** 1593-1599, (1998).
141 E. C. Reynolds. Anticariogenic complexes of amorphous calcium phosphate stabilized by casein phosphopeptides: a review. *Special Care in Dentistry* **18,** 8-16, (1998).
142 E. Reynolds. Remineralization of enamel subsurface lesions by casein phosphopeptide-stabilized calcium phosphate solutions. *Journal of Dental Research* **76,** 1587-1595, (1997).
143 N. Blumenthal, F. Betts & A. Posner. Stabilization of amorphous calcium phosphate by Mg and ATP. *Calcified Tissue International* **23,** 245-250, (1977).
144 C. A. Chen & H. Okayama. Calcium phosphate-mediated gene transfer: a highly efficient transfection system for stably transforming cells with plasmid DNA. *Biotechniques* **6,** 632, (1988).
145 M. Jordan, A. Schallhorn & F. M. Wurm. Transfecting mammalian cells: optimization of critical parameters affecting calcium-phosphate precipitate formation. *Nucleic Acids Research* **24,** 596-601, (1996).
146 I. Roy, S. Mitra, A. Maitra & S. Mozumdar. Calcium phosphate nanoparticles as novel non-viral vectors for targeted gene delivery. *International Journal of Pharmaceutics* **250,** 25-33, (2003).
147 C. Chen & H. Okayama. High-efficiency transformation of mammalian cells by plasmid DNA. *Molecular and Cellular Biology* **7,** 2745-2752, (1987).
148 X. Wu *et al.* Innovative delivery of siRNA to solid tumors by super carbonate apatite. *PloS One* **10,** e0116022, (2015).
149 C. Zhou *et al.* Lipid-coated nano-calcium-phosphate (LNCP) for gene delivery. *International Journal of Pharmaceutics* **392,** 201-208, (2010).
150 S. Bisht, G. Bhakta, S. Mitra & A. Maitra. pDNA loaded calcium phosphate nanoparticles: highly efficient non-viral vector for gene delivery. *International Journal of Pharmaceutics* **288,** 157-168, (2005).
151 M. P. Mattson & S. L. Chan. Calcium orchestrates apoptosis. *Nature Cell Biology* **5,** 1041-1043, (2003).
152 C. Cui, R. Merritt, L. Fu & Z. Pan. Targeting calcium signaling in cancer therapy. *Acta Pharmaceutica Sinica B* **7,** 3-17, (2017).
153 G. R. Monteith, D. McAndrew, H. M. Faddy & S. J. Roberts-Thomson. Calcium and cancer: targeting Ca^{2+} transport. *Nature Reviews: Cancer* **7,** 519-530, (2007).

154 V. V. Sokolova, I. Radtke, R. Heumann & M. Epple. Effective transfection of cells with multi-shell calcium phosphate-DNA nanoparticles. *Biomaterials* **27,** 3147-3153, (2006).
155 J. Schwiertz, A. Wiehe, S. Gräfe, B. Gitter & M. Epple. Calcium phosphate nanoparticles as efficient carriers for photodynamic therapy against cells and bacteria. *Biomaterials* **30,** 3324-3331, (2009).
156 M. Wiemann *et al.* Oriented growth of osteoblast-like cells on two-dimensionally structured films of functionalized calcium phosphate nanoparticles on a silicon substrate. *Advanced Engineering Materials* **9,** 1077-1081, (2007).
157 D. Arcos & M. Vallet-Regí. Bioceramics for drug delivery. *Acta Materialia* **61,** 890-911, (2013).
158 J. Li, Y.-C. Chen, Y.-C. Tseng, S. Mozumdar & L. Huang. Biodegradable calcium phosphate nanoparticle with lipid coating for systemic siRNA delivery. *Journal of Controlled Release* **142,** 416-421, (2010).
159 S. Zhang, J. Li, G. Lykotrafitis, G. Bao & S. Suresh. Size-dependent endocytosis of nanoparticles. *Advanced Materials* **21,** 419-424, (2009).
160 A. Xu *et al.* A physical model for the size-dependent cellular uptake of nanoparticles modified with cationic surfactants. *International Journal of Nanomedicine* **7,** 3547-3554, (2012).
161 D. Olton *et al.* Nanostructured calcium phosphates (NanoCaPs) for non-viral gene delivery: influence of the synthesis parameters on transfection efficiency. *Biomaterials* **28,** 1267-1279, (2007).
162 K.-J. Westin & Å. C. Rasmuson. Crystal growth of aragonite and calcite in presence of citric acid, DTPA, EDTA and pyromellitic acid. *Journal of Colloid and Interface Science* **282,** 359-369, (2005).
163 E. Davies *et al.* Citrate bridges between mineral platelets in bone. *Proceedings of the National Academy of Sciences* **111,** E1354-E1363, (2014).
164 Y.-Y. Hu, A. Rawal & K. Schmidt-Rohr. Strongly bound citrate stabilizes the apatite nanocrystals in bone. *Proceedings of the National Academy of Sciences* **107,** 22425-22429, (2010).
165 W. Jiang *et al.* Biomimetically triggered inorganic crystal transformation by biomolecules: a new understanding of biomineralization. *The Journal of Physical Chemistry B* **113,** 10838-10844, (2009).
166 M. P. Pechini. Method of preparing lead and alkaline earth titanates and niobates and coating method using the same to form a capacitor. US3330697 (1967).
167 H. Eufinger *et al.* Performance of functionally graded implants of polylactides and calcium phosphate/calcium carbonate in an ovine model for computer assisted craniectomy and cranioplasty. *Biomaterials* **28,** 475-485, (2007).
168 N. Pramanik, A. Tarafdar & P. Pramanik. Capping agent-assisted synthesis of nanosized hydroxyapatite: comparative studies of their physicochemical properties. *Journal of Materials Processing Technology* **184,** 131-138, (2007).
169 P. Somasundaran. Zeta potential of apatite in aqueous solutions and its change during equilibration. *Journal of Colloid and Interface Science* **27,** 659-666, (1968).
170 T. Liu *et al.* Calcium phosphate nanoparticles as a novel nonviral vector for efficient transfection of DNA in cancer gene therapy. *Cancer Biotherapy and Radiopharmaceuticals* **20,** 141-149, (2005).

171 J. Li, Y. Yang & L. Huang. Calcium phosphate nanoparticles with an asymmetric lipid bilayer coating for siRNA delivery to the tumor. *Journal of Controlled Release* **158,** 108-114, (2012).

172 Y. Zhang, N. M. Schwerbrock, A. B. Rogers, W. Y. Kim & L. Huang. Codelivery of VEGF siRNA and gemcitabine monophosphate in a single nanoparticle formulation for effective treatment of NSCLC. *Molecular Therapy* **21,** 1559-1569, (2013).

173 J. Yao *et al.* Hydroxyapatite nanostructure material derived using cationic surfactant as a template. *Journal of Materials Chemistry* **13,** 3053-3057, (2003).

174 F. Chen *et al.* Multifunctional biodegradable mesoporous microspheres of Eu^{3+}-doped amorphous calcium phosphate: microwave-assisted preparation, pH-sensitive drug release, and bioimaging application. *Journal of Materials Chemistry B* **2,** 7132-7140, (2014).

175 G.-J. Ding *et al.* Porous microspheres of amorphous calcium phosphate: block copolymer templated microwave-assisted hydrothermal synthesis and application in drug delivery. *Journal of Colloid and Interface Science* **443,** 72-79, (2015).

176 L. Chen *et al.* Nanostructured calcium phosphate carriers for deliver of poor water-soluble drug silybin. *Materials Letters* **143,** 252-255, (2015).

177 X.-Y. Zhao, Y.-J. Zhu, F. Chen & J. Wu. Calcium phosphate nanocarriers dual-loaded with bovine serum albumin and ibuprofen: facile synthesis, sequential drug loading and sustained drug release. *Chemistry – An Asian Journal* **7,** 1610-1615, (2012).

178 I. Rodríguez-Ruiz *et al.* pH-responsive delivery of doxorubicin from citrate–apatite nanocrystals with tailored carbonate content. *Langmuir* **29,** 8213-8221, (2013).

179 D. Li *et al.* Redox-responsive nanoreservoirs based on collagen end-capped mesoporous hydroxyapatite nanoparticles for targeted drug delivery. *Journal of Materials Chemistry B* **2,** 6089-6096, (2014).

180 Z. Li *et al.* Aptamer-capped multifunctional mesoporous strontium hydroxyapatite nanovehicle for cancer-cell-responsive drug delivery and imaging. *Biomacromolecules* **13,** 4257-4263, (2012).

181 T. Bein, H. Engelke, H. Feckl & C. von Schirnding. Mesoporous calcium phosphate-citrate nanoparticles and uses thereof. PCT/EP2016/068231 (2015).

CHAPTER 2

CHARACTERIZATION

The physical and chemical characterization of the synthesized products was achieved with several techniques. Dynamic light scattering (DLS) was employed to determine the hydrodynamic diameter of the nanoparticles. Zeta potential measurements gave information about the surfaces´ electrical charge. Fluorescence microscopy was applied to visualize fluorescently labeled matter. With fluorescence spectrometry the function of the supported lipid membrane encapsulating the nanoparticles as closure mechanism was investigated. Infrared (IR) spectroscopy and solid-state nuclear magnetic resonance (ssNMR) spectroscopy revealed detailed information on the chemical composition and bonding of the obtained materials. Nitrogen sorption analysis was used to determine the pore size, the pore volume, and the specific surface area. With scanning electron microscopy (SEM) and transmission electron microscopy (TEM), the morphology and porous structure of the obtained materials were visualized. Furthermore, energy dispersive X-ray (EDX) spectroscopy and inductively coupled plasma spectroscopy (ICP) were used to identify the elementary composition of the samples. Computer tomography (CT) measurements and magnetic resonance imaging (MRI) techniques were applied for the analysis of physical properties of the functionalized nanoparticles. Thermogravimetric analysis (TGA) was used to investigate the amount of attached organic residues of the porous materials. To obtain information about crystallinity and the regularity of the pore structure, X-ray diffraction was applied.

In the following chapter the analysis methods used primarily throughout this work are described.

2.1 Dynamic Light Scattering

Dynamic light scattering (DLS) reveals information about the hydrodynamic diameter of nanoparticles in solution.[1] It is a non-destructive and fast method by measuring Brownian motion and correlating it to the hydrodynamic size of the nanoparticles. For this purpose a monochromatic and coherent light source, such as a laser, is focused in the sample solution (Figure 2.1).

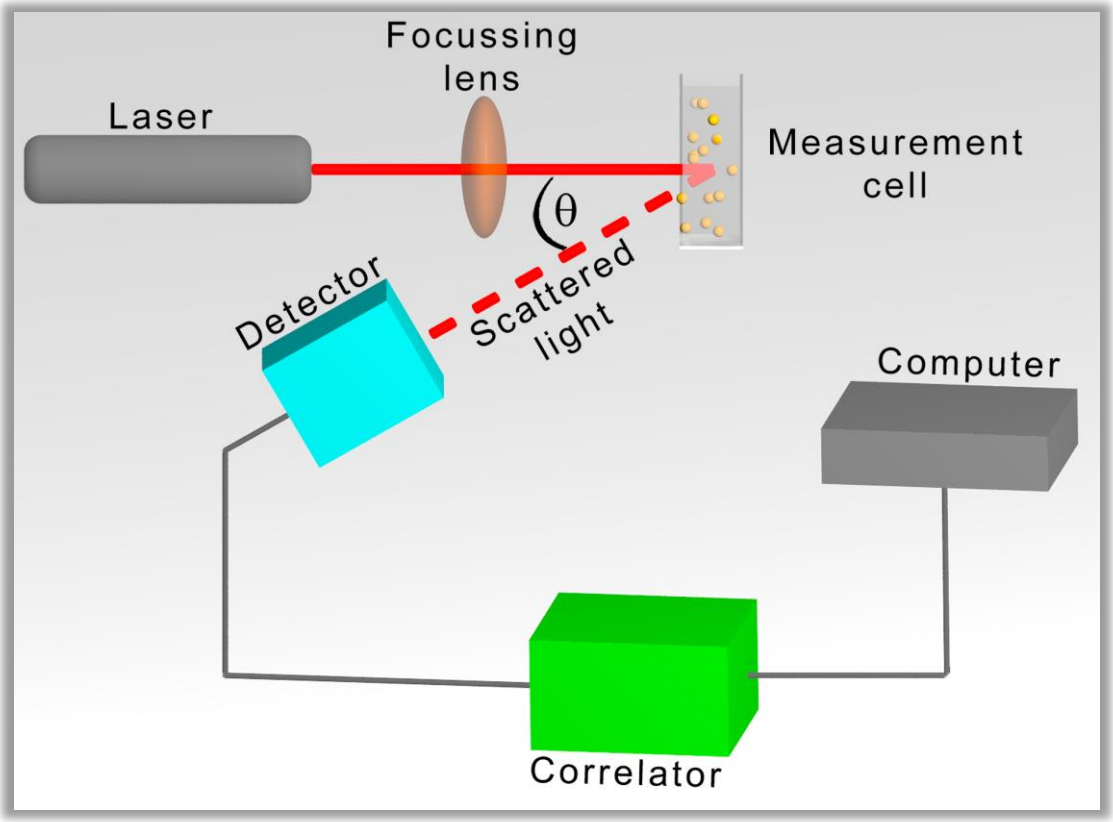

Figure 2.1: Schematic drawing of the analysis method of dymamic light scattering.

If the particle size is small compared to the wavelength of the laser beam, the latter can interfere elastically and therefore is scattered equally in all directions. This effect is known as Rayleigh scattering. The particles move in the solution due to Brownian motion. Thus, the interparticle distance varies continuously. This results in intensity fluctuations of the constructive and destructive interference of the scattered light and generates a speckle pattern. Due to the movement of the particles in the solution the

intensity of a particular spot of the speckle pattern changes with respect to the time. These changes in intensity are detected and a second order autocorrelation function is generated.

$$g^{II}(q;\tau) = \frac{\langle I(t)I(t+\tau)\rangle}{\langle I(t)\rangle^2} \tag{2.1}$$

q: Wave vector, τ: Delay time, I: Intensity.

Single-exponential decays can be gained from the above function, which give information about the diffusion coefficient D of the particles. Since smaller particles move faster than larger particles in solution, the rate of decay in the correlation function is much faster for the smaller particles. In contrast, for larger particles the rate of decay is a lot slower. In a monodisperse particle solution, exactly one single-exponential decay would be obtained. The size of the particles can then be obtained from the resulting diffusion coefficient D from the respective correlation function.

$$g^{I}(q;\tau) = e^{-q^2 D\tau} \tag{2.2}$$

q: Wave vector, τ: Delay time, D: Diffusion coefficient.

The hydrodynamic particle diameter d (spherical particle shape is assumed) can be calculated with the known diffusion coefficient D from the Stokes-Einstein equation.

$$D = \frac{k_B T}{3\pi\eta d} \tag{2.3}$$

k_B: Boltzmann constant, T: Temperature, η: Solvent viscosity,
d: Hydrodynamic particle diameter.

In the case of particles in solution being much larger than the wavelength of the incident laser beam, the particle size would be overestimated, if Rayleigh scattering

is used as calculation model. In fact the intensity of Rayleigh scattering is proportional to d^6.

$$I = I_0 \frac{1 + \cos^2\theta}{2\,R^2} \left(\frac{2\pi}{\lambda}\right)^4 \left(\frac{n^2 - 1}{n^2 + 2}\right)^2 \left(\frac{d}{2}\right)^6 \qquad (2.4)$$

I_0: Incident light intensity, R: Distance to particle, Θ: Scattering angle,
λ: Wavelength of incident light, n: Refractive index of the particles,
d: Hydrodynamic particle diameter.

Instead the Mie theory can be applied for particle size calculation, which shows no size limitations. Here, the particles are displayed as volume size distribution or number size distribution, which are proportional to d^3 and d, respectively. Therefore, a more realistic size distribution of polydisperse particle solutions with larger particles can be obtained.

Dynamic light scattering measurements were carried out using a Malvern Zetasizer-Nano instrument with a 4 mW He-Ne laser ($\lambda = 633$ nm) and an avalanche photo detector.

2.2 Zeta Potential Measurement

By measuring zeta potential (Figure 2.2), information is gained about the surface charge of nanoparticles in a solution, often depending on its pH value. Particles in suspension can exhibit surface charges that may result from functional groups bound to or constituent ions of the nanoparticle, or from ionic species strongly adsorbed to the surface.

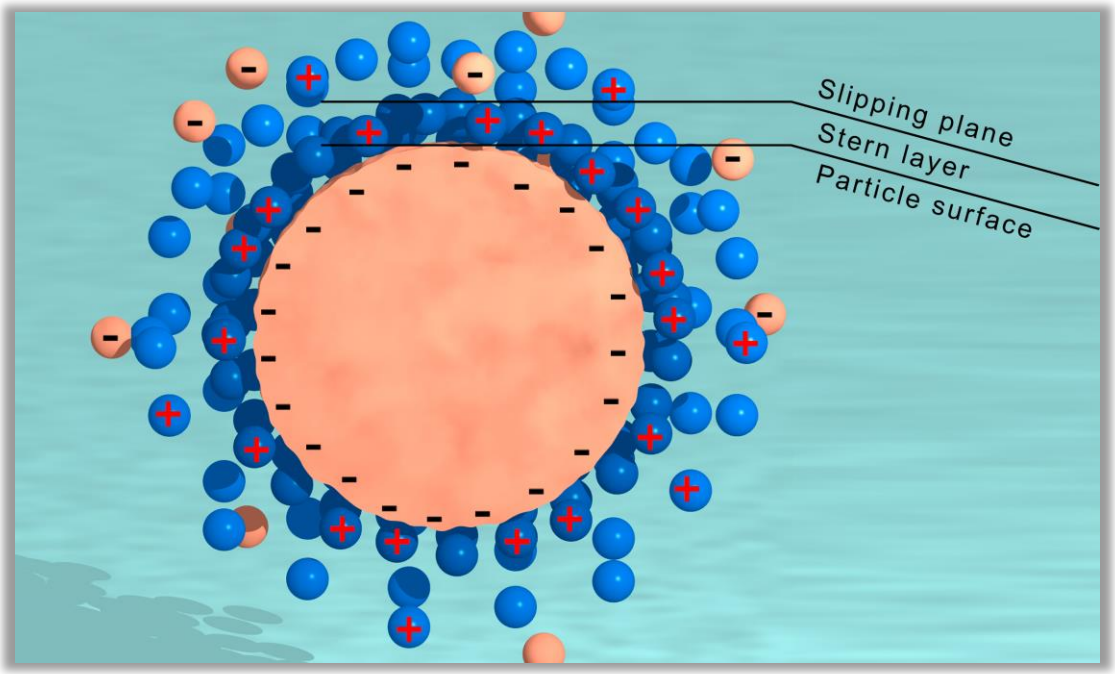

Figure 2.2: Schematic representation of the ionic interaction of a negatively charged particle with positive counter ions (Stern layer) and loosely bound ions (slipping plane).

As a result, the nanoparticle attracts counter ions with opposite charge with respect to the initial surface charge, which form a second layer - the so called Stern layer. With increasing distance from the surface of the particle the Coulomb attraction is decreasing. The resulting loosely bound ions form the slipping plane or hydrodynamic shear plane and eventually are connected to the ionic strength of the dispersion medium. The zeta potential is defined as the potential difference of a particle between the slipping plane and the dispersion medium.[2]

The zeta potential is not measurable directly, but can be obtained indirectly by measuring the electrophoretic mobility of nanoparticles in an electrical field with given strength and polarization. The particles move to the electrode of opposite charge. This motion depends on the dielectric constant of the dispersion medium, the strength of the external electric field, the viscosity of the dispersion medium, and the zeta potential. The Henry equation connects the electrophoretic mobility with the zeta potential.[3] The formula is given in equation (2.5).

$$U_E = \frac{2\varepsilon\zeta f(\kappa\alpha)}{3\eta} \tag{2.5}$$

U_E: Electrophoretic mobility, ζ: Zeta potential, $f(\kappa\alpha)$: Henry function, η: Viscosity of the dispersion medium.

The electrophoretic mobility is measured by using Laser Doppler Velocimetry. The laser beam with the incident frequency f_L scatters at the particle moving with the speed $\vec{v}$. This leads to a frequency shift f of the emitter´s frequency, which is depicted in equation (2.6).

$$f = f_L\left(1 - \frac{\vec{v}}{c}(\overrightarrow{e_L} - \overrightarrow{e_D})\right) \tag{2.6}$$

f: Frequency of the scattered light, f_L: Frequency of the laser beam, $\vec{v}$: Speed of the particles in solution, c: Speed of light, $\overrightarrow{e_L}$: Direction of the incident beam, $\overrightarrow{e_D}$: Direction from particle to the stationary detector.

The frequency shift of the incident beam passing through the suspension is then used to determine the velocity of the particles. The Hückel approximation is an established method for particles smaller than 200 nm and low dielectric constant media. The Henry function $f(\kappa\alpha)$ in this case becomes 1.0. The Smoluchowski approximation is used for particles larger than 200 nm and solutions with salt concentrations > 1 mM.

Then the Henry function $f(\kappa\alpha)$ becomes 1.5. With these approximations the zeta potential of the particles can be calculated.

Zeta potential measurements were carried out using a Malvern Zetasizer-Nano instrument with a 4 mW He-Ne laser (λ = 633 nm) and an avalanche photo detector.

2.3 Thermogravimetric Analysis

Thermogravimetric analysis (TGA) was used to gain information about the quantitative amounts of attached organic moieties and/or adsorbed guest molecules. Thereby, the mass change of the sample related to the temperature of a heating ramp is investigated.[4] While the temperature is raised at a constant heating rate the sample is weighed. During a heating process different reactions can occur. The sample can either evaporate, sublime or react/decompose. Depending on the given conditions the sample can also react via oxidation or reduction. This is controlled by an inert gas or a synthetic air atmosphere. All these processes can result in a change of the sample mass. Additionally, a mass change at a specific temperature can be associated with a specific component or intermediate. By carrying out a simultaneous measurement of differential scanning calorimetry (DSC), conclusions about physical and chemical modifications can be made. Hereby, an inert reference is compared to the sample during the heating process and the amount of heat required to increase the sample temperature is recorded. Therefore, DSC gives information about endothermic or exothermic processes related to a mass change in TGA. Desorption processes are endothermic, e.g. desorption of H_2O, while combustions are of exothermic nature, e.g. decomposition of citric acid to CO_2.

Thermogravimetric analysis of the samples in this work was performed on a Netzsch STA 440 C TG/DSC in a stream of synthetic air with a flow rate of 25 mL/min and a heating rate of 10 K/min.

2.4 Infrared and Raman Spectroscopy

For infrared (IR) spectroscopy radiation between 200 and 4000 cm^{-1} is predominantly used to gain information about the vibrational and rotational energy states of a sample.[5] Therefore, this technique offers great potential for determining the composition and the chemical bonding of a sample. For samples to be IR-active, the dipole moment of the molecules has to change during the excitation (Figure 2.3a).

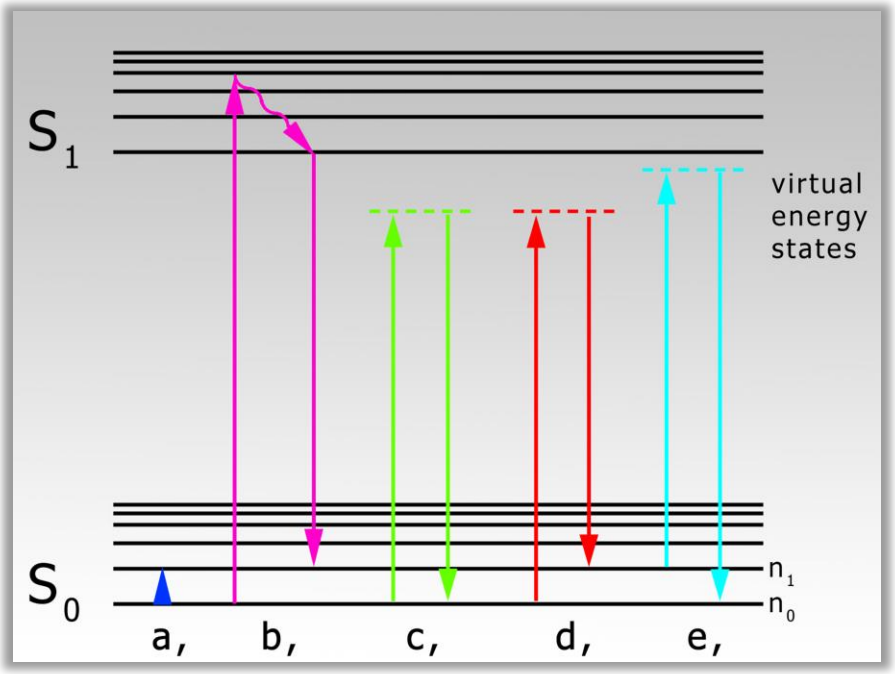

Figure 2.3: Schematic representation of electronic energy levels (S_0 and S_1), of vibrational energy states (n_0, n_1, etc.), and virtual energy states. **a,** IR absorption. **b,** Fluorescence. **c,** Rayleigh scattering. **d,** Stokes-Raman scattering. **e,** Anti-Stokes-Raman scattering.

In older instruments the intensity of the transmitted or scattered monochromatic IR light was detected after it passed through the sample and then was compared to a reference beam. With the use of the modern Fourier transform infrared spectrometer (FTIR) the analysis of samples became very fast, highly accurate, and easy. Polychromatic IR light passes through a Michelson interferometer, then through the sample and after a background subtraction, a Fourier transformation is performed with the recorded interferogram.

Raman spectroscopy relies on a different physical phenomenon in comparison to IR spectroscopy. Even though Raman spectroscopy was not used in this work, it is relevant to describe it at this point. Because Raman spectroscopy is a complementary analysis method to IR spectroscopy, it is necessary to distinguish it from IR spectroscopy. For vibrations to be Raman active, the polarizability of bonds has to change due to scattering of (monochromatic) light. The absorbed light excites an electron from a vibrational state into a virtual energy state. Immediately, the relaxation process begins and can be classified into three categories (Figure 2.3c-e). In case of an elastic scattering process relaxation brings the system back into its initial state - the emitted photon has the same energy as the absorbed photon. This process is called Rayleigh scattering and occurs most often. However, if an inelastic scattering process takes place, relaxation processes bring back the photon to either a higher or a lower energy with respect to the initial energy state. These processes are known as Stokes-Raman or Anti-Stokes-Raman scattering. With the Boltzmann factor the probability of electrons in a certain state can be calculated. The ground state N_0 exhibits the highest probability to be occupied. This leads to a greater probability that the Stokes-Raman process occurs over the Anti-Stokes-Raman process. Therefore, the Stokes-Raman process is used to illustrate Raman spectroscopy. The Boltzmann factor is depicted in equation (2.7).

$$\frac{N_1}{N_0} = e^{\left(\frac{-\Delta E}{k_B T}\right)} \quad (2.7)$$

N_0: Density of electrons at ground state, N_1: Density of electrons at excited state, ΔE: Difference of energy levels, k_B: Boltzmann constant, T: Temperature.

Infrared spectra were measured with a Thermo Scientific Nicolet iN 10 infrared microscope.

2.5 Fluorescence Microscopy

Fluorescence microscopy harnesses the physical principle of fluorescence to visualize samples.[6,7] Thus the sample needs to fulfill the criteria to be fluorescently active. Typically, fluorophores contain an aromatic ring system, like in fluorescein, quinine or some amino acids. Conjugated fatty acids can also be fluorescent. Parinaric acid can be pointed out as an example.[8] Incident light is absorbed by the fluorophore and the relaxation from the excited state can then result in fluorescence. The process that occurs between the absorption and the emission of light is usually depicted in a Jablonski diagram (Figure 2.3b). The electrons from the ground electronic energy level are excited into a higher electronic energy level with a number of possible vibrational energy levels. Internal conversion generally occurs within 10^{-12} s, when the electron relaxes to the lowest vibrational level of the excited electronic energy level S_1.[9] This is a non-radiative process leading to conformational changes in the molecule and is constrained by various environmental interactions. The return to the ground state S_0 can lead to the emission of light, which is called fluorescence. Because the energy of the emitted light is lower than that of the excitation light, this process always leads to a red shift of the emission wavelength compared to the excitation wavelength. This bathochromic shift is called Stokes shift

and is inevitable for the fluorescent process. Therefore, optical filters can be used to separate the sometimes overlapping excitation and emission spectra of molecules. Next to the fluorescent relaxation of the electrons in the excited state, there are other possible relaxation processes to the ground state S_0. These non-radiative processes include intersystem crossing (leading to phosphorescence), internal conversion (fluorescence energy transfer), or quenching.

For the observation of biological processes fluorescent microscopy has become an indispensable tool because of the possibility to resolve even single fluorescent molecules. Until the developments initiated by S. Hell the maximum resolution in optical microscopy was restricted.[10,11] The minimal distance d between the two minimally sized objects to be imaged is defined by the Abbe diffraction limit, which is proportional to the wavelength λ of the incident beam. The Abbe diffraction limit is depicted in equation (2.8).

$$d = \frac{\lambda}{2n \sin\theta} \tag{2.8}$$

d: Minimal distance between two resolvable objects, λ: Wavelength of the light, n: Index of refraction, Θ: Maximal half-angle of the cone of light.

The distance that is resolvable depends strongly on the hardware of the instrument and the aperture but is nearly half of the visible wavelength. Therefore, for a long time the maximum resolution was limited to objects with a size of approximately 200 nm.[12] Hell *et al.* developed a microscopy method for high resolution with two different lasers. The first one excites the molecule to emit fluorescence. By canceling out all fluorescence (by stimulated emission) with a second laser pulse except fluorescence in a nanometer sized volume, and by scanning over the sample, a mapped image with spatial resolution below the Abbe diffraction limit is obtained.[13]

For fluorescence microscopy images in this work we used a confocal fluorescence microscope based on the Zeiss Cell Observer SD utilizing a Yokogawa spinning disk unit CSU-X1. The aim of confocal fluorescence microscopy is to optimize the optical resolution in all three spatial dimensions compared to a standard light microscope. Minsky invented the confocal microscopy technique by combining a lamp, a lens, and a pinhole.[14] After illumination of the sample, light coming from different image plans, is rejected by the pinhole. Thus, only a single spot of the sample can be recorded by a point detector. Therefore, to acquire an entire image the sample needs to be scanned over. This time-consuming procedure was then speeded up with two spinning disks that contain multiple pinholes and lenses. This unit enables fast scanning over the sample leading to an accelerated image acquisition.

2.6 X-Ray Diffraction

Direct information about the crystallinity of materials can be obtained with the method of X-ray diffraction. Diffraction occurs if a wave encounters an obstacle or a slit. Then bending of the wave around the edges of the obstacle is observed in the region of the geometrical obstacle's shadow. If a single wavelength encounters an object with two holes, the diffracted light can interfere in a constructive or destructive way. A related effect is used for sample analysis with X-rays.

The wavelength of X-ray photons lies in the range of Ångstrom (0.1 nm)[15], which is in the same region as the scale of atoms and chemical bonds. Because the distances between atoms correspond to the wavelength, the crystalline structure can be determined. X-rays are emitted from a metal source with characteristic wavelength e.g. Cu-K_α = 1.54182 Å. The interaction of X-rays with electron densities of the lattice planes of a periodic network lead to constructive or destructive interference.

Bragg´s relation, depicted in equation (2.9),[16] is used that defines conditions at which scattered X-rays interfere in a constructive way.

$$n\lambda = 2dsin\Theta \tag{2.9}$$

n: Integer number, λ: Wavelength of X-rays, d: Distance of the lattice planes, Θ: Angle of incident X-rays.

Geometric laws lead to the solution of $2\delta = 2d\sin\Theta$ as being the difference of the traversed extra length of one of the two beams. Therefore, constructive interference can only occur if the extra length of the path difference is an integral multiple of the wavelength of X-rays and can then be detected (Figure 2.4).

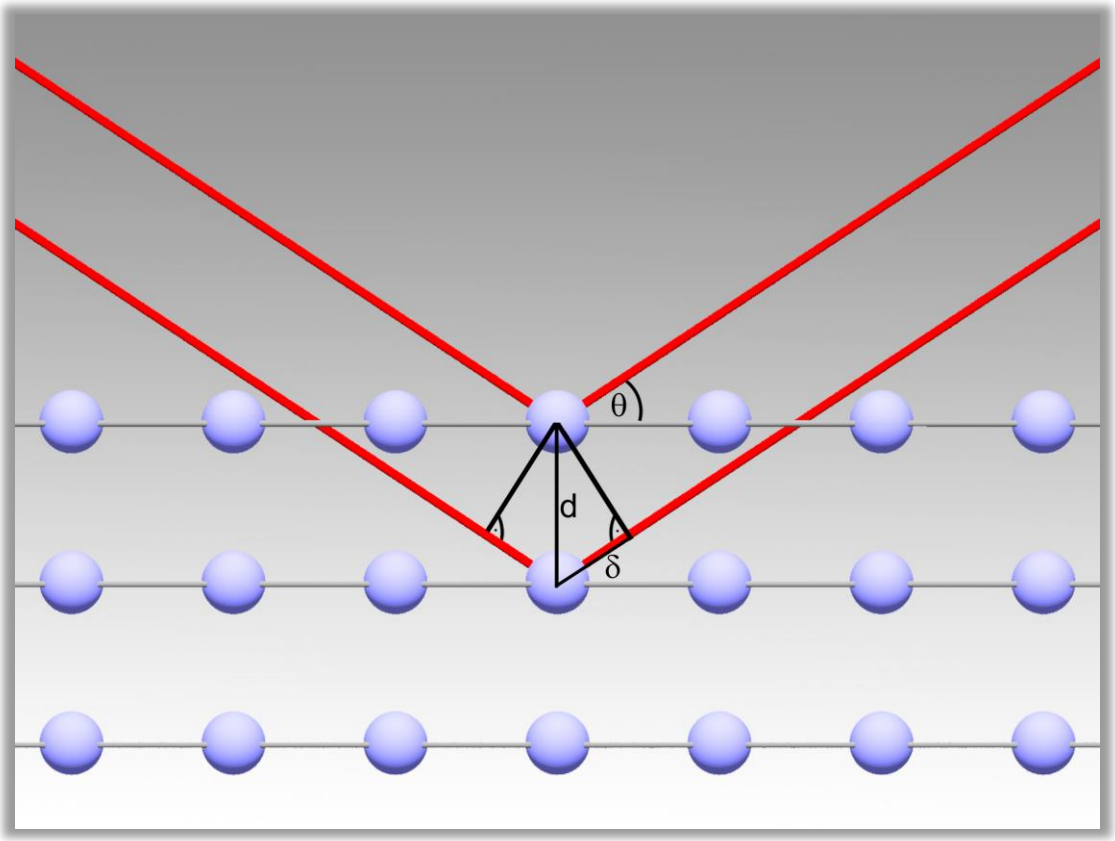

Figure 2.4: Scheme of the Bragg condition.

The smaller the distance between the lattice planes, the larger will be the angles of the reflections. Vice versa, if a material exhibits rather large regular domains, the

reflections occur at small angles. This can be observed for porous materials with periodically arranged porous structures, if the material itself is non-crystalline. Therefore, small angle X-ray scattering (SAXS) typically refers to 2Θ from 0.5° to 10°, which was used in this work for determining the mesoporous features of the nanoparticles. On the other hand, wide angle X-ray scattering (WAXS) refers to 2Θ from 10° to 60° and more, which was used for the investigation of the crystalline or amorphous nature of the nanoparticles.

XRD patterns for samples in this work were obtained with a Bruker D8 Discover X-ray diffractometer using Cu-K_α radiation with a θ/θ Bragg-Brentano scattering geometry.

2.7 Nitrogen Sorption Analysis

Sorption analysis is used to gain information about the porosity of a sample. The adsorption and desorption behavior of gas (adsorbate) on a porous substrate (adsorbent) give information about the specific surface area, the pore size distribution, the shape of the pores, and the pore volume.[17] The amount of adsorbed volume of nitrogen is measured at different relative pressures (p/p_0) at constant temperature (77 K) during a nitrogen sorption experiment. The interactions of the adsorbate and adsorbent rely on van-der-Waals forces in the case of physisorption. In that sense, the adsorbent and adsorbate stay unchanged during a sorption experiment.[18] Depending on the sorption characteristics of the material, the pore structure, and the pore size, six different major types of isotherms can be distinguished (Figure 2.5). These major types were categorized by the International Union of Pure and Applied Chemistry (IUPAC).[17]

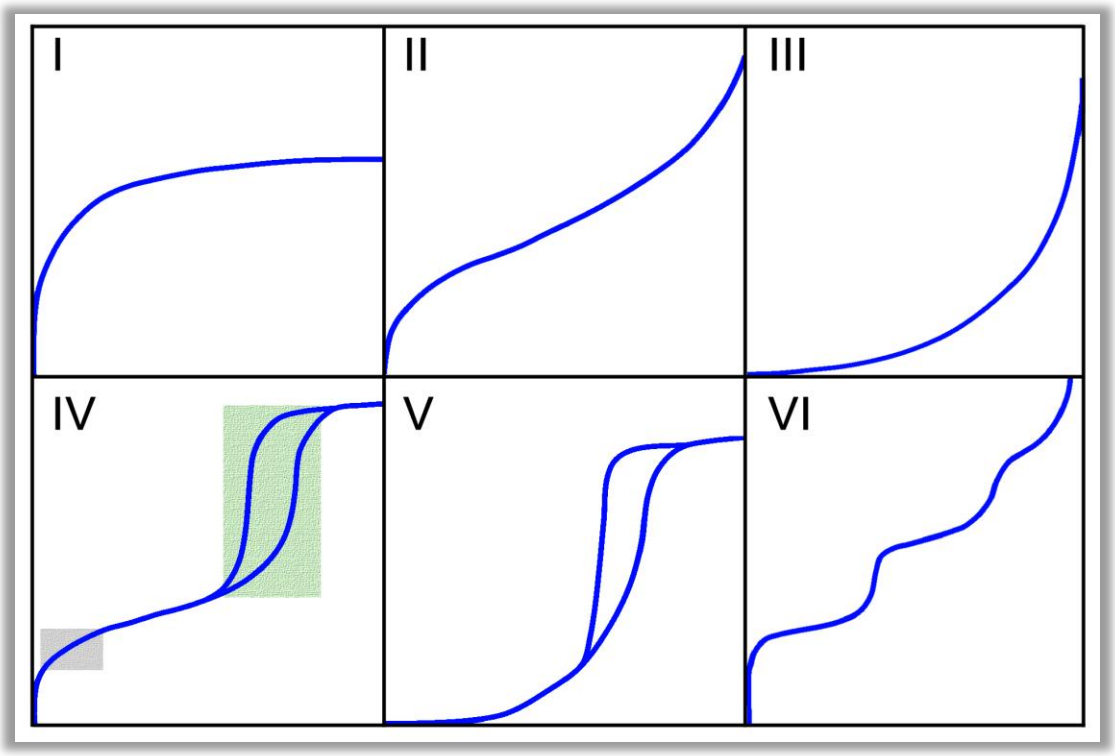

Figure 2.5: Six major types of sorption isotherms defined by the International Union of Pure and Applied Chemistry. For Typ IV isotherm the BET area (gray box) and the area of the capillary condensation (green box) are marked. Adapted from reference [17].

Type I isotherm exhibits a concave curve shape representing microporous materials with relatively small external surfaces. Type II isotherm is typical for non-porous or macroporous materials which represents materials with unrestricted monolayer-multilayer adsorption. Type III isotherm is indicated by a convex curve shape where the material is non-porous or macroporous and low adsorbate-adsorbent interaction occurs. This effect arises if the competing interaction between the adsorbate molecules is stronger. Typical for many mesoporous materials is the type IV isotherm. Characteristics of type IV isotherm include the monolayer-multilayer adsorption (gray box, Figure 2.5) and the hysteresis loop (green box, Figure 2.5), which is associated with capillary condensation phenomena. As the relative pressure is reduced, the condensed adsorbate molecules in the capillary cracks do not desorb as readily as they were adsorbed. The reason for this is that the vapor pressure over

the concave meniscus formed by the condensed liquid in the pores, is lower compared to the bulk liquid phase.[19] Type V isotherms are uncommon and related to Type III isotherms, because of the low adsorbate-adsorbent interaction. However, it resembles certain porous materials due to the observable hysteresis loop. Type VI isotherm arises with stepwise multilayer adsorption on a uniform non-porous substrate. The step height gives information about each monolayer capacity of the adsorbed layer.[17,19,20]

To calculate the surface area of the porous material, some calculation models were described. First, the Langmuir interpretation[21] was described, which is based on four assumptions:[22]

1. the adsorbing gas adsorbs into an immobile state,
2. all adsorption sites are equivalent,
3. each site can hold at most one adsorbate molecule,
4. no interaction of the adsorbate molecules on adjacent sites.

The Langmuir model predicts the adsorption of an adsorbate on an adsorbent following a Type I isotherm. Thus, in accordance with IUPAC definitions the Langmuir interpretation describes only monolayer adsorption. To also include multilayer adsorption the Brunnauer, Emmett, and Teller (BET)[23,24] theory became more relevant. In their theory the following assumptions were set:

1. there is no limit for multilayer adsorption,
2. only the first adsorbed layer has a distinct adsorption enthalpy resulting from the interaction with the adsorbate,
3. the next adsorbed layers exhibit the same adsorption enthalpy due to the fact that they only interact with the monolayer underneath.

These assumptions are depicted in equation (2.10).

$$\frac{p}{n^a(p_0 - p)} = \frac{1}{n_m^a C} + \frac{(C-1)}{n_m^a C} \cdot \frac{p}{p_0} \tag{2.10}$$

n^a: Amount of the adsorbate at a relative pressure p/p_0, n_m^a: Capacity of a single monolayer, C: BET constant.

According to the BET equation, a linear relation of $p/n^a(p_0-p)$ is plotted against the relative pressure p/p_0. The range of linearity of the BET plot is always restricted to a limited part of the isotherm, normally not above $p/p_0 = 0.3$. From that it is possible to obtain n_m^a. The BET surface area can then be calculated from equation (2.11).

$$A(BET) = n_m^a \cdot N_A \cdot a_m \tag{2.11}$$

n_m^a: Capacity of a single monolayer, N_A: Avogadro constant, a_m: Area of one single adsorbate (N_2 at 77 K = 0.162 nm^2).

For the calculation of the pore size and pore volume the BJH method[25] or the density functional theory (DFT) can be applied. The DFT method has gained more relevance and developed as standard method. DFT is used to describe the interaction between fluids and hard walls of solids. It is based on microscopic methods such as the non-local density functional theory (NLDFT)[26]. NLDFT has been demonstrated to be a validated method for the calculation of porous siliceous materials and zeolites.[26,27] This method also exhibits limitations due to the fact that smooth and homogeneous pore walls are implied. Nevertheless, the use of the NLDFT method allows for an accurate pore size analysis over the full range from micro- to mesoporous materials. An updated and modern approach relies on the quenched solid density functional theory (QSDFT). This also takes into account the surface roughness and heterogeneity of the material.[28,29]

Throughout this work the BET model was used for calculations of the surface area. Furthermore, the QSDFT method was applied for the analysis of the pore size distribution and the pore volume. The inclusion of the heterogeneity of the investigated materials led to smaller fitting errors compared to the NLDFT method.[28]

Nitrogen sorption analysis was performed on a Quantachrome Instrument Nova 4000e at 77 K. All samples were degassed previously to the measurements for 12 h at 120 °C.

2.8 Nuclear Magnetic Resonance Spectroscopy

With nuclear magnetic resonance (NMR) spectroscopy the chemical environment of certain nuclear isotopes can be investigated by applying a static magnetic field.[18,30] Therefore, the analysis of samples with NMR spectroscopy provides information about the structural properties of individual atoms. The investigated elements need to have a spin different from zero, which is the case for the elements, e.g., ^{1}H, ^{13}C, ^{19}F, and ^{31}P. An external magnetic field influences the energy states of these nuclei possessing a permanent magnetic dipole moment. These energy states are distinct with 2J+1, where J indicates the nuclear spin. Without an external magnetic field these distinct states are degenerated. The alignment of the nuclear spins is therefore dependent on the external magnetic field. For example, the spin quantum number of the nucleus for the isotope ^{13}C is ½, so the energy level will split up into two levels when a homogenous magnetic field is applied. If radio-frequency in the form of a pulse is applied at the Larmor frequency of the nuclear spin, typically ranging from a few kHz to several hundred MHz, an imbalance of the aligned nuclear spins is generated. This imbalance is leading to a variation of the magnetic field, depicted in equation (2.12).[31]

$$\omega_0 = \gamma(B_0 + B_{int}) \tag{2.12}$$

ω_0: Larmor frequency, γ: Gyromagnetic ratio, B_0: Applied external magnetic field, B_{int}: Change in magnetic field caused by the opposing electron magnetic moment.

While the nuclei relax again, characteristic electromagnetic waves are emitted. These waves are then specific for the structural properties and chemical bonds of the investigated sample. The emitted characteristic radio-frequency is picked up at the electromagnetic coil and is called free induction decay (FID). After Fourier transformation of the time-dependent domain, the frequency domain is extracted to yield the NMR spectrum.

In solid-state NMR (ssNMR) spectroscopy the anisotropic interactions interfere with the sharpness of the signals whereas in liquids this anisotropic effect is averaged out due to the very fast Brownian motion. Therefore, these dipole-dipole interactions between the magnetic moments of nearby nuclei in solids lead to line broadening in the spectra. By means of the "magic angle spinning" technique, the sample is rotating at high velocity at the angle of 54.74° with respect to the applied external magnetic field. This allows sharpening of the peaks even in solid samples.[32]

^{1}H, ^{13}C, and ^{31}P solid-state NMR (ssNMR) measurements were performed on a Bruker DSX Avance500 FT spectrometer in a 4 mm ZrO_2 rotor under magic angle spinning conditions. ^{1}H ss-NMR data were obtained at 500.2 MHz with 1 run. ^{13}C ss-NMR data were obtained at 125.8 MHz under cross-polarization conditions with 52000 transients. ^{31}P ss-NMR data were acquired at 202.5 MHz under cross-polarization conditions with 8 transients.

2.9 Scanning and Transmission Electron Microscopy

With optical microscopy there is a classical ultimate limit to the resolution due to diffraction (which can be circumvented with the modern super-resolution techniques). This fact is explained by the Abbe diffraction limit in equation (2.8), where the wavelength is proportional to the maximal resolvable object. Therefore, if the incident wavelength becomes smaller the resolution of objects is expected to become better. De Broglie postulated the wave character of moving particles possessing distinct mass in 1924. He based his theory on the previous work of Albert Einstein and Max Planck.[33] De Broglie correlated the wavelength λ with the momentum p of moving particles, see equation (2.13), which won him the Nobel Prize for Physics in 1929.

$$\lambda = \frac{h}{p} = \frac{h}{mv} \tag{2.13}$$

λ: Wavelength, h: Planck´s constant, p: Momentum,
m: Mass, v: Velocity.

Electrons are particles with known mass that generate a wavelength of roughly λ = 1.97 pm when accelerated by the high voltage of 300 kV.[34] These electrons can then be used for electron-optical imaging techniques.

Accelerated electrons that are focused with electrostatic and electromagnetic lenses onto a specimen interact in various ways with the sample (Figure 2.6). No energy is transferred to the sample and no directional change of the electrons occurs if they pass directly through the sample. These electrons exhibit the same energy as the incident beam.

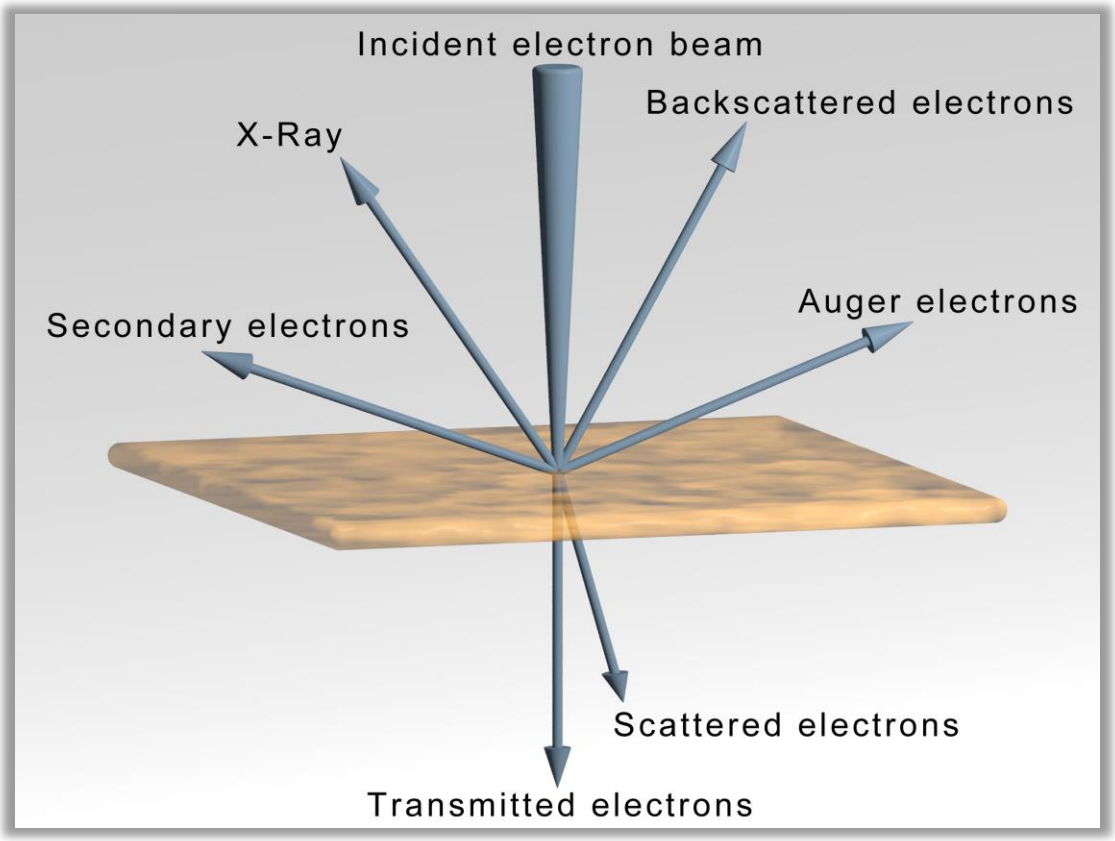

Figure 2.6: Schematic graphic of an electron beam interacting with a sample.

If the incident beam loses energy, the electrons have had interactions with the matter on their path. This electron-matter interaction is typically classified into two types of events. Thus, the electrons from the incident electron beam can be scattered elastically or inelastically.

Elastic scattering occurs when the electron is deflected from its path by Coulomb interactions with the electron clouds.[35] If the distances between the charges of the negative electron and the positive nucleus are fairly large, these electrons lose only a very small amount of energy and are mainly exploited in transmission electron microscopy. Therefore, the scattering angle of the electrons depends strongly on the elemental composition of the sample. Heavy elements deflect the electrons stronger than lighter elements leading to a variation in brightness on a detection device. The deflected electrons are recorded with a CCD camera or a fluorescent screen.[36]

Therefore, in principle the internal structure, the composition, the crystallinity, and structural defects can be visualized.

Back-scattered electrons also result from an elastic scattering event, if the path of the electrons is deflected by the nucleus into the opposite direction. This event also relies on the atomic number of the elements. Heavy elements cause more backscattering than lighter ones resulting in an intensity variation on the detection device. These gained images depict the contrast of a material and can be used for evaluation of the elemental distribution.[37]

Inelastic scattering results in the production of Auger electrons, X-rays, secondary electrons and heat, if the incident beam transfers energy to the sample.[36] In the case of the Auger effect a core electron is removed from an atom leaving a hole behind. This hole is filled with an outer shell electron of higher energy, leading to excess energy, equal to the difference of the orbital energy of the two electrons. The excess energy is transferred to a second electron of an outer shell, which then is ejected into the vacuum. This process is very surface sensitive, because the ejected electrons of deeper layers are readily absorbed within the material. Therefore, this method is mainly used for the analysis of surfaces that have been chemically modified.

Very similar to the effect of Auger electrons is the emission of X-rays. First, the incident electron hits out an inner core electron. Now the hole is filled up with an electron from an outer shell. Here, the gained energy is emitted as X-rays and not used up to produce Auger electrons. Clearly, these emitted X-rays are characteristic for each atomic level the electrons are related to and therefore can be assigned to single elements. The energy of these X-rays can be detected and used in energy dispersive X-ray analysis to yield the elemental composition of the investigated sample.

The detection of secondary electrons is the most used effect for the analysis in scanning electron microscopy. The secondary electrons are ejected from the sample very easily, if the electrons are located in the conduction or the valence band. For generating secondary electrons only small amounts of energy need to be transferred from the incident beam to the sample to overcome the work function. Then the ejection of secondary electrons into the vacuum is enabled. However, secondary electrons possess energies below 50 eV and thus only can reach the vacuum if the electrons were produced close to the sample surface.[34] Then the emerged electrons are collected at a fixed detector position.[38] In scanning electron microscopy the incident electron beam is rastered stepwise over the specimen. The detection of secondary electrons with respect to the corresponding spot leads to a contrast image of the topography. With this technique the morphology of very small structures below the Abbe limit can be investigated.

Transmission electron microscopy was performed on a JEOL JEM 2011 and a FEI TECNAI G2 at an acceleration voltage of 200 kV. Samples were prepared on a carbon-coated copper grid. Scanning electron microscopy images were obtained on a JEOL JSM-6400F and a FEI HELIOS NanoLab G3 UC. Samples were prepared on an aluminum holder and sputtered with carbon.

2.10 References

1 R. Pecora. *Dynamic Light Scattering: Applications of Photon Correlation Spectroscopy*. (Plenum Press, 1985).

2 H. Butt, K. Graf & M. Kappl. *Physics and Chemistry of Interfaces*. (Wiley VCH, 2003).

3 D. C. Henry. The cataphoresis of suspended particles. Part I. The equation of cataphoresis. *Proceedings of the Royal Society of London A: Mathematical, Physical and Engineering Sciences* **133,** 106-129, (1931).

4 G. R. Heal. *Thermogravimetry and Derivative Thermogravimetry* in *Principles of Thermal Analysis and Calorimetry*, Chapter 2, 10-54 (The Royal Society of Chemistry, 2002).

5 M. Hesse, H. Meier & B. Zeeh. *Spectroscopic Methods in Organic Chemistry*. Edition 2, (Thieme, 2008).

6 M. Sauer & J. Hofkens. *Handbook of Fluorescence Spectroscopy and Imaging: from Ensemble to Single Molecules*. (John Wiley & Sons, 2010).

7 J. R. Lakowicz. *Principles of Fluorescence Spectroscopy*. (Springer US, 2013).

8 F. A. Kuypers, J. J. van den Berg, C. Schalkwijk, B. Roelofsen & J. A. O. den Kamp. Parinaric acid as a sensitive fluorescent probe for the determination of lipid peroxidation. *Biochimica et Biophysica Acta (BBA)-Lipids and Lipid Metabolism* **921,** 266-274, (1987).

9 R. Plessow. *Entwicklung und Charakterisierung einer Methode zur Untersuchung von Makromolekülen mit Hilfe zeitaufgelöster laserinduzierter Fluoreszenz und Anregungs-Emissionsspektroskopie*. (Cuvillier, 2004).

10 S. W. Hell & J. Wichmann. Breaking the diffraction resolution limit by stimulated emission: stimulated-emission-depletion fluorescence microscopy. *Optics letters* **19,** 780-782, (1994).

11 M. Ehrenberg. *The Nobel Prize in Chemistry 2014 - Press Release*, (2014).

12 M. A. Thompson, M. D. Lew & W. Moerner. Extending microscopic resolution with single-molecule imaging and active control. *Annual Review of Biophysics* **41,** 321-342, (2012).

13 L. Möckl, D. C. Lamb & C. Bräuchle. Super-resolved fluorescence microscopy: Nobel prize in chemistry 2014 for Eric Betzig, Stefan Hell, and William E. Moerner. *Angewandte Chemie International Edition* **53,** 13972-13977, (2014).

14 M. Minsky. Microscopy apparatus. US3013467 (1961).

15 A. Markowicz. *X-Ray Physics* in *Handbook of X-Ray Spectrometry* Volume 2, Chapter 1, 1-92 (CRC Press, 2001).

16 W. H. Bragg & W. L. Bragg. The reflection of X-rays by crystals. *Proceedings of the Royal Society of London. Series A* **88,** 428-438, (1913).

17 K. S. Sing. Reporting physisorption data for gas/solid systems with special reference to the determination of surface area and porosity (Recommendations 1984). *Pure and Applied Chemistry* **57,** 603-619, (1985).

18 P. W. Atkins & J. De Paula. *Physikalische Chemie*. Edition 5, (John Wiley & Sons, 2013).

19 T. Allen. *Particle Size Measurement*. Edition 3, (Springer, 1981).

20 T. Allen. *Particle Size Measurement*. Edition 5, (Springer, 1997).

21 I. Langmuir. The adsorption of gases on plane surfaces of glass, mica and platinum. *Journal of the American Chemical Society* **40,** 1361-1403, (1918).

22 R. I. Masel. *Principles of Adsorption and Reaction on Solid Surfaces*. Volume 3 (John Wiley & Sons, 1996).
23 S. Brunauer, P. H. Emmett & E. Teller. Adsorption of gases in multimolecular layers. *Journal of the American Chemical Society* **60,** 309-319, (1938).
24 J. Rouquerol *et al.* Recommendations for the characterization of porous solids (Technical Report). *Pure and Applied Chemistry* **66,** 1739-1758, (1994).
25 E. P. Barrett, L. G. Joyner & P. P. Halenda. The determination of pore volume and area distributions in porous substances. I. Computations from nitrogen isotherms. *Journal of the American Chemical Society* **73,** 373-380, (1951).
26 Quantachrome. *Application of QSDFT (quenched solid density functional theory) - a Novel Density Functional Theory for an Accurate Pore Size Analysis of Disordered Porous Carbons*. Volume 40 (Quantachrome Instruments USA).
27 C. Lastoskie, K. E. Gubbins & N. Quirke. Pore size distribution analysis of microporous carbons: a density functional theory approach. *The Journal of Physical Chemistry* **97,** 4786-4796, (1993).
28 Quantachrome. *Application of Quenched Solid Density Functional Theory (QSDFT) for Pore Size Analysis of Cylindrical and Spherical Pore Carbons*. Volume 53 (Quantachrome Instruments).
29 P. I. Ravikovitch & A. V. Neimark. Density functional theory model of adsorption on amorphous and microporous silica materials. *Langmuir* **22,** 11171-11179, (2006).
30 S. Bienz, L. Bigler, T. Fox, M. Hesse & H. Meier. *Spektroskopische Methoden in der organischen Chemie*. (Georg Thieme Verlag, 2016).
31 J. C. Edwards. *Principles of NMR*. (Process NMR Associates LLC, 1998-2008).
32 J. Keeler. *Understanding NMR Spectroscopy*. Volume 2 (John Wiley & Sons, 2010).
33 L. De Broglie. *Recherches sur la théorie des Quanta*, Migration - Université en Cours d'affectation, (1924).
34 F. Krumeick. Properties of electrons, their interactions with matter and applications in electron microscopy. *Laboratory of Inorganic Chemistry***,** 3-08, (2011).
35 P. W. Hawkes & L. Reimer. *Transmission Electron Microscopy: Physics of Image Formation and Microanalysis*. (Springer Berlin Heidelberg, 2013).
36 D. B. Williams & C. B. Carter. *Transmission Electron Microscopy: a Textbook for Materials Science*. (Springer, 2009).
37 R. F. Egerton. *Physical Principles of Electron Microscopy: an Introduction to TEM, SEM, and AEM*. (Springer International Publishing, 2016).
38 T. E. Everhart & R. F. M. Thornley. Wide-band detector for micro-microampere low-energy electron currents. *Journal of Scientific Instruments* **37,** 246, (1960).

CHAPTER 3

THE INFLUENCE OF CITRIC ACID ON THE MESOPOROSITY OF CALCIUM PHOSPHATE-CITRATE NANOPARTICLES

Constantin von Schirnding, Markus Siegert, Durbis Pazos, Johann Feckl, Hanna Engelke, and Thomas Bein.

3.1 Introduction

Calcium phosphate-based materials are the main inorganic components found in the human body.[1,2] These materials are mainly located in the skeleton and teeth as crystalline apatite ($Ca_{10}(PO_4)_6(OH)_2$). The synthesis of apatite can be achieved using different techniques like wet precipitation, hydrothermal, or microwave assisted methods.[3,4] Depending on the synthesis strategy, different morphologies of apatite structures appear. There have been reports about rod-shaped[5,6], spherical-shaped[7,8], and hollow spheres[9,10], as well as mesoporous nanoparticles[11,12,13,14,15,16] and bulk materials[17,18,19]. Synthetic apatite shows a high potential for artificial bone or teeth tissue engineering due to its high biocompatibility and ability to enhance osteoblastic activity.[20,21,22,23,24] Nevertheless, the risk of infections from surgery is present. To overcome this problem the patient receives high doses of antibiotics either orally, mixed together with the artificial bone cement, or gentamicin loaded poly(methyl methacrylate) (PMMA) beads are implanted at the site of surgery.[20] Still, these solutions can cause other drawbacks. For artificial bone cements so called "burst-releases" have been observed[25,26], instead of long-term release of antibiotics. The implanted PMMA beads have to be removed by a secondary surgery after the complete antibiotic release.[27,28] Therefore, our initial goal was to synthesize a biocompatible and bioactive calcium phosphate nanomaterial with a large surface area for enhanced drug loading, which enables slower release kinetics and renders a second surgery unnecessary. Recently, citrate has been discussed to be involved in the growth of natural bone as a complexing agent for calcium ions.[29,30] The crystallization process of apatite is drastically slowed down by the addition of citric acid.[29,31]

Here, we present a novel synthesis strategy for highly mesoporous calcium phosphate-citrate nanoparticles (CPCs) with tunable porosity. Therefore, the amount of required drugs like antibiotics can be adjusted by the adsorption capacities of CPCs. This enables a personalized fabrication of bone cement for the patient's needs. In aqueous solution, amorphous CPCs transform into crystalline apatite. We characterized CPCs with IR spectroscopy, thermogravimetric analysis, X-ray diffraction, dynamic light scattering, sorption analysis, and electron microscopy.

3.2 Results and Discussion

Calcium phosphate-citrate nanoparticles (CPCs) were synthesized with a modified Pechini sol-gel process.[32,33] Calcium ions were dissolved in water. After addition of citric acid (CA) a complex with calcium ions is formed in aqueous solution. The pH of such solutions turns acidic during the complexation process. When adding phosphate ions a precipitation of calcium phosphate is prevented. Instead phosphate ions can interact with the Ca-CA-complex. In order to obtain a mesoporous structure the surfactant template cetyltrimethylammonium chloride (CTAC) was added in a concentration above the critical micelle concentration. The precursor complex and the micelles form an ordered mesophase. Due to a rapid change in pH to basic conditions, precipitation is induced. The extraction of the surfactant template with an ethanolic ammonium nitrate solution yielded the mesoporous CPCs. The addition of citric acid facilitates the gelation process in the formation of calcium phosphate.[34] Therefore, we believe that the kinetics of the precipitation reaction are slowed down. In consequence, the formation of a framework around the micellar structure is favored. We investigated the influence of the concentration of citric acid on the formation of the mesoporous structure. Here, we kept the concentration of calcium

and phosphate ions constant at a molar ratio of 1:0.66 as in stoichiometric apatite ($Ca_{10}(PO_4)_6(OH)_2$). Additionally, the amount of CTAC was kept above the critical micelle concentration at a fixed value. The amount of triethanolamine was kept constant as well. We synthesized four samples that only differed regarding the molar ratio of calcium to citric acid (Ca:CA). The molar ratios of Ca:CA were 1:2, 1:1, 1:0.6, and 1:0.2.

After precipitation and extraction of CPCs, we determined the particle size with dynamic light scattering (DLS) and scanning and transmission electron microscopy. The hydrodynamic particle size of CPCs in ethanolic solution is depicted in Figure 3.1a. All samples show a narrow size distribution. The smallest particles with a maximum at 240 nm were obtained for the sample with a molar ratio of Ca:CA =1:1. For the other samples we observed larger particles. The samples with a molar ratio of Ca:CA = 1:0.6 and 1:0.2 each exhibited a maximum at 300 nm, whereas the largest particles were obtained for the sample with a molar ratio of Ca:CA = 1:2 at a maximum of 615 nm. Scanning electron microscopy (SEM) of the sample with a molar ratio of Ca:CA = 1:1 showed spherical shape (Figure 3.1b). A wormlike mesoporous structure was determined by transmission electron microscopy (TEM). The particles aggregated strongly during the drying process and featured an average diameter of 50 nm (Figure 3.1c and d). Therefore, electron microscopy supports the findings from DLS measurements for the sample with a molar ratio of Ca:CA = 1:1.

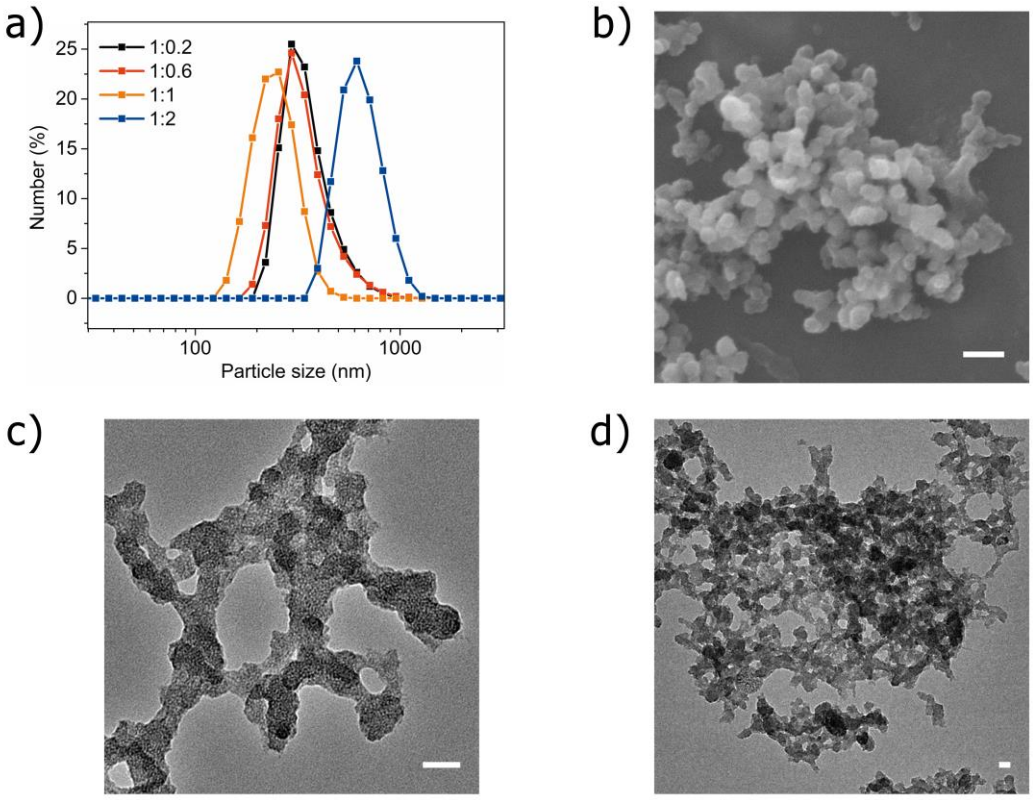

Figure 3.1: **a,** Dynamic light scattering measurements of colloidal CPCs with respect to the molar ratio of calcium to citric acid in ethanolic solution. The maxima of the peaks are at 240 nm (orange colored line), 300 nm (black and red colored lines), and 615 nm (blue colored line). **b,** SEM image of the sample with a molar ratio of Ca:CA = 1:1 depicts spherical particles with an average diameter of 50 nm. Scale bar: 200 nm. **c,** and **d,** TEM images of the sample with a molar ratio of Ca:CA = 1:1 depicts mesoporous structure and the strong aggregation due to the drying process. Scale bars: 50 nm.

With increasing concentration of CA we observed an incorporation of citrate ions into the calcium phosphate structure. Figure 3.2 illustrates IR-spectra of the four different samples. All samples show the typical $\nu_3(PO_4)$ band at 1079 cm^{-1}. This vibrational mode is broadened in amorphous calcium phosphates thus the $\nu_1(PO_4)$ only appears as a shoulder at 950 cm^{-1}.[35,36] The vibrational mode $\nu_4(PO_4)$ appears as one peak with a maximum at 570 cm^{-1} due to the amorphous nature.[36] The incorporation of carbonate ions due to solvation in the aqueous phase from the air is indicated by the $\nu_2(CO_3)$ vibration at 844 cm^{-1} and the strong $\nu_3(CO_3)$ vibration at 1390 cm^{-1}.[36,37] The vibrations at 1255 cm^{-1} and 894 cm^{-1} indicate a calcium-deficient

structure due to $H\text{-}OPO_3^{2-}$ and $HO\text{-}PO_3^{2-}$, respectively, to maintain charge neutrality.[38] The precipitation of calcium phosphate in the presence of citric acid leads to vibrations of COO^- at 1410 cm^{-1} and 1590 cm^{-1}.[39] With respect to the initial concentration of citric acid in the reaction solution, the intensities of the corresponding absorption bands decreased with lower concentrations relative to calcium ions. For concentrations of citric acid above a molar ratio of 1:1 no further increase of the corresponding absorptions was observed. Instead, for the sample with a molar ratio of 1:2 the intensities of the COO^- vibrations even decreased. Therefore, the maximum concentration of incorporated citrate ions into the calcium phosphate structure was reached at a molar ratio of Ca:CA of 1:1. The dotted box of Figure 3.2b depicts a section of the IR-spectrum from the sample with a molar ratio of Ca:CA = 1:1 before and after template extraction. In the region of 3000 cm^{-1} the typical –CH vibrations resulting from the template can be observed. The absence of the –CH vibrations in the spectra of all extracted samples indicates complete removal of the template.

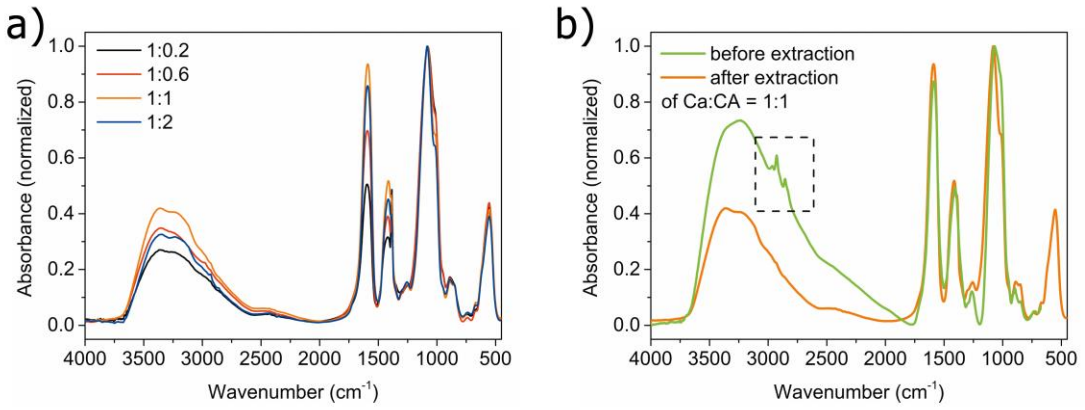

Figure 3.2: IR-spectra of CPCs with respect to the molar ratio of calcium to citric acid. **a,** With lower initial concentration of citric acid the incorporation of citrate ions into the structure of CPCs decreased, indicated by the strong COO^- vibrations at 1410 cm^{-1} and 1590 cm^{-1}. The typical PO_4^{3-} vibrations are assigned to the peaks at 570 cm^{-1} and 1079 cm^{-1}. **b,** CPCs before extraction (green colored line) and after

extraction (orange colored line) of the sample with a molar ratio of Ca:CA = 1:1. The dotted box displays the –CH vibrations of the alkane chain of the template.

To quantify the amount of incorporated citrate ions into the calcium phosphate structure, we performed thermogravimetric analysis (TGA) on all samples up to 900 °C with a heating rate of 10 K/min in a stream (25 mL/min) of synthetic air (Figure 3.3). The moderate mass loss of all samples up to 200 °C is assigned to weakly bound organics and mainly water (~ 7 wt%). Between 200 °C and 450 °C a significant mass loss is observed for all samples. Above 450 °C the mass stays almost constant up to 900 °C. We attribute the decomposition of strongly bound organics to the massive mass loss. Before the extraction of CTAC from the sample with a molar ratio of Ca:CA = 1:1 (green colored line) the mass loss of organics adds up to 36 wt%. For the same sample after extraction (orange colored line) a mass loss of 29 wt% was observed. Therefore, the template CTAC adds up to 7 wt%. We attribute the mass loss of 29 wt% to the decomposition of citrate ions incorporated in the structure of CPCs. The shift to higher decomposition temperatures compared to pure citric acid (175 °C) is attributed to the strong interactions with the calcium ions in CPCs. In accordance with IR data, the incorporation of citrate ions into the structure of CPCs is dependent on the initial molar ratio of Ca:CA. The mass loss of the sample with a molar ratio Ca:CA = 1:0.6 (red colored line) is observed to be 25 wt%. For the sample with a molar ratio Ca:CA = 1:0.2 (black colored line) the mass loss amounts to 21 wt%. With the molar ratio of Ca:CA = 1:2 we observed a mass loss of 26 wt%.

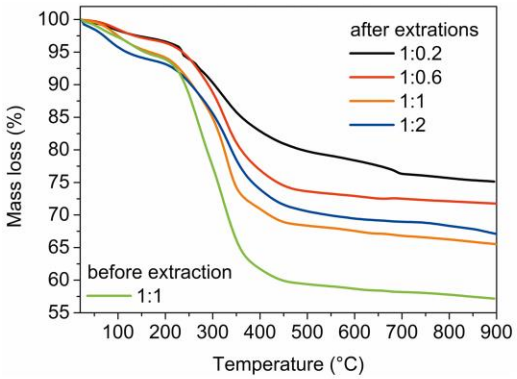

Figure 3.3: Thermogravimetric analysis measurements of extracted CPCs with different molar ratios of Ca:CA, with a heating rate of 10 K/min in a stream of synthetic air (25 mL/min). The mass loss of CPCs before (green colored line) extraction is depicted for the sample with a molar ratio of Ca:CA = 1:1.

The integrated areas underneath the IR vibration at 1590 cm^{-1} and the values for the calculated mass losses are listed in Table 3.1 for all samples. For the samples with a molar ratios of Ca:CA = 1:0.2, 1:0.6, and 1:1 we obtained a linear correlation with the citrate ions incorporated into the calcium phosphate structure (Figure 3.4). When comparing the samples with a molar ratio of Ca:CA = 1:1 and 1:2, we observed less intensity of the carboxylic IR vibration at 1590 cm^{-1} and less mass loss from organics for the latter one. Instead, more intensity of the IR vibration and a greater mass loss would have been expected. Therefore, the obtained values for the sample with a molar ratio of Ca:CA = 1:2 were fitted into the linear correlation. According to the fit, a ratio of Ca:CA = 1:0.79 regarding the IR data is obtained and 1:0.70 regarding the TGA measurement. We believe that the large excess of citric acid during the synthesis hinders the complete precipitation of CPCs, which also is confirmed by the observed lower yield. Therefore, calcium ions stay complexed during the change in pH and remain in solution.

Table 3.1: Correlating values of incorporated citrate ions in the calcium phosphate-citrate samples with different molar ratios of Ca:CA.

Molar ratio of Ca:CA	**1:0.2**	**1:0.6**	**1:1**	**1:2**
Integrated area (a.u.)	39.5	58.9	76.8	67.4
Mass loss (%)	21	25	29	26

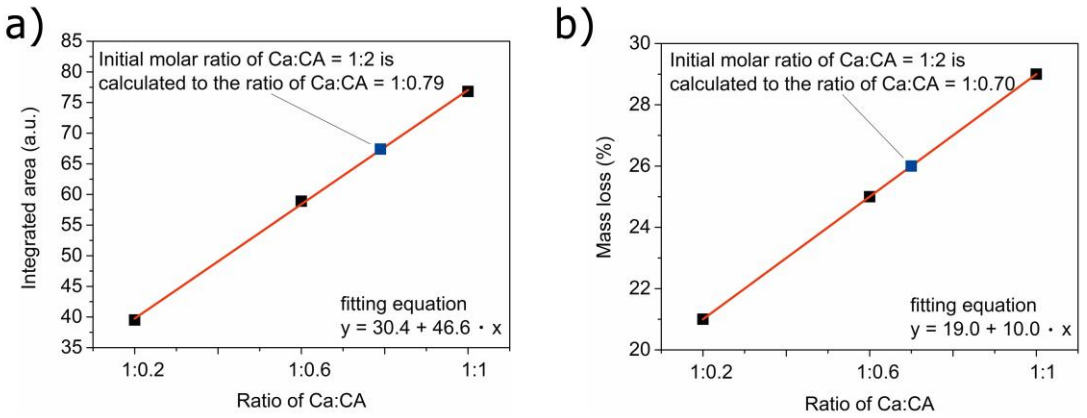

Figure 3.4: **a,** Integrated areas of the IR vibrational peak at 1590 cm^{-1} for the samples with a molar ratio of Ca:CA = 1:0.2, 1:0.6, and 1:1 (black squares). The red line resembles the linear fit of the values. The blue square marks the initial molar ratio of the sample Ca:CA = 1:2, which is calculated to a ratio of Ca:CA = 1:0.79. **b,** Mass loss of the samples with a molar ratio of Ca:CA = 1:0.2, 1:0.6, and 1:1 (black squares). The red line resembles the linear fit. The blue square marks the initial molar ratio of the sample Ca:CA = 1:2, which is calculated to a ratio of Ca:CA = 1:0.79 and 1:0.70, repectively.

The X-ray analysis revealed an amorphous structure for all samples (Figure 3.5). This is in accordance with the PO_4^{3-} vibration at 1079 cm^{-1} observed in the IR-spectra, which is shifted to higher wavenumbers compared to crystalline apatite. After extraction of CTAC we observed different scattering behavior of small angle X-rays with respect to the Ca:CA molar ratio. With increasing concentration of citric acid a relatively broad reflection arises at $2\Theta = 1.34°$. The intensity of this reflection decreased again when the molar ratio of Ca:CA exceeded 1:1. We calculated a d-spacing of approximately 6.6 nm for the sample with a molar ratio Ca:CA = 1:1.

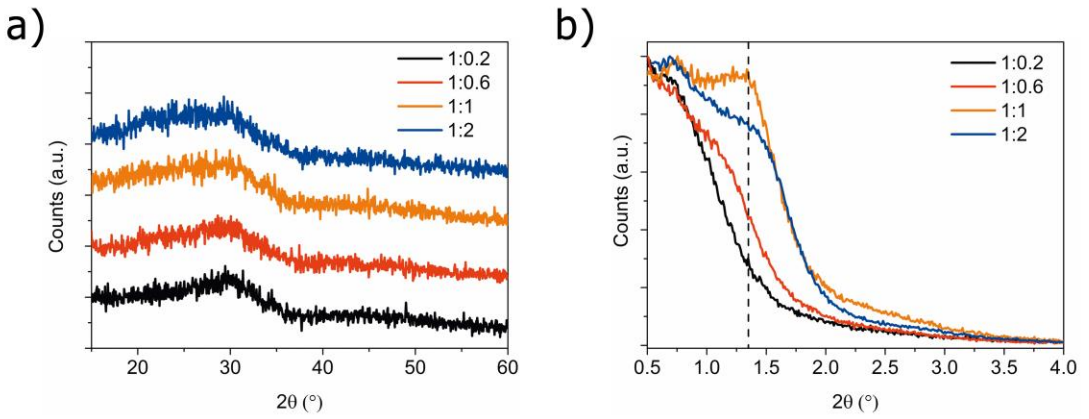

Figure 3.5: **a,** Wide angle X-ray scattering of amorphous CPCs with different molar ratios of Ca:CA (the graphs were shifted along the y-axis for clarity reasons). **b,** Small angle X-ray scattering of CPCs with different molar ratios of Ca:CA is depicted (graphs were normalized for clarity reasons). The regularity of the pore structure for the sample Ca:CA = 1:1 is visible at $2\Theta = 1.34°$ as a broad peak (dashed vertical line).

The influence of the molar ratio of Ca:CA on the resulting porosity was also investigated. Nitrogen sorption analysis was conducted for all samples (Figure 3.6). For the molar ratios Ca:CA = 1: 0.6; 1:1, and 1:2 the isotherms exhibit typical type IV shape for mesoporous materials. The sample with the molar ratio Ca:CA = 1:0.2 can also be interpreted as type VI isotherm, even so it looks like type II. Therefore, we calculated mesopore sizes from all isotherms and obtained different values with respect to the initial concentration of citric acid.[40] The calculated pore width varies between 4.8 nm and 5.4 nm for all samples. Due to the small size of the particles, textural porosity is indicated by the hysteresis loop at higher relative pressures. Therefore, the cumulative pore volumes were calculated up to 10 nm pore width in order to eliminate the textural porosity. The calculated pore volumes range from 0.11 cm^3/g to 0.56 cm^3/g. We observed a maximum BET surface area of 575 m^2/g for the sample with a molar ratio Ca:CA = 1:1, the BET surface area for the sample with a molar ratio Ca:CA = 1:0.2 was 190 m^2/g. Table 3.2 presents the calculated

data for all samples. Obviously, the degree of porosity is dependent on the concentration of citric acid added to the solution.

Summarizing, the addition of citric acid during the synthesis of CPCs has a strong influence on the porosity of the nanoparticles. Therefore, the amount of required drugs such as antibiotics in bone cements can be tuned due to the adsorption capacities of CPCs. This enables a personalized treatment with antibiotics based on the patient's needs at the site of bone cement induction.

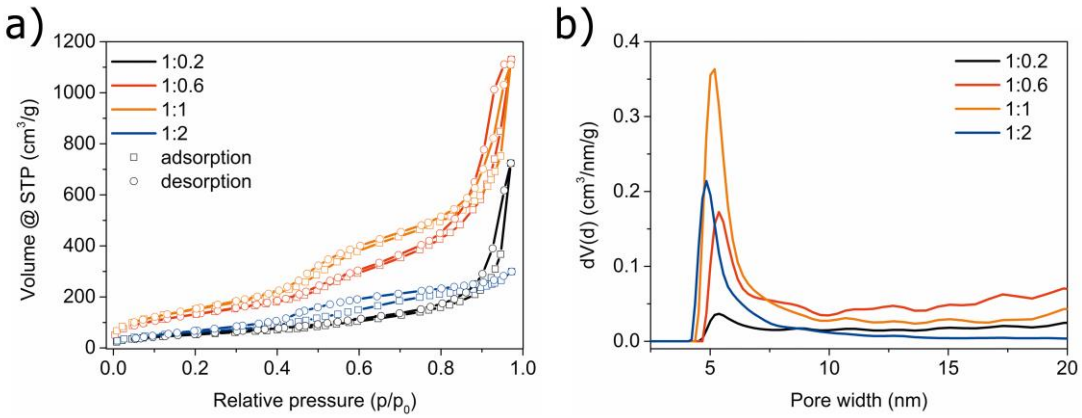

Figure 3.6: **a,** Nitrogen sorption analysis of mesoporous CPCs with a molar ratio of Ca:CA = 1:0.2, 1:0.6, 1:1, and 1:2. **b,** Pore size distribution of mesoporous CPCs with a molar ratio of Ca:CA = 1:0.2, 1:0.6, 1:1, and 1:2.

Table 3.2: Calculated porosity parameters of CPCs with different molar ratios of Ca:CA, from nitrogen sorption data.

Ca:CA molar ratio	**Pore size distribution**		**BET surface area (m^2/g)**
	Size (nm)	**Volume (cm^3/g)**	
1:2	4.8	0.32	240
1:1	5.2	0.56	575
1:0.6	5.4	0.37	490
1:0.2	5.4	0.11	190

Time-dependent X-ray diffraction measurements were performed to investigate the stability of the amorphous CPCs in water at room temperature. 10 mg of the sample with a molar ratio of Ca:CA = 1:1 was stirred in bi-distilled H_2O at a pH value of 6.5 and 1.5 mg each was withdrawn from the solution after 2, 4, 8, 96, 265, and 433 hours. The dried samples were investigated in the range of 2Θ = 15-60° (Figure 3.7). After 8 hours a transition of the amorphous phase into crystalline apatite is observed. The typical reflections for apatite structures increase with increasing storage time in water and are indicated with crosses. The decrease of the amorphous phase is indicated by the vanishing of the typical amorphous bump within 433 h. After 265 h an additional reflex at 2Θ = 18° arises (marked with an asterisk). This is attributed to crystalline calcium citrate.

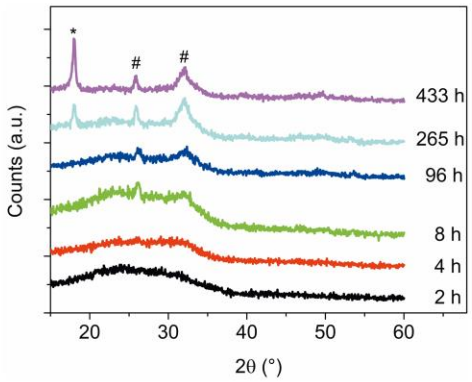

Figure 3.7: Wide angle X-ray scattering of CPCs with a molar ratio of Ca:CA = 1:1 after storage in H_2O (pH = 6.5) for 2, 4, 8, 96, 265, and 433 hours. The crosses mark the typical reflexes of crystalline apatite. The asterisk marks the reflection of crystalline calcium citrate (the graphs were shifted along the y-axis for clarity reasons).

3.3 Conclusion

We present a novel synthesis of calcium phosphate-citrate nanoparticles with tunable porosity. Calcium- and phosphate ions were combined with a surfactant template and citric acid in aqueous solution. Due to a rapid change in pH CPCs precipitated. After

the extraction of the surfactant template mesoporous spherical particles with a particle size of 50 nm were obtained. The incorporation of citrate ions into the structure of CPCs was confirmed by IR spectroscopy. Next to the intense phosphate vibrations at 570 cm^{-1} and 1079 cm^{-1} we observed strong vibrations at 1410 cm^{-1} and 1590 cm^{-1}, which are assigned to COO^- from the incorporated citrate ions. The amount of incorporated citrate ions into CPCs was quantified by TGA measurements and revealed a linear dependency of the incorporation with respect to the initial amount of citric acid until saturation was reached. Depending on the initial concentration of citric acid, the BET surface area varied between 190 and 575 m^2/g. Pore sizes ranging from 4.8 to 5.4 nm were obtained. Accordingly, the cumulative pore volume reached values from 0.11 to 0.56 cm^3/g. CPCs exhibited an amorphous structure that transformed into crystalline apatite upon the addition of water after 8 h.

The highly porous nature of CPCs offers many opportunities for molecular interactions with pharmaceutical and biological agents. Therefore, our CPCs provide a new promising, biocompatible platform for advanced drug delivery applications. Additionally, the transformation into crystalline apatite over time enables the utilization of CPCs as novel bone cement material with controlled drug release.

3.4 Experimental

Chemicals:

Calcium nitrate tetrahydrate (AppliChem, 99 %), ammonium dihydrogenphosphate (Alfa Aeser, 99 %), citric acid (Aldrich, 99.5 %), cetyltrimethylammonium chloride (CTAC, Fluka, 25 wt% in H_2O), triethanolamine (TEA, Aldrich, 98%), ethanol (EtOH, Aldrich, >99.5 %), ammonium nitrate (Sigma, 99 %), dipotassium hydrogen phosphate trihydrate (Sigma, 99 %).

All chemicals were used as received without further purification. Doubly distilled water from a Millipore system (Milli-Q Academic A10) was used for all synthesis steps.

Synthesis of Calcium Phosphate-Citrate Nanoparticles (CPCs):

The synthesis of CPCs was carried out following a modified Pechini sol-gel process.[32,33] In a 50 mL polypropylene reactor citric acid (CA, 480 mg/240 mg/144 mg/48 mg, 2.5 mmol/1.25 mmol/0.75 mmol/0.25 mmol), $Ca(NO_3)_2 \cdot 4\ H_2O$ (295 mg, 1.25 mmol) and $(NH_4)H_2PO_4$ (86.3 mg, 0.75 mmol) were dissolved in water (20 mL, 1.11 mmol) to obtain solutions with Ca:CA molar ratios of 1:2, 1:1, 1:0.6 and 1:0.2, respectively. Then, cetyltrimethylammonium chloride (622 mg, 1.94 mmol) was added and stirred for 5 minutes. The solution was added under vigorous stirring to another polypropylene reactor containing triethanolamine (7.15 g, 48 mmol). The obtained suspension was stirred at 500 rpm at room temperature for 10 minutes. Then, the suspension was diluted approximately 1:1 with ethanol. The particles were separated by centrifugation at 19,000 rpm (43,146 rcf) for 15 minutes and redispersed in NH_4NO_3/EtOH (2 wt%, 80 mL). To extract the template, the suspension was heated under reflux conditions at 90 °C for 30 minutes. Then, the particles were separated by centrifugation at 19,000 rpm (43,146 rcf) for 10 minutes and redispersed in 80 mL ethanol. The mixture was again heated under reflux conditions at 90 °C for 30 minutes. The particles were separated by centrifugation at 19,000 rpm (43,146 rcf) for 10 minutes and redispersed in 20 mL ethanol.

3.5 Characterization

Nitrogen sorption analysis was performed on a Quantachrome Instrument Nova 4000e at 77 K. Samples (25 mg) were outgassed at 120 °C for 12 h *in vacuo* (10 mTorr). Pore size and pore volume were calculated by a QSDFT equilibrium model of N_2 on carbon, based on the desorption branch of the isotherms. The QSDFT method takes into account the effects of surface roughness and heterogeneity.[41] Pore volumes were evaluated up to a pore size of 10 nm, in order to remove the contribution of inter-particle textural porosity. Surface areas were calculated with the BET model.[42] Thermogravimetric analysis of the samples was performed on a Netzsch STA 440 C TG/DSC in a stream of synthetic air with a flow rate of 25 mL/min and a heating rate of 10 K/min. Dynamic light scattering measurements were performed on a Malvern Zetasizer-Nano instrument with a 4 mW He-Ne laser (633 nm) in ethanolic suspension with a concentration of 0.5 mg/mL. Scanning electron microscopy (SEM) images were obtained on a JEOL JSM-6400F. For sample preparation a droplet of the ethanolic colloidal suspension was placed on a 60 °C preheated carbon pad. Samples were sputtered with carbon before measurement. Transmission electron microscopy (TEM) was performed on a JEOL JEM 2011 at an acceleration voltage of 200 kV. For sample preparation a droplet of a diluted ethanolic colloidal suspension was deposited on a carbon-coated copper grid and the solvent was allowed to evaporate. Infrared spectra were measured with a Thermo Scientific Nicolet iN 10 infrared microscope. XRD patterns were obtained with a Bruker D8 Discover X-ray diffractometer using Cu-K_α radiation (1.5406 Å).

3.6 References

1 S. V. Dorozhkin & M. Epple. Biological and medical significance of calcium phosphates. *Angewandte Chemie-International Edition* **41,** 3130-3146, (2002).

2 L. C. Palmer, C. J. Newcomb, S. R. Kaltz, E. D. Spoerke & S. I. Stupp. Biomimetic systems for hydroxyapatite mineralization inspired by bone and enamel. *Chemical Reviews* **108,** 4754-4783, (2008).

3 C. Qi *et al.* Hydroxyapatite hierarchically nanostructured porous hollow microspheres: rapid, sustainable microwave-hydrothermal synthesis by using creatine phosphate as an organic phosphorus source and application in drug delivery and protein adsorption. *Chemistry-A European Journal* **19,** 5332-5341, (2013).

4 T. Traykova, C. Aparicio, M. P. Ginebra & J. A. Planell. Bioceramics as nanomaterials. *Nanomedicine: Nanotechnology, Biology, and Medicine* **1,** 91-106, (2006).

5 J. Fan, J. Lei, C. Yu, B. Tu & D. Zhao. Hard-templating synthesis of a novel rod-like nanoporous calcium phosphate bioceramics and their capacity as antibiotic carriers. *Materials Chemistry and Physics* **103,** 489-493, (2007).

6 X. Zhao *et al.* Cytotoxicity of hydroxyapatite nanoparticles is shape and cell dependent. *Archives of Toxicology* **87,** 1037-1052, (2013).

7 W. Paul & C. P. Sharma. Development of porous spherical hydroxyapatite granules: application towards protein delivery. *Journal of Materials Science: Materials in Medicine* **10,** 383-388, (1999).

8 T. Hirai, M. Hodono & I. Komasawa. The preparation of spherical calcium phosphate fine particles using an emulsion liquid membrane system. *Langmuir* **16,** 955-960, (2000).

9 K.-W. Wang, Y.-J. Zhu, F. Chen, G.-F. Cheng & Y.-H. Huang. Microwave-assisted synthesis of hydroxyapatite hollow microspheres in aqueous solution. *Materials Letters* **65,** 2361-2363, (2011).

10 K.-W. Wang *et al.* Flower-like hierarchically nanostructured hydroxyapatite hollow spheres: facile preparation and application in anticancer drug cellular delivery. *Chemistry – An Asian Journal* **5,** 2477-2482, (2010).

11 Y. Guo, Y. Zhou, D. Jia & H. Tang. Fabrication and characterization of hydroxycarbonate apatite with mesoporous structure. *Microporous and Mesoporous Materials* **118,** 480-488, (2009).

12 F. Chen *et al.* Multifunctional biodegradable mesoporous microspheres of Eu^{3+}-doped amorphous calcium phosphate: microwave-assisted preparation, pH-sensitive drug release, and bioimaging application. *Journal of Materials Chemistry B* **2,** 7132-7140, (2014).

13 N. Ikawa, H. Hori, T. Kimura, Y. Oumi & T. Sano. Templating route for mesostructured calcium phosphates with carboxylic acid- and amine-type surfactants. *Langmuir* **24,** 13113-13120, (2008).

14 N. Ikawa, H. Hori, T. Kimura, Y. Oumi & T. Sano. Unique surface property of surfactant-assisted mesoporous calcium phosphate. *Microporous and Mesoporous Materials* **141,** 56-60, (2011).

15 C. K. Poh *et al.* In vitro characterizations of mesoporous hydroxyapatite as a controlled release delivery device for VEGF in orthopedic applications. *Journal of Biomedical Materials Research Part A* **100A,** 3143-3150, (2012).

16 J. Moeller-Siegert, J. Parmentier, K. Anselme & C. Vix-Guterl. Mesoporous hydroxyapatite by hard templating of silica and carbon foams for protein release. *Journal of Materials Science* **48,** 3722-3730, (2013).
17 T. Dutta Roy *et al.* Performance of hydroxyapatite bone repair scaffolds created via three-dimensional fabrication techniques. *Journal of Biomedical Materials Research Part A* **67,** 1228-1237, (2003).
18 J. M. Cordell, M. L. Vogl & A. J. W. Johnson. The influence of micropore size on the mechanical properties of bulk hydroxyapatite and hydroxyapatite scaffolds. *Journal of the Mechanical Behavior of Biomedical Materials* **2,** 560-570, (2009).
19 K. A. Hing, S. M. Best, K. E. Tanner, W. Bonfield & P. A. Revell. Mediation of bone ingrowth in porous hydroxyapatite bone graft substitutes. *Journal of Biomedical Materials Research Part A* **68,** 187-200, (2004).
20 D. Arcos & M. Vallet-Regí. Bioceramics for drug delivery. *Acta Materialia* **61,** 890-911, (2013).
21 M. Iafisco *et al.* Smart delivery of antitumoral platinum complexes from biomimetic hydroxyapatite nanocrystals. *Journal of Materials Chemistry* **19,** 8385-8392, (2009).
22 S. A. Redey *et al.* Behavior of human osteoblastic cells on stoichiometric hydroxyapatite and type A carbonate apatite: role of surface energy. *Journal of Biomedical Materials Research* **50,** 353-364, (2000).
23 Y.-F. Chou, W. Huang, J. C. Dunn, T. A. Miller & B. M. Wu. The effect of biomimetic apatite structure on osteoblast viability, proliferation, and gene expression. *Biomaterials* **26,** 285-295, (2005).
24 C. Serre, M. Papillard, P. Chavassieux, J. Voegel & G. Boivin. Influence of magnesium substitution on a collagen–apatite biomaterial on the production of a calcifying matrix by human osteoblasts. *Journal of Biomedical Materials Research* **42,** 626-633, (1998).
25 Y. Liu, P. Layrolle, J. de Bruijn, C. van Blitterswijk & K. de Groot. Biomimetic coprecipitation of calcium phosphate and bovine serum albumin on titanium alloy. *Journal of Biomedical Materials Research* **57,** 327-335, (2001).
26 C. Agrawal, J. Best, J. Heckman & B. Boyan. Protein release kinetics of a biodegradable implant for fracture non-unions. *Biomaterials* **16,** 1255-1260, (1995).
27 G. Wei *et al.* A bioabsorbable delivery system for antibiotic treatment of osteomyelitis. The use of lactic acid oligomer as a carrier. *Journal of Bone & Joint Surgery, British Volume* **73,** 246-252, (1991).
28 T. Gerhart *et al.* Antibiotic release from an experimental biodegradable bone cement. *Journal of Orthopaedic Research* **6,** 585-592, (1988).
29 B. Xie & G. H. Nancollas. How to control the size and morphology of apatite nanocrystals in bone. *Proceedings of the National Academy of Sciences* **107,** 22369-22370, (2010).
30 Y.-Y. Hu, A. Rawal & K. Schmidt-Rohr. Strongly bound citrate stabilizes the apatite nanocrystals in bone. *Proceedings of the National Academy of Sciences* **107,** 22425-22429, (2010).
31 E. Davies *et al.* Citrate bridges between mineral platelets in bone. *Proceedings of the National Academy of Sciences* **111,** E1354-E1363, (2014).
32 M. P. Pechini. Method of preparing lead and alkaline earth titanates and niobates and coating method using the same to form a capacitor. US3330697 (1967).

33 P. Yang, P. Yang, X. Teng, J. Lin & L. Huang. A novel luminescent mesoporous silica/apatite composite for controlled drug release. *Journal of Materials Chemistry* **21,** 5505-5510, (2011).

34 W. Weng, G. Han, P. Du & G. Shen. The effect of citric acid addition on the formation of sol–gel derived hydroxyapatite. *Materials Chemistry and Physics* **74,** 92-97, (2002).

35 C. Drouet. Apatite formation: why it may not work as planned, and how to conclusively identify apatite compounds. *BioMed Research International* **2013**, (2013).

36 K. Zilm. Mechanism of CO_3^{2-} substitution in carbonate-fluorapatite: evidence from FTIR spectroscopy, ^{13}C NMR and quantum mechanical calculations. *American Mineralogist*, (1994).

37 C. Rey, B. Collins, T. Goehl, I. R. Dickson & M. J. Glimcher. The carbonate environment in bone mineral: a resolution-enhanced fourier transform infrared spectroscopy study. *Calcified Tissue International* **45,** 157-164, (1989).

38 E. E. Berry. The structure and composition of some calcium-deficient apatites. *Journal of Inorganic and Nuclear Chemistry* **29,** 317-327, (1967).

39 L. Brečević & H. Füredi-Milhofer. Precipitation of calcium phosphates from electrolyte solutions V. The influence of citrate ions. *Calcified Tissue International* **28,** 131-136, (1979).

40 K. S. Sing. Reporting physisorption data for gas/solid systems with special reference to the determination of surface area and porosity (Recommendations 1984). *Pure and Applied Chemistry* **57,** 603-619, (1985).

41 Quantachrome. *Application of QSDFT (quenched solid density functional theory) - a Novel Density Functional Theory for an Accurate Pore Size Analysis of Disordered Porous Carbons*. Volume 40 (Quantachrome Instruments USA).

42 S. Brunauer, P. H. Emmett & E. Teller. Adsorption of gases in multimolecular layers. *Journal of the American Chemical Society* **60,** 309-319, (1938).

CHAPTER 4

FUNCTIONALIZATION OF CALCIUM PHOSPHATE-CITRATE NANOPARTICLES WITH CALCEIN, A LIPID MEMBRANE COATING, MANGANESE, AND STRONTIUM FOR DETECTION AND DIAGNOSIS

Constantin von Schirnding, Stefan Datz, Andreas Zimpel, Hanna Engelke, and Thomas Bein.

4.1 Introduction

Engineering nanomaterials for drug delivery applications will eventually lead to contact of these nanomaterials with humans and the environment.[1] Therefore, it is mandatory to be able to track the nanoparticles and record their traces. This need motivated the introduction of functionalized nanomaterials. The possibility to functionalize nanoparticles with other molecules or with active linking groups opened many opportunities in this direction.[2,3] Additionally, nanoparticles can then readily be used for detection and as a diagnostic tool.[4] In recent years, many methods have been developed to synthesize functionalized nanoparticles, specifically for drug delivery to tumor sites, for diagnostics, and for tissue engineering.[5,6,7] Depending on the functionalization, a number of different properties such as photoluminescence (e.g. fluorescence), attachment of targeting ligands, high electron density, or magnetic moment can be achieved.[8] If nanoparticles are fluorescently labeled, the interaction of living matter with nanoparticles could easily be investigated with microscopy - not only on the cellular level but also in living tissue.[9] If nanoparticles are functionalized in a way that targeting ligands could be attached, e.g., at a lipid membrane, delivery to the tumor sites could be achieved and/or diagnostic methods could be introduced.[10,11] If nanoparticles are functionalized with elements with high atomic numbers, materials could become radiopaque leading to detectability with X-rays.[12,13] Finally, if nanoparticles are functionalized with paramagnetic elements, the detection could be performed with MRI methods.[14,15,16] In any case, it would be desirable if a single type of nanoparticle could offer a platform on which all such properties can be achieved by functionalization. This would enhance the flexibility of the platform for diagnostics and detectability.

Here, we describe the functionalization of calcium phosphate-citrate nanoparticles (CPCs). Our first goal was the functionalization for detectability of the nanoparticles *in vitro* and *in vivo*. Furthermore, the molecules introduced into CPCs by functionalization were intended to belong to the group of biocompatible substances. The tuning of calcium phosphate materials towards medical uses has already become an advancing field.[17] Thus, a number of divalent cations (Sr^{2+}, Ba^{2+}, Mn^{2+}, Pb^{2+}, etc.) have been introduced into the structure of calcium phosphate materials.[18,19,20,21] Here, we chose as functionalizing agents strontium for its radiopacity properties[22,23], manganese for paramagnetic properties[24], and calcein for fluorescence properties.[25] First, we established the synthesis of Sr-CPCs, Mn-CPCs, and Cal-CPCs. Furthermore, we attached a lipid membrane to Cal-CPCs to enable cellular uptake. We investigated the functionalized CPCs with IR spectroscopy, thermogravimetric analysis, dynamic light scattering, X-ray analysis, and sorption analysis, as well as scanning and transmission electron microscopy. In a computer tomography experiment we confirmed the enhanced X-ray contrast of functionalized Sr-CPCs compared to unfunctionalized CPCs. Using MRI, we monitored the relaxation times of functionalized Mn-CPCs and calculated the material´s specific relaxivity. We recorded the fluorescent properties of calcein-calcium phosphate-citrate nanoparticles (Cal-CPCs) and investigated the interactions with HeLa cells. After coating Cal-CPCs with a lipid membrane, we were able to monitor nanoparticle uptake by HeLa cells. The above functionalization strategies for CPCs open new possibilities for the detection and diagnosis in living matter.

4.2 Results and Discussion

The functionalization of calcium phosphate-citrate nanoparticles (CPCs) was carried out following a modified Pechini sol-gel process[26,27] and co-precipitation of the doping materials. The partial substitution of the divalent calcium cation with Sr^{2+} or Mn^{2+} led to strontium-calcium phosphate-citrate nanoparticles (Sr-CPCs) or manganese-calcium phosphate-citrate nanoparticles (Mn-CPCs). The partial substitution of the anionic citrate with calcein led to calcein-calcium phosphate-citrate nanoparticles (Cal-CPCs). Calcium ions were dissolved in aqueous solution containing citric acid. Citric acid leads to a complexation of the calcium ions and a drop in pH due to its acidity. This prevents precipitation of calcium phosphate after the addition of phosphate ions. Additionally, the addition of citric acid facilitates the gelation process in the formation of calcium phosphate-citrate and slows down the precipitation kinetics.[28] The respective dopants were mixed into the reaction solution at fixed concentrations. For the functionalization with strontium or manganese a concentration of 10 mol% with respect to the calcium amount was substituted. The functionalization with calcein was performed with 1 mol% with respect to the to the citric acid amount. To obtain mesoporosity, the template surfactant cetyltrimethylammonium chloride (CTAC) was added to form a mesophase containing dopant-calcium phosphate-citrate and micellar structures. A rapid change in pH to basic conditions induces the precipitation of the functionalized CPCs. Extraction of the surfactant template with an ethanolic ammonium nitrate solution yielded the mesoporous functionalized CPCs.

The formation of calcium phosphate-citrate nanoparticles was demonstrated with IR spectroscopy and thermogravimetric analysis (TGA). In Figure 4.1a the IR-spectra of three different CPCs are depicted. All samples show the typical $\nu_3(PO_4)$

band at 1079 cm^{-1}.[29] This vibrational mode is broadened in amorphous calcium phosphate-citrate, thus the $\nu_1(PO_4)$ only appears as a shoulder at 950 cm^{-1}.[30,31] The vibrational mode $\nu_4(PO_4)$ appears as one peak with a maximum at 570 cm^{-1} due to the amorphous nature of the material.[31] The vibrations at 1255 cm^{-1} and 894 cm^{-1} indicate the presence of $H\text{-}OPO_3^{2-}$ and $HO\text{-}PO_3^{2-}$ and thus a calcium-deficient structure to maintain charge neutrality.[32] The precipitation of calcium phosphate in the presence of citric acid leads to vibrations of COO^- at 1410 cm^{-1} and 1590 cm^{-1}.[33] The above data are in accordance with our mesoporous calcium phosphate-citrate nanoparticles introduced in Chapter 3. Additionally, we investigated the functionalized CPCs with TGA in the temperature range between 25 and 900 °C with a heating rate of 10 K/min in synthetic air (25 mL/min) to quantify the amount of citrate ions incorporated into the calcium phosphate structure (Figure 4.1b). In comparison to the unfunctionalized CPCs (see Figure 3.3, orange line) we observed a similar mass loss for Sr-CPCs. The mass loss of the sample up to 200 °C is assigned to weakly bound organics and mainly water (~ 4 wt%). Between 200 °C and 400 °C a significant mass loss is observed. Above 400 °C the mass remains almost constant up to 900 °C. We attribute the decomposition of strongly bound organics to the massive mass loss which is in agreement with unfunctionalized CPCs where the same trend is observable. This leads to the conclusion that for Sr-CPCs an organic content (citrate) of around 29 wt% is incorporated into the Sr-CPC structure. For the sample Mn-CPC we observed similar thermogravimetric results as for the sample Sr-CPC. The mass loss up to 150 °C is related to the weakly bound organics and water, the mass loss between 150 °C and 450 °C is attributed to citrate and adds up to 25 wt%. For the sample Cal-CPC we observed a mass loss of 11 wt% up to a temperature of 150 °C resulting from weakly bound organics, mainly water, and degradation of calcein at the outer surface.[34,35] Between 150 °C and 650 °C we

assigned the mass loss to the decomposition of citric acid adding up to 20 wt%. Above 650 °C we observed an additional mass loss, attributed to the complete degradation of the incorporated calcein. In the literature the decomposition of calcein is reported to start below 150 °C.[34] The mass loss above 650 °C is assigned to the combustion of intermediates formed during the heating of Cal-CPCs.[35]

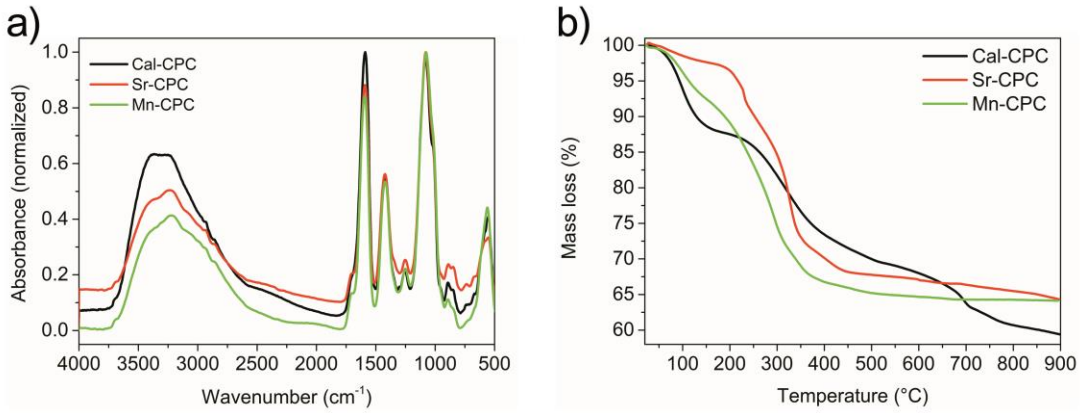

Figure 4.1: **a,** IR-spectra of Cal-CPCs, Sr-CPCs, and Mn-CPCs with strong COO^- vibrations at 1410 cm^{-1} and 1590 cm^{-1} due to the citrate incorporated into the structure. **b,** Thermogravimetric analysis of Cal-CPCs, Sr-CPCs, and Mn-CPCs.

Colloidal stability and the particle size of functionalized CPCs were measured with dynamic light scattering (DLS). The hydrodynamic particle size of functionalized CPCs in ethanolic solution is depicted in Figure 4.2a. All functionalized CPC samples show a narrow size distribution with a maximum at 290 nm. After drying the samples from ethanolic solutions at 60 °C for 12 hours, X-ray diffraction analysis (Figure 4.2b) revealed amorphous materials. This is in agreement with the shifted and broadened vibrational $\nu_3(PO_4)$ band at 1079 cm^{-1}.[31] The scanning electron microscopy images reveal spherical nanoparticles with a size of around 50 nm for all functionalized CPC samples. The particles strongly aggregate due to the drying process on the sample holder (Figure 4.2c-e). In transmission electron microscopy indications for the mesoporous structure can be observed with all samples. The

sponge-like formation of aggregated CPC particles from the drying process was observed as well (Figure 4.2f-h).

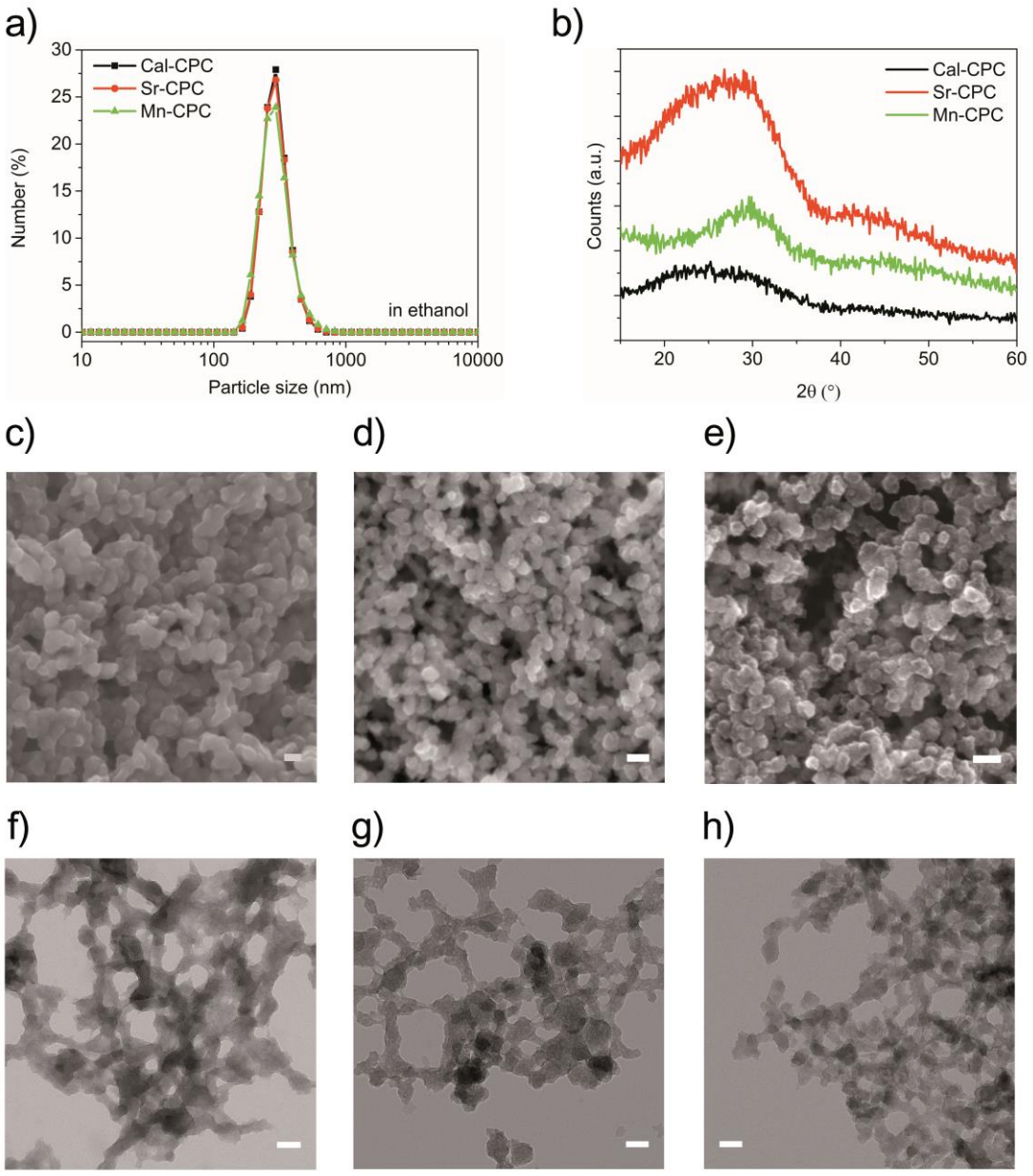

Figure 4.2: **a,** Dynamic light scattering in ethanolic solution of Cal-CPCs, Sr-CPCs, and Mn-CPCs. **b,** X-ray diffraction measurements reveal amorphous nature of Cal-CPCs, Sr-CPCs, and Mn-CPCs. **c-e,** Scanning electron microscopy images of Cal-CPCs, Sr-CPCs, and Mn-CPCs. Scale bars: 100 nm. **f-h,** Transmission electron microscopy images of Cal-CPCs, Sr-CPCs, and Mn-CPCs. Scale bars: 50 nm.

For all functionalized CPCs the analysis of the nitrogen sorption isotherms revealed a very large BET surface area and a narrow pore size distribution with a large

corresponding pore volume. All isotherms (Figure 4.3) exhibit the typical type IV shape for mesoporous materials. We calculated porosity parameters from all isotherms.[36] The calculated pore size for all samples varies between 4.5 nm and 4.8 nm. The cumulative pore volumes were calculated up to 10 nm pore size to eliminate the influence of textural porosity. The calculated pore volumes range from 0.52 cm^3/g to 0.59 cm^3/g. We observed a maximum BET surface area of 600 m^2/g for the sample Cal-CPC. Table 4.1 presents the calculated data for all functionalized CPC samples. The porosity parameters are mostly consistent for functionalization with calcein, strontium, or manganese in calcium phosphate-citrate nanoparticles.

Table 4.1: Calculated parameters from nitrogen sorption data of functionalized CPCs.

Sample	**Pore size distribution**		**BET surface area**
	Size (nm)	**Volume (cm^3/g)**	**(m^2/g)**
Cal-CPCs	4.5	0.59	600
Sr-CPCs	4.8	0.55	530
Mn-CPCs	4.5	0.52	590

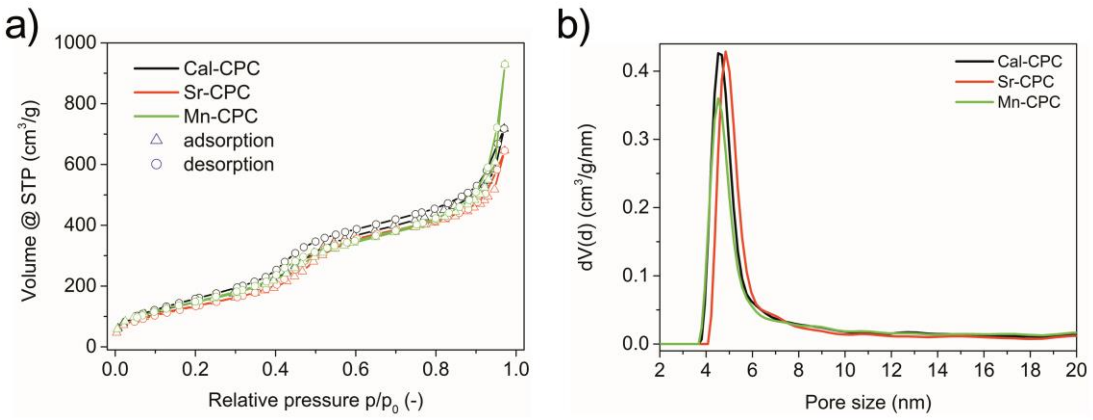

Figure 4.3: Sorption data for CPCs functionalized with calcein (Cal-CPCs, black curve), strontium (Sr-CPCs, red curve), and manganese (Mn-CPCs, green curve). **a,** Adsorption and desorption isotherms of Cal-CPCs, Sr-CPCs, and Mn-CPCs. **b,** Calculated pore size distributions of Cal-CPCs, Sr-CPCs, and Mn-CPCs.

The energy dispersive X-ray analysis reveals the difference in the chemical composition of the functionalized CPCs. For the sample Cal-CPC the quantification of the carbon or nitrogen content is not representative due to the small atomic numbers of these atoms and the carbon sputtering during sample preparation. Therefore, no difference in the elemental analysis data of Cal-CPCs and unfunctionalized CPCs can be detected. The averaged ratio of calcium to phosphorus is 1.62. This is in accordance with the calcium-deficient structure indicated in the IR-spectra. Both Sr-CPCs and Mn-CPCs are functionalized/doped with 10 mol% with respect to the calcium content of CPCs. For the sample Sr-CPCs an averaged dopant/calcium to phosphorus ratio of 1.79 was obtained. For the sample Mn-CPCs an averaged dopant/calcium to phosphorus ratio of 1.78 was observed. In comparison to Cal-CPCs, the samples Sr-CPCs and Mn-CPCs exhibit higher dopant/calcium amounts with respect to phosphate.

Table 4.2: Avaraged energy dispersive X-ray (EDX) and inductively coupled plasma (ICP) analysis of functionalized CPCs. Previously for ICP anaylsis, the solid samples were dissolved in HNO_3.

Sample	**Analysis**	**Calcium (atom%)**	**Functionalization: Sr^{2+} or Mn^{2+} (atom%)**	**Phosphor (atom%)**	**Dopant/Ca:P**
Cal-CPCs	EDX	8.35	-	5.52	1.51
	ICP	5.78	-	3.34	1.73
Sr-CPCs	EDX	4.91	0.72	3.26	1.73
	ICP	4.61	0.87	2.98	1.86
Mn-CPCs	EDX	5.51	1.02	3.47	1.88
	ICP	5.48	0.81	3.74	1.68

The obtained functionalized calcium phosphate-citrate nanoparticles can be used for diagnostic and sensing applications. Reported investigations on calcium phosphate

materials often aim at applications as bone cement.[19] This is due to their mechanical performance, biocompatibility, bioactivity and osteoconductivity as well as the easy handling.[37,38] Calcium phosphate bone cements can be functionalized to enhance their performance. Strontium ions have attracted attention because of their unique potential to stimulate new bone formation.[23] Additionally, strontium functionalized calcium phosphate materials are radiopaque which leads to better visualization with X-rays.[22,23] The functionalized Sr-CPCs in this work contain up to 15 atom% of strontium. Therefore, we expect Sr-CPCs being a more radiopaque material than unfunctionalized CPCs. This enables the combination of better detectability in X-ray imaging and the advantages of biocompatible colloidal mesoporous nanoparticles.

Sr-CPCs were compared to unfunctionalized CPCs with computer tomography. The two samples were recorded 6 mm stepwise (standard measurement conditions) in a glass vial in ethanolic solution at a concentration of 1 mg/mL to obtain a 3D image. Ethanol as a solvent with a purity of 99.9 % shows a mean Hounsfield value of -196.8±2.8 HU.[39] Sr-CPCs show a larger Hounsfield value (-193.2±1.5 HU) and thereby show stronger X-ray absorbance. Compared to unfunctionalized CPCs (-197.1±3.1 HU) the Hounsfield value is close to the value of pure ethanol. Therefore, for Sr-CPCs a better X-ray contrast is observed and thus can be distinguished from unfunctionalized CPCs at least if dispersed in ethanolic solution.[22] How Sr-CPCs and unfunctionalized CPCs will perform under aqueous conditions will be explored in the future. It would be desirable if Sr-CPCs can also be distinguished from natural bone. For bone a mean Hounsfield value from 300 to 3000 HU is reported.[40,41]

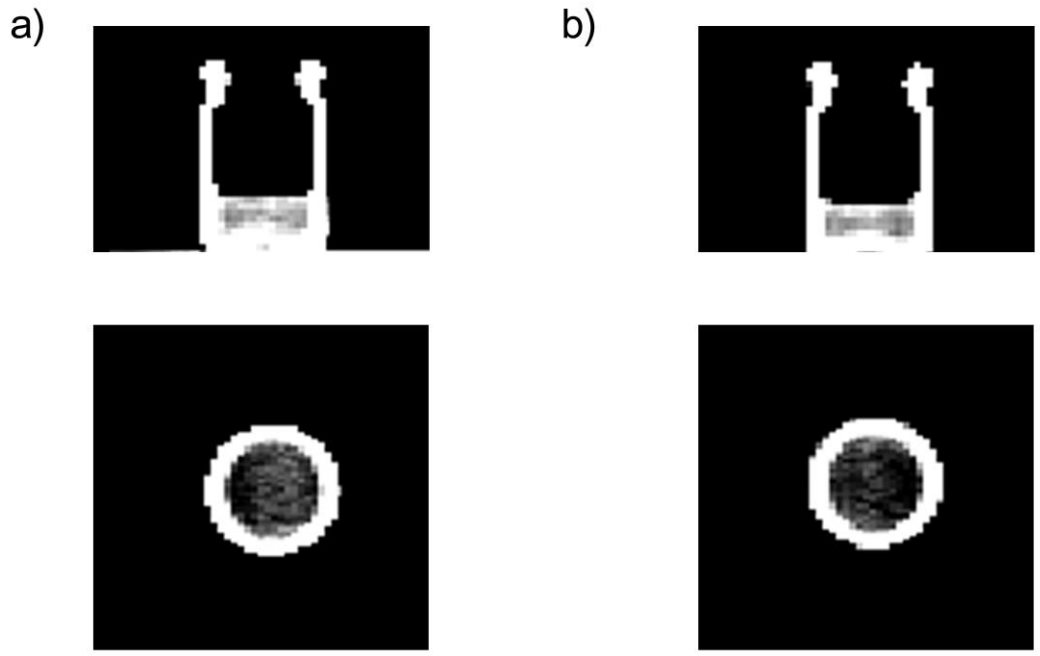

Figure 4.4: Computer tomography images of **a,** Sr-CPCs, exhibiting a greater Hounsfield unit (-193.2±1.5 HU) than **b,** unfunctionalized CPCs (-197.1±3.1 HU). Nanoparticles dispersed in ethanolic solution were recorded in a glass vial, which appears very bright (995 HU). Sr-CPCs show stronger contrast (brighter) than unfunctionalized CPCs. The top row depicts the transverse view while the bottom row depicts the coronal view of the images.

Magnetic resonance imaging (MRI) is a technique that relies on strong magnetic fields, field gradients, and radio waves to generate images. For magnetic resonance imaging in clinics, hydrogen atoms, in the form of water, are used for detecting the emitted radio-frequency signal when an external strong magnetic field is applied. The relaxation time of these hydrogen atoms is influenced by the close surroundings leading to a contrast in imaging. Therefore, relaxation rates of water can be influenced by certain atoms that are MRI active. Due to the paramagnetic properties of manganese[24] the relaxation rates of Mn-CPCs were analyzed with MRI methods in aqueous solution. Four samples of Mn-CPCs at concentrations of 0.5, 1.0, 3.0, and 6.0 mg/mL in aqueous solution were investigated. For each sample the relaxation rates for T1 and T2 were recorded (Figure 4.5). For calculations from mg/mL to

mmol/L, a stoichiometric composition of Mn-CPCs with the formula of $Ca_{4.5}Mn_{0.5}(PO_4)_3OH$ was employed, based on elemental analysis data.

The relaxation rate was measured at a clinical 1.5 T MRI system using T1-weighted saturation recovery sequences and T2-weighted multi-echo sequences.

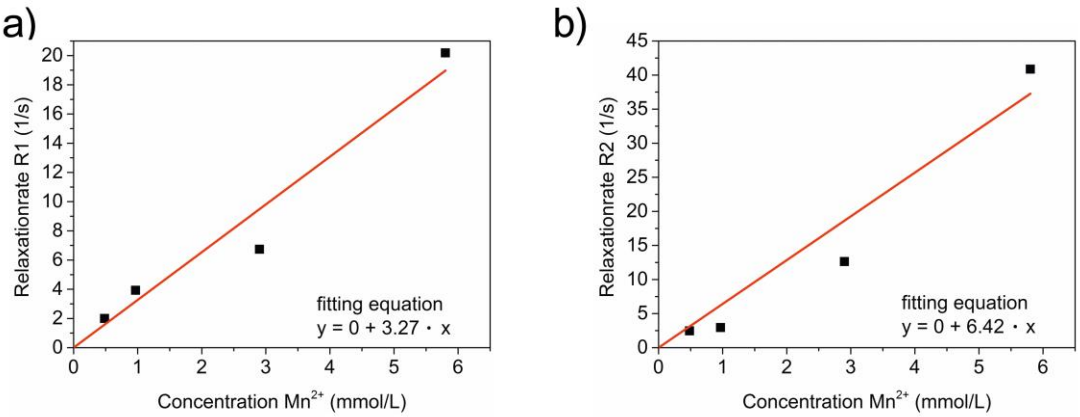

Figure 4.5: Plots of relaxation rates (**a,** R1 and **b,** R2) versus the manganese concentration of the Mn-CPCs. The slope of the fitting equations indicates the specific relaxivity (**a,** r_1 and **b,** r_2).

The nanoparticles significantly shortened the T1 and T2 values of water protons. The specific relaxivity was obtained by fitting the relaxation rates $R_{1/2} = 1/T_{1/2}$ of the different concentration of Mn-CPCs. The slope of the fitting curve of the obtained relaxation rates indicates the material specific relaxivity r_1 and r_2. For Mn-CPCs the specific relaxivity was calculated to be r_1 = 3.27 L/mmol/s and r_2 = 6.42 L/mmol/s with respect to the manganese content. In comparison, a Mn-EDTA complex exhibits a specific relaxivity of r_1 = 5.8 L/mmol/s.[42] Molecular $MnCl_2$ exhibits specific relaxivity values at the order of r_1 = 7-8 L/mmol/s and r_2 = 30-125 L/mmol/s.[43] This could be interpreted such that if manganese ions are sterically blocked with EDTA or in our case embedded into a CPC structure, the r_1 value is lowered. Generally, the higher the r_1 value the better is the positive contrast in imaging. Even more significant is the ratio of r_2/r_1 for imaging in clinics. The closer the ratio of r_2/r_1 is to

1, the better the material is suited as contrast agent.[44,45] A commercially available gadolinium complex, Magnevist®, has an optimal r_2/r_1 ratio of 1 (r_1 = 4.6 L/mmol/s, r_2 = 4.5 L/mmol/s) at 1.5 T.[35] For our Mn-CPCs the specific relaxivity ratio of r_2/r_1 shows a value of 1.96, making them presumably easily detectable with MRI methods during *in vivo* experiments.

X-ray analysis and magnetic resonance imaging of functionalized Sr-CPCs and Mn-CPCs are attractive for detecting and tracing the CPCs in *in vivo* experiments. But for *in vitro* experiments fluorescence microcopy is the analysis method of choice.[9]

For the sample Cal-CPC we investigated the fluorescent properties of the colloidal nanoparticles. To this end, we recorded the excitation and emission spectra of nanoparticles dispersed in bi-distilled water (Figure 4.6a, solid lines). The maxima of the spectra are located at 507 nm for the excitation wavelength (emission at 545 nm) and 525 nm for the emission wavelength (excitation at 488 nm). In comparison with free calcein (Figure 4.6a, dashed lines) we observed spectra red-shifted by 10 nm for the excitation and the emission in Cal-CPCs. The incorporation of calcein into the structure of the CPCs therefore influences the fluorescent properties of calcein. In Figure 4.6b the measurement cuvette is depicted with the blue excitation wavelength and the green emission color of the colloidal particles in the cuvette. In Figure 4.6c the colloidal yellow-colored Cal-CPCs are depicted.

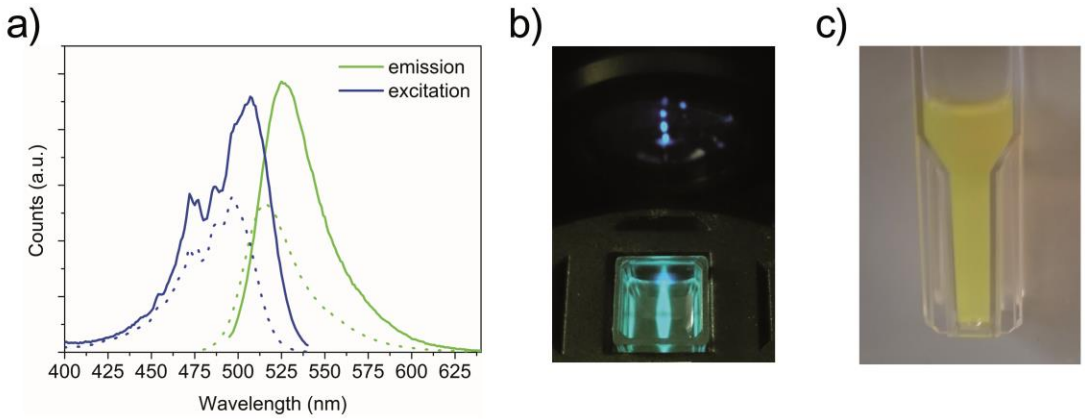

Figure 4.6: Fluorescently functionalized CPCs (Cal-CPCs). **a,** Excitation and emission spectra of Cal-CPCs (solid lines), excitation and emission of free calcein (dashed lines). **b,** Photograph of green fluorescent colloidal Cal-CPCs with blue excitation light. **c,** Colloidal stable calcein-functionalized CPCs.

Next, we studied the cellular uptake of the functionalized calcein-calcium phosphate-citrate nanoparticles. Cal-CPCs were incubated with a concentration of 50µg/mL with HeLa cells up to 24 h to determine the cell uptake behavior. In Figure 4.7 the HeLa cell membranes are colored in red using wheat germ agglutinin Alexa Fluor 647 conjugate for visibility and the green dots represent the Cal-CPC particles. The fluorescent green bare Cal-CPC particles could neither be localized at the outer cell membrane nor inside the cell membrane. Within an incubation of 24 h, no particle uptake into cells could be observed. At a physiological pH value of 7.4 HeLa cell membranes exhibit a negatively charged surface.[46,47] For Cal-CPCs the zeta potential is negative as well at pH = 7.4, with a value of -5 mV, apparently leading to a repulsion of the particles from the cell membrane.[48]

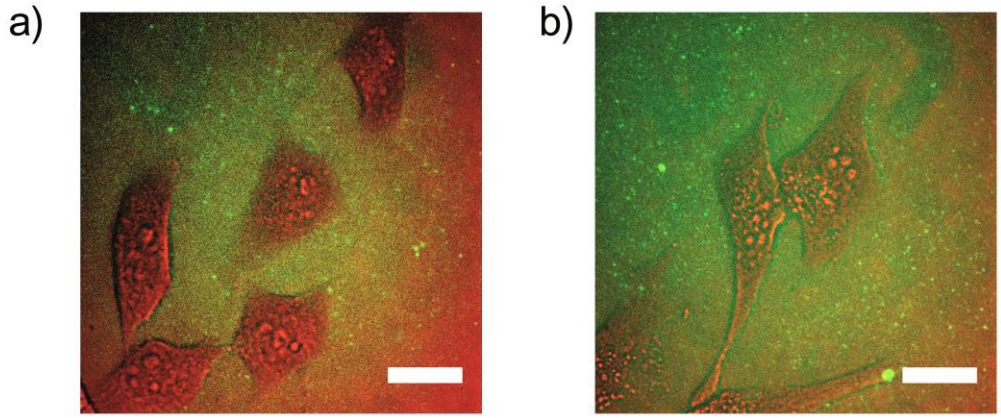

Figure 4.7: **a,** and **b,** Fluorescently functionalized CPCs (Cal-CPCs) excited with 488 nm in a confocal fluorescence microscope. The green dots represent Cal-CPCs. For visualization the HeLa cell membranes were colored in red. The red features of the cells visualize internalized dye. Scale bars: 50 µm.

To enhance the uptake of nanoparticles by HeLa cells, we developed a two-step synthesis method for a lipid coating. Elsewhere, lipid calcium phosphate nanoparticles (LCPs) have been coated with a supported lipid membrane.[49,50,51] As a result, the uptake of lipid-coated nanoparticles by cells was observed. Here, we formed a lipid coating consisting of 1,2-dioleoyl-3-trimethylammonium-propane (DOTAP) and 1,2-dioleoyl-sn-glycero-3-phosphocholine (DOPC) encapsulating the particles employing the established solvent exchange method[52] in combination with a layer-by-layer approach. First, after centrifugation of 1 mg of Cal-CPCs we redispersed the nanoparticles in a solution containing DOTAP to form a coating. Here, the head group part of the positively charged lipid is responsible for the interaction with the negatively charged nanoparticle surface.[53] After a second centrifugation step a lipid mixture consisting of DOTAP/DOPC is added to the particles forming a supported lipid bilayer around the Cal-CPCs after the solvent exchange to yield lipid@Cal-CPCs. Successful formation of the lipid coating resulted in a drastic increase in zeta potential from -5 mV to +20 mV at pH 7.4, due to the positively charged DOTAP.[54] After 24 h incubation of lipid@Cal-CPCs with HeLa cells (Figure 4.8a and b) we observed an attachment of particles to the

WGA647-stained cell membrane (blue arrows) and additionally confirmed particle internalization (yellow arrows). Hence, we showed that the uptake of Cal-CPCs can be facilitated with the formation of a supported lipid bilayer consisting of DOTAP and DOPC.

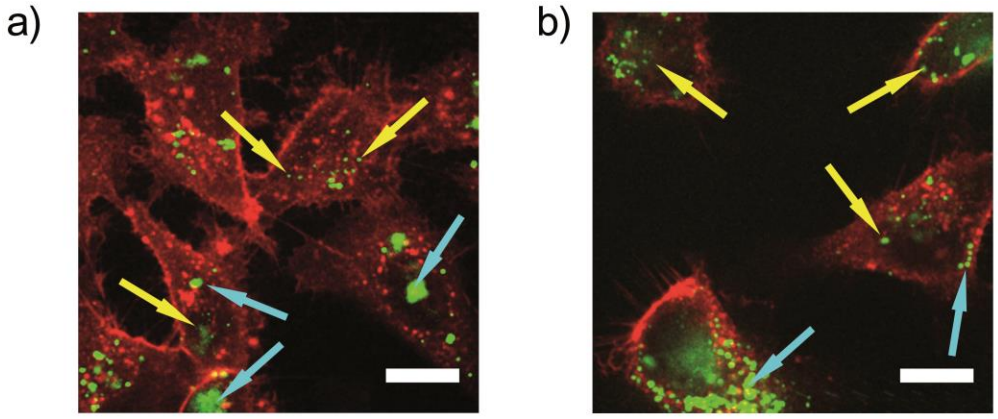

Figure 4.8: **a,** and **b,** Fluorescently functionalized lipid-coated CPCs (lipid@Cal-CPCs) excited with 488 nm in a confocal fluorescence microscope. The green dots represent lipid@Cal-CPCs. For visualization the cell membrane was stained in red with WGA647. The blue arrows point out lipid@Cal-CPCs that are attached to the cell membrane or large aggreates. The yellow arrows represent internalized lipid@Cal-CPCs. Scale bars: 20 µm.

4.3 Conclusion

Mesoporous calcium phosphate-citrate nanoparticles (CPCs) were synthesized via a precipitation reaction. The addition of strontium, manganese, or calcein into the reaction solution led to functionalized CPCs. Using energy dispersive X-ray spectroscopy, inductive coupled plasma analysis, and fluorescence measurements, we demonstrated the successful functionalization of CPCs. We established that the functionalization had only minor impact on the mesoporosity and that it led to nanoparticles with BET surface areas between 530 m^2/g to 600 m^2/g, pore sizes between 4.5 nm and 4.8 nm and corresponding calculated pore volumes in the range from 0.52 cm^3/g to 0.59 cm^3/g. All functionalized particles exhibited very similar

particle size distributions with maxima at 290 nm. The incorporation of citrate into the structure of the functionalized CPCs was demonstrated with thermogravimetric analysis and was quantified between 20 wt% and 29 wt%. Additionally, the vibrations in IR spectroscopy at 1410 cm^{-1} and 1590 cm^{-1} were assigned to the COO^- groups of citrate.

The functionalization of CPCs with strontium enabled them to have a higher X-ray contrast under ethanolic conditions than the calcium-only CPCs. This led to a greater Hounsfield unit of Sr-CPCs compared to bare CPCs. Mn-CPCs exhibit a specific relaxivity ratio r_2/r_1 of 1.96 at 1.5 T and therefore show great potential for tracking and imaging with MRI methods.

For calcein functionalized CPCs we recorded fluorescence excitation and emission spectra. Cal-CPCs can be excited at 507 nm and exhibit a maximum emission peak at 525 nm. Additionally, we showed with confocal fluorescence microscopy that bare Cal-CPCs are not taken up by HeLa cells. Therefore, we employed a two-step approach for coating Cal-CPCs with a cationic lipid membrane. This raised the zeta potential of the Cal-CPCs from -5 mV to +25 mV, leading to enhanced attraction to the negatively charged cell surface. The lipid coating enabled efficient uptake of the lipid@Cal-CPCs by HeLa cells within 24 hours.

In conclusion, we have demonstrated the diverse functionalization of CPCs without compromising the morphology, composition, BET surface area, pore size, or pore volume, respectively. With the additional features accessible through the functionalization, the CPCs can be better detected with X-ray tomography, magnetic resonance imaging, and with fluorescence microcopy techniques. This is expected to open up novel biomedical applications for CPCs in detection and diagnosis.

4.4 Experimental

Chemicals for Nanoparticle Synthesis:

Calcium nitrate tetrahydrate (AppliChem, 99 %), ammonium dihydrogenphosphate (Alfa Aeser, 99 %), citric acid (Aldrich, 99.5 %), cetyltrimethylammonium chloride (CTAC, Fluka, 25 wt% in H_2O), Pluronic® F127 (Aldrich), ethylene glycol (Aldrich, 99.8 %), triethanolamine (TEA, Aldrich, 98%), ethanol (EtOH, Aldrich, >99.5 %), ammonium nitrate (Sigma, 99 %), calcein (Sigma), manganese(II) nitrate tetrahydrate (Sigma, 98 %), strontium nitrate (Sigma, 99 %), simulated body fluid (SBF, prepared as written elsewhere[55], contains: Na^+, K^+, Mg^{2+}, Ca^{2+}, Cl^-, CO_3^{2-}, SO_4^{2-}, PO_4^{3-}, and tris(hydroxymethyl) aminomethane, Sigma, >99 %), 1,2-dioleoyl-3-trimethylammonium-propane (DOTAP, Avanti Polar Lipids), 1,2-dioleoyl-sn-glycero-3-phosphocholine (DOPC, Avanti Polar Lipids), sodium hydroxide (Aldrich, 0.1 M).

All chemicals were used as received without further purification. Doubly distilled water from a Millipore system (Milli-Q Academic A10) was used for all synthesis steps.

Cell Line and Culture:

HeLa human cervical cancer cells were purchased from and cultured according to American Type Culture Collection (ATCC). HeLa cells were grown in DMEM medium low glucose (Sigma Aldrich) supplemented with 10 % FCS (Gibco) and 2 mM L-glutamine (Gibco) at 37 °C and 5 % CO_2. Cells were routinely tested and confirmed as mycoplasma free.

Synthesis of Unfunctionalized and Functionalized Calcium Phosphate-Citrate Nanoparticles (CPCs):

In a 50 mL polypropylene reactor calcium nitrate tetrahydrate (265 mg, 1.13 mmol), ammonium dihydrogenphosphate (86.3 mg, 0.75 mmol) and citric acid (240 mg, 1.25 mmol) were dissolved in water (20 mL, 1.11 mmol). Depending on the functionalization strontium nitrate (26.5 mg, 0.125 mmol, 10 mol%), manganese(II) nitrate tetrahydrate (31.4 mg, 0.125 mmol, 10 mol%), or calcein (7.8 mg, 12.5 µmol, 1 mol%) were added to the solution and stirred until dissolution was complete. If unfunctionalized CPCs were synthesized, supplementary calcium nitrate tetrahydrate (30 mg, 0.125 mmol) was added to the initial reaction solution. Then, cetyltrimethylammonium chloride (622 mg, 1.94 mmol) and the triblock copolymer Pluronic® F127 (100 mg) were added and the synthesis mixture was stirred at 500 rpm at room temperature. After 10 minutes of stirring, ethylene glycol (7.15 g, 115 mmol) was added and the solution was cooled 5 minutes at 0 °C. Then, the clear solution was combined with triethanolamine (7.15 g, 48 mmol) under vigorous stirring and was allowed to reach room temperature. The suspension was stirred at 500 rpm at room temperature for 10 minutes. Then, the suspension was diluted approximately 1:1 with ethanol. The particles were separated by centrifugation at 7,830 rpm (7,197 rcf) for 15 minutes and redispersed in NH_4NO_3/EtOH (2 wt%, 80 mL). To extract the template, the suspension was heated under reflux conditions at 90 °C for 30 minutes. Then, the particles were separated by centrifugation at 7,830 rpm (7,197 rcf) for 10 minutes and redispersed in 80 mL ethanol. The mixture was again heated under reflux conditions at 90 °C for 30 minutes. The particles were separated by centrifugation at 7,830 rpm (7,197 rcf) for 10 minutes and redispersed in 20 mL ethanol.

Functionalization of Calcein-Calcium Phosphate-Citrate Nanoparticles with a Lipid Membrane Coating:

1 mg of calcein-calcium phosphate-citrate nanoparticles was separated by centrifugation at 14,000 rpm (16,873 rcf) for 3 minutes. The particles were redispersed in a lipid solution of 1,2-dioleoyl-3-trimethylammonium-propane (DOTAP, 100 µL of a solution with 12.5 mg/mL 60/40 vol% H_2O/EtOH), and bi-distilled water (900 µL, pH adjusted to 9.4 with NaOH) was added. Then, the particles were separated by centrifugation at 14,000 rpm (16,873 rcf) for 5 minutes. The particles were redispersed in 100 µL of a 1:1 vol lipid solution of DOTAP and 1,2-dioleoyl-sn-glycero-3-phosphocholine (DOPC, 12.5 mg/mL 60/40 vol% H_2O/EtOH) and SBF (900 µL, pH 7.4) was added. The lipid-coated calcein-calcium phosphate-citrate nanoparticles were washed twice by centrifugation at 12,000 rpm (12,396 rcf, 13 °C) for 5 minutes with SBF (500 µL, pH 7.4) to yield lipid@Cal-CPCs.

Magnetic Resonance Imaging (MRI) methods:

Samples were prepared in 2 mL tubes (Mn-CPCs at concentrations of 0.5, 1.0, 3.0, and 6.0 mg/mL in 2 mL aqueous solution) and placed in a sample holder in a basin filled with 650 mL water and 0.4 mL Gd-DTPA at 24 °C. This setup was imaged in an MRI head coil. After orientation with standard MRI pulse sequences, a gradient echo sequence with a nonselective saturation recovery (SR) preparation pulse was applied for the calculation of T1 parameter maps. The saturation recovery time was varied from 130-5000 ms in 30 steps (echo time = 1.71 ms, repetition time = 747 ms, matrix = 128 x 128, in plane resolution = 1 mm, slice thickness = 6 mm, $\alpha = 15°$, parallel imaging acceleration factor = 2). T2-weighted multi contrast 2D spin echo sequences (SE MC) were repeated by varying the echo time 16 times in steps of

15 ms starting with 15 ms and ending with 240 ms for T2 parameter map calculation (repetition time = 3 s, in plane resolution = 0.5 mm, echo train length = 16, matrix = 256 x 256, slice thickness = 6 mm, α = 180°, parallel imaging acceleration factor = 2). Calculations were done using mean signal intensity values that were determined in the regions of interest. For calculations, a stoichiometric composition of Mn-CPCs with the formula of $Ca_{4.5}Mn_{0.5}(PO_4)_3OH$ was employed, based on elemental analysis data.

Table 4.3: Specific relaxivity values of r_1 and r_2 per mmol manganese in Mn-CPCs.

Sample	**Calculation per mmol Mn^{2+}**	
	Relaxivity r_1	**Relaxivity r_2**
Mn-CPCs	3.27 L/mmol/s	6.42 L/mmol/s

4.5 Characterization

Characterization of Nanoparticles:

Nitrogen sorption analysis was performed on a Quantachrome Instrument Nova 4000e at 77 K. Samples (25 mg) were outgassed at 120 °C for 12 h *in vacuo* (10 mTorr). Pore size and pore volume were calculated by a QSDFT equilibrium model of N_2 on carbon, based on the desorption branch of the isotherms. The QSDFT method takes into account the effects of surface roughness and heterogeneity.[56] Pore volumes were evaluated up to a pore size of 10 nm, in order to remove the contribution of inter-particle textural porosity. Surface areas were calculated with the BET model.[57] Thermogravimetric analysis of the samples was performed on a Netzsch STA 440 C TG/DSC in a stream of synthetic air with a flow rate of 25 mL/min and a heating rate of 10 K/min. Dynamic light scattering measurements

were performed on a Malvern Zetasizer-Nano instrument with a 4 mW He-Ne laser (633 nm) in ethanolic suspension with a concentration of 0.5 mg/mL. Infrared spectra were measured with a Thermo Scientific Nicolet iN 10 infrared microscope. XRD patterns were obtained with a Bruker D8 Discover X-ray diffractometer using Cu-K_α radiation (1.5406 Å). Scanning electron microscopy (SEM) images were obtained on a JEOL JSM-6400F. For sample preparation a droplet of the ethanolic colloidal suspension was placed on a 60 °C preheated sample holder. Samples were sputtered with carbon before measurement. EDX spectra were recorded with an EDAX Apollo XLT SDD Detector (30 mm^2). For ICP measurements the samples were dissolved in concentrated HNO_3 and heated at 110 °C for 30 minutes. After dilution with H_2O the data collection was carried out with a Varian Vista RL ICP-OES with radially viewed plasma. Transmission electron microscopy was performed on a FEI TECNAI G2 with an acceleration voltage of 200 kV. For sample preparation a droplet of a diluted ethanolic colloidal suspension was deposited on a carbon-coated copper grid and the solvent was allowed to evaporate. Computer tomography experiments were carried out with a conventional ECAT EXACT HR^+ PET tomograph (Siemens/CTI) and the image analysis was performed with the software Amide®. Magnetic Resonance Imaging (MRI) was performed with a 1.5 T clinical MRI system (Magnetom Aera, Siemens Health Care).

Live-Cell Fluorescence Microscopy:

To visualize nanoparticle internalization by cells, live-cell imaging was performed on a spinning disc microscope based on the Zeiss Cell Observer SD utilizing a Yokogawa spinning disk unit CSU-X1. The system was equipped with a 1.40 NA 63x Plan apochromat oil immersion objective from Zeiss. For all experiments the exposure time was 0.1 s and z-stacks were recorded. Cal-CPCs were imaged with

approximately 0.4 W/mm^2 of 488 nm excitation light. Atto647 was excited with approximately 11 mW/mm^2 of 639 nm. In the excitation path a quad-edge dichroic beamsplitter (FF410/504/582/669-Di01-25x36, Semrock) was used. For two-color detection of calcein and Atto647, a dichroic mirror (560 nm, Semrock) and band-pass filters 525/50 and 690/60 (both Semrock) were used in the detection path. Separate images for each fluorescence channel were acquired using two separate electron multiplier charge coupled device (EMCCD) cameras (PhotometricsEvolve^{TM}). Immediately before imaging, cell membranes were stained using wheat germ agglutinin Alexa Fluor 647 conjugate at a final concentration of 5 µg/mL. After application of the dye, cells were washed twice.

4.6 References

1 M. N. Moore. Do nanoparticles present ecotoxicological risks for the health of the aquatic environment? *Environment International* **32,** 967-976, (2006).

2 N. T. Thanh & L. A. Green. Functionalisation of nanoparticles for biomedical applications. *Nano Today* **5,** 213-230, (2010).

3 I. Brigger, C. Dubernet & P. Couvreur. Nanoparticles in cancer therapy and diagnosis. *Advanced Drug Delivery Reviews* **54,** 631-651, (2002).

4 Q. A. Pankhurst, J. Connolly, S. K. Jones & J. Dobson. Applications of magnetic nanoparticles in biomedicine. *Journal of Physics D: Applied Physics* **36,** R167, (2003).

5 R. Subbiah, M. Veerapandian & K. S Yun. Nanoparticles: functionalization and multifunctional applications in biomedical sciences. *Current Medicinal Chemistry* **17,** 4559-4577, (2010).

6 R. Hao *et al.* Synthesis, functionalization, and biomedical applications of multifunctional magnetic nanoparticles. *Advanced Materials* **22,** 2729-2742, (2010).

7 N. Sanvicens & M. P. Marco. Multifunctional nanoparticles – properties and prospects for their use in human medicine. *Trends in Biotechnology* **26,** 425-433, (2008).

8 R. A. Sperling & W. J. Parak. Surface modification, functionalization and bioconjugation of colloidal inorganic nanoparticles. *Philosophical Transactions of the Royal Society A: Mathematical, Physical and Engineering Sciences* **368,** 1333-1383, (2010).

9 R. Yuste. Fluorescence microscopy today. *Nature Methods* **2,** 902-904, (2005).

10 S. C. Baetke, T. Lammers & F. Kiessling. Applications of nanoparticles for diagnosis and therapy of cancer. *The British Journal of Radiology* **88,** 20150207, (2015).

11 E. C. Wang & A. Z. Wang. Nanoparticles and their applications in cell and molecular biology. *Integrative Biology: Quantitative Biosciences from Nano to Macro* **6,** 9-26, (2014).

12 D. P. Cormode, P. C. Naha & Z. A. Fayad. Nanoparticle contrast agents for computed tomography: a focus on micelles. *Contrast Media & Molecular Imaging* **9,** 37-52, (2014).

13 R. Popovtzer *et al.* Targeted gold nanoparticles enable molecular CT imaging of cancer. *Nano Letters* **8,** 4593-4596, (2008).

14 J. Estelrich, M. J. Sánchez-Martín & M. A. Busquets. Nanoparticles in magnetic resonance imaging: from simple to dual contrast agents. *International Journal of Nanomedicine* **10,** 1727-1741, (2015).

15 J. Huang, X. Zhong, L. Wang, L. Yang & H. Mao. Improving the magnetic resonance imaging contrast and detection methods with engineered magnetic nanoparticles. *Theranostics* **2,** 86-102, (2012).

16 P. Mi *et al.* A pH-activatable nanoparticle with signal-amplification capabilities for non-invasive imaging of tumour malignancy. *Nature Nanotechnology* **11,** 724-730, (2016).

17 W. Habraken, P. Habibovic, M. Epple & M. Bohner. Calcium phosphates in biomedical applications: materials for the future? *Materials Today* **19,** 69-87, (2016).

18 Y. Pan & M. E. Fleet. Compositions of the apatite-group minerals: substitution mechanisms and controlling factors. *Reviews in Mineralogy and Geochemistry* **48,** 13-49, (2002).

19 M. Epple *et al.* Application of calcium phosphate nanoparticles in biomedicine. *Journal of Materials Chemistry* **20,** 18-23, (2010).

20 B. Bracci *et al.* Effect of Mg^{2+}, Sr^{2+}, and Mn^{2+} on the chemico-physical and *in vitro* biological properties of calcium phosphate biomimetic coatings. *Journal of Inorganic Biochemistry* **103,** 1666-1674, (2009).

21 A. Bandyopadhyay, S. Bernard, W. Xue & S. Bose. Calcium phosphate-based resorbable ceramics: influence of MgO, ZnO, and SiO_2 dopants. *Journal of the American Ceramic Society* **89,** 2675-2688, (2006).

22 X. Wang, J. Ye & Y. Wang. Influence of a novel radiopacifier on the properties of an injectable calcium phosphate cement. *Acta Biomaterialia* **3,** 757-763, (2007).

23 M. Schumacher & M. Gelinsky. Strontium modified calcium phosphate cements–approaches towards targeted stimulation of bone turnover. *Journal of Materials Chemistry B* **3,** 4626-4640, (2015).

24 D. Pan, A. H. Schmieder, S. A. Wickline & G. M. Lanza. Manganese-based MRI contrast agents: past, present and future. *Tetrahedron* **67,** 8431-8444, (2011).

25 E. Boanini, M. Gazzano & A. Bigi. Ionic substitutions in calcium phosphates synthesized at low temperature. *Acta Biomaterialia* **6,** 1882-1894, (2010).

26 M. P. Pechini. Method of preparing lead and alkaline earth titanates and niobates and coating method using the same to form a capacitor. US3330697 (1967).

27 P. Yang, P. Yang, X. Teng, J. Lin & L. Huang. A novel luminescent mesoporous silica/apatite composite for controlled drug release. *Journal of Materials Chemistry* **21,** 5505-5510, (2011).

28 W. Weng, G. Han, P. Du & G. Shen. The effect of citric acid addition on the formation of sol–gel derived hydroxyapatite. *Materials Chemistry and Physics* **74,** 92-97, (2002).

29 I. Sopyan & A. N. Natasha. Preparation of nanostructured manganese-doped biphasic calcium phosphate powders via sol–gel method. *Ionics* **15,** 735-741, (2009).

30 C. Drouet. Apatite formation: why it may not work as planned, and how to conclusively identify apatite compounds. *BioMed Research International* **2013**, (2013).

31 K. Zilm. Mechanism of CO_3^{2-} substitution in carbonate-fluorapatite: evidence from FTIR spectroscopy, ^{13}C NMR and quantum mechanical calculations. *American Mineralogist*, (1994).

32 E. E. Berry. The structure and composition of some calcium-deficient apatites. *Journal of Inorganic and Nuclear Chemistry* **29,** 317-327, (1967).

33 L. Brečević & H. Füredi-Milhofer. Precipitation of calcium phosphates from electrolyte solutions V. The influence of citrate ions. *Calcified Tissue International* **28,** 131-136, (1979).

34 J. W. Furry. Preparation, properties and applications of calcein in a highly pure form. (1985).

35 C. Orellana-Tavra *et al.* Amorphous metal-organic frameworks for drug delivery. *Chemical Communications* **51,** 13878-13881, (2015).

36 K. S. Sing. Reporting physisorption data for gas/solid systems with special reference to the determination of surface area and porosity (Recommendations 1984). *Pure and Applied Chemistry* **57,** 603-619, (1985).

37 A. J. Ambard & L. Mueninghoff. Calcium phosphate cement: review of mechanical and biological properties. *Journal of Prosthodontics* **15,** 321-328, (2006).

38 R. Z. LeGeros. Calcium phosphate-based osteoinductive materials. *Chemical Reviews* **108,** 4742-4753, (2008).

39 X. X. Xu *et al.* CT-guided sclerotherapy with ethanol concentration monitoring for treatment of renal cysts. *American Journal of Roentgenology* **196,** W78-W82, (2011).

40 M. R. Norton & C. Gamble. Bone classification: an objective scale of bone density using the computerized tomography scan. *Clinical Oral Implants Research* **12,** 79-84, (2001).

41 J. J. Schreiber, P. A. Anderson, H. G. Rosas, A. L. Buchholz & A. G. Au. Hounsfield units for assessing bone mineral density and strength: a tool for osteoporosis management. *Journal of Bone and Joint Surgery* **93,** 1057-1063, (2011).

42 J. S. Troughton *et al.* Synthesis and evaluation of a high relaxivity manganese(II)-based MRI contrast agent. *Inorganic Chemistry* **43,** 6313-6323, (2004).

43 A. C. Silva, J. H. Lee, I. Aoki & A. P. Koretsky. Manganese-enhanced magnetic resonance imaging (MEMRI): methodological and practical considerations. *NMR in Biomedicine* **17,** 532-543, (2004).

44 W. S. Seo *et al.* FeCo/graphitic-shell nanocrystals as advanced magnetic-resonance-imaging and near-infrared agents. *Nature Materials* **5,** 971-976, (2006).

45 T. Kim *et al.* Mesoporous silica-coated hollow manganese oxide nanoparticles as positive T1 contrast agents for labeling and MRI tracking of adipose-derived mesenchymal stem cells. *Journal of the American Chemical Society* **133,** 2955-2961, (2011).

46 B. Chen *et al.* Targeting negative surface charges of cancer cells by multifunctional nanoprobes. *Theranostics* **6,** 1887-1898, (2016).

47 S. E. A. Gratton *et al.* The effect of particle design on cellular internalization pathways. *Proceedings of the National Academy of Sciences* **105,** 11613-11618, (2008).

48 C. R. Miller, B. Bondurant, S. D. McLean, K. A. McGovern & D. F. O'Brien. Liposome−cell interactions *in vitro*: effect of liposome surface charge on the binding and endocytosis of conventional and sterically stabilized liposomes. *Biochemistry* **37,** 12875-12883, (1998).

49 J. Li, Y.-C. Chen, Y.-C. Tseng, S. Mozumdar & L. Huang. Biodegradable calcium phosphate nanoparticle with lipid coating for systemic siRNA delivery. *Journal of Controlled Release* **142,** 416-421, (2010).

50 Y. Zhang, N. M. Schwerbrock, A. B. Rogers, W. Y. Kim & L. Huang. Codelivery of VEGF siRNA and gemcitabine monophosphate in a single nanoparticle formulation for effective treatment of NSCLC. *Molecular Therapy* **21,** 1559-1569, (2013).

51 Y.-C. Tseng, Z. Xu, K. Guley, H. Yuan & L. Huang. Lipid–calcium phosphate nanoparticles for delivery to the lymphatic system and SPECT/CT imaging of lymph node metastases. *Biomaterials* **35,** 4688-4698, (2014).

52 V. Cauda *et al*. Colchicine-loaded lipid bilayer-coated 50 nm mesoporous nanoparticles efficiently induce microtubule depolymerization upon cell uptake. *Nano Letters* **10,** 2484-2492, (2010).

53 P. Jurkiewicz, A. Olżyńska, M. Langner & M. Hof. Headgroup hydration and mobility of DOTAP/DOPC bilayers: a fluorescence solvent relaxation study. *Langmuir* **22,** 8741-8749, (2006).

54 A. López-Macipe & J. Gómez-Morales. The role of pH in the adsorption of citrate ions on hydroxyapatite. *Journal of Colloid and Interface Science* **200,** 114-120, (1998).

55 M. R. Marques, R. Loebenberg & M. Almukainzi. Simulated biological fluids with possible application in dissolution testing. *Dissolution Technologies* **18,** 15-28, (2011).

56 Quantachrome. *Application of QSDFT (quenched solid density functional theory) - a Novel Density Functional Theory for an Accurate Pore Size Analysis of Disordered Porous Carbons*. Volume 40 (Quantachrome Instruments USA).

57 S. Brunauer, P. H. Emmett & E. Teller. Adsorption of gases in multimolecular layers. *Journal of the American Chemical Society* **60,** 309-319, (1938).

CHAPTER 5

MESOPOROUS CALCIUM PHOSPHATE-CITRATE NANOPARTICLES WITH DIFFERENTIAL EFFICIENCY AGAINST EPITHELIAL AND MESENCHYMAL CANCER CELLS

Constantin von Schirnding, Adam Hermawan, Ann-Kathrin Sommer, Veronika Weiß, Johann Feckl, Andreas Roidl, Malamati Vreka, Maria Papageorgopoulou, Georgios Stathopoulos, Christoph Bräuchle, Ernst Wagner, Hanna Engelke, and Thomas Bein.

5.1 Introduction

Conventional chemotherapeutics lead to severe side effects since toxic substances are usually administered systemically to the patient at high dosage. In recent years strategies have been developed to encapsulate chemotherapeutics and to deliver them efficiently and selectively to the target tissue.[1,2] However, these concepts still rely on transport of toxic substances and any premature leakage or residues of those substances can lead to serious side effects. Here, we present a new concept based on colloidal mesoporous hybrid calcium phosphate-citrate nanoparticles (CPCs) for intracellular delivery of calcium ions that efficiently kill cancer cells without encapsulation of additional toxic drugs. After cellular uptake facilitated by a lipid coating, CPCs are dissolved by the acidic environment in the endolysosome. Endosomal release into the cytosol is induced by small amounts of incorporated amphiphile cetyltrimethylammonium chloride. The particles are neither toxic before endosomal release nor after their degradation. Remarkably, CPCs affect mesenchymal cancer cells even more strongly than epithelial cancer cells, which was established using fourteen different cell lines. In first experiments, we treated tumor bearing mice in a nude mouse xenograft model implanted in the intrapleural space with CPCs. After one single injection of CPCs, we observed a reduction in tumor weight of ~40 wt%.

5.2 Results and Discussion

Calcium phosphate materials, such as hydroxyapatite ($Ca_{10}(PO_4)_6(OH)_2$), the main inorganic component of bone and teeth, have recently been discussed as a new promising platform for advanced drug delivery applications due to their high biocompatibility and non-toxicity.[3,4,5] Calcium phosphate is biodegradable[6] and thus

addresses the challenge of finding a material that has no toxic side effects. For this reason various drugs[7,8,9,10,11] have been adsorbed on calcium phosphate materials and their effect has been investigated on cells. Co-precipitation of Ca^{2+}- and PO_4^{3-}-ions with gemcitabine, siRNA, or proteins[12,13] has also been shown to be an efficient method to deliver drugs employing Lipid/Calcium/Phosphate (LCP) combinations due to their biocompatibility and the encapsulation of the drugs with lipids in the calcium/phosphate core.

However, calcium phosphate has also been reported to have toxic effects on cells at high concentrations above 125 µg/mL.[14,15,16] This toxicity can be attributed to a sudden intracellular release of soluble calcium into the cytosol of a cell;[14,15,16,17,18] the physiological concentration of free intracellular calcium (100 nM) is very low, 10.000 fold lower than in plasma. A slow or extracellular increase in calcium from nanoparticles can be well managed by cells. Physical cytosolic delivery of Ca^{2+} at toxic levels by electroporation has recently been introduced as a potent tumor therapy *in vitro* and *in vivo* and clinical studies with cancer patients have been initiated.[19] Toxic calcium levels were shown to activate Ca^{2+}-ATPases which consume and deplete cellular ATP.[17,20]

Physical delivery by electroporation requires local tumor injection for calcium delivery. Known calcium phosphate nanoparticles can be systemically targeted to tumors via the blood circulation, but do not intracellularly release cytotoxic calcium levels. Thus, for efficient nanoparticle dissolution in the acidifying endolysosome followed by delivery of calcium into the cytosol, we designed novel hybrid mesoporous calcium phosphate-citrate nanoparticles (CPCs).

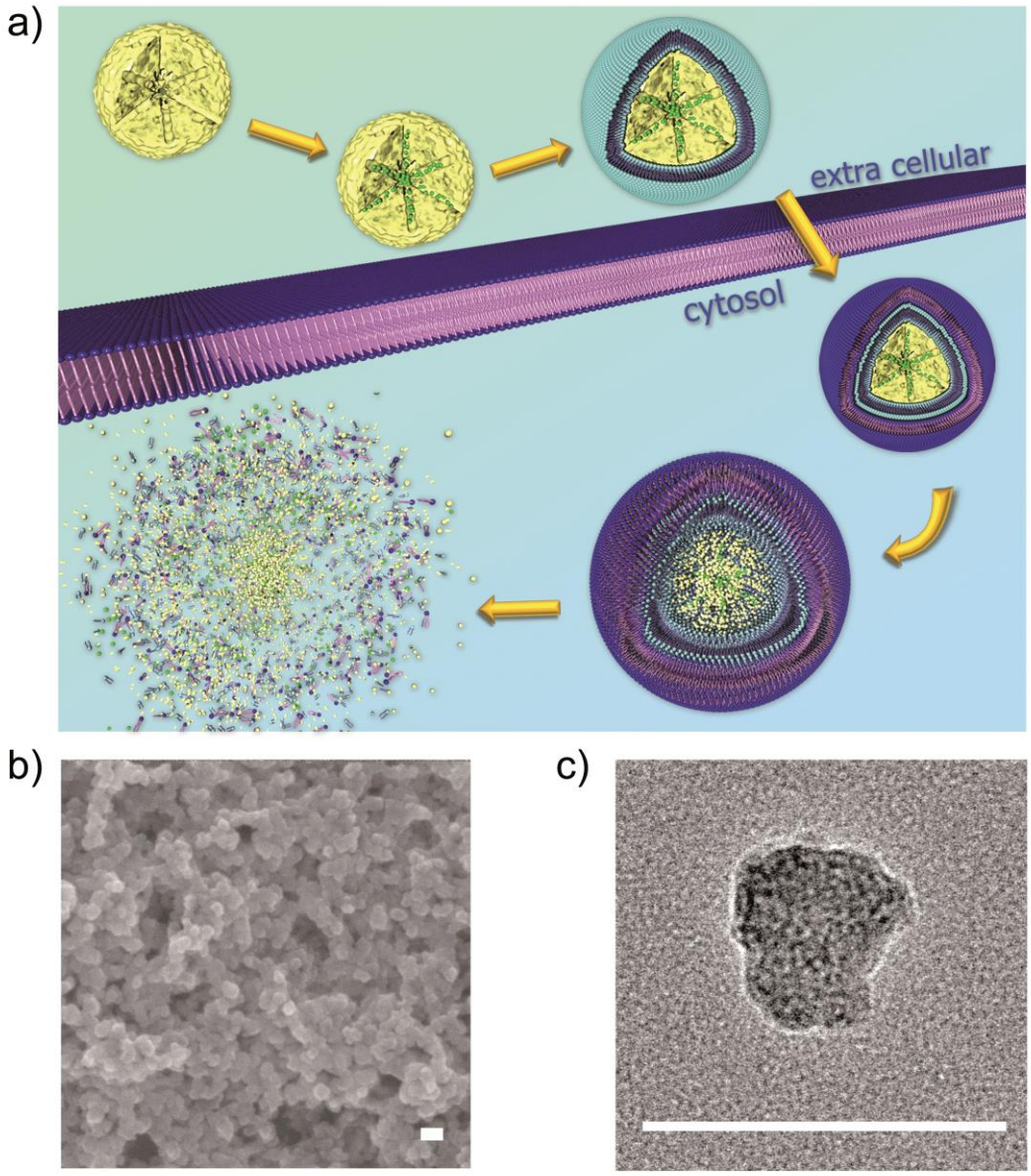

Figure 5.1: Schematic pathway of cellular uptake and dissolution of calcium phosphate-citrate nanoparticles (CPCs) in the endolysosome, and electron microscopy of the mesoporous particles. **a,** Mesoporous CPCs are loaded with a fluorescent dye and coated with a lipid membrane. The particles are internalized by a cell via endocytosis, followed by dissolution due to acidification in the endosome. The process is aided by small amounts of CTAC, acting as membrane destabilizer, eventually leading to endosomal escape. **b,** Scanning electron microscopy and **c,** transmission electron microscopy images of spherical particles sized about 50 nm on average. Scale bars: 100 nm.

We synthesized CPCs by reacting Ca^{2+}- and PO_4^{3-}-ions with citric acid at a molar ratio of 5:3:5. Citric acid complexes calcium ions and thus plays an important role in the reaction kinetics during formation of calcium phosphates.[21] Precipitation of

nanoparticles is induced by rapid pH change upon addition of triethanolamine, and formation of a mesoporous structure is achieved by addition of the surfactant templates cetyltrimethylammonium chloride and Pluronic® F127. Extraction of the surfactant templates yielded the desired mesoporous hybrid calcium phosphate-citrate nanoparticles as depicted in Figure 5.1c. The successful synthesis of amorphous (see Experimental Information, Figure 5.9) calcium phosphate-citrate nanoparticles was verified by IR-measurements: the IR-spectrum of CPCs, as shown in Figure 5.2a, resembles that of crystalline apatite. It also shows two strong additional vibrations at 1414 cm^{-1} and 1590 cm^{-1} that are attributed to the symmetric and the anti-symmetric stretching modes of COO^- groups of citric acid incorporated into the CPCs structure.[22]

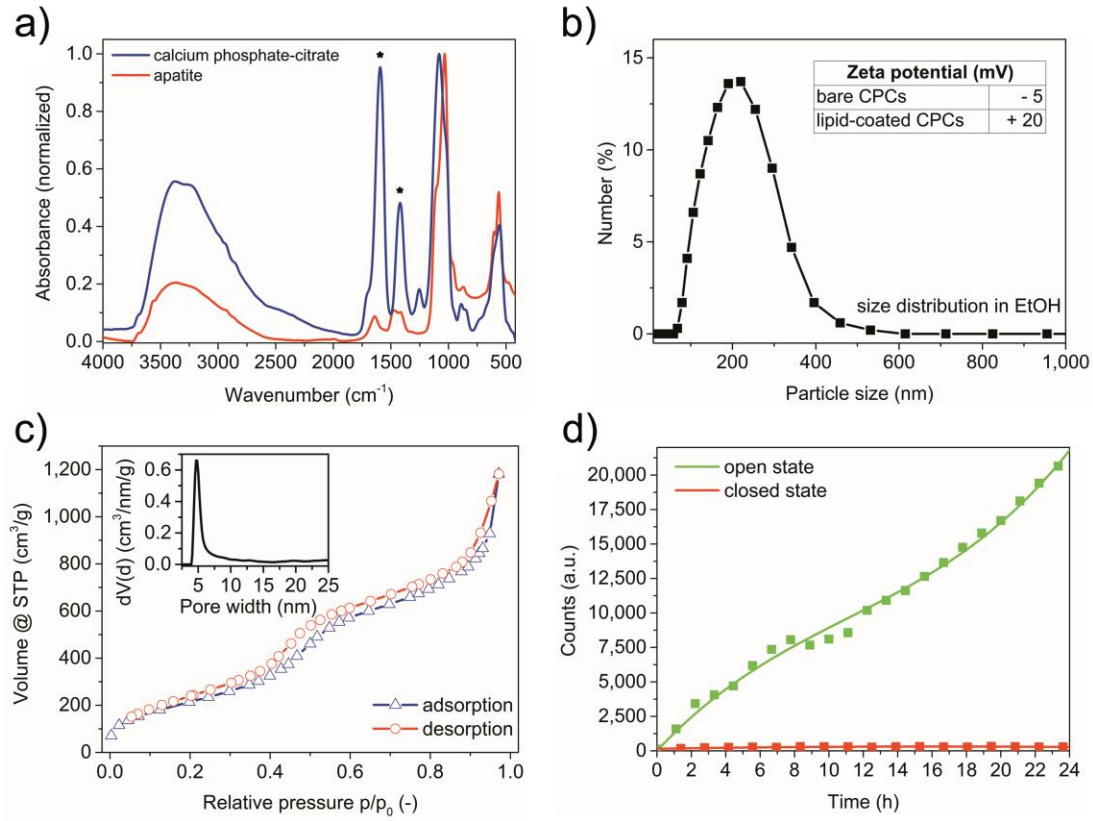

Figure 5.2: Characterization of mesoporous calcium phosphate-citrate nanoparticles (CPCs). **a,** Infrared spectra of CPCs with strong C-O vibrations at 1414 cm^{-1} and 1590 cm^{-1} (marked with asterisk) due to the incorporated citrate in the structure (blue

line), in comparison with crystalline apatite (red line). **b,** Dynamic light scattering data of colloidal CPCs show a maximum at a size of 220 nm. Zeta potential measurements (table insert) in simulated body fluid (pH 7.4) show an increase upon deposition of a positively charged lipid membrane. **c,** Nitrogen sorption analysis of mesoporous CPCs with a BET surface area of 900 m^2/g, pore size of 4.8 nm (insert), and a pore volume of 1.0 cm^3/g. **d,** Fluorescence release measurement over 24 hours showing no premature release (red line) and a strong increase upon pH-triggered release (green line).

The incorporation of citric acid was further confirmed by solid-state (ss)-NMR spectroscopy and determined to be about 20 wt% using thermogravimetric analysis (see Experimental Information, Figure 5.8 and Figure 5.10). Energy dispersive X-ray and inductively coupled plasma methods yielded an atomic ratio Ca:P of 1.61 (see Experimental Information, Table 5.1). Without further filtration, the particles showed a narrow size distribution with a hydrodynamic radius of 220 nm in ethanolic solution as measured by dynamic light scattering. Electron microscopy images showed particles of about 50 nm; taken together with the light scattering data these results show that some weak aggregation appears in solution (Figure 5.1b and Figure 5.2b). The size of 50 nm renders the particles perfectly suited for cellular uptake. The porosity of the resulting particles was analyzed with nitrogen sorption measurements. As shown in Figure 5.2c, we observed a typical type IV isotherm, which is characteristic of mesoporous systems. The particles feature an extraordinary BET surface area of 900 m^2/g, a very narrow pore size distribution with a maximum at 4.8 nm (insert), and a cumulative pore volume of 1.0 cm^3/g. The loading capacity of CPCs was probed with ibuprofen as drug molecule, and showed a significant absorption capacity and release of 15.6 wt% within about 48 h (Figure 5.7). These characteristics are unprecedented for calcium phosphate-based nanoparticles and very similar to those of the well-established mesoporous silica particles.[23] Our observed surface area is almost three times larger than that reported before for calcium phosphate-based materials with surface areas of 315 m^2/g.[7]

Next, we studied cellular uptake of the newly synthesized CPCs. Notably, we could not detect any cellular uptake of the bare as-synthesized and purified CPCs (see Chapter 4, cell experiments with Cal-CPCs). In analogy to LCP particles[12,13] that are taken up by cells due to their lipid coating, we sought to enhance particle uptake with a lipid bilayer. We formed a lipid coating consisting of 1,2-dioleoyl-3-trimethylammonium-propane (DOTAP) and 1,2-dioleoyl-sn-glycero-3-phosphocholine (DOPC) around the particles employing a solvent exchange method.[24] Successful formation of the lipid coating resulted in a drastic increase in zeta potential from -5 mV to +20 mV at pH 7.4, due to the positively charged DOTAP. To assess the integrity of the lipid coating, we loaded the particles with the membrane non-permeable fluorescent dye calcein and measured its release over a time period of 24 h in a two-compartment cuvette experiment (see Experimental Information, Figure 5.6). We could not detect any significant premature release (< 1 %), thus confirming a successful lipid coating. Acidification by addition of 0.1 M HCl dissolved the particles and led to a dramatic increase in released fluorescent dye, as measured after neutralization to pH 7.4 (Figure 5.2d).

We then investigated the uptake of lipid-coated CPCs loaded with calcein by HeLa cells. As depicted in Figure 5.3a, the lipid-coated CPCs were successfully internalized by cells. We monitored the cells over a period of several days. While the internalized particles were still very close to the cell membrane after 24 h, they were close to the nucleus after 48 h and no further development could be observed during the following days (Figure 5.3a). Compared to other nanoparticles such as mesoporous silica, endocytosis of CPCs seems rather slow. We attribute this to the presence of citric acid and phosphate ions from the lipid-coated CPCs, forming effectively a McIlvaine's buffer with high buffering capacity that slows down the

proton pump-driven process. We could not detect any impact of the internalized CPCs on cell viability up to very high particle concentrations, nor could we observe any intracellular release from purely lipid-coated CPCs loaded with calcein (Figure 5.3c-e and see Experimental Information, Figure 5.11, red line). These particles were still caught in the endosome thus preventing release of calcein or toxic calcium amounts.

To enable endosomal release, we loaded the particles with a small amount of cetyltrimethylammonium chloride. CTAC is a positively charged surfactant that can destabilize lipid membranes. While adsorbed in the particle, its attraction to the negatively charged particle prevents leakage and destabilization of the lipid coating of the particles. Once the endosomal pH turns acidic[25], the particle dissolves and releases the CTAC molecules. When incubating HeLa cells with lipid-coated CPCs loaded with calcein and CTAC, we observed a release of calcein in the cells within 72 h, quickly followed by cell death (see Experimental Information, Movie E1). We attribute this observation to a rupture of the endosome containing the dissolved particle and its cargo calcein. The dissolved particles strongly increase the ionic concentration inside the endosome causing an influx of water. This process leads to the enlargement and weakening of the endosomal membrane, and eventually to its rupture assisted by the destabilizing effect of CTAC.[26] The subsequent release of the endosomal content leads to a sudden increase of intracellular calcium levels. Calcium ions act as second messenger to regulate gene transcription, cell proliferation, migration, and cell death.[27,28] The level of intracellular Ca^{2+} is tightly controlled and a misbalance may lead to severe cellular malfunction and eventually cell death.[29] We propose that the efficient calcium release of our novel CPCs is based on their amorphous nature and their extremely thin walls with very high surface area. These

unique properties create conditions for dissolution and release of high amounts of Ca^{2+}, which is suggested to induce the observed apoptosis.[17,20]

In order to test the effect of the remaining substances on the viability of the surrounding cells after successful treatment, we incubated dissolved CPCs loaded with calcein and CTAC on HeLa cells. We did not detect any significant loss in cell viability (see Experimental Information, Figure 5.11l). The toxic effect of CPCs loaded with calcein and CTAC seems to be limited to sudden intracellular release of high amounts of calcium upon endosomal rupture, thus preventing undesired further damage to neighboring cells.

The above results on HeLa cells suggest very promising properties of CPCs when applied as chemotherapeutic agents avoiding highly toxic substances. We next studied their effect on several other cell lines to assess their general performance. For this purpose we chose seven mesenchymal cancer cell lines (HeLa, H1299, MDA-MB-231, LLC, Neuro 2A, AE17, B16), six epithelial cancer cell lines (BT-474, MCF7, HuH7, 293T, A549, MC38), and one epithelial cell line derived from non-tumorigenic tissue (MCF 10A). All tested cell lines internalized lipid-coated CPCs (Figure 5.3a). We then performed MTT assays to measure cell viability after 72 h. Neither uncoated CPCs nor lipid-coated CPCs without CTAC showed significant toxicity up to concentrations of 100 µg/mL in any of the cell lines (Figure 5.3c-k and see Experimental Information, Figure 5.11, red and green lines). However, viability of all cancerous cell lines was strongly decreased after incubation with lipid-coated CPCs loaded with the small amount of the additive CTAC - even at concentrations of less than 30 µg/mL of CPCs (Figure 5.3b, Figure 5.3d-e and see Experimental Information, Figure 5.11, black line). Strikingly, the non-cancerous cell line MCF 10A was not affected significantly by the particles up to concentrations of

100 µg/mL (Figure 5.3c, black line). For cancerous cells we observed activated caspase-3/7 protease, which induces the apoptotic execution pathway (see graphs in Experimental Information, Figure 5.12).[30] The caspase-3/7 protease activity in the non-cancerous cell line MCF 10A was not detectable. Thus, no induction of apoptosis is initiated in the non-cancerous cell line MCF 10A (see Experimental Information, Figure 5.12). These results suggest a strong selectivity regarding the toxic effect of CPCs, thus demonstrating their great potential as chemotherapeutic agents.

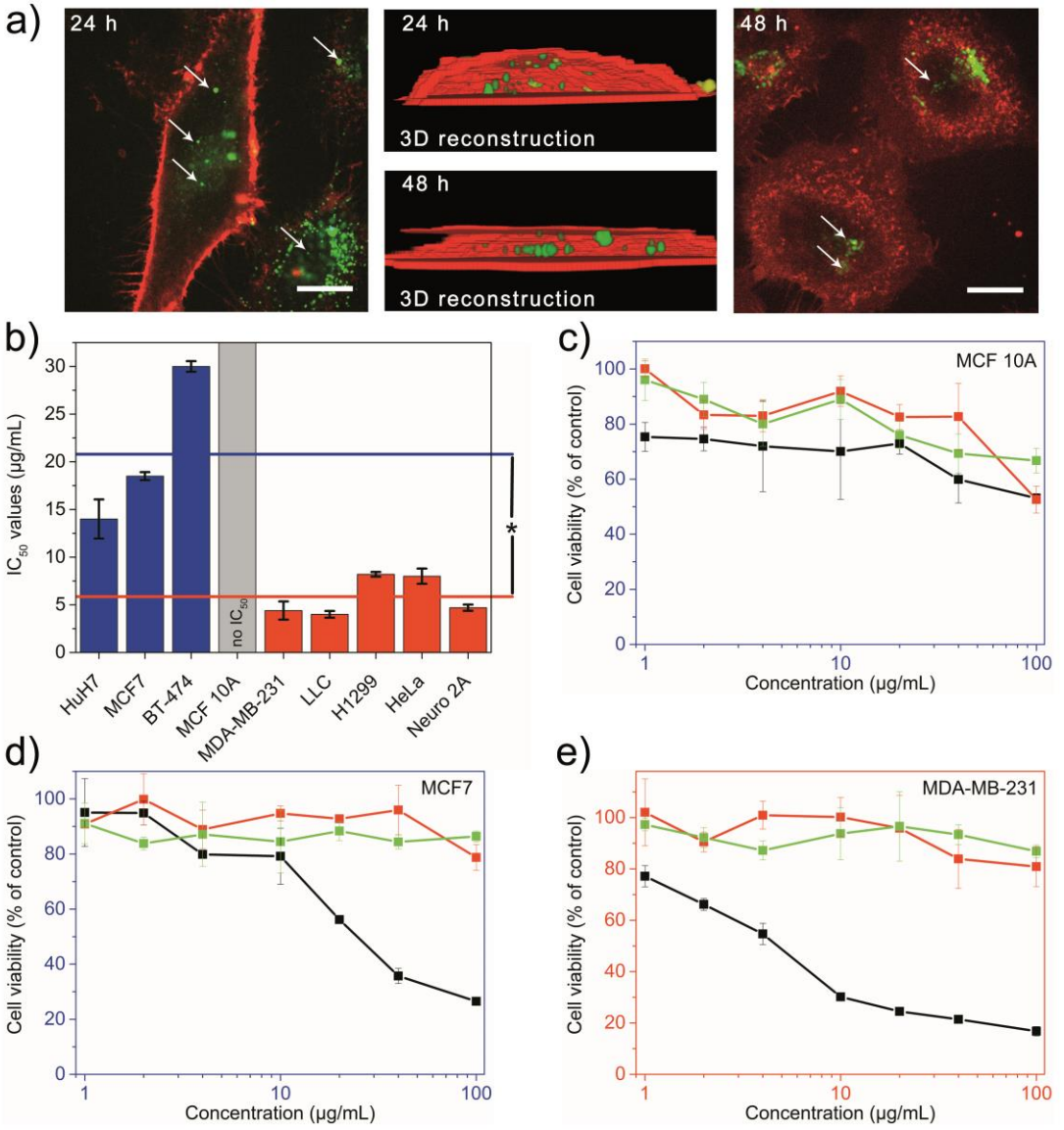

Figure 5.3: Cell studies of calcium phosphate-citrate nanoparticles (CPCs) with respect to their toxicity towards different cell lines. **a,** Confocal microscopy images of HeLa cells with lipid-coated CPCs in green (arrows) very close to the WGA-stained cell membrane in red (incubation for 24 h) and the completely internalized lipid-coated CPCs after 48 h of incubation. 3D reconstruction[31] of the particle uptake after 24 h and 48 h of incubation. Scale bars: 20 µm. **b,** IC_{50} values of the investigated cancerous epithelial (blue bars), the non-tumorigenic epithelial (gray bar, no significant cell death observed and no IC_{50} was calculated), and the cancerous mesenchymal (red bars) cell lines after treatment with lipid-coated CPCs that escape from the endosome. The horizontal lines mark the average IC_{50} values from the same cell line types (blue for cancerous epithelial and red for cancerous mesenchymal cell lines) for comparison of the selectivity of the CPCs. * indicates $p<0.05$. **c,** Cell viability of the non-tumorigenic epithelial breast cell line MCF 10A with lipid-coated CPCs that escape from the endosome (black line), that do not escape from the endosome but are taken up (red line), and CPCs without a membrane that are not taken up (green line). **d,** Same as Figure 5.3c) but for epithelial breast cancer cell line MCF7. **e,** Same as Figure 5.3c) but for mesenchymal breast cancer cell line MDA-MB-231. For details on all investigated cell lines see Experimental Information.

We further determined the IC_{50} values for all tested cell lines (see Experimental Information, Table 5.2). They are depicted in Figure 5.3b and exhibit a large difference between mesenchymal and epithelial cancer cells. Mesenchymal cells are about 4.8 fold more affected than epithelial tumor cells. With these unusual properties, CPCs belong to the small group of substances such as the cancer stem cell drug salinomycin[32] that can be used to selectively treat mesenchymal tumor cells. Salinomycin also facilitates an elevated intracellular calcium concentration[33], which was shown to induce natural cell-protective autophagy. In contrast to normal cells, mesenchymal cancer cells lack this protective mechanism.[34] The enhanced sensitivity of mesenchymal cancer cells against CPCs might result from missing such a compensation mechanism that attenuates the intracellular calcium levels. In sum, CPCs offer a great potential as antitumoral agents. Surface modifications with targeting and shielding agents may further enhance the inherent selectivity of the new material towards cancer cells.

To further investigate the mechanism of therapeutically active CPCs in comparison to lipid-coated CPCs without CTAC, we measured the NADH and ATP levels in a

time course bulk experiment. NADH participates in oxidation-reduction reactions in cells.[35] ATP stores and regulates the energy balance of cells.[35] The levels of NADH and ATP are benchmarks for cell activity and vitality. In Figure 5.4a, we show that the NADH levels rapidly reduce after incubation with both types of CPCs. We ascribe this general observation to processes relating to the nanoparticle uptake by cells.[36] After 10 h of incubation the NADH levels of therapeutically active CPCs decrease (black line), while lipid-coated CPCs (red line) keep a steady level of NADH. The downregulation of cell viability is followed by ATP depletion (Figure 5.4b, black line) after 30 h of incubation with therapeutically active CPCs. Toxic levels of cytosolic calcium activate Ca^{2+}-ATPases that consume cellular ATP.[17,20] For lipid-coated CPCs ATP depletion was not observable, which we believe is caused by the absent lysosomal rupture for lipid-coated CPCs without CTAC.

In additional single cell fluorescence microscopy experiments, we measured the cytosolic calcium levels with the transfected intracellular Ca^{2+}-sensor CAR-GECO.[37] Simultaneously, we measured the amount of calcein in the cytosol released from dissolved therapeutically active CPCs loaded with calcein due to lysosomal rupture. Figure 5.4c depicts the area-corrected total cell fluorescence of a single exemplary HeLa cell following the fluorescence intensity for each channel. Within 16 hours (dashed vertical line, marked with asterisk) after incubating HeLa cells with therapeutically active CPCs we observe the internalization of particles (steady increase of calcein channel). Then the particular HeLa cell underwent cell division. Shortly before the cell division, an increase of intracellular calcium (CAR-GECO channel) with a maximum fluorescence after 15 h was observable. Cell division can independently be activated with increase of calcium levels, confirming the importance of the calcium signaling pathways for cells.[38,39,40] Furthermore, within a

16 h time span, cell division is a natural process and does not necessarily need to be a result of treatment with CPCs. Consequently, fluorescence signal intensity is approximately halved after cell division. At hour 35 after incubation, we observed a dramatic increase in intensity in both channels, for the calcium as well as for the calcein channel. The intensity of the calcein channel increased 4.5 fold, the Ca^{2+} level increased 6 fold. Thereby, we relate the increase in concentration of intracellular Ca^{2+} to the sudden endosomal release of dissolved CPCs. From 47 hours on after incubation an additional increase of intracellular Ca^{2+} is observed, which we attribute to the breakdown of the membrane potential typical for apoptotic cells.[41,42,43] The event of the complete break up into several apoptotic bodies coincides with additional ruptures of endosomes and increased Ca^{2+} levels (vertical line marked with pound).[44] (For a movie see Experimental Information, Movie E2).

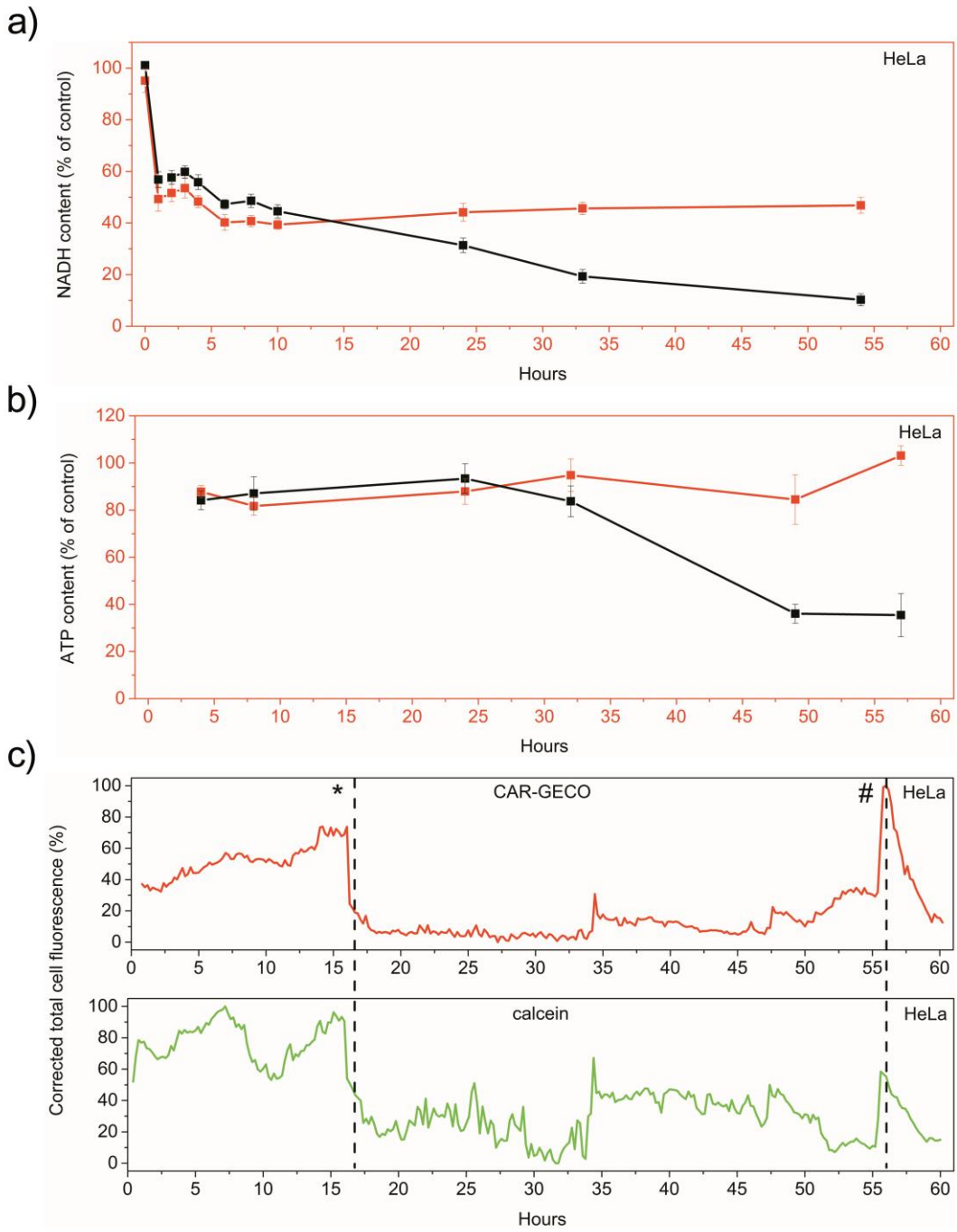

Figure 5.4: Time-dependent tracking of therapeutically active CPCs (black line) and lipid-coated CPCs (red line) on HeLa cells with respect to the **a,** NADH content and **b,** ATP content. Therapeutically active CPCs trigger NADH and ATP reduction over time, while for lipid-coated CPCs no effect was observed. **c,** Single cell fluorescence measurement of CAR-GECO transfected HeLa cells treated with therapeutically active CPCs labeled with calcein. CAR-GECO depicts the relative Ca^{2+} amount in the cytosol, while calcein depicts the release of dissolved CPCs from the endosome. The asterisk indicates cell division. At 35 h after treatment a strong increase in fluorescence intensity for both channels is observed resembling the induced calcium shock into the cell. The pound marks the death of the cell and the apoptotic cell compartment disassembly.

Moreover, we tested therapeutically active CPCs in a malignant pleural effusion (MPE) mouse model. MPE is immensely related to patients with lung or breast adenocarcinomas.[45,46] There is nearly no treatment available except palliative attempts.[47] MPE represents a distinct form of metastatic disease from lung cancer with a very short survival time.[48,49] We implanted Lewis lung carcinoma (LLC) into the intrapleural cavity of *C57BL/6* mice and let tumors grow for seven days. After randomization into two groups, we injected on day seven 3 mg of therapeutically active CPCs into the intrapleural space of the treated mice while the control group received simulated body fluid. After 12 days post-tumor cell injection, mice were sacrificed and the tumor weight was analyzed. After one single injection of therapeutically active CPCs, we already observed a reduction in tumor weight of 40 wt% compared to the control group (significance = $p<0.08$, Figure 5.5). Taking into account that CPCs need three days to unfold their mode of action, this leaves only two days for tumor reduction during this experimental setup. The green arrow in Figure 5.5b marks agglomerated CPCs that were not effective within the experimental window. Due to ethical reasons an earlier treatment with CPCs before day seven post-tumor cell injection or a second treatment with additional CPCs was not possible. Therefore, these initial findings underline the great potential for treatment of the very aggressive mesenchymal cancer model *in vivo*. Additionally, we could not observe any side effects from the treatment with CPCs indicated by the constant weight of the mice, their behavior, and the non-inflammatory response at the treatment site.

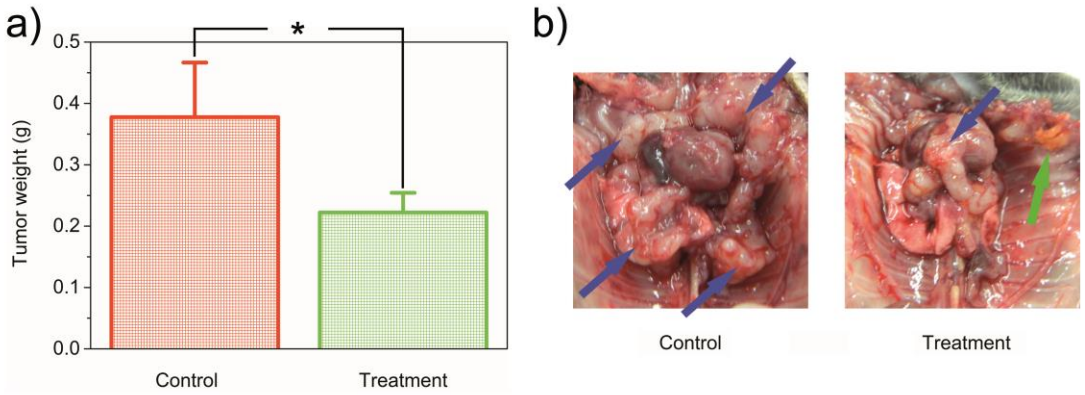

Figure 5.5: Depicted is the reduction of tumor of an *in vivo* mouse experiment after treatment with therapeutically active CPCs. **a,** The tumor weight of the treatment group was reduced by 40 wt% with respect to the untreated control group. Error bars = ±SEM. * indicates $p<0.08$. **b,** The blue arrows mark the areas where the tumorous tissue is located. For the treatment group the reduction in tumorous tissue can be visualized optically. The green arrow marks agglomerated orange colored CPCs, that were not effective during the therapeutic window. The adjacent tissue of the treatment group shows no signs of inflammatory responses to the therapeutically active CPCs confirming low side effects *in vivo*.

5.3 Conclusion

We reported on a novel synthesis of colloidal mesoporous calcium phosphate-citrate nanoparticles (CPCs) with an extremely high BET surface area. We have demonstrated the encapsulation with a lipid membrane for efficient cell uptake. After cell internalization, CPCs dissolved in the acidic endolysosome. Triggered by a small dose of an on-board amphiphile, the dissolved particles can then be released from the endolysosome. When dissolved CPC contents escaped rapidly from the endolysosome, cells received a Ca^{2+} shock that is toxic for cancer cells. Additionally, CPCs affected mesenchymal cancer cells much more strongly than epithelial cancer cells. Therefore, CPCs belong to the small group of substances that can selectively kill mesenchymal cancer cells. Importantly, CPCs did not affect non-tumorigenic cells. Because CPCs are comprised of non-toxic and biodegradable compounds and due to their selective toxicity towards cancer cells, we believe that CPCs show great

potential as combined nanocarriers and chemotherapeutic agents in one without the need for additional toxic drugs. Thus, they are anticipated to strongly reduce side effects in chemotherapy.

5.4 Experimental Information

Synthesis of Calcium Phosphate-Citrate Nanoparticles (CPCs):

The synthesis of CPCs was carried out following a modified Pechini sol-gel process.[50] In a 50 mL polypropylene reactor calcium nitrate tetrahydrate (295 mg, 1.25 mmol), ammonium dihydrogenphosphate (86.3 mg, 0.75 mmol) and citric acid (240 mg, 1.25 mmol) were dissolved in water (20 mL, 1.11 mmol). Then, cetyltrimethylammonium chloride (622 mg, 1.94 mmol) and the triblock copolymer Pluronic® F127 (100 mg) were added and the synthesis mixture was stirred at 500 rpm at room temperature. After 10 minutes of stirring, ethylene glycol (7.15 g, 115 mmol) was added and the solution was cooled 5 minutes at 0 °C. Then, the clear solution was combined with triethanolamine (7.15 g, 48 mmol) under vigorous stirring and was allowed to reach room temperature. The suspension was stirred at 500 rpm at room temperature for 10 minutes. Then, the suspension was diluted approximately 1:1 with ethanol. The particles were separated by centrifugation at 19,000 rpm (43,146 rcf) for 15 minutes and redispersed in NH_4NO_3/EtOH (2 wt%, 80 mL). To extract the template, the suspension was heated under reflux conditions at 90 °C for 30 minutes. Then, the particles were separated by centrifugation at 19,000 rpm (43,146 rcf) for 10 minutes and redispersed in 80 mL ethanol. The mixture was again heated under reflux conditions at 90 °C for 30 minutes. The particles were separated by centrifugation at 19,000 rpm (43,146 rcf) for 10 minutes and redispersed in 20 mL ethanol.

Synthesis of Crystalline Apatite:

For the synthesis of crystalline apatite D-(+)-pantothenic acid calcium salt (476 mg, 1 mmol) was dissolved in 12 mL water and the pH was adjusted to a value of 1.5 with hydrochloric acid (2 M). Then, dipotassium hydrogen phosphate trihydrate (136.5 mg, 0.6 mmol) was dissolved in 2 mL water and added to the calcium containing solution. Sodium hydroxide (2 M) was added dropwise under vigorous stirring until the pH reached a value of 12. The particles were washed 4 times with ethanol by centrifugation at 19,000 rpm (43,146 rcf) for 10 minutes and were finally redispersed in 20 mL ethanol.

Preparation of Calcium Phosphate-Citrate Nanoparticles for Release and Cell Experiments:

0.5 mg of calcium phosphate-citrate nanoparticles were loaded in 1 mL aqueous calcein solution (0.62 mg, 1 mmol, pH 9.4) and if needed with cetyltrimethylammonium chloride (6.25 µg, 19.5 nmol, diluted from aqueous stock solutions) for 30 minutes. The particles were separated by centrifugation at 14,000 rpm (16,873 rcf) for 3 minutes. The loaded particles were redispersed in a lipid solution of 1,2-dioleoyl-3-trimethylammonium-propane (DOTAP, 100 µL of a solution with 12.5 mg/mL 60/40 vol% H_2O/EtOH) and bi-distilled water (900 µL, pH adjusted to 9.4 with NaOH) was added. Then, the particles were separated by centrifugation at 14,000 rpm (16,873 rcf) for 5 minutes. The particles were redispersed in 100 µL of a 1:1 vol% lipid solution of DOTAP and 1,2-dioleoyl-sn-glycero-3-phosphocholine (DOPC, 12.5 mg/mL 60/40 vol% H_2O/EtOH) and SBF (900 µL, pH 7.4) was added. The lipid-coated calcium phosphate-citrate nanoparticles were washed twice by centrifugation at 12,000 rpm (12,396 rcf, 13 °C) for 5 minutes with simulated body fluid (SBF, 500 µL, pH 7.4).

***In vitro* Release Fluorescence Measurements:**

Lipid-coated calcium phosphate-citrate nanoparticles were transferred into the cap of a homebuilt fluorescence setup (0.5 mg particles in 200 µL SBF) and separated by a cellulose membrane from the measuring cell (cuvette), which is filled with SBF (Figure 5.6a). Dye that is released from the particles diffuses through the membrane and can be detected in the measuring cell over time (Figure 5.6b). While detecting the fluorescence of calcein with a spectrometer at 512 nm (excitation at 495 nm) as a function of time, the stimulated release can be observed.

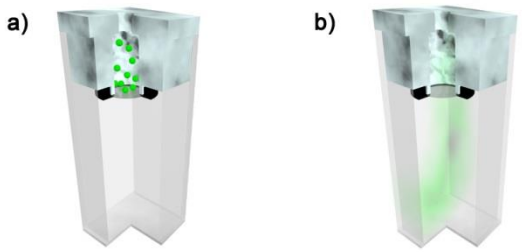

Figure 5.6: Examplary setup for release measurements. **a,** Lipid-coated calcium phosphate-citrate particles in green are separated in the reservoir cap from the measuring compartment by a cellulose membrane (molecular weight cutoff = 14,000 Da) in simulated body fluid with pH at 7.4. **b,** Dissolved lipid-coated calcium phosphate-citrate particles release the loaded model drug calcein, which can penetrate through the cellulose membrane into the measuring compartment and be detected.

Loading of Calcium Phosphate-Citrate Particles with Ibuprofen:

Calcium phosphate-citrate particles were loaded with ibuprofen in hexane, and release of the drug was shown with UV-Vis methods. The maximal loading was 15.6 wt% (Figure 5.7).

For this purpose, 2.5 mg of calcium phosphate-citrate particles were redispersed in 1 mL hexane and loaded with ibuprofen (4 mg, 19.4 µmol) for 24 hours. The particles were separated by centrifugation at 14,000 rpm (16,873 rcf) for 3 minutes

and washed with 1 mL hexane. After a second step of centrifugation the supernatant was discarded and the particles were dried at 60 °C. The dried particles were transferred into the cap of a home built UV-Vis setup (2.5 mg particles in 200 µL SBF) and separated by a cellulose membrane from the measuring cell. Ibuprofen released from the particles diffuses through the membrane and can be detected in the measuring cell (Figure 5.6). While detecting the absorption of ibuprofen at 264 nm over time, the release was quantified.

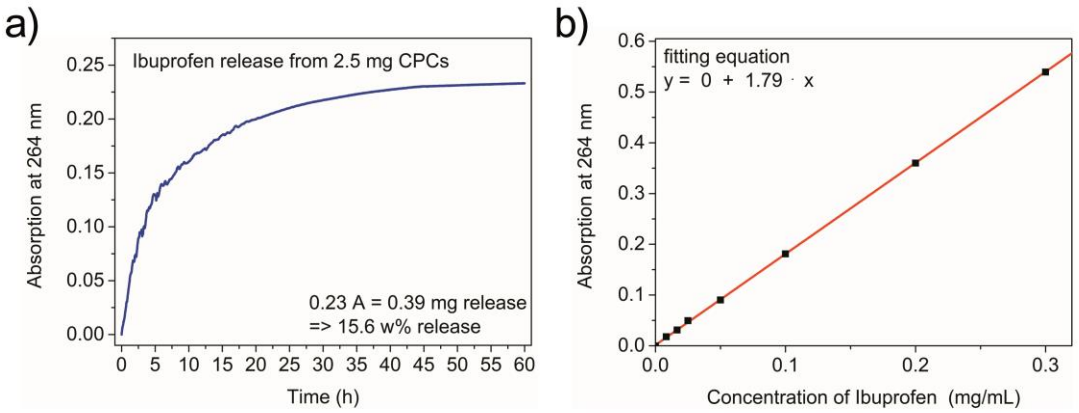

Figure 5.7: **a,** UV-Vis measurement of the release kinetics of ibuprofen detected at 264 nm in simulated body fluid at pH 7.4 over 60 hours. **b,** Absorption fitting curve of ibuprofen with different concentrations measured at 264 nm.

IR-Spectra:

The obtained IR-spectra (Figure 5.1a main text) are normalized to the PO_4^{3-} stretching vibration at 1083 cm^{-1}. The peak at 556 cm^{-1} is attributed to the bending vibration of the PO_4^{3-} group.[51] The vibrations at 1414 cm^{-1} and 1590 cm^{-1} are attributed to the symmetric and the anti-symmetric stretching mode of COO^- groups of the incorporated citric acid in the structure.[22] The vibrations from 3100 cm^{-1} to 2800 cm^{-1} also result from the C-H vibrations of citric acid. We also synthesized crystalline apatite, where the C-O vibrations were drastically reduced compared to calcium phosphate-citrate. The visible C-O bands result from carbonate-

containing crystalline apatite.[51] The PO_4^{3-} vibration for apatite is shifted to lower wavenumbers at 1033 cm^{-1}, indicating crystalline apatite.[52]

Elemental Analysis:

The ratio of Ca:P in calcium phosphate-citrate particles is 1.61, as determined with EDX and ICP methods (Table 5.1). This value is similar to the stoichiometric value for apatite of Ca:P of 1.66.

Table 5.1: Atomic ratio of calcium and phosphorus obtained with EDX and ICP methods.

Measurement		Calcium (atom%)	Phosphor (atom%)	Ca:P
EDX	I	8,69	5,30	1.64
	II	7,04	4,39	1.60
	III	8,69	5,43	1.60
	IV	6,04	3,81	1,58
	V	3,59	2,21	1,62
	VI	6,20	3,91	1,58
	VII	8,69	5,43	1,60
ICP	I	6.21	3.89	1.59
	II	6.19	3.85	1.60
Average (EDX)		6.99	4.35	**1.61**
Average (ICP)		6.20	3.87	**1.60**

Thermogravimetric Analysis:

The incorporation of citric acid into the framework of the hybrid calcium phosphate-citrate particles was additionally established with TGA measurements (Figure 5.8). Thus, the mass loss of calcium phosphate-citrate particles before and after the solvent extraction was investigated with TGA. A moderate mass loss up to 200 °C is

attributed to adsorbed water and weakly bound organics (7 wt%). Between 200 °C and 450 °C significant mass loss is observed, which we attribute to strongly bound organics. Above 450 °C the mass stays constant up to 900 °C. Before the extraction of CTAC and Pluronic® F127, the mass loss of the organics adds up to 36 wt%. For particles that have been extracted, the mass loss of organics is lowered to 20 wt% which we attribute to the decomposition of citric acid. Due to the incorporation of citric acid in the calcium phosphate-citrate structure the mass loss is shifted to higher temperatures compared to pure citric acid (decomposition temperature: 175 °C). Based on the above data, we can calculate the amount of CTAC/Pluronic® F127 in the pore structure to be 16 wt%.

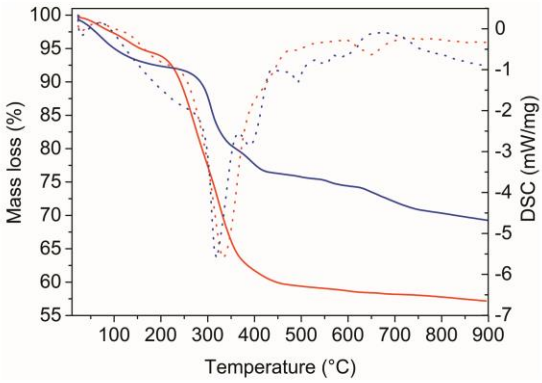

Figure 5.8: Thermogravimetric analysis. Mass loss (left y-axis) of calcium phosphate-citrate particles before (red solid line) and after (blue solid line) extraction. DSC (right y-axis) of calcium phosphate-citrate particles before (red dotted line) and after (blue dotted line) extraction.

X-Ray Diffraction:

Small angle X-ray scattering data show a broad reflection at 2Θ = 1.44°, which corresponds to a d-spacing of 6.13 nm. With a pore size of 5 nm obtained from nitrogen sorption analysis, a wall thickness of 1.1 nm is estimated. In wide angle X-ray scattering data a typical shape for amorphous compounds is observed (Figure 5.9).

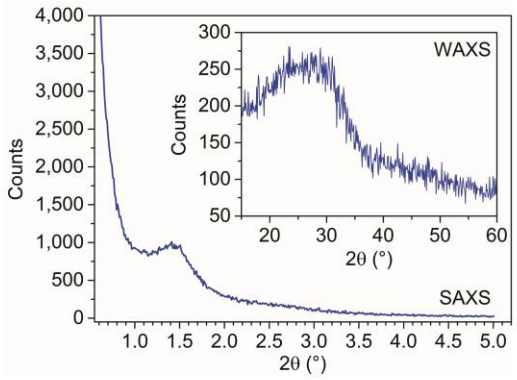

Figure 5.9: Small angle and wide angle (inset) X-ray scattering data of calcium phosphate-citrate particles obtained with Cu-K_α radiation.

ss-NMR:

The resonance of PO_4^{3-} is located at 1.62 ppm in the ^{31}P ss-NMR spectrum (Figure 5.10a). Using ^{13}C ss-NMR, we established the successful implementation of citric acid. The resonance of the primary C-atoms is located at 179 ppm, the secondary C-atoms are observed at 44 ppm, and the tertiary C-atom is located at 74 ppm (Figure 5.10b).[53] The ^{1}H ss-NMR data show the resonance of structural O-H at 1.14 ppm and a small shoulder from adsorbed H_2O (Figure 5.10c).

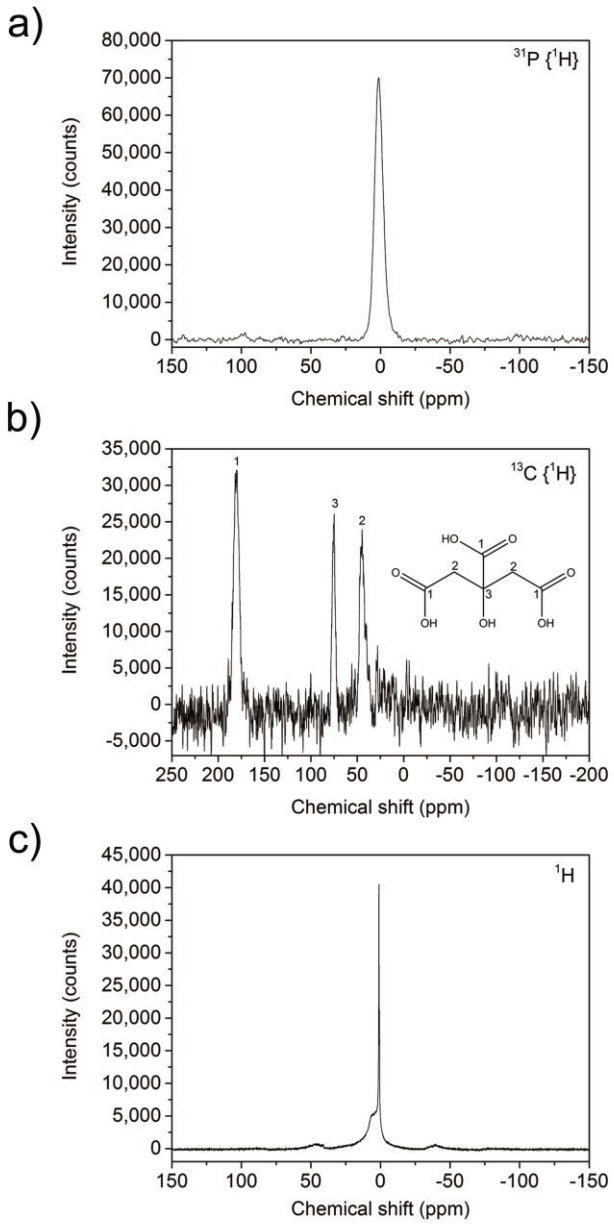

Figure 5.10: ss-NMR of calcium phosphate-citrate nanoparticles (CPCs). Magic angle spinning ss-NMR of CPCs. **a,** ^{31}P ss-NMR data were acquired at 202.5 MHz under proton cross-polarization conditions with 8 transients. **b,** ^{13}C ss-NMR data were obtained at 125.8 MHz under proton cross-polarization conditions with 52000 transients. **c,** ^{1}H ss-NMR data were obtained at 500.2 MHz with 1 run.

Cell Viability:

Cell viability assays (MTT-assay) were carried out with a total of fourteen cell lines. For MCF 10A, MCF7, and MDA-MB-231 see Chapter 5.2. For BT-474, MC38, 293T, HuH7, A549, AE17, B16, Neuro 2A, H1299, LLC, and HeLa see Figure

5.11a-k. As a reference experiment we dissolved 1 mg of lipid-coated CPCs with 1 mL of 0.1 M HCl that was loaded with calcein and CTAC (6.25 µg, 19.5 nmol). Therefore, these particles plus solvent had the same overall composition as the ones that induce apoptosis in cancerous cells within 72 hours. HeLa cells were treated with this solution that exhibited the same concentrations as the particle solution that contained therapeutically active particles. Strikingly, the previously dissolved particles had no effect on cell viability in HeLa cells up to concentrations of ~100 µg/mL, while the therapeutically active CPCs induced apoptosis with an IC_{50} of 8.0 µg/mL (Figure 5.11l). In conclusion, the additive CTAC, the model drug calcein, and the calcium ions as molecules respectively ions do not affect cell viability, if cells were treated directly. However, with therapeutically active CPCs that are able to escape from the endosome, we show effective cell death with low IC_{50} values (Table 5.2).

Table 5.2: IC_{50} values for investigated cell lines. Therapeutically active CPCs were incubated with the corresponding cell lines at concentrations from 1 to 100 µg/mL. MTT-assays were performed after 72 h of incubation. IC_{50} values were calculated with GraphPad Prism 5 and OriginPro 9. Detailed discription of the used buffers can be found in part: 5.5 Methods.

Epithelial cell lines		**Mesenchymal cell lines**	
Cell line	**IC_{50} (µg/mL)**	**Cell line**	**IC_{50} (µg/mL)**
MCF 10A	-	AE17	15.7
A549	63.8	B16	11.5
293T	61.0	H1299	8.2
MC38	44.8	HeLa	8.0
BT-474	30.0	Neuro 2A	4.7
MCF7	18.5	MDA-MB-231	4.4
HuH7	14.0	LLC	4.0

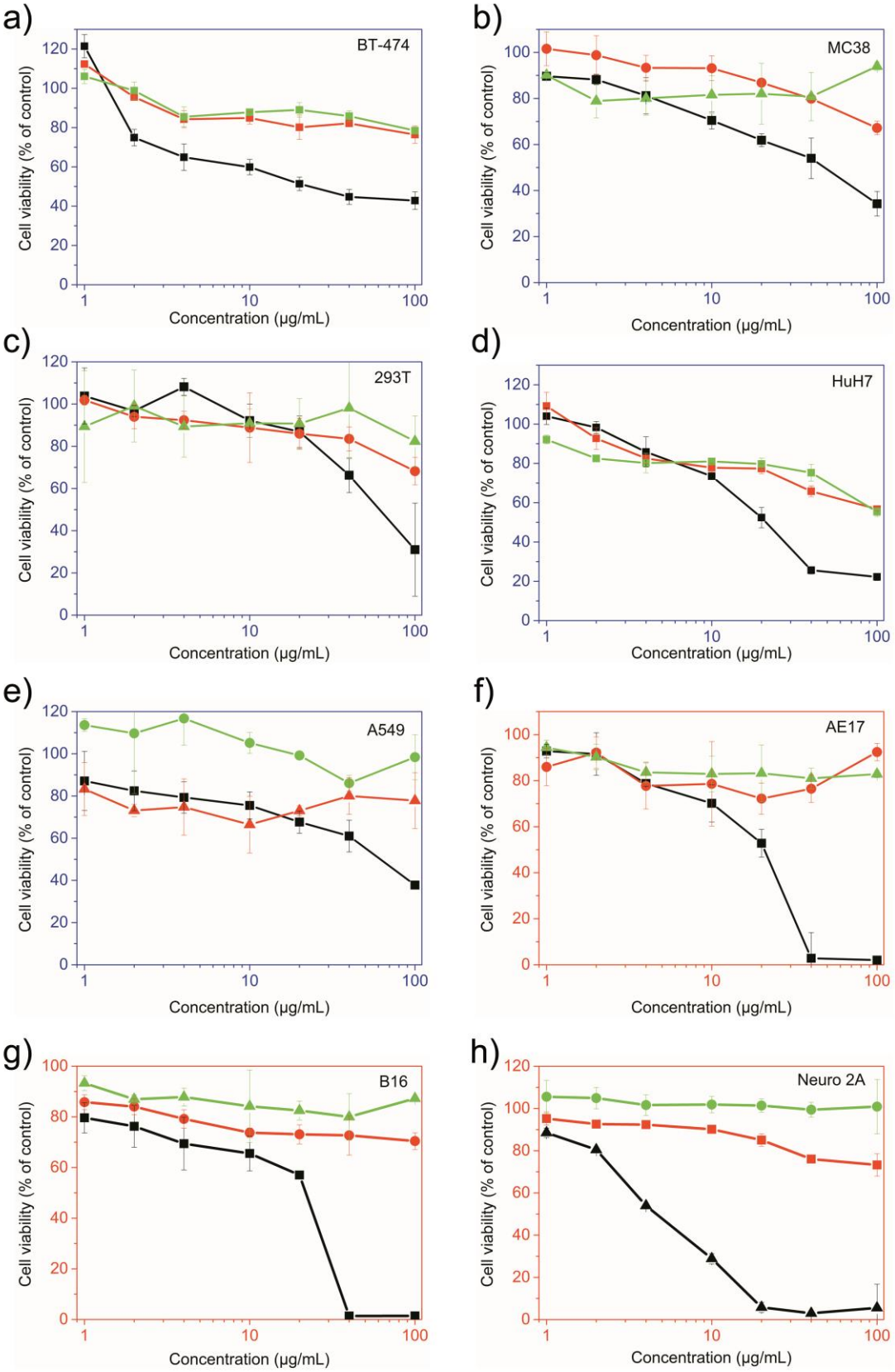
a)
BT-474
b)
MC38
c)
293T
d)
HuH7
e)
A549
f)
AE17
g)
B16
h)
Neuro 2A
Cell viability (% of control)
Concentration (µg/mL)

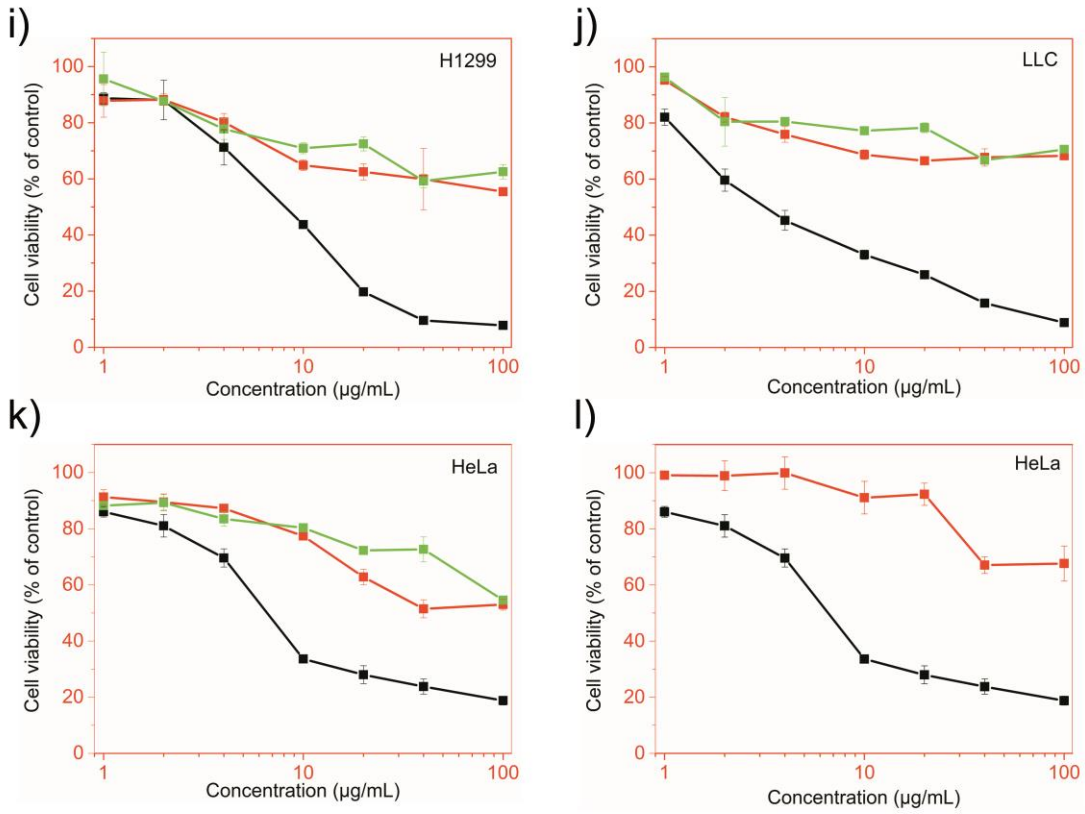

Figure 5.11: Cell viability of investigated cell lines. MTT-assay with readout 72 h after treatment. **a-k,** five epithelial cell lines (blue box), six mesenchymal cell lines (red box). Cell lines are named in the upper right corner. Green lines display calcium phosphate-citrate nanoparticles (CPCs), which were not taken up by cells. Red lines display lipid-coated CPCs, which were taken up by cells but did not escape from the endosome due to the lack of additive. Black lines display lipid-coated CPCs that were taken up by cells and showed endosomal escape. **l,** Reference experiment of previously dissolved lipid-coated CPCs (red line) compared to lipid-coated CPCs that escape from the endosome (black line).

Caspase-3/7 activity:

The caspase-3/7 activity was measured in a time course after treatment of cells with therapeutically active CPCs and with lipid-coated CPCs. We investigated the caspase-3/7 activity on HeLa and MCF 10A cells, to establish the cause for the different response of cancerous and non-cancerous cells towards therapeutically active CPCs. For HeLa cells the caspase-3/7 activity strongly increased after 7 h of incubation with therapeutically active CPCs (Figure 5.12a, black line) demonstrating the induction of the apoptotic pathway. A second increase in caspase-3/7 activity is

observable within 25 h after treatment. The caspase-3/7 activity in the non-cancerous cell line MCF 10A was not detectable during the time course (Figure 5.12b, black line). Thus, no induction of apoptosis is initiated in the non-cancerous cell line MCF 10A. Additionally, the caspase-3/7 activity was not activated for either of the cell lines after treatment with lipid-coated CPCs (Figure 5.12, red line). Therefore, no apoptotic pathway is induced for lipid-coated CPCs in both cell lines.

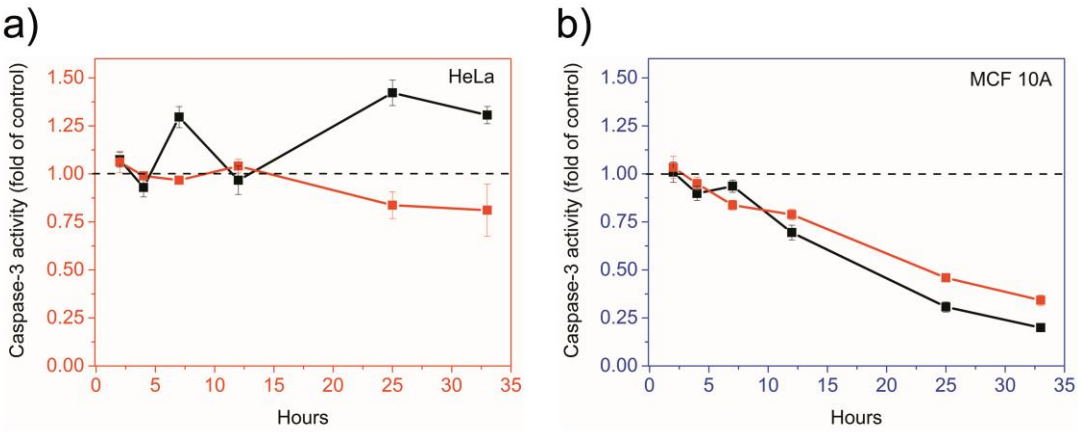

Figure 5.12: Caspase-3/7 activity of therapeutically active CPCs (black line) and lipid-coated CPCs (red line) in a time course measurement. **a,** Mesenchymal cell line HeLa (red box). **b,** Non-cancerous cell line MCF 10A (blue box).

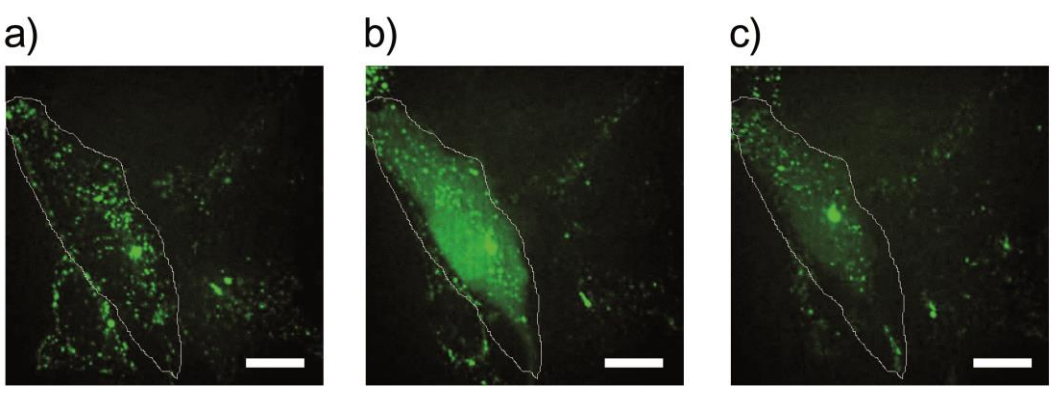

Movie E1. Movie of HeLa cells between 48 and 65 h after incubation with therapeutically active CPCs. The green dots mark the calcein loaded CPCs. Every 15 minutes an image of one z-slice was recorded with live-cell confocal fluorescence microscopy and joined together to a time-lapse movie with 4 fps. Scale bars: 20 µm. a, Start of the movie. White line markes the cell outline. b, After 4 seconds (4 hours in real time, 52 hours after incubation) a strong increase in fluorescence of calcein released from the endosome is visualized. c, Afterwards, the morphology of the cell

undergoes changes due to the apoptotic pathway that was induced after the Ca^{2+} shock from the release of the dissolved CPCs. Movie E1 is available on the data CD that accompanies the printed version of this thesis.

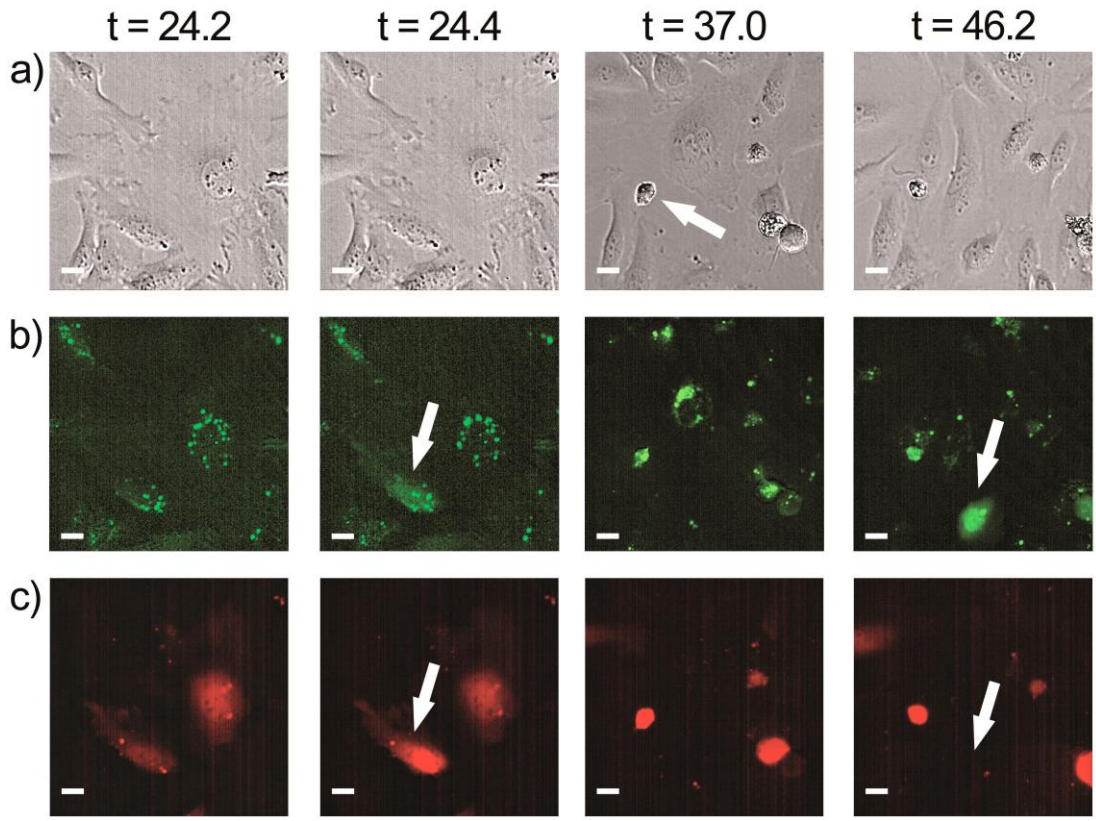

Movie E2. Movie of HeLa cells between 21 and 54 h after incubation with therapeutically active CPCs. Every 12 minutes an image was recorded with high content live-cell fluorescence microscopy and cut together to a movie with 4 fps. Images are depicted at t = 24.2, 24.4, 37.0, and 46.2 hours. Scale bars: 20 µm. **a,** Transmission images. **b,** Images of the calcein channel. The green dots mark the calcein loaded CPCs. **c,** Images of CAR-GECO channel. The red color depicts the Ca^{2+} amount in the cytosol. After 24.4 hours of incubation the release of set free calcein from the endosome into the cytosol is visualized by a strong increase in fluorescence (arrow in **b**). At the same time the calcium concentration in the cytosol increases drastically, visualized by the fluorescence increase of the CAR-GECO (arrow in **c**). After 37.0 hours of incubation the investigated cell changed its morphology due to the apoptotic pathway (arrow in **a**) which eventually resulted in apoptotic membrane blebbing (t = 46.2 h). The arrows at t = 46.2 h point out the rapid release of calcein for another cell which was randomly not expressing CAR-GECO. The intensity increase in the calcein channel was not observable in the CAR-GECO channel. This proves the independency of the the two channels. Therefore, the effect of a Stokes shift of the calcein channel into the CAR-GECO channel can be excluded. Movie E2 is available on the data CD that accompanies the printed version of this thesis.

5.5 Methods

Chemicals for Nanoparticle Synthesis:

Calcium nitrate tetrahydrate (AppliChem, 99 %), ammonium dihydrogenphosphate (Alfa Aeser, 99 %), citric acid (Aldrich, 99.5 %), cetyltrimethylammonium chloride (CTAC, Fluka, 25 wt% in H_2O), Pluronic® F127 (Aldrich), ethylene glycol (Aldrich, 99.8 %), triethanolamine (TEA, Aldrich, 98%), ethanol (EtOH, Aldrich, >99.5 %), ammonium nitrate (Sigma, 99 %), D-(+)-pantothenic acid calcium salt (Sigma, 99 %), hydrochloric acid (Sigma, 2 M), dipotassium hydrogen phosphate trihydrate (Sigma, 99 %), sodium hydroxide (Sigma, 2 M), simulated body fluid (SBF, prepared as written elsewhere[54], contains: Na^+, K^+, Mg^{2+}, Ca^{2+}, Cl^-, CO_3^{2-}, SO_4^{2-}, PO_4^{3-}, and tris(hydroxymethyl) aminomethane, Sigma, >99 %), calcein (Sigma), 1,2-dioleoyl-3-trimethylammonium-propane (DOTAP, Avanti Polar Lipids), 1,2-dioleoyl-sn-glycero-3-phosphocholine (DOPC, Avanti Polar Lipids), sodium hydroxide (Aldrich, 0.1 M).

All chemicals were used as received without further purification. Doubly distilled water from a Millipore system (Milli-Q Academic A10) was used for all synthesis steps.

Cell Lines and Culture:

MCF7, BT-474, and MDA-MB-231 human breast cancer cells, NCI-H1299 human lung cancer cells, HeLa human cervical cancer cells, A549 lung carcinoma, and 293T human embryonic kidney cells were purchased from and cultured according to American Type Culture Collection (ATCC). MCF 10A human mammary cell line was purchased from American Type Culture Collection (ATCC) and cultured according to reference[55]. HuH7 human hepatocellular carcinoma cells were

purchased from and cultured according to Japanese Collection of Research Bioresources (JCRB) Cell Bank. Neuro 2A mouse neuroblastoma, LLC mouse lewis lung carcinoma, B16-F0 mouse melanoma, AE17 mouse mesothelioma, and MC38 mouse colon carcinoma were purchased from and cultured according to American Type Culture Collection (ATCC).

MCF7 cells were grown in DMEM medium high glucose (Sigma Aldrich) supplemented with 20 % fetal calf serum (FCS) (Gibco) and 2 mM L-glutamine (Gibco) at 37 °C and 5 % CO_2. HeLa and 293T cells were grown in DMEM medium low glucose (Sigma Aldrich) supplemented with 10 % FCS (Gibco) and 2 mM L-glutamine (Gibco) at 37 °C and 5 % CO_2. BT-474 and NCI-H1299 cells were grown in RPMI 1640 medium (Sigma Aldrich) supplemented with 10 % FCS and 2 mM L-glutamine (Gibco) at 37 °C and 5 % CO_2. A549 cells were grown in Ham's F12 medium (Sigma Aldrich) supplemented with 10 % FCS and 2 mM L-glutamine (Gibco) at 37 °C and 5 % CO_2. HuH7 cells were grown in a 50:50 mixture of DMEM and Ham's F12 medium (Sigma Aldrich) supplemented with 10 % FCS and 2 mM L-glutamine (Gibco) at 37 °C and 5 % CO_2. MCF 10A cells were grown in DMEM-F12 medium (Gibco) supplemented with 10 % fetal bovine serum (FBS) and 20 ng/mL EGF (Gibco) and hydrocortisone (0.5 µg/mL) at 37 °C and 5 % CO_2. MDA-MB-231 cells were grown in L-15 Leibovitz's medium (Biochrom) supplemented with 10 % FCS and 2 mM L-glutamine (Gibco) at 37 °C without CO_2. LLC, B16-F0 cells were grown in DMEM medium low glucose (Sigma Aldrich) supplemented with 10 % FCS (Gibco) and 4 mM L-glutamine (Gibco) at 37 °C and 5 % CO_2. Neuro 2A cells were grown in DMEM medium low glucose (Sigma Aldrich) supplemented with 10 % FCS (Gibco) and 2 mM L-glutamine (Gibco) at 37 °C and 5 % CO_2. AE17 cells were grown in 987 CYM medium (ATCC) at 37 °C

and 5 % CO_2. MC38 cells were grown in RPMI 1640 medium (Sigma Aldrich) supplemented with 10 % FCS and 2 mM L-glutamine (Gibco) at 37 °C and 5 % CO_2. Cells were routinely tested and confirmed to be mycoplasma free.

Cell Viability with MTT-Assay:

For MTT-assays we treated 5000 cells per well containing 100 µL of the respective medium with therapeutically active CPCs. As reference, control cells were treated with simulated body fluid. After 72 h of treatment, 10 µL 3-(4,5-dimethylthiazol-2-yl)-2,5-diphenyltetrazolium bromide (MTT) was added to the calcium phosphate-citrate treated cells and incubated for further 2 h. Unreacted MTT and medium were removed and the 96-well plates were stored at -80 °C for at least 1 h. Then, 100 µL DMSO was added to each well. The absorbance was read out by a Tecan plate reader. All studies were performed in triplicates. IC_{50} values were calculated with GraphPad Prism 5 and OriginPro 9. Statistical Analysis: All data are presented as mean ± SD, and were analyzed using GraphPad Prism 5. Statistical analysis was conducted using Student's t-test. The asterisk indicates $p<0.05$.

Transfection of CAR-GECO1 to HeLa cells:

For experiments regarding the measurement of cytosolic Ca^{2+} levels, we used CAR-GECO1 as calcium indicator.[37,56] The plasmid CAR-GECO1 was purchased form Addgene and transfected according to the X-tremeGENE® protocol by Roche Diagnostics to HeLa cells. 5.0 x 10^4 cell/well HeLa cells were grown in 1 mL of the respective medium for 24 hours in a 24-well plate. To 500 µL of Opti-MEM I Reduced Serum Medium (Sigma Aldrich), 15 µL of X-tremeGENE® 9 DNA Transfection Reagent (Sigma Aldrich) was added. Then, 5 µg of CAR-GECO1 plasmid was added and gently mixed. 100 µL of the transfection solution was added

dropwise to each well of the 24-well plate. The cells were incubated for 24 hours. One day after transfection, cells were re-seeded into a 96-well plate at a concentration of 5.0 x 10^3 cells/well.

RealTime-Glo™ MT Cell Viability Assay (Promega):

To measure NADH content over time, HeLa cells (5.0 x 10^3 cells/well) were incubated in 100 µL of the respective medium for 24 hours in a 96-well plate. Then, RealTime-Glo™ MT Cell Viability Substrate and NanoLuc®Enzyme were added (0.2 µL/well) after addition of 50 µg/mL therapeutically active CPCs and lipid-coated CPCs to each well. As reference control, cells were treated with simulated body fluid. Luminescence was measured at the given time points.

CellTiter-Glo® Cell Viability Assay (Promega):

To measure ATP content over time, HeLa cells (5.0 x 10^3 cells/well) were incubated in 100 µL of the respective medium for 24 hours in a 96-well plate. Then, cells were treated with 50 µg/mL therapeutically active CPCs and lipid-coated CPCs for each well. As reference control, cells were treated with simulated body fluid. CellTiter-Glo® Reagent was added (100 µL/well) at given time points to the wells of interest and incubated for another 10 minutes. Then, luminescence of the well of interest was measured. This procedure was repeated for all wells to record a time series.

Caspase-Glo® 3/7 Assay (Promega):

To measure caspase-3/7 activity over time, HeLa cells (5.0 x 10^3 cells/well) were incubated in 100 µL of the respective medium for 24 hours in a 96-well plate. Additionally, MCF 10A cells (5.0 x 10^3 cells/well) were incubated in 100 µL of the

respective medium for 24 hours in a 96-well plate. Then, cells were treated with 10 µg/mL therapeutically active CPCs and lipid-coated CPCs for each well. As reference control, cells were treated with simulated body fluid. Caspase-Glo® 3/7 Reagent was added (100 µL/well) at given time points to the wells of interest and gently shaken. After an incubation period of 60 minutes, luminescence of the well of interest was measured. This procedure was repeated for all wells to record a time series.

***In vivo* Experiments:**

For all *in vivo* experiments *C57BL/6* mice (Jackson Laboratories) were housed in isolated cages with a 12 h day/night cycle and food/water ad libitum. Animals were bred at the Center for Animal Models of Disease of the University of Patras. Animal experiments were performed according to guidelines of the European law of protection of animal life (2010/63/EU) and were approved a priori by the Veterinary Administration. Lewis lung carcinoma (LLC) were cultured according to American Type Culture Collection (ATCC). Experimental mice were weight-matched (20-25 g) and age-matched (6-12 weeks). 24 Mice were anesthetized under isoflurane and each mouse was injected 300.000 LLC cells into the intrapleural cavity for MPE generation. Intrapleural injections were done under direct stereoscopic vision via a small incision in the left anterolateral chest skin and fascia. The tumors were allowed to grow for seven days and the mice were separated into two equally sized groups. One group was injected a single dose of 300 µL (10 mg/mL) of therapeutically active CPCs into the right side of the mouse into the intrapleural cavity. The other 12 mice were injected 300 µL of SBF and treated as control group. On day 12 after the implantation of the tumor, mice were sacrificed with CO_2 and the tumor weight was analyzed. Data analysis was performed with GraphPad Prism5.

5.6 Characterization

Characterization of Nanoparticles:

Nitrogen sorption analysis was performed on a Quantachrome Instrument Nova 4000e at 77 K. Samples (25 mg) were outgassed at 120 °C for 12 h *in vacuo* (10 mTorr). Pore size and pore volume were calculated by a QSDFT equilibrium model of N_2 on carbon, based on the desorption branch of the isotherms. The QSDFT method takes into account the effects of surface roughness and heterogeneity.[57] Cumulative pore volumes were evaluated up to a pore size of 10 nm, in order to remove the contribution of inter-particle textural porosity. Surface areas were calculated with the BET model in the range $p/p_0 = 0.05–0.2$. Thermogravimetric analysis of the samples was performed on a Netzsch STA 440 C TG/DSC in a stream of synthetic air with a flow rate of 25 mL/min and a heating rate of 10 K/min. Dynamic light scattering measurements were performed on a Malvern Zetasizer-Nano instrument with a 4 mW He-Ne laser (633 nm) in ethanolic suspension with a concentration of 0.5 mg/mL. Scanning electron microscopy (SEM) images were obtained on a JEOL JSM-6400F. For sample preparation a droplet of the ethanolic colloidal suspension was placed on a 60 °C preheated carbon pad. Samples were sputtered with carbon before measurement. Transmission electron microscopy (TEM) was performed on a JEOL JEM 2011 at an acceleration voltage of 200 kV. For sample preparation a droplet of a diluted ethanolic colloidal suspension was deposited on a carbon-coated copper grid and the solvent was allowed to evaporate. EDX spectra were recorded with an EDAX Apollo XLT SDD Detector (30 mm^2). For ICP measurements the samples were dissolved in concentrated HNO_3 and heated at 110 °C for 30 minutes. After dilution with H_2O the data collection was carried out with a Varian Vista RL ICP-OES with radially viewed plasma. UV/Vis

measurements were performed on a Perkin Elmer Lambda 1050 UV-Vis/NIR spectrophotometer with a deuterium arc lamp and a tungsten filament equipped with a 150 mm integrating sphere and an InGaAs detector. Infrared spectra were measured with a Thermo Scientific Nicolet iN 10 infrared microscope. XRD patterns were obtained with a Bruker D8 Discover X-ray diffractometer using Cu-K_α radiation (1.5406 Å). ^{13}C, ^{31}P, and ^{1}H solid-state NMR (ss-NMR) measurements were performed on a Bruker DSX Avance500 FT spectrometer in a 4 mm ZrO_2 rotor under magic angle spinning conditions. ^{13}C ss-NMR data were obtained at 125.8 MHz under cross-polarization conditions with 52000 transients. ^{31}P ss-NMR data were acquired at 202.5 MHz under cross-polarization conditions with 8 transients. ^{1}H ss-NMR data were obtained at 500.2 MHz with 1 run.

Live-Cell Confocal Fluorescence Microscopy:

To visualize nanoparticle internalization by cells, live-cell imaging was performed on a spinning disc microscope based on the Zeiss Cell Observer SD utilizing a Yokogawa spinning disk unit CSU-X1. The system was equipped with a 1.40 NA 63x Plan apochromat oil immersion objective from Zeiss. For all experiments the exposure time was 0.1 s and z-stacks were recorded. Calcein-loaded CPCs were imaged with approximately 0.4 W/mm^2 of 488 nm excitation light. Atto647 was excited with approximately 11 mW/mm^2 of 639 nm. In the excitation path a quad-edge dichroic beamsplitter (FF410/504/582/669-Di01-25x36, Semrock) was used. For two-color detection of calcein and Atto647, a dichroic mirror (560 nm, Semrock) and band-pass filters 525/50 and 690/60 (both Semrock) were used in the detection path. Separate images for each fluorescence channel were acquired using two separate electron multiplier charge coupled device (EMCCD) cameras (PhotometricsEvolve^{TM}). Immediately before imaging, cell membranes were stained

using wheat germ agglutinin Alexa Fluor 647 conjugate at a final concentration of 5 µg/mL. After application of the dye, cells were washed twice.

High Content Live-Cell Fluorescence Microscopy:

Image capture was performed using automated multiparametric analysis on the ImageXpress Micro XLS (Molecular Devices) wide-field high content imaging system, and data were analyzed using MetaMorph software and ImageJ. To CAR-GECO1 transfected HeLa cells 5 µL of therapeutically active CPCs were added. After 4 hours the cells were washed with DMEM medium low glucose (Sigma Aldrich) supplemented with 10 % fetal calf serum (FCS) (Gibco) and 2 mM L-glutamine (Gibco). Cells were kept under environmental control at 37 °C with 5 % CO_2 inside the ImageXpress Micro XLS device, and every 15 minutes an image was recorded for each channel. The objective 20x Super Plan Fluor ELWD DM and Semrock GFP and Cy5 filter cubes were used.

5.7 References

1 D. J. Irvine. Drug delivery: one nanoparticle, one kill. *Nature Materials* **10,** 342-343, (2011).

2 V. P. Torchilin. Multifunctional, stimuli-sensitive nanoparticulate systems for drug delivery. *Nature Reviews: Drug Discovery* **13,** 813-827, (2014).

3 M. Zhang & K. Kataoka. Nano-structured composites based on calcium phosphate for cellular delivery of therapeutic and diagnostic agents. *Nano Today* **4,** 508-517, (2009).

4 S. V. Dorozhkin & M. Epple. Biological and medical significance of calcium phosphates. *Angewandte Chemie-International Edition* **41,** 3130-3146, (2002).

5 L. C. Palmer, C. J. Newcomb, S. R. Kaltz, E. D. Spoerke & S. I. Stupp. Biomimetic systems for hydroxyapatite mineralization inspired by bone and enamel. *Chemical Reviews* **108,** 4754-4783, (2008).

6 D. Arcos & M. Vallet-Regí. Bioceramics for drug delivery. *Acta Materialia* **61,** 890-911, (2013).

7 F. Chen *et al.* Multifunctional biodegradable mesoporous microspheres of Eu^{3+}-doped amorphous calcium phosphate: microwave-assisted preparation, pH-sensitive drug release, and bioimaging application. *Journal of Materials Chemistry B* **2,** 7132-7140, (2014).

8 G.-J. Ding *et al.* Porous microspheres of amorphous calcium phosphate: block copolymer templated microwave-assisted hydrothermal synthesis and application in drug delivery. *Journal of Colloid and Interface Science* **443,** 72-79, (2015).

9 L. Chen *et al.* Nanostructured calcium phosphate carriers for deliver of poor water-soluble drug silybin. *Materials Letters* **143,** 252-255, (2015).

10 X.-Y. Zhao, Y.-J. Zhu, F. Chen & J. Wu. Calcium phosphate nanocarriers dual-loaded with bovine serum albumin and ibuprofen: facile synthesis, sequential drug loading and sustained drug release. *Chemistry – An Asian Journal* **7,** 1610-1615, (2012).

11 I. Rodríguez-Ruiz *et al.* pH-responsive delivery of doxorubicin from citrate–apatite nanocrystals with tailored carbonate content. *Langmuir* **29,** 8213-8221, (2013).

12 J. Li, Y. Yang & L. Huang. Calcium phosphate nanoparticles with an asymmetric lipid bilayer coating for siRNA delivery to the tumor. *Journal of Controlled Release* **158,** 108-114, (2012).

13 Y. Zhang, N. M. Schwerbrock, A. B. Rogers, W. Y. Kim & L. Huang. Codelivery of VEGF siRNA and gemcitabine monophosphate in a single nanoparticle formulation for effective treatment of NSCLC. *Molecular Therapy* **21,** 1559-1569, (2013).

14 W. Tang *et al.* Differential cytotoxicity and particle action of hydroxyapatite nanoparticles in human cancer cells. *Nanomedicine: Nanotechnology, Biology, and Medicine* **9,** 397-412, (2014).

15 X. Zhao *et al.* Cytotoxicity of hydroxyapatite nanoparticles is shape and cell dependent. *Archives of Toxicology* **87,** 1037-1052, (2013).

16 M. Motskin *et al.* Hydroxyapatite nano and microparticles: correlation of particle properties with cytotoxicity and biostability. *Biomaterials* **30,** 3307-3317, (2009).

17 S. Orrenius, B. Zhivotovsky & P. Nicotera. Regulation of cell death: the calcium–apoptosis link. *Nature Reviews: Molecular Cell Biology* **4,** 552-565, (2003).
18 M. P. Mattson & S. L. Chan. Calcium orchestrates apoptosis. *Nature Cell Biology* **5,** 1041-1043, (2003).
19 S. K. Frandsen *et al.* Direct therapeutic applications of calcium electroporation to effectively induce tumor necrosis. *Cancer Research* **72,** 1336-1341, (2012).
20 E. L. Hansen *et al.* Dose-dependent ATP depletion and cancer cell death following calcium electroporation, relative effect of calcium concentration and electric field strength. *PloS One* **10,** e0122973, (2015).
21 E. Davies *et al.* Citrate bridges between mineral platelets in bone. *Proceedings of the National Academy of Sciences* **111,** E1354-E1363, (2014).
22 I. Cifuentes, P. González-Díaz & L. Cifuentes-Delatte. Is there a "citrate-apatite" in biological calcified systems? *Calcified Tissue International* **31,** 147-151, (1980).
23 I. I. Slowing, J. L. Vivero-Escoto, C.-W. Wu & V. S.-Y. Lin. Mesoporous silica nanoparticles as controlled release drug delivery and gene transfection carriers. *Advanced Drug Delivery Reviews* **60,** 1278-1288, (2008).
24 V. Cauda *et al.* Colchicine-loaded lipid bilayer-coated 50 nm mesoporous nanoparticles efficiently induce microtubule depolymerization upon cell uptake. *Nano Letters* **10,** 2484-2492, (2010).
25 J. Gruenberg. The endocytic pathway: a mosaic of domains. *Nature Reviews: Molecular Cell Biology* **2,** 721-730, (2001).
26 A. K. Varkouhi, M. Scholte, G. Storm & H. J. Haisma. Endosomal escape pathways for delivery of biologicals. *Journal of Controlled Release* **151,** 220-228, (2011).
27 M. J. Berridge, P. Lipp & M. D. Bootman. The versatility and universality of calcium signalling. *Nature Reviews: Molecular Cell Biology* **1,** 11-21, (2000).
28 C. Cui, R. Merritt, L. Fu & Z. Pan. Targeting calcium signaling in cancer therapy. *Acta Pharmaceutica Sinica B* **7,** 3-17, (2017).
29 M. J. Berridge, M. D. Bootman & H. L. Roderick. Calcium signalling: dynamics, homeostasis and remodelling. *Nature Reviews: Molecular Cell Biology* **4,** 517-529, (2003).
30 A. G. Porter & R. U. Jänicke. Emerging roles of caspase-3 in apoptosis. *Cell Death and Differentiation* **6,** 99-104, (1999).
31 A. A. Torrano *et al.* A fast analysis method to quantify nanoparticle uptake on a single cell level. *Nanomedicine: Nanotechnology, Biology, and Medicine* **8,** 1815-1828, (2013).
32 P. B. Gupta *et al.* Identification of selective inhibitors of cancer stem cells by high-throughput screening. *Cell* **138,** 645-659, (2009).
33 W. Boehmerle & M. Endres. Salinomycin induces calpain and cytochrome c-mediated neuronal cell death. *Cell Death & Disease* **2,** e168, (2011).
34 J. R. Jangamreddy *et al.* Salinomycin induces activation of autophagy, mitophagy and affects mitochondrial polarity: differences between primary and cancer cells. *Biochimica et Biophysica Acta (BBA)-Molecular Cell Research* **1833,** 2057-2069, (2013).
35 B. Alberts *et al. Essential Cell Biology*. (Garland Science, 2013).
36 S. Mayor & R. E. Pagano. Pathways of clathrin-independent endocytosis. *Nature Reviews: Molecular Cell Biology* **8,** 603-612, (2007).

37 J. Wu *et al.* Improved orange and red Ca^{2+} indicators and photophysical considerations for optogenetic applications. *ACS Chemical Neuroscience* **4,** 963-972, (2013).
38 M. J. Berridge. Calcium signalling and cell proliferation. *Bioessays* **17,** 491-500, (1995).
39 T. A. McKinsey, C. L. Zhang & E. N. Olson. MEF2: a calcium-dependent regulator of cell division, differentiation and death. *Trends in Biochemical Sciences* **27,** 40-47, (2002).
40 H. Hennings *et al.* Calcium regulation of growth and differentiation of mouse epidermal cells in culture. *Cell* **19,** 245-254, (1980).
41 M. Zoratti & I. Szabò. The mitochondrial permeability transition. *Biochimica et Biophysica Acta (BBA)-Reviews on Biomembranes* **1241,** 139-176, (1995).
42 B. Tombal, S. R. Denmeade & J. T. Isaacs. Assessment and validation of a microinjection method for kinetic analysis of $[Ca^{2+}]i$ in individual cells undergoing apoptosis. *Cell Calcium* **25,** 19-28, (1999).
43 R. Rizzuto *et al.* Calcium and apoptosis: facts and hypotheses. *Oncogene* **22,** 8619-8627, (2003).
44 S. Elmore. Apoptosis: a review of programmed cell death. *Toxicologic Pathology* **35,** 495-516, (2007).
45 M. E. Roberts, E. Neville, R. G. Berrisford, G. Antunes & N. J. Ali. Management of a malignant pleural effusion: British Thoracic Society pleural disease guideline 2010. *Thorax* **65,** ii32-ii40, (2010).
46 J.-S. Ryu *et al.* Prognostic impact of minimal pleural effusion in non–small-cell lung cancer. *Journal of Clinical Oncology* **32,** 960-967, (2014).
47 H. E. Davies & Y. G. Lee. Management of malignant pleural effusions: questions that need answers. *Current Opinion in Pulmonary Medicine* **19,** 374-379, (2013).
48 P. E. Postmus *et al.* The IASLC lung cancer staging project: proposals for revision of the M descriptors in the forthcoming (seventh) edition of the TNM classification of lung cancer. *Journal of Thoracic Oncology* **2,** 686-693, (2007).
49 S.-G. Wu *et al.* Survival of lung adenocarcinoma patients with malignant pleural effusion. *European Respiratory Journal* **41,** 1409-1418, (2013).
50 M. P. Pechini. Method of preparing lead and alkaline earth titanates and niobates and coating method using the same to form a capacitor. US3330697 (1967).
51 W. Weng, G. Han, P. Du & G. Shen. The effect of citric acid addition on the formation of sol–gel derived hydroxyapatite. *Materials Chemistry and Physics* **74,** 92-97, (2002).
52 S. Gadaleta, E. Paschalis, F. Betts, R. Mendelsohn & A. Boskey. Fourier transform infrared spectroscopy of the solution-mediated conversion of amorphous calcium phosphate to hydroxyapatite: new correlations between X-ray diffraction and infrared data. *Calcified Tissue International* **58,** 9-16, (1996).
53 Y.-Y. Hu, A. Rawal & K. Schmidt-Rohr. Strongly bound citrate stabilizes the apatite nanocrystals in bone. *Proceedings of the National Academy of Sciences* **107,** 22425-22429, (2010).
54 M. R. Marques, R. Loebenberg & M. Almukainzi. Simulated biological fluids with possible application in dissolution testing. *Dissolution Technologies* **18,** 15-28, (2011).

55 J. Debnath, S. K. Muthuswamy & J. S. Brugge. Morphogenesis and oncogenesis of MCF-10A mammary epithelial acini grown in three-dimensional basement membrane cultures. *Methods* **30,** 256-268, (2003).

56 Y. Zhao *et al.* An expanded palette of genetically encoded Ca^{2+} indicators. *Science* **333,** 1888-1891, (2011).

57 Quantachrome. *Application of QSDFT (quenched solid density functional theory) - a Novel Density Functional Theory for an Accurate Pore Size Analysis of Disordered Porous Carbons*. Volume 40 (Quantachrome Instruments USA).

CHAPTER 6

STUDY ON MESOPOROUS MAGNESIUM-CALCIUM PHOSPHATE-CITRATE NANOPARTICLES DEVELOPING A GENERAL METHOD FOR THE SYNTHESIS OF MESOPOROUS METAL PHOSPHATE-CITRATE NANOPARTICLES

Constantin von Schirnding, Jonathan Sappl, Florian Fink, Hanna Engelke, and Thomas Bein.

6.1 Introduction

Cancer is the second most common cause for death in the world.[1,2] It has been a challenge for researchers to develop appropriate, effective, and selective medication against cancer.[3] To overcome the drawbacks of medication with small molecules like doxorubicin, cisplatin and many more, the focus of research has been shifting to personalized medicine.[4,5,6,7,8] The concept of personalized medicine in combination with nanotechnology-based tools is expected to advance the treatment and even pre-symptomatic diagnoses of cancer towards highly effective targeted therapy.[9,10,11] Employing nanoconstructs such as dendrimers, liposomes, silica-based nanoparticles, etc., great progress has been made regarding the development of targeted delivery.[6,12,13,14,15,16] Previously, we have demonstrated the synthesis of calcium phosphate-citrate nanoparticles as a novel platform for drug delivery applications.[17] We established the synthesis strategy with a variation of the Pechini process to form a complex of calcium ions with citric acid.[18,19] The precipitation of calcium phosphate-citrate nanoparticles (CPCs) in the presence of surfactants by a rapid change in pH led to novel porous materials that under certain conditions efficiently killed cancer cells without encapsulation of additional toxic drugs due to intracellular delivery of calcium ions.[20,21,22,23,24] Toxic calcium levels are known to activate Ca^{2+}-ATPases, which consume and deplete cellular ATP leading to cell death.[23,25] Although the Ca^{2+} delivery system acts already as chemotherapeutic agent by itself and offers many advantages, we were interested in the development of a calcium free drug delivery carrier. Such a drug delivery system could act as a nontoxic and vanishing platform to load different chemotherapeutics to enhance the pharmacological and therapeutic properties of drugs administered parenterally.[26]

Here, we transferred the knowledge from the synthesis of mesoporous calcium phosphate-citrate nanoparticles to the development of a biodegradable and biocompatible drug delivery system. Therefore, we exchanged calcium ions with magnesium ions in calcium phosphate-citrate nanoparticles. We gradually increased the concentration of magnesium ions in CPCs and analyzed the resulting materials. We observed a pH dependence in the formation of magnesium-calcium phosphate-citrate particles. Increasing contents of Mg^{2+} under fixed pH conditions led to the inhibition of nanoparticle formation and instead generated large crystal morphologies. By tuning the pH values during the synthesis, we developed a preparation method for the incorporation of citrate into the walls of magnesium phosphate-citrate structures leading to mesoporosity and nanoparticle formation. Thus, here we present mesoporous magnesium phosphate-citrate nanoparticles (MPCs) with sizes of about 250 nm and a BET surface area of 560 m^2/g. The pore size is about 6.3 nm with a corresponding pore volume of 0.8 cm^3/g. This enables MPCs to become a platform for advanced drug delivery applications.

Additionally, we adapted the preparation method and applied it to the divalent cation manganese. We showed that the incorporation of citric acid into the metal phosphate-citrate structures leads to mesoporous materials opening the way to new materials with different properties. In the case of manganese phosphate-citrate nanoparticles (MnPCs), the use as MRI active substance or as cathode material for the exchange of lithium could lead to applications in both, diagnosis or Li-ion batteries.[27,28,29,30] Hence, we present novel mesoporous managanese phosphate-citrate nanoparticles and establish a previously unknown synthesis route to obtain mesoporous metal phosphate-citrate structures.

6.2 Results and Discussion

First, for the characterization of magnesium-calcium phosphate-citrate we synthesized calcium phosphate-citrate nanoparticles as a reference material. The synthesis of calcium phosphate-citrate nanoparticles (CPCs) was carried out with a variation of the Pechini sol-gel process.[18,19] The stepwise exchange of the divalent calcium cations with Mg^{2+} led to magnesium-calcium phosphate-citrate particles (Mg-CPCs). For CPC synthesis, calcium ions were dissolved in citric acid-containing aqueous solution. Citric acid acidifies the solution and leads to a complexation of the calcium ions. This prevents precipitation of calcium phosphate after the addition of phosphate ions.[31] Additionally, the addition of citric acid facilitates the gelation process in the formation of calcium phosphate-citrate and slows down the precipitation kinetics.[32] To obtain mesoporosity, the template surfactant cetyltrimethylammonium chloride (CTAC) and Pluronic® F127 was added to form a mesophase containing calcium phosphate-citrate and micellar aggregates. A rapid change in pH to basic conditions induced the precipitation of the CPCs. The extraction of the surfactant template with an ethanolic ammonium nitrate solution yielded the mesoporous CPCs.

For the synthesis of magnesium-calcium phosphate-citrate particles (Mg-CPCs) calcium ions were substituted with magnesium ions.[33] The stability constant of a magnesium citrate complex is smaller compared to a calcium citrate complex.[34] This leads to a competing system forming an equilibrium. In preparing the synthesis mixtures, the addition of phosphate ions, CTAC and Pluronic® F127 to the acidic solution was kept constant. The change of pH to basic conditions by addition of triethanolamine (TEA) led to the precipitation of Mg-CPCs. We investigated five different Mg-CPC samples with varying magnesium concentrations ranging from 0,

20, 40, 60, to 100 mol% with respect to the calcium concentration. Samples are labeled according to their content of magnesium 0 Mg-CPC, 20 Mg-CPC, 40 Mg-CPC, 60 Mg-CPC, and 100 Mg-CPC. For clarification, the sample 0 Mg-CPC is identical to plain calcium phosphate-citrate nanoparticles.

We analyzed the obtained samples with IR spectroscopy and depict the spectra of the five different samples in Figure 6.1. All samples show the typical $\nu_3(PO_4)$ band at 1080 cm^{-1} to which the spectra were normalized. This vibrational mode is broadened in amorphous calcium phosphates[35,36] thus the $\nu_1(PO_4)$ only appears as a shoulder at 950 cm^{-1}. This holds true for the magnesium containing calcium phosphate-citrate materials as well, and the broadening can be detected in all samples. The incorporation of carbonate ions into all samples due to solvation in the aqueous phase from the air is indicated by the $\nu_2(CO_3)$ vibration at around 844 cm^{-1}.[36,37] The vibrations at 1255 cm^{-1} and 894 cm^{-1} are visible in all samples. These vibrations indicate calcium-, respectively magnesium-deficient structures. Maintaining charge neutrality accounts for the incorporation of $H\text{-}OPO_3^{2-}$ and $HO\text{-}PO_3^{2-}$, respectively.[38] These two vibrations were detected in the samples 0 Mg-CPC, 20 Mg-CPC, 40 Mg-CPC, and 60 Mg-CPC. For comparison, the successful synthesis of calcium phosphate-citrate nanoparticles (0 Mg-CPC) leads the incorporation of citric acid. Therefore, vibrations from citrate are detectable at 1410 cm^{-1} and 1590 cm^{-1}.[17,39] The COO^- vibrations were also detected for magnesium-containing samples. However, the amount of incorporated citrate into the structure decreases with higher magnesium contents, even though the same initial citric acid concentration was used during the synthesis.

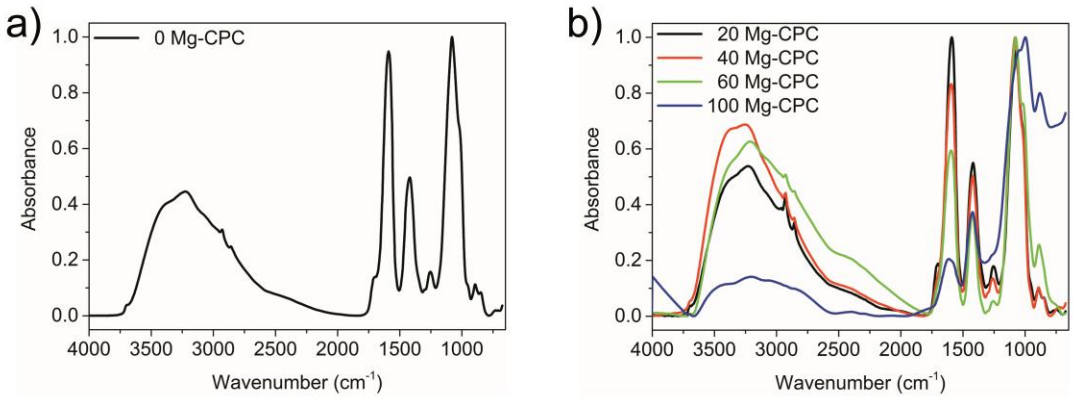

Figure 6.1: Normalized IR-spectra of Mg-CPCs with respect to the increasing amount of magnesium. **a,** IR-spectrum of 0 Mg-CPCs with the strong COO^- vibrations at 1410 cm^{-1} and 1590 cm^{-1}. The typical PO_4^{3-} vibration is attributed to the broad peak at 1080 cm^{-1}. **b,** IR-spectra of 20 Mg-CPC, 40 Mg-CPC, 60 Mg-CPC, and 100 Mg-CPC with a decreasing amount of citrate incorporated into the structure, visible at the COO^- vibrations at 1410 cm^{-1} and 1590 cm^{-1}.

The reduced ability to incorporate citrate ions into the structure of Mg-CPCs with increasing magnesium content was also in agreement with the thermogravimetric analysis (TGA) that was performed on all samples. The amount of incorporated citrate ions into the magnesium-calcium phosphate-citrate structure was quantified with thermogravimetric analysis up to 900 °C with a heating rate of 10 K/min in synthetic air (Figure 6.2). The moderate mass loss of all samples up to 200 °C is assigned to weakly bound organics and mainly water (~8 wt%). Between 200 °C and 450 °C, a significant mass loss is observed for all samples. Above 450 °C the mass stays almost constant up to 850 °C. We attribute the significant mass loss to the decomposition of citrate. The mass loss of 0 Mg-CPC**,** 20 Mg-CPC, and 40 Mg-CPC between 200 °C and 450 °C was almost the same of around 25 wt%. For the sample 60 Mg-CPC the mass loss in that temperature range added up to 23 wt% and for the sample 100 Mg-CPC it added up to 14 wt%, respectively. We attribute the mass loss in this temperature range to the decomposition of residues of template and citrate incorporated in the structure of Mg-CPCs. The shift to higher decomposition temperatures compared to pure citric acid (175 °C) is attributed to the strong

interactions with the magnesium-calcium ions in Mg-CPCs. In the IR-spectra we assigned the vibrational modes at 1410 cm^{-1} and 1590 cm^{-1} to citrate incorporated into the Mg-CPC structure. These observations correlate with the results from TGA methods.

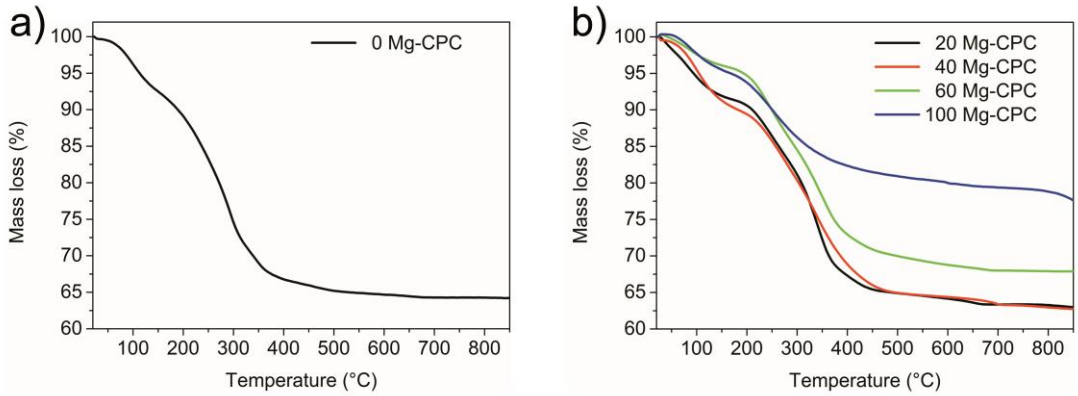

Figure 6.2: Thermogravimetric measurements with a heating rate of 10 K/min in a stream of synthetic air (25 mL/min) of **a,** 0 Mg-CPC and **b,** 20 Mg-CPC, 40 Mg-CPC, 60 Mg-CPC, and 100 Mg-CPC.

To analyze the size distribution and colloidal stability of the Mg-CPCs we performed dynamic light scattering experiments with all samples (Figure 6.3). All samples show a narrow size distribution. The colloidal particles 0 Mg-CPC exhibit the smallest size with a maximum at 220 nm. The samples 20 Mg-CPC and 40 Mg-CPC show a hydrodynamic radius with a maximum size of 295 nm and the particles stay colloidally stable in ethanolic solution. The samples 60 Mg-CPC and 100 Mg-CPC settle down in ethanolic solution within minutes and exhibit sizes with a maximum at 1500 nm and 1300 nm, respectively. These are approximate values only, since the determination of sizes with dynamic light scattering above 1000 nm is not accurate due to physical limitations.[40,41,42]

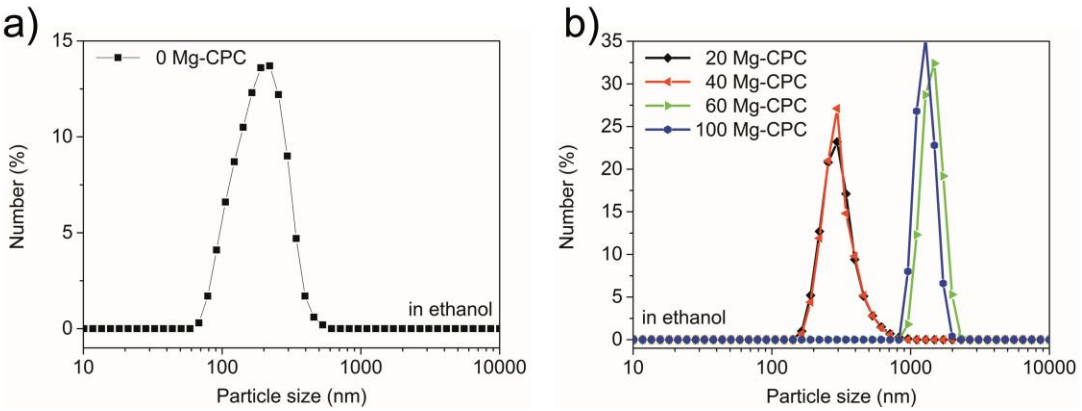

Figure 6.3: Dynamic light scattering (DLS) in ethanol of the samples **a,** 0 Mg-CPC and **b,** 20 Mg-CPC, 40 Mg-CPC, 60 Mg-CPC, and 100 Mg-CPC.

To visualize the different samples, we performed scanning electron microscopy (SEM). The particles aggregate strongly during the drying process. However, the spherical morphologies of the single particles are still visible. They feature an average diameter of 50 nm for the samples 0 Mg-CPC, 20 Mg-CPC, and 40 Mg-CPC. Hence, the particle morphology was not affected by the addition of magnesium ions. For the samples 60 Mg-CPC and 100 Mg-CPC a very different morphology emerged. Here, a crystalline faceted and partially intergrown morphology with particle sizes up to 10 µm in length was observed (Figure 6.4).

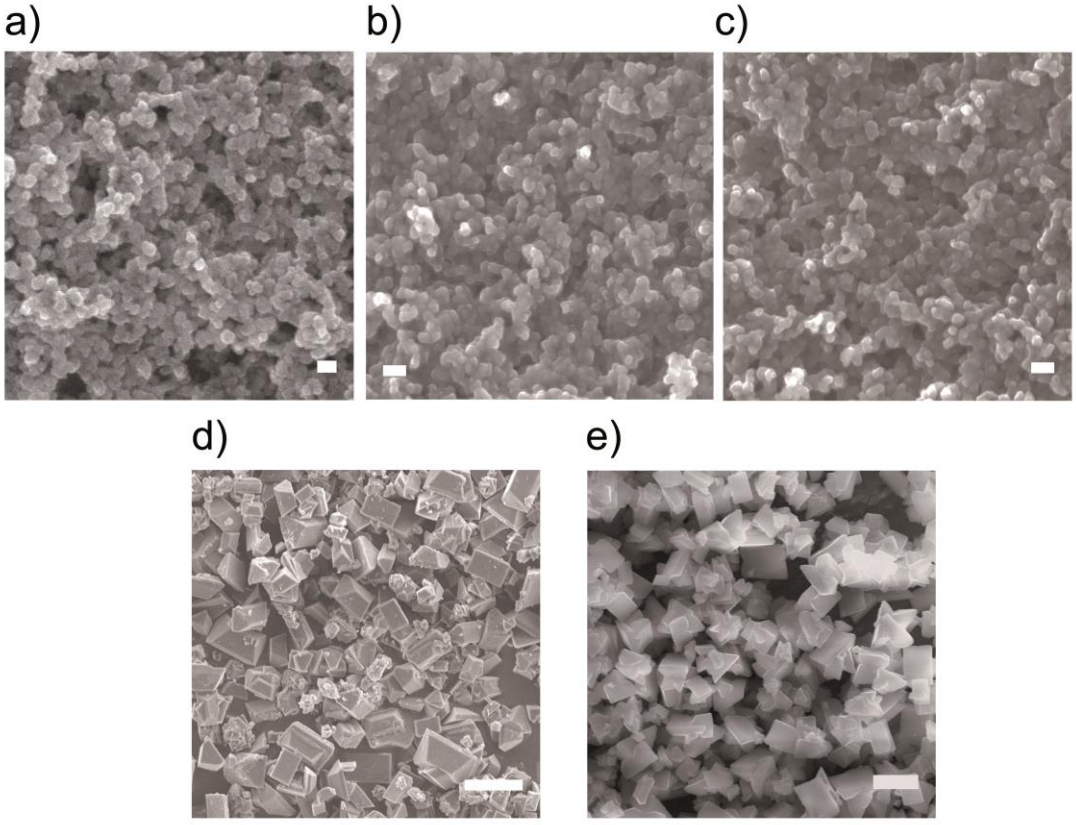

Figure 6.4: Scanning electron microscopy images of spherically shaped nanoparticles with diameters of ~50 nm for the samples **a,** 0 Mg-CPC, **b,** 20 Mg-CPC, and **c,** 40 Mg-CPC. Scale bars: 100 nm. For the samples **d,** 60 Mg-CPC and **e,** 100 Mg-CPC a crystal-shaped morphology with sizes of ~10 µm in length was observed. Scale bars: 10 µm.

The concentration of magnesium in the samples was confirmed with energy dispersive X-ray spectroscopy (EDX). All obtained values are listed in Table 6.1. For the sample 0 Mg-CPC we obtained a Ca:P ratio of 1.61, which is similar to the stoichiometric value for apatite of Ca:P = 1.66. With increasing concentration of magnesium in the reaction solution, the Mg-Ca:P ratio became smaller. Accordingly, for the samples 20 Mg-CPC and 40 Mg-CPC the ratio of Mg-Ca:P was around 1.5. Interestingly, the amount of magnesium incorporated into the Mg-CPC structure was not identical to the initial molar ratio in the synthesis solution. As indicated above, the stability constant for the complex of citrate and Mg^{2+} compared to Ca^{2+} is much smaller. Therefore, the precipitation is shifted towards the calcium phosphate-citrate species and consequently has to be adjusted by increasing the magnesium

concentration to obtain higher amounts of magnesium in the Mg-CPC structure. However, at concentrations above 40 mol% magnesium in the reaction solution, the Mg-Ca:P ratio drastically changes to a stoichiometry close to Mg/Ca:P = 1:1. In this context we note that in struvite, a magnesium ammonium phosphate with the formula ($NH_4MgPO_4 \cdot 6H_2O$), a stoichiometric ratio of Mg/P = 1:1 is observed. Struvite crystallizes in the orthorhombic system in pyramidal forms.[43,44] For the samples 60 Mg-CPC and 100 Mg-CPC we observed pyramidal morphology as well. Since nitrogen atoms, introduced as ammonium dihydrogenphosphate as an educt, are undetectable with EDX, we believe that our products resemble calcium-substituted struvite rather than magnesium-substituted calcium phosphate.

Table 6.1: Avaraged energy dispersive X-ray data of Mg-CPCs with different magnesium contents.

Sample	Calcium (atom%)	Magnesium (atom%)	Atom% of magnesium	Phosphorus (atom%)	Mg-Ca:P
0 Mg-CPC	6.99	-	-	4.35	1.61
20 Mg-CPC	3.65	0.46	11	2.77	1.48
40 Mg-CPC	3.60	1.14	24	3.13	1.51
60 Mg-CPC	1.74	2.71	60	3.83	1.16
100 Mg-CPC	-	5.17	100	5.91	0.87

Thereafter, the samples were dried from ethanolic solutions at 60 °C for 12 hours and analyzed with X-ray diffraction. We observed amorphous materials for every sample (Figure 6.5). For the samples 0 Mg-CPC, 20 Mg-CPC, and 40 Mg-CPC this finding is in accordance with the observations in IR spectroscopy, where we found the shifted and broadened vibrational mode $\nu_3(PO_4)$ at 1080 cm^{-1}, which is typical for amorphous materials.[36] Regarding the samples 60 Mg-CPC and 100 Mg-CPC, an amorphous structure was not expected for these well-defined faceted morphologies

observed in SEM. It has been reported that if struvite is substituted with calcium ions, less crystallinity was observed as the calcium content increased.[45,46] In comparison to our investigation, Le Corre *et al.*[45] could not observe distinct shapes resembling crystals anymore after substituting the magnesium with 50 mol% calcium and higher. Thus, in accordance with literature we find an amorphous signature in the X-ray pattern for these samples. We attribute the highly symmetric morphology observed with SEM to the effects of the templating surfactants. Templating surfactants strongly influence the morphology of the obtained materials.[47] To underline our findings, we performed an *in situ* XRD measurement in ethanoic solution to exclude any solvent effects from the drying process. Nevertheless, we found amorphous material for the samples 60 Mg-CPC and 100 Mg-CPC (see Experimental part, Figure 6.13).

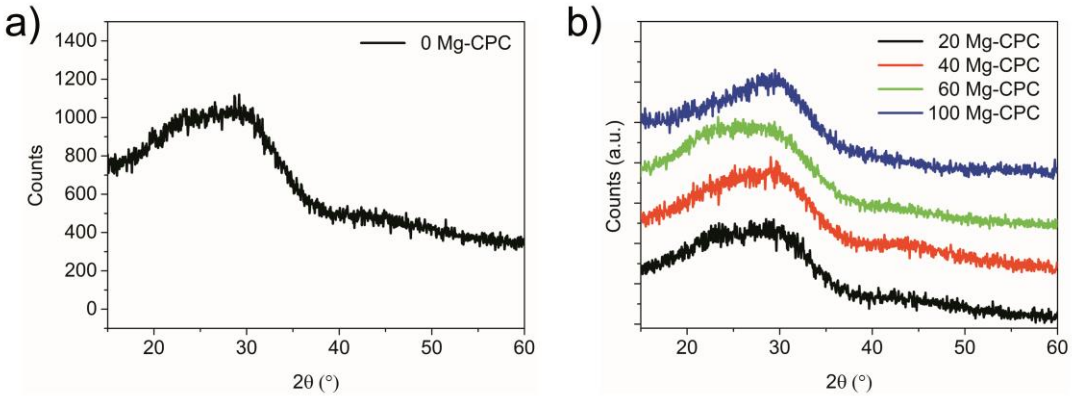

Figure 6.5: X-ray diffraction after drying the samples at 60 °C for 12 hours from ethanolic solution **a,** 0 Mg-CPC and **b,** 20 Mg-CPC, 40 Mg-CPC, 60 Mg-CPC, and 100 Mg-CPC. Graphs were shifted in y-direction for clarity reasons.

The influence of the surfactant templates was analyzed with nitrogen sorption for all samples (Figure 6.6). For all samples the isotherms exhibit type IV shape typical for mesoporous materials. We evaluated the porosity parameters from all isotherms, the values for each sample are depicted in Table 6.2.[48] The calculated pore size varies between 4.4 nm and 6.6 nm. The cumulative pore volumes were calculated up to

10 nm pore size in order to eliminate possible textural porosity. The calculated pore volumes range from 0.42 cm^3/g to 1.00 cm^3/g. We observed a maximum BET surface area of 900 m^2/g for the sample 0 Mg-CPC, while this value continuously decreased with higher magnesium content, to 260 m^2/g for the sample 100 Mg-CPC. Hence, all samples exhibit mesoporosity due to the surfactant template. A drastic drop in mesoporosity was observed for samples 60 Mg-CPC and 100 Mg-CPC. Here, the surfactant template seems to direct mainly the overall morphology contributing to the crystalline looking shape rather than guiding the mesopore formation.

Table 6.2: Calculated parameters from nitrogen sorption analysis data of Mg-CPCs with different magenesium concentration.

Samples	**Pore size distribution**		**BET surface area**
	Size (nm)	**Volume (cm^3/g)**	**(m^2/g)**
0 Mg-CPC	4.8	1.00	900
20 Mg-CPC	4.4	0.66	740
40 Mg-CPC	4.5	0.61	710
60 Mg-CPC	5.0	0.47	370
100 Mg-CPC	6.6	0.42	260

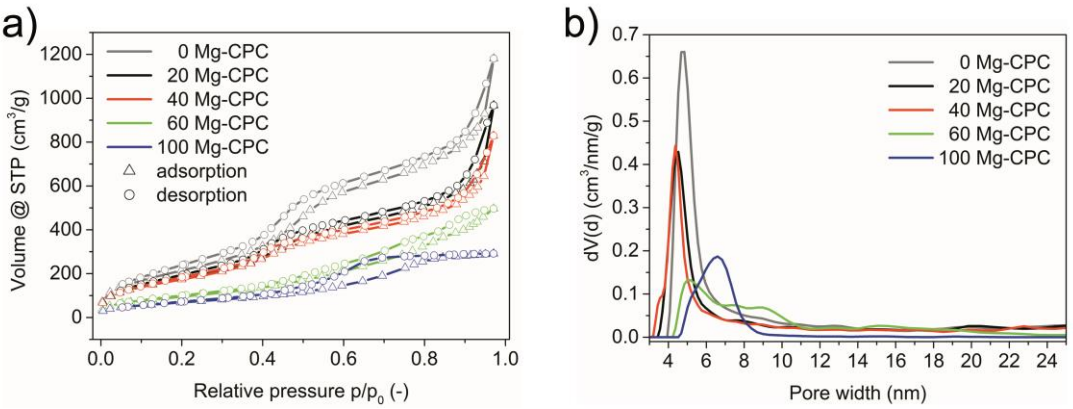

Figure 6.6: **a,** Nitrogen sorption isotherms of mesoporous Mg-CPCs with different magensium content. **b,** Pore size distributions of mesoporous Mg-CPCs with different magensium content.

Note that for all particles precipitated so far the pH was rapidly changed with triethanolamine to a pH value of 8.5, not acting only as complexation agent but also as a base.[49] As reported, the formation of struvite depends strongly on the pH value.[50,51] Consequently, to overcome the thermodynamically driven reaction to the formation of struvite like morphology in samples with high magnesium content, we increased the pH value of the reaction mixture to enhance the kinetics by adding ethanolamine, a strong base with complexation ability. We explored this hypothesis with pure magnesium phosphate-citrate nanoparticles (MPCs). In order to do so, magnesium ions were dissolved in citric acid-containing aqueous solution. Then, ammonium phosphate and the template surfactant cetyltrimethylammonium chloride (CTAC) were added to the reaction solution. In contrast to the above samples, a rapid change in pH to basic conditions was induced with a mixture of triethanolamine and ethanolamine. The resulting solution had a pH value of 12.9, compared to solutions without the addition of ethanolamine with pH = 8.5. The extraction of the surfactant template with an ethanolic ammonium nitrate solution yielded the mesoporous MPCs.

The IR-spectrum of the obtained MPCs is depicted in Figure 6.7a and was normalized to the $\nu_3(PO_4)$ stretching vibration at 1081 cm^{-1}. The presence of citrate ions in MPCs is clearly demonstrated by the symmetric and asymmetric vibrations of the carboxylic groups at 1423 cm^{-1} and 1616 cm^{-1}.[52] In contrast to the sample 100 Mg-CPC, these vibrations drastically increased as a result of the adjusted synthesis. Therefore, following this approach the incorporation of citrate into 100 Mg-CPC was successful after all. The vibrations at 1269 cm^{-1} and 879 cm^{-1} are assigned to the $H\text{-}OPO_3^{2-}$ and $HO\text{-}PO_3^{2-}$ ions, respectively.[53] These vibrations indicate a magnesium-deficient structure. The broad band between 3600 cm^{-1} and 2200 cm^{-1} is attributed to the O–H vibration of water remaining in the mesopores of the samples.

The incorporation of citrate ions into the structure of MPCs was also examined with thermogravimetric analysis (Figure 6.7b). MPCs were heated at a rate of 10 K/min up to 850 °C in synthetic air. The moderate mass loss up to 120 °C is assigned to mainly water (~ 8 wt%). Up to 180 °C we attribute the mass loss to weakly bound organics (~ 6 wt%). Between 180 °C and 700 °C a significant mass loss is observed. We again attribute the decomposition of strongly bound organics to this massive mass loss. Above 700 °C the mass stays almost constant up to 850 °C. The amount of decomposing organics from MPCs adds up to 28 wt%. These decomposing organics are residues of surfactant template and mainly citrate ions incorporated into the structure of MPCs.

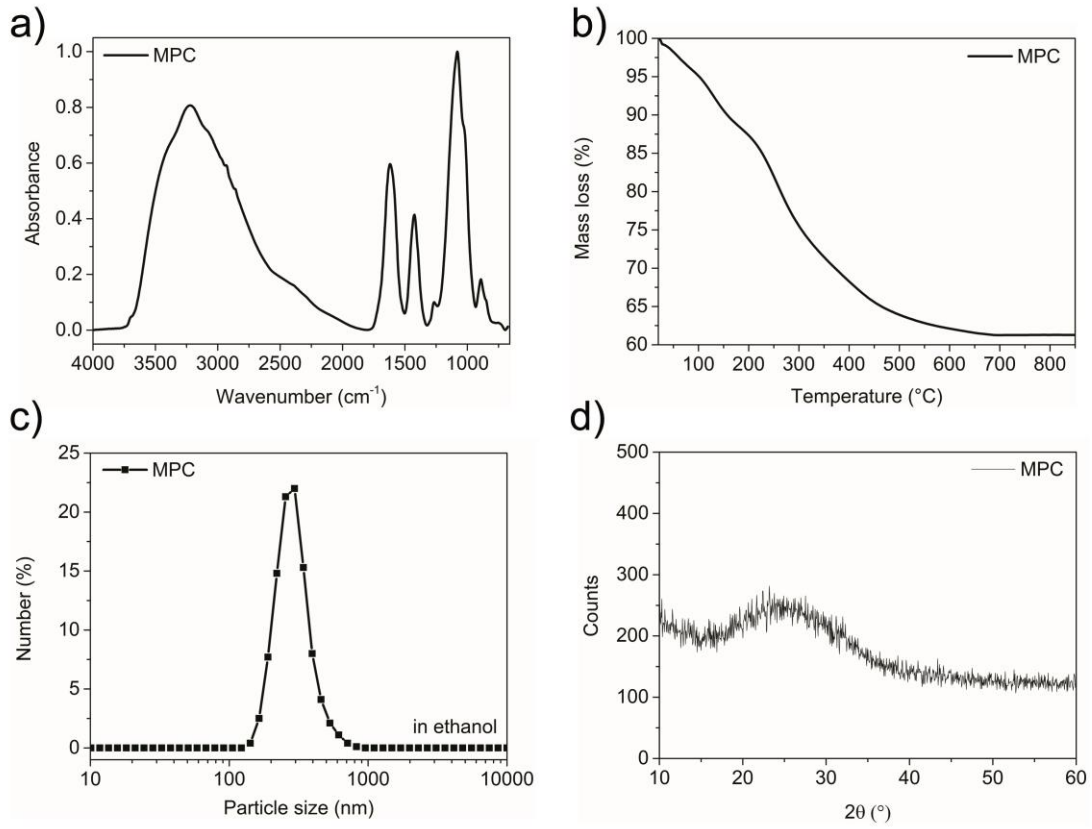

Figure 6.7: **a,** IR-spectrum of MPCs normalized to the PO_4^{3-} vibration with the strong COO^- vibrations at 1423 cm^{-1} and 1616 cm^{-1}. The peak at 1081 cm^{-1} is assigned to the typical PO_4^{3-} vibration. **b,** Thermogravimetric analysis of MPCs with a heating rate of 10 K/min in a stream of synthetic air (25 mL/min). **c,** Dynamic light scattering (DLS) of MPCs in ethanol with a size maximum at 255 nm. **d,** X-ray diffraction of amorphous MCPs after drying at 60 °C for 12 hours from ethanolic solution.

Figure 6.7c depicts the result from the dynamic light scattering experiment of MPCs in ethanolic solution, featuring a size maximum at 255 nm with a narrow size distribution of the particles. Due to the increase of the pH during synthesis, much smaller and colloidally stable particles were obtained compared to 100 Mg-CPCs. Furthermore, the MPCs exhibit an amorphous structure as shown by X-ray diffraction (Figure 6.7d).

Scanning and transmission electron microscopy images of MPCs are depicted in Figure 6.8. Strikingly, for the MPCs we observed spherical nanoparticles and not the pyramidal morphologies of 100 Mg-CPCs. MPCs strongly aggregate during the drying process of sample preparation. Individual particles can be distinguished,

showing a diameter of 40-60 nm. The mesoporous structure was visualized with TEM. Energy dispersive X-ray analysis revealed a Mg/P ratio of 1.25. This is in accordance with the proposed magnesium-deficient structure concluded from IR analysis. The obtained Mg/P ratio is rather similar to that of stoichiometric $Mg_3(PO_4)_2$.

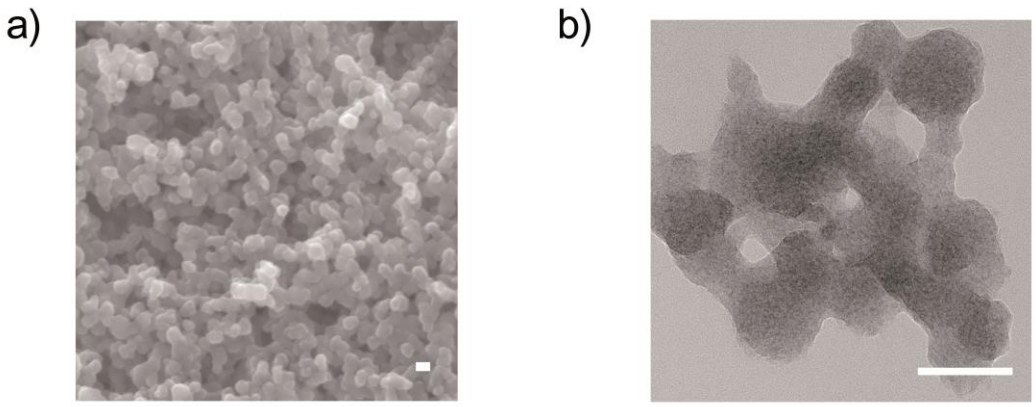

Figure 6.8: **a,** Scanning electron microscopy image of aggregated MPCs. Scale bar: 100 nm. **b,** Transmission electron microscopy image with visualisation of the mesoporous structure of MPCs. Scale bar: 100 nm.

As mentioned above, a large surface area would be desirable for the application of these porous particles as drug delivery system. Nitrogen sorption analysis revealed the typical type IV isotherm for MPCs (Figure 6.9). A BET surface area of 560 m^2/g, a pore size maximum of 6.3 nm and a corresponding pore volume of 0.8 cm^3/g was calculated.

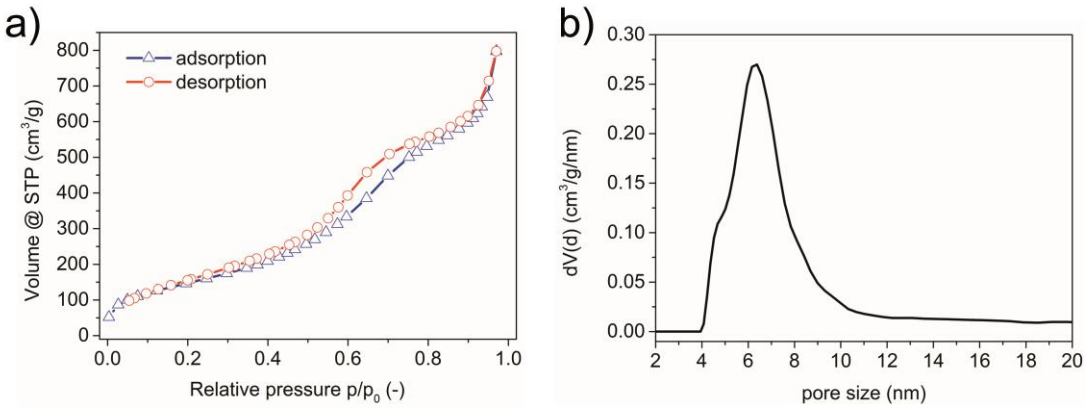

Figure 6.9: Nitrogen sorption analysis data for MPCs. **a,** Adsorption and desorption isotherms reveal a BET surface area of 560 m^2/g. **b,** Calculated pore size distribution with a maximum at 6.3 nm and a corresponding pore volume of 0.8 cm^3/g.

The insights gained in the synthesis of nanoparticles with the modified Pechini process[18] led to the formation of mesoporous calcium phosphate-citrate and magnesium phosphate-citrate nanoparticles. To explore the generality of this approach, we wondered if this procedure could be adapted to other divalent cations to form metal phosphate-citrate nanoparticles. We were interested in the synthesis of manganese phosphate-citrate based on potential attractive applications as MRI active substance or as cathode material in Li-ion batteries.[27,28,29,30] Hence, we dissolved manganese ions and citric acid in aqueous solution. Then, ammonium phosphate and the template surfactant cetyltrimethylammonium chloride (CTAC) were added to the reaction solution. A rapid change in pH to basic conditions was induced by adding a mixture of triethanolamine and ethanolamine, with a final pH value reaching 12.8. The subsequent extraction of the surfactant template with an ethanolic ammonium nitrate solution yielded the desired mesoporous MnPCs.

The IR-spectrum of the new MnPCs is depicted in Figure 6.10a, normalized to the $\nu_3(PO_4)$ stretching vibration at 1081 cm^{-1}. The presence of citrate ions in MnPCs is demonstrated by the symmetric and asymmetric vibrations of the carboxylic group at 1424 cm^{-1} and 1590 cm^{-1}.[52] The small band at 1244 cm^{-1} and the one appearing as a

shoulder at 879 cm^{-1} are assigned to H-OPO_3^{2-} and HO-PO_3^{2-}, respectively.[53] Therefore, for MnPCs a manganese-deficient structure was obtained, similar to the other metal phosphate citrate materials investigated. The broad band between 3600 cm^{-1} and 2200 cm^{-1} is attributed to the O–H vibration of water remaining in the mesopores of the sample.

Furthermore, the incorporation of citrate ions into the structure of MnPCs was investigated with thermogravimetric analysis (Figure 6.10b). MnPCs were heated at a rate of 10 K/min up to 800 °C in synthetic air. The moderate mass loss up to 120 °C is assigned to mainly water (~ 3 wt%). Between 170 °C and 550 °C a significant mass loss is observed. The total amount of decomposing organics from MnPCs adds up to 10 wt%. Above 550 °C the mass stays relatively constant up to 800 °C. In agreement with the other samples described here, we attribute the decomposing organics to residues of template and mainly citrate ions incorporated into the structure of MnPCs.

Figure 6.10c depicts the result from the dynamic light scattering experiment of MnPCs in ethanolic solution, which features a maximum at 240 nm with a narrow size distribution of the particles. Furthermore, MnPCs exhibit amorphous structure indicated by X-ray diffraction (Figure 6.10d).

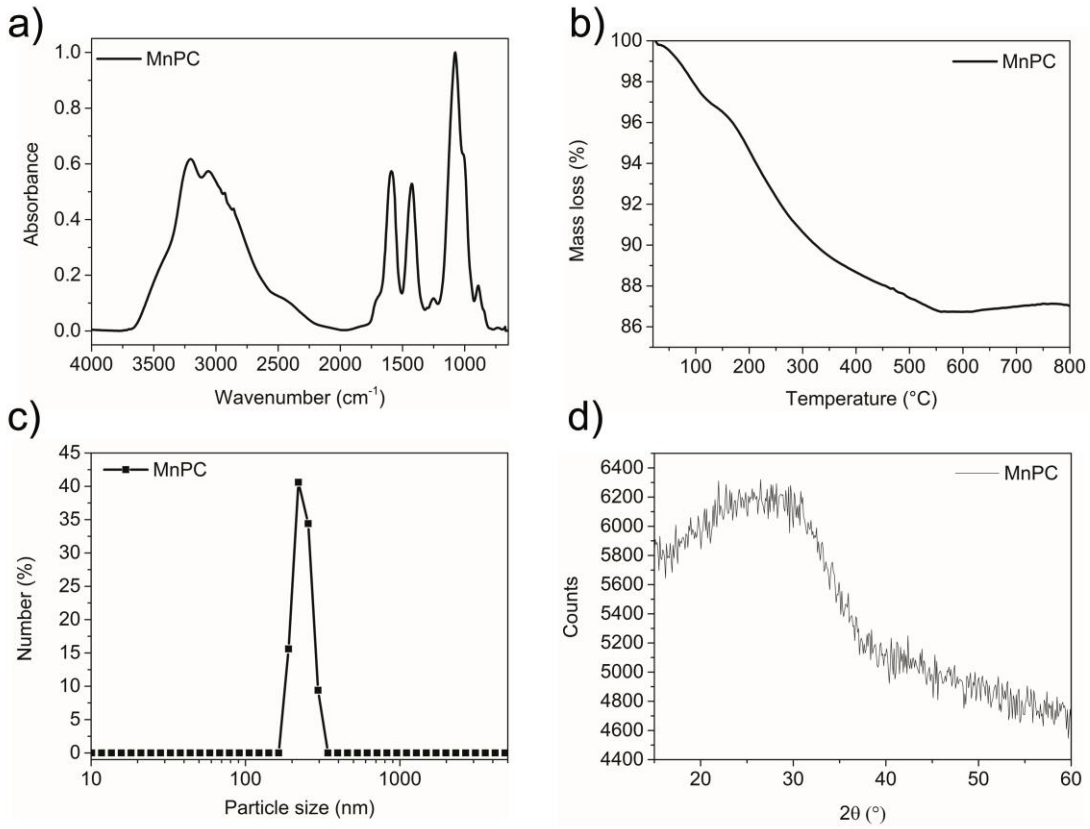

Figure 6.10: **a,** IR-spectrum of MnPCs normalized to the PO_4^{3-} vibration with the COO^- vibrations at 1424 cm^{-1} and 1590 cm^{-1}. The peak at 1081 cm^{-1} is attributed to the typical PO_4^{3-} vibration. **b,** Thermogravimetric analysis of MnPCs with a heating rate of 10 K/min in a stream of synthetic air (25 mL/min). **c,** Dynamic light scattering (DLS) of MnPCs in ethanol with a maximum at 240 nm. **d,** X-ray diffraction of amorphous MnPCs after drying at 60 °C for 12 hours from ethanolic solution.

Nitrogen sorption analysis revealed the typical type IV isotherm for MnPCs (Figure 6.11). A BET surface area of 300 m^2/g, a fairly wide pore size distribution from 8 nm to 20 nm and a corresponding pore volume of 1.1 cm^3/g was calculated.

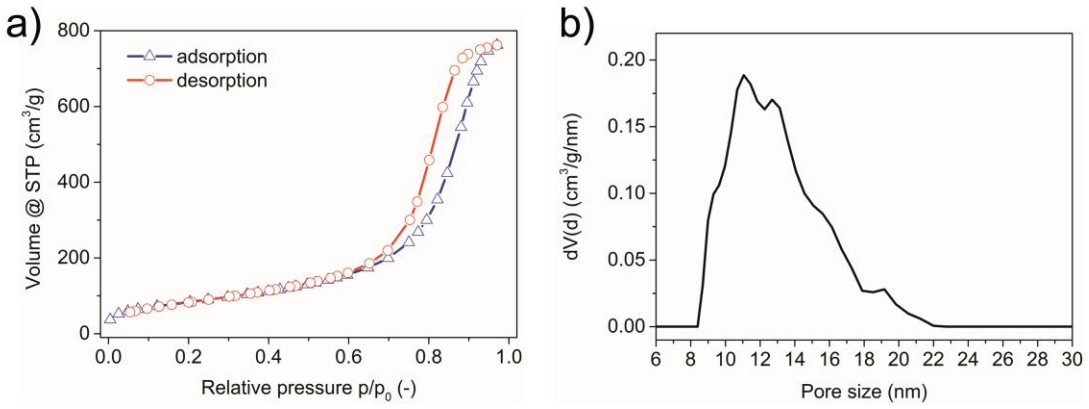

Figure 6.11: Nitrogen sorption analysis data for MnPCs. **a,** Adsorption and desorption isotherms reveal a BET surface area of 300 m^2/g. **b,** Calculated pore size distribution with a maximum at 11 nm pore size and a corresponding pore volume of 1.1 cm^3/g.

Scanning and transmission electron microscopy images of the strongly aggregated MnPCs are depicted in Figure 6.12. The aggregation is a result of the drying process during the sample preparation. The individual particles can be distinguished and are estimated to have a diameter of 40-80 nm. The mesoporous structure was visualized with TEM. Energy dispersive X-ray analysis revealed a Mn/P ratio of 1.23. This is consistent with the proposed manganese-deficient structure suggested by the IR analysis. The obtained Mn/P ratio is rather similar to the stoichiometric $Mn_3(PO_4)_2$. All the characterization techniques employed here thus confirm the successful synthesis of amorphous, mesoporous MnPCs.

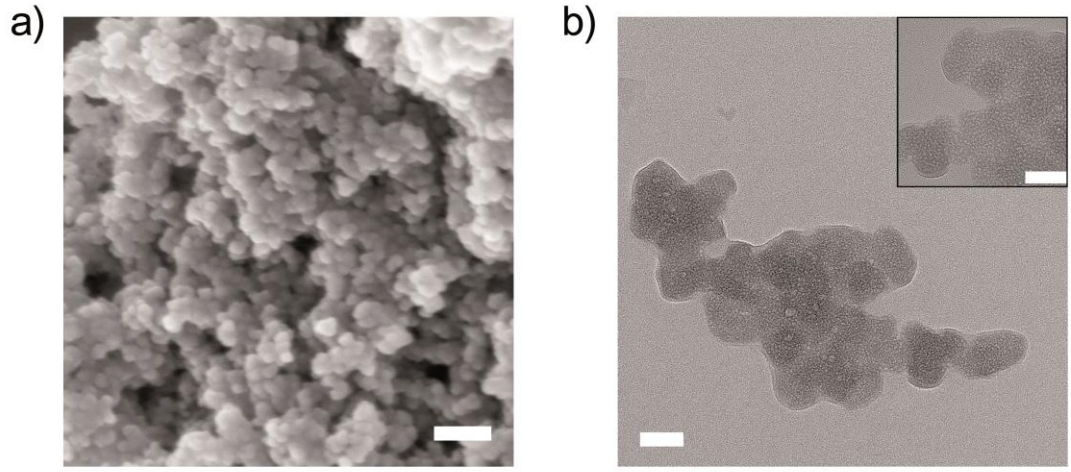

Figure 6.12: **a,** Scanning electron microscopy image of aggreated MnPCs. Scale bar: 100 nm. **b,** Transmission electron microscopy image showing the mesoporous structure (insert) of MnPCs. Scale bars: 50 nm.

6.3 Conclusion

In this study we have gradually substituted calcium ions against magnesium ions in metal phosphate-citrate materials aiming at the use of magnesium phosphate-citrate nanoparticles as biocompatible drug delivery vehicles. Starting from the established calcium phosphate-citrate nanoparticles and substituting calcium stepwise with increasing amounts of magnesium offered insights regarding the precipitation behavior of metal phosphate-citrate nanoparticles. The ability to incorporate citrate ions into the structure of Mg-CPCs decreased with increasing amounts of magnesium. We observed a drastic change in the overall characteristics at magnesium concentrations above 60 mol%. In that case, the materials seem to resemble struvite, an ammonium magnesium phosphate, regarding the structure and chemical composition. However, while the morphology of 60 Mg-CPC and 100 Mg-CPC showed defined pyramidal structures, surprisingly the materials were amorphous.

The pH value was identified as a critical parameter during the precipitation of the metal phosphate-citrate particles. With an increase of the pH value during the precipitation, we were able to synthesize colloidal mesoporous magnesium phosphate-citrate nanoparticles. The resulting characteristics make them promising candidates as platform for advanced drug delivery systems.

Based on the above insights, we surmised that if the pH value during the precipitation is chosen correctly, the formation of other mesoporous metal phosphate-citrate nanoparticles may be possible. This was demonstrated for the synthesis of novel mesoporous manganese phosphate-citrate nanoparticles.

Concluding, we have developed a general method for the synthesis of mesoporous metal phosphate-citrate nanoparticles by judiciously tuning the pH value during the precipitation reaction. We suggest that this approach could lead to numerous additional metal phosphate-citrate nanoparticles with promising characteristics. The metals could include for example strontium, zinc, iron etc. In future studies, their synthesis will be investigated and suitable applications will be identified. As a first example, we will investigate the use of magnesium phosphate-citrate nanoparticles for drug delivery applications.

6.4 Experimental

Chemicals for Particle Synthesis:

Magnesium nitrate hexahydrate (Sigma, 99 %), calcium nitrate tetrahydrate (AppliChem, 99 %), manganese nitrate tetrahydrate (Sigma, 98 %), ammonium dihydrogenphosphate (Alfa Aeser, 99 %), citric acid (Aldrich, 99.5 %), cetyltrimethylammonium chloride (CTAC, Fluka, 25 wt% in H_2O), Pluronic® F127

(Aldrich), ethylene glycol (Aldrich, 99.8 %), triethanolamine (TEA, Aldrich, 98%), ethanolamine (Fluka, >99 %), ethanol (EtOH, Aldrich, >99.5 %), ammonium nitrate (Sigma, 99 %).

All chemicals were used as received without further purification. Doubly distilled water from a Millipore system (Milli-Q Academic A10) was used for all synthesis steps.

Synthesis of Magnesium-Calcium Phosphate-Citrate Nanoparticles (Mg-CPCs):

In a 50 mL polypropylene reactor magnesium nitrate hexahydrate (0 mg, 0.00 mmol/ 64 mg, 0.25 mmol/ 132 mg, 0.50 mmol/ 192 mg, 0.75 mmol/ 320 mg, 1.25 mmol), calcium nitrate tetrahydrate (295 mg, 1.25 mmol/ 236 mg, 1.0 mmol/ 177 mg, 0.75 mmol/ 118 mg, 0.50 mmol/ 0 mg, 0.00 mmol), ammonium dihydrogenphosphate (86.3 mg, 0.75 mmol) and citric acid (240 mg, 1.25 mmol) were dissolved in water (20 mL, 1.11 mmol), leading to the samples 0 Mg-CPC, 20 Mg-CPC, 40 Mg-CPC, 60 Mg-CPC, and 100 Mg-CPC. Then, cetyltrimethylammonium chloride (622 mg, 1.94 mmol) and the triblock copolymer Pluronic® F127 (100 mg) were added and the synthesis mixture was stirred at 500 rpm at room temperature. After 10 minutes of stirring, ethylene glycol (7.15 g, 115 mmol) was added and the solution was stirred for another 5 minutes. The clear solution was combined with triethanolamine (7.15 g, 48 mmol) under vigorous stirring and was allowed to reach room temperature. The suspension was stirred at 500 rpm at room temperature for 10 minutes. Then the suspension was diluted approximately 1:1 with ethanol. The resulting particles were separated by centrifugation at 7,830 rpm (7,197 rcf) for 15 minutes and redispersed in NH_4NO_3/EtOH (2 wt%, 80 mL). To extract the template, the suspension was heated under reflux conditions at 90 °C for 30 minutes. The particles were separated by

centrifugation at 7,830 rpm (7,197 rcf) for 10 minutes and redispersed in 80 mL ethanol. The mixture was heated under reflux conditions at 90 °C for 30 minutes. The particles were again separated by centrifugation at 7,830 rpm (7,197 rcf) for 10 minutes and redispersed in 20 mL ethanol.

XRD measurement of the sample 60 Mg-CPC

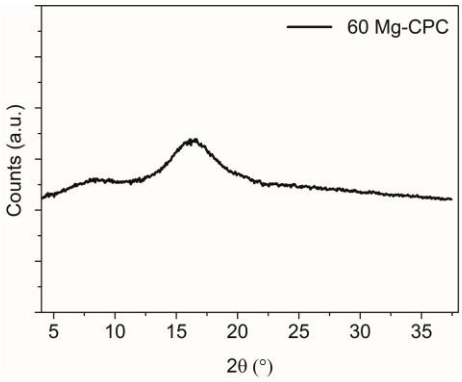

Figure 6.13: X-ray diffraction of the amorphous sample 60 Mg-CPC. An ethanolic solution of 60 Mg-CPC (10 mg/mL) was transferred into a glass capillary and sealed at the end. The capillary was measured in the sample chamber of an Anton Paar SAXSpace instrument equipped with an Eiger Detector and a Cu-K_α micro source (1.5406 Å). The broad bump at $2\Theta = 17°$ results from the capillary background.

Synthesis of Magnesium Phosphate-Citrate Nanoparticles (MPCs):

In a 50 mL polypropylene reactor magnesium nitrate hexahydrate (320 mg, 1.25 mmol) and citric acid (270 mg; 1.41 mmol) were dissolved in water (17 mL, 0.94 mmol). Then, ammonium dihydrogenphosphate (142 mg, 1.25 mmol) was added to the solution and stirred until dissolution was complete. Then, cetyltrimethylammonium chloride (622 mg, 1.94 mmol) and ethylene glycol (7.15 g, 115 mmol) were added and the synthesis mixture was stirred at 500 rpm at room temperature. The clear solution was combined with triethanolamine (7.15 g, 48 mmol) and ethanolamine (3.00 g, 49.1 mmol) under vigorous stirring for three minutes. The suspension was diluted approximately 1:1 with ethanol. The particles

were separated by centrifugation at 7,830 rpm (7,197 rcf) for 5 minutes and redispersed in NH_4NO_3/EtOH (2 wt%, 80 mL). To extract the template, the suspension was heated under reflux conditions at 90 °C for 30 minutes. Then, the particles were separated by centrifugation at 7,830 rpm (7,197 rcf) for 5 minutes and redispersed in 80 mL ethanol. The mixture was again heated under reflux conditions at 90 °C for 30 minutes and the particles were again separated by centrifugation at 7,830 rpm (7,197 rcf) for 5 minutes, and redispersed in 20 mL ethanol.

Synthesis of Manganese Phosphate-Citrate Nanoparticles (MnPCs):

In a 50 mL polypropylene reactor, manganese nitrate tetrahydrate (314 mg, 1.25 mmol) and citric acid (270 mg; 1.41 mmol) were dissolved in water (17 mL, 0.94 mmol). Then, ammonium dihydrogenphosphate (142 mg, 1.25 mmol) was added to the solution and stirred until dissolution was complete. Cetyltrimethylammonium chloride (622 mg, 1.94 mmol) and ethylene glycol (7.15 g, 115 mmol) were added and the synthesis mixture was stirred at 500 rpm at room temperature. The clear solution was combined with triethanolamine (7.15 g, 48 mmol) and ethanolamine (3.00 g, 49.1 mmol) under vigorous stirring for three minutes. The suspension was diluted approximately 1:1 with ethanol. The resulting particles were separated by centrifugation at 7,830 rpm (7,197 rcf) for 5 minutes and redispersed in NH_4NO_3/EtOH (2 wt%, 80 mL). To extract the template, the suspension was heated under reflux conditions at 90 °C for 30 minutes. The particles were separated by centrifugation at 7,830 rpm (7,197 rcf) for 5 minutes and redispersed in 80 mL ethanol. The mixture was again heated under reflux conditions at 90 °C for 30 minutes, and the particles were again separated by centrifugation at 7,830 rpm (7,197 rcf) for 5 minutes, and redispersed in 20 mL ethanol.

6.5 Characterization

Characterization of Nanoparticles:

Nitrogen sorption analysis was performed on a Quantachrome Instrument Nova 4000e at 77 K. Samples (25 mg) were outgassed at 120 °C for 12 h *in vacuo* (10 mTorr). Pore size and pore volume were calculated by a QSDFT equilibrium model of N_2 on carbon, based on the desorption branch of the isotherms. The QSDFT method takes into account the effects of surface roughness and heterogeneity.[54] Cumulative pore volumes were evaluated up to a pore size of 12 nm (for Mn-CPCs up to 20 nm), in order to remove the contribution of inter-particle textural porosity. Surface areas were calculated with the BET model in the range $p/p_0 = 0.05–0.2$. Thermogravimetric analysis of the samples was performed on a Netzsch STA 440 C TG/DSC in a stream of synthetic air with a flow rate of 25 mL/min and a heating rate of 10 K/min. Dynamic light scattering measurements were performed on a Malvern Zetasizer-Nano instrument with a 4 mW He-Ne laser (633 nm) in ethanolic suspension with a concentration of 0.5 mg/mL. Scanning electron microscopy (SEM) images were obtained on a JEOL JSM-6400F and a FEI HELIOS NanoLab G3 UC. For sample preparation, a droplet of the ethanolic colloidal suspension was placed on a 60 °C preheated aluminum sample holder. Samples were sputtered with carbon before measurement. Transmission electron microscopy (TEM) was performed on a FEI TECNAI G2 at an acceleration voltage of 200 kV. For sample preparation a droplet of a diluted ethanolic colloidal suspension was deposited on a carbon-coated copper grid and the solvent was allowed to evaporate. Infrared spectra were measured with a Thermo Scientific Nicolet iN 10 infrared microscope. XRD patterns were obtained with a Bruker D8 Discover X-ray diffractometer using Cu-K_α radiation (1.5406 Å). Small angle X-ray scattering (SAXS) data were obtained with

an Anton Paar SAXSpace instrument equipped with an Eiger Detector and a Cu-K_α micro source (1.5406 Å).

6.6 References

1 J. Ferlay *et al.* Cancer incidence and mortality worldwide: sources, methods and major patterns in Globocan 2012. *International Journal of Cancer* **136,** E359-E386, (2015).

2 B. Stewart & C. P. Wild. World cancer report 2014. (2014).

3 L. Brannon-Peppas & J. O. Blanchette. Nanoparticle and targeted systems for cancer therapy. *Advanced Drug Delivery Reviews* **64,** 206-212, (2012).

4 L. Chin, J. N. Andersen & P. A. Futreal. Cancer genomics: from discovery science to personalized medicine. *Nature Medicine* **17,** 297-303, (2011).

5 K. Cho, X. Wang, S. Nie, Z. Chen & D. M. Shin. Therapeutic nanoparticles for drug delivery in cancer. *Clinical Cancer Research* **14,** 1310-1316, (2008).

6 D. Peer *et al.* Nanocarriers as an emerging platform for cancer therapy. *Nature Nanotechnology* **2,** 751-760, (2007).

7 R. A. Petros & J. M. DeSimone. Strategies in the design of nanoparticles for therapeutic applications. *Nature Reviews: Drug Discovery* **9,** 615-627, (2010).

8 V. Wagner, A. Dullaart, A.-K. Bock & A. Zweck. The emerging nanomedicine landscape. *Nature Biotechnology* **24,** 1211-1217, (2006).

9 S. D. Caruthers, S. A. Wickline & G. M. Lanza. Nanotechnological applications in medicine. *Current Opinion in Biotechnology* **18,** 26-30, (2007).

10 T. M. Allen. Ligand-targeted therapeutics in anticancer therapy. *Nature Reviews: Cancer* **2,** 750-763, (2002).

11 M. Ferrari. Cancer nanotechnology: opportunities and challenges. *Nature Reviews: Cancer* **5,** 161-171, (2005).

12 Y. H. Bae & K. Park. Targeted drug delivery to tumors: myths, reality and possibility. *Journal of Controlled Release* **153,** 198-205, (2011).

13 I. Brigger, C. Dubernet & P. Couvreur. Nanoparticles in cancer therapy and diagnosis. *Advanced Drug Delivery Reviews* **54,** 631-651, (2002).

14 R. Esfand & D. A. Tomalia. Poly (amidoamine)(PAMAM) dendrimers: from biomimicry to drug delivery and biomedical applications. *Drug Discovery Today* **6,** 427-436, (2001).

15 C. Argyo, V. Weiss, C. Bräuchle & T. Bein. Multifunctional mesoporous silica nanoparticles as a universal platform for drug delivery. *Chemistry of Materials* **26,** 435-451, (2014).

16 G. Gregoriadis & A. T. Florence. Liposomes in drug delivery. *Drugs* **45,** 15-28, (1993).

17 T. Bein, H. Engelke, H. Feckl & C. von Schirnding. Mesoporous calcium phosphate-citrate nanoparticles and uses thereof. PCT/EP2016/068231 (2015).

18 M. P. Pechini. Method of preparing lead and alkaline earth titanates and niobates and coating method using the same to form a capacitor. US3330697 (1967).

19 P. Yang, P. Yang, X. Teng, J. Lin & L. Huang. A novel luminescent mesoporous silica/apatite composite for controlled drug release. *Journal of Materials Chemistry* **21,** 5505-5510, (2011).

20 W. Tang *et al.* Differential cytotoxicity and particle action of hydroxyapatite nanoparticles in human cancer cells. *Nanomedicine: Nanotechnology, Biology, and Medicine* **9,** 397-412, (2014).

21 X. Zhao *et al.* Cytotoxicity of hydroxyapatite nanoparticles is shape and cell dependent. *Archives of Toxicology* **87,** 1037-1052, (2013).

22 M. Motskin *et al.* Hydroxyapatite nano and microparticles: correlation of particle properties with cytotoxicity and biostability. *Biomaterials* **30,** 3307-3317, (2009).

23 S. Orrenius, B. Zhivotovsky & P. Nicotera. Regulation of cell death: the calcium–apoptosis link. *Nature Reviews: Molecular Cell Biology* **4,** 552-565, (2003).

24 G. R. Monteith, D. McAndrew, H. M. Faddy & S. J. Roberts-Thomson. Calcium and cancer: targeting Ca^{2+} transport. *Nature Reviews: Cancer* **7,** 519-530, (2007).

25 E. L. Hansen *et al.* Dose-dependent ATP depletion and cancer cell death following calcium electroporation, relative effect of calcium concentration and electric field strength. *PloS One* **10,** e0122973, (2015).

26 T. M. Allen & P. R. Cullis. Drug delivery systems: entering the mainstream. *Science* **303,** 1818-1822, (2004).

27 D. Pan, A. H. Schmieder, S. A. Wickline & G. M. Lanza. Manganese-based MRI contrast agents: past, present and future. *Tetrahedron* **67,** 8431-8444, (2011).

28 T. Kim *et al.* Synthesis of lithium manganese phosphate nanoparticle and its properties. *Journal of Physics and Chemistry of Solids* **68,** 1203-1206, (2007).

29 J. Xiao, W. Xu, D. Choi & J.-G. Zhang. Synthesis and characterization of lithium manganese phosphate by a precipitation method. *Journal of the Electrochemical Society* **157,** A142-A147, (2010).

30 A. C. Silva, J. H. Lee, I. Aoki & A. P. Koretsky. Manganese-enhanced magnetic resonance imaging (MEMRI): methodological and practical considerations. *NMR in Biomedicine* **17,** 532-543, (2004).

31 A. López-Macipe & J. Gómez-Morales. The role of pH in the adsorption of citrate ions on hydroxyapatite. *Journal of Colloid and Interface Science* **200,** 114-120, (1998).

32 W. Weng, G. Han, P. Du & G. Shen. The effect of citric acid addition on the formation of sol–gel derived hydroxyapatite. *Materials Chemistry and Physics* **74,** 92-97, (2002).

33 B. Bracci *et al.* Effect of Mg^{2+}, Sr^{2+}, and Mn^{2+} on the chemico-physical and *in vitro* biological properties of calcium phosphate biomimetic coatings. *Journal of Inorganic Biochemistry* **103,** 1666-1674, (2009).

34 T. E. Furia. *CRC Handbook of Food Additives*. Edition 2, (Taylor & Francis, 1973).

35 C. Drouet. Apatite formation: why it may not work as planned, and how to conclusively identify apatite compounds. *BioMed Research International* **2013**, (2013).

36 K. Zilm. Mechanism of CO_3^{2-} substitution in carbonate-fluorapatite: evidence from FTIR spectroscopy, ^{13}C NMR and quantum mechanical calculations. *American Mineralogist*, (1994).

37 C. Rey, B. Collins, T. Goehl, I. R. Dickson & M. J. Glimcher. The carbonate environment in bone mineral: a resolution-enhanced fourier transform infrared spectroscopy study. *Calcified Tissue International* **45,** 157-164, (1989).

38 E. E. Berry. The structure and composition of some calcium-deficient apatites. *Journal of Inorganic and Nuclear Chemistry* **29,** 317-327, (1967).

39 L. Brečević & H. Füredi-Milhofer. Precipitation of calcium phosphates from electrolyte solutions V. The influence of citrate ions. *Calcified Tissue International* **28,** 131-136, (1979).

40 R. M. Murphy. Static and dynamic light scattering of biological macromolecules: what can we learn? *Current Opinion in Biotechnology* **8,** 25-30, (1997).

41 S. Myhra & J. C. Rivière. *Characterization of Nanostructures*. (CRC Press, 2012).

42 A. L. Papish, L. W. Tari & H. J. Vogel. Dynamic light scattering study of calmodulin–target peptide complexes. *Biophysical Journal* **83,** 1455-1464, (2002).

43 F. Abbona & R. Boistelle. Growth morphology and crystal habit of struvite crystals ($MgNH_4PO_4 \cdot 6\ H_2O$). *Journal of Crystal Growth* **46,** 339-354, (1979).

44 N. C. Bouropoulos & P. G. Koutsoukos. Spontaneous precipitation of struvite from aqueous solutions. *Journal of Crystal Growth* **213,** 381-388, (2000).

45 K. S. Le Corre, E. Valsami-Jones, P. Hobbs & S. A. Parsons. Impact of calcium on struvite crystal size, shape and purity. *Journal of Crystal Growth* **283,** 514-522, (2005).

46 D. Crutchik & J. Garrido. Struvite crystallization versus amorphous magnesium and calcium phosphate precipitation during the treatment of a saline industrial wastewater. *Water Science and Technology* **64,** 2460-2467, (2011).

47 S. Mann & G. A. Ozin. Synthesis of inorganic materials with complex form. *Nature* **382,** 313-318, (1996).

48 K. S. Sing. Reporting physisorption data for gas/solid systems with special reference to the determination of surface area and porosity (Recommendations 1984). *Pure and Applied Chemistry* **57,** 603-619, (1985).

49 K. Möller, J. Kobler & T. Bein. Colloidal suspensions of nanometer-sized mesoporous silica. *Advanced Functional Materials* **17,** 605-612, (2007).

50 Z. Xiaoqi, G. B. Joel, S. Rao & W. Jun. Engineered struvite precipitation: impacts of component-ion molar ratios and pH. (2005).

51 J. Prywer, A. Torzewska & T. Płociński. Unique surface and internal structure of struvite crystals formed by Proteus mirabilis. *Urological Research* **40,** 699-707, (2012).

52 K. Nakamoto. *Infrared and Raman Spectra of Inorganic and Coordination Compounds, Applications in Coordination, Organometallic, and Bioinorganic Chemistry*. (Wiley, 2009).

53 V. Koleva & V. Stefov. Phosphate ion vibrations in dihydrogen phosphate salts of the type $M(H_2PO_4)_2 \cdot 2H_2O$ (M = Mg, Mn, Co, Ni, Zn, Cd): spectra–structure correlations. *Vibrational Spectroscopy* **64,** 89-100, (2013).

54 Quantachrome. *Application of QSDFT (quenched solid density functional theory) - a Novel Density Functional Theory for an Accurate Pore Size Analysis of Disordered Porous Carbons*. Volume 40 (Quantachrome Instruments USA).

CHAPTER 7

MESOPOROUS MAGNESIUM PHOSPHATE-CITRATE NANOPARTICLES AS BIOCOMPATIBLE DRUG DELIVERY SYSTEM

Constantin von Schirnding, Marie Bayer, Hanna Engelke, and Thomas Bein.

7.1 Introduction

Since the consideration of nanoparticles for drug delivery applications, many materials including inorganic silica[1,2,3,4], carbon materials[5,6], layered double hydroxides[7,8], liposomes[9,10] and polymers,[11,12,13] and DNA-origami[14] have been investigated.[15,16] Nevertheless, the search for improved drug delivery systems with respect to their efficient uptake by specific cells, their ability to escape the endosome, their increased efficacy, and their biodistribution and biocompatibility has not declined.[17,18,19,20] Especially the investigation of biocompatible materials has gained great interest in this field.[21] Magnesium phosphate (MgP) based materials provide an attractive alternative to conventional drug delivery systems,[22] because the human body possesses mechanisms to degrade MgP materials and therefore the risks of side effects are decreased.[23] Additionally, magnesium and phosphate ions are inherently components of a humans body. Generally, different MgP based materials have been synthesized under various conditions such as Mg/P ratio, temperature, and pH value.[24] MgP based materials are mainly investigated as material for bone repair and substitution, for example as bone cement or also as a reservoir for anti-inflammatory drugs.[25] Bhakta *et al.* presented a co-precipitation synthesis to yield magnesium phosphate nanoparticles with encapsulated pDNA.[26,27] Their nanoparticles were dense precipitates and did not contain any mesoporosity. Mesoporosity is an attractive feature as it may enable the design of flexible drug delivery platforms.[28,29,30] Regarding mesoporous magnesium-based materials, only combinations with calcium phosphates[31,32], silicates[33] or oxides[34] have been published. For example, a BET surface area of 306 m^2/g was reported for a porous magnesium oxide structure.[34] A much smaller BET surface area of 132 m^2/g was reported for a magnesium-calcium phosphate structure.[31] However, to our knowledge

there are no publications on the synthesis of purely magnesium containing colloidal mesoporous magnesium phosphate-based nanoparticles. The development of colloidal mesoporous magnesium phosphate-based materials at the nanometer scale would open the possibility for the use as drug delivery system on the cellular level and combine the attractive properties of MgP-based bulk materials with the requirements for nano-medical applications.

Here, we present an advanced drug delivery system that offers large BET surface area with negligible premature release of incorporated drugs, which is achieved by a lipid membrane coating. Furthermore, the drug delivery system is efficiently taken up by cells and exhibits high biocompatibility. We introduce a method for the synthesis of mesoporous colloidal magnesium phosphate-citrate nanoparticles (MPCs). First, we investigated the influence of the complexing agent on the formation of mesopores. For this purpose, we gradually changed the amount of citric acid in the reaction solution, while keeping the concentrations of the other reactants constant. With optimized conditions, we were able to synthesize MPCs with diameters of about 250 nm with a BET surface area of 560 m^2/g. The pore size was calculated to be about 6.3 nm with a corresponding pore volume of 0.8 cm^3/g. Further characterization and visualization of the mesoporous framework was performed with transmission and scanning electron microscopy. Additionally, we also present data on dynamic light scattering, zeta potential measurements, and thermogravimetric analysis. We investigated the cellular uptake of fluorescently labeled MPCs and their effect *in vitro* on HeLa cells with viability assays. The bare nanoparticles are nontoxic up to concentrations of 100 µg/mL. Loaded with the chemotherapeutic agent methotrexate, which is encapsulated in the porous structure of the MPCs with a lipid membrane, the drug delivery system induced efficient cell

death with an IC_{50} value of 1.1 µg/mL MPCs mass. These findings open up a new approach towards the development of biocompatible drug delivery systems.

7.2 Results and Discussion

Magnesium phosphate-citrate nanoparticles (MPCs) were synthesized with a modified Pechini sol-gel process.[35,36] Magnesium ions are dissolved in a citric acid (CA) containing aqueous solution, resulting in complexation of magnesium and an acidic pH. This prevents the rapid precipitation of magnesium phosphate after the addition of phosphate ions and leads to a stabilized solution of magnesium, phosphate, and citrate ions. To obtain a mesoporous structure, the surfactant template cetyltrimethylammonium chloride (CTAC) is added, forming micelles in an ordered mesophase to yield a Mg-P-CA-complex. The interaction of citric acid with the magnesium ions facilitates the gelation ability of the mixed solution and influences the precipitation behavior.[37] Nanoparticles are formed after a rapid increase of the pH to strongly alkaline. This is achieved with a mixture of triethanolamine and ethanolamine, which not only act as base but additionally as complexing agents, facilitating formation of nanoparticles.[38] The extraction of the surfactant template with an ethanolic ammonium nitrate solution yielded the mesoporous MPCs.

Initially, we investigated the influence of citric acid during the reaction while keeping the concentrations of the other reactants constant. To this end, we prepared three different samples with a molar ratio of Mg/CA = 1:0, 1:0.5, and 1:1.12. After extraction of the resulting MPCs, we determined the hydrodynamic radius with dynamic light scattering (DLS) and scanning electron microscopy (SEM). The hydrodynamic particle size of MPCs in ethanolic solution and corresponding SEM images are depicted in

Figure 7.1. All samples show a narrow size distribution. However, the samples Mg/CA = 1:0 and 1:0.5 have a maximum particle size at 530 nm and 615 nm, respectively. For the sample Mg/CA = 1:1.12 the smallest particle size with a maximum at 255 nm is observed. SEM images show that all particles exhibit spherical morphology and show agglomeration due to the drying process during sample preparation (Figure 7.1). In contrast to the findings from DLS, in the SEM we measure much smaller particle sizes between 40-120 nm for all samples. The content of citric acid during the synthesis may influence the colloidal stability in solution. This is of importance for applications as drug delivery systems, which makes sample Mg/CA = 1:1.12 preferable for our investigations.

Additionally, energy dispersive X-ray (EDX) measurements were performed with the samples having molar ratios of Mg/CA = 1:0, 1:0.5, and 1:1.12, and the averaged results are presented in Table 7.1. The results suggest magnesium-deficient structures with respect to the stoichiometry of $Mg_3(PO_4)_2$.

Table 7.1: Energy dispersive X-ray analysis for MPCs with a molar ratio of Mg/CA = 1:0, 1:0.5, and 1:1.12.

Mg/CA molar ratio	**Magnesium (atom%)**	**Phosphor (atom%)**	**Mg:P**
1:1.12	4.20	3.36	1.25
1:0.5	5.12	4.23	1.21
1:0	6.25	5.23	1.19

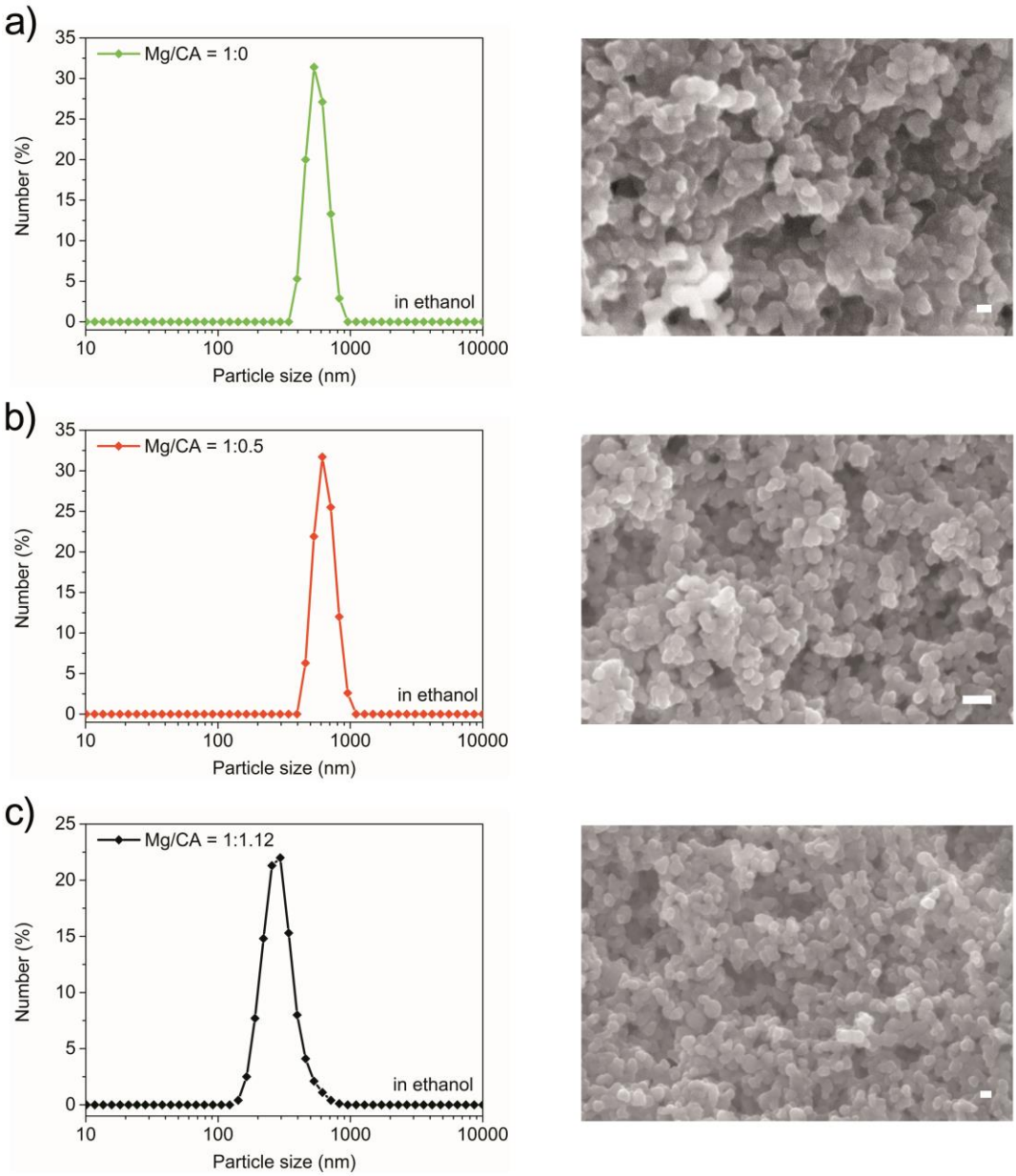

Figure 7.1: Left column depicts the dynamic light scattering data, right column depicts the corresponding scanning electron micropcopy images. Scale bars: 100 nm **a,** MPCs with a molar ratio of Mg/CA = 1:0 (green line). **b,** MPCs with a molar ratio of Mg/CA = 1:0.5 (red line). **c,** MPCs with a molar ratio of Mg/CA = 1:1.12 (black line).

The IR-spectra of the MPC samples obtained with a molar ratio of Mg/CA = 1:0, 1:0.5, and 1:1.12 are depicted in Figure 7.2a. They are normalized to the $\nu_3(PO_4)$ stretching vibration at 1081 cm^{-1}.

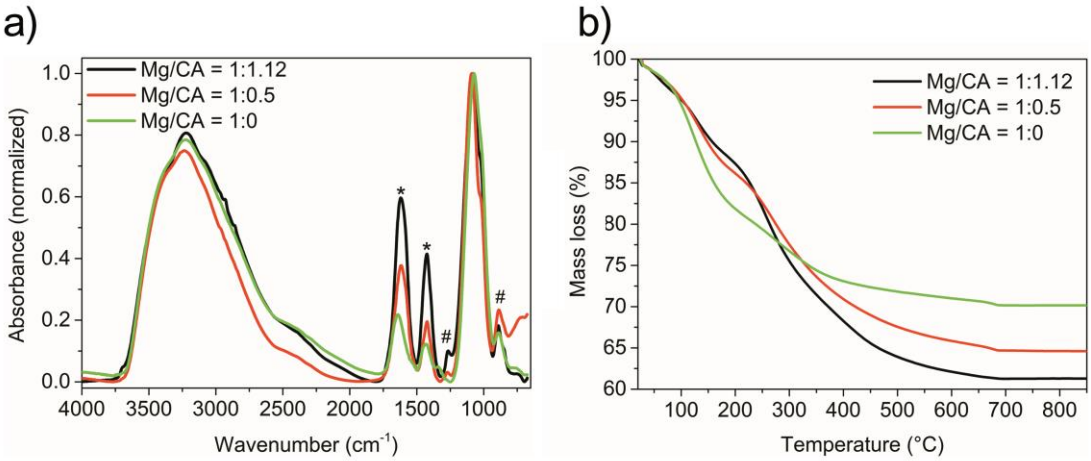

Figure 7.2: **a,** Infrared spectra of MPCs with a molar ratio of Mg/CA = 1:1.12 (black line), 1:0.5 (red line), and 1:0 (green line). **b,** Thermogravimetric analysis of the samples with a molar ratio of Mg/CA = 1:1.12 (black line), 1:1.05 (red line), and 1:0 (green line).

The presence of citrate ions in the samples is clearly demonstrated by the symmetric and asymmetric vibrations of the carboxylic groups at 1423 cm^{-1} and 1616 cm^{-1} (marked with asterisks).[39] The vibrations at 1428 cm^{-1} and 1635 cm^{-1} of the sample with no citric acid result from the incorporation of carbonate ions into the structure.[40] The incorporation of carbonate ions is attributed to their presence in the aqueous reaction solution. The intensity increase of these COO^- vibrations with the relative citric acid content Mg/CA = 1:0, 1:0.5, and 1:1.12 in the sample reflects the amount of citrate and carbonate ions incorporated into the magnesium phosphate-citrate nanoparticle structure. The vibrations at 1269 cm^{-1} and 879 cm^{-1} are assigned to $H\text{-}OPO_3^{2-}$ and $HO\text{-}PO_3^{2-}$, respectively (marked with pounds).[41] These findings suggest that MPCs exhibit a magnesium-deficient structure, which is in accordance with the EDX results. The broad band between 3600 cm^{-1} and 2200 cm^{-1} is attributed to the O–H vibration of water remaining in the pores of the samples.

To quantify the amount of citrate in the MPC structure, thermogravimetric analysis (TGA) was performed on all samples up to 850 °C with a heating rate of 10 K/min in

a stream (25 mL/min) of synthetic air (see Figure 7.2b). The moderate mass loss of all samples up to 120 °C is assigned to mainly water (~ 8 wt%). Up to 180 °C, we attribute the mass loss in all samples to weakly bound organics (~ 6 wt%). Between 180 °C and 700 °C a significant mass loss is observed for all samples, attributed to the decomposition of strongly bound organics incorporated in the MPCs. Above 700 °C the mass stays almost constant up to 850 °C. In the sample Mg/CA = 1:0, the mass loss of organics adds up to 13 wt%. This drop is caused by residues of surfactant template, carbonates and crystal water within the nanoparticles.[42] The sample Mg/CA = 1:0.5 loses mass of 23 wt%, the sample Mg/CA = 1:1.12 loses 28 wt%. Therefore, in the samples containing citric acid an additional mass loss of 10 wt% and 15 wt%, respectively is recorded in comparison to the sample without citric acid. We attribute these mass losses to the decomposition of citrate ions incorporated in the structure of MPCs. The results show that the incorporation of citrate ions into the structure of MPCs is dependent on the initial molar ratio of Mg/CA. This finding is in accordance with the IR data, indicating the increase in intensity of the COO^- vibrations at 1423 cm^{-1} and 1616 cm^{-1} with respect to the initial CA concentration.

For the application as drug delivery system a large surface area is desired.[28,29] The porosity of the MPCs was investigated with nitrogen sorption analysis. The measurements revealed the typical type IV isotherm for all samples. The isotherms with the molar ratios of Mg/CA = 1:0, 1:0.5, and 1:1.12 are shown in Figure 7.3a and the pore size distributions of all samples are represented in Figure 7.3b. With increasing amounts of citric acid in the reaction solution, the degree of porosity of MPCs increases. While the samples Mg/CA = 1:0 and 1:0.5 show rather low mesoporosity, the sample Mg/CA = 1:1.12 exhibits the largest BET surface area with 560 m^2/g, a maximum of the pore size distribution at 6.3 nm and a corresponding

pore volume of 0.8 cm^3/g. The presence of mesoporosity is also visible in the strong increase of adsorbed nitrogen volume at relative pressures between 0.4 and 0.8, while a narrow pore size distribution is apparent for all samples. We conclude that the amount of citric acid strongly influences the formation of mesoporous MPCs. The coordination complex Mg-citrate apparently slows down the kinetics of the precipitation reaction, allowing the solid structure to form around the micelles of the surfactant template. The obtained porosity parameters are listed in Table 7.2.

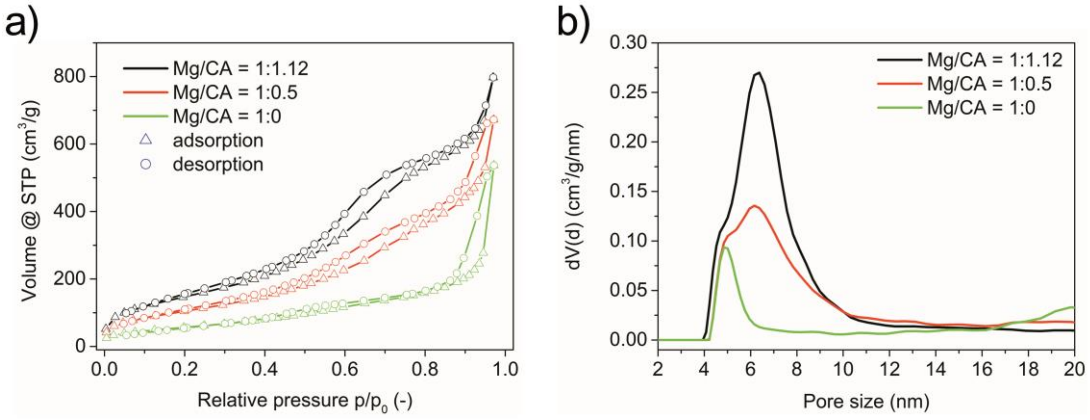

Figure 7.3: Sorption data for MPCs with a molar ratio of Mg/CA = 1:1.12 (black line), 1:0.5 (red line), and 1:0 (green line). **a,** Adsorption and desorption isotherms. **b,** Calculated pore size distributions.

Table 7.2: Sorption data analysis for MPCs with a molar ratio of Mg/CA = 1:0, 1:0.5, and 1:1.12.

Mg/CA molar ratio	**Pore size distribution**		**BET surface area (m^2/g)**
	Size (nm)	**Volume (cm^3/g)**	
1:1.12	6.3	0.80	560
1:0.5	6.2	0.52	390
1:0	4.8	0.13	215

The X-ray analysis reveals an amorphous structure for all samples (Figure 7.4a). This is in accordance with the observed $\nu_3(PO_4)$ stretching vibration at 1081 cm^{-1} in the IR-spectra, which is shifted to higher wavenumbers compared to crystalline

magnesium phosphate structures.[43] With transmission electron microscopy the mesoporous structure of MPCs can be visualized. The nanoparticles are strongly agglomerated due to the drying process during the sample preparation (Figure 7.4b).

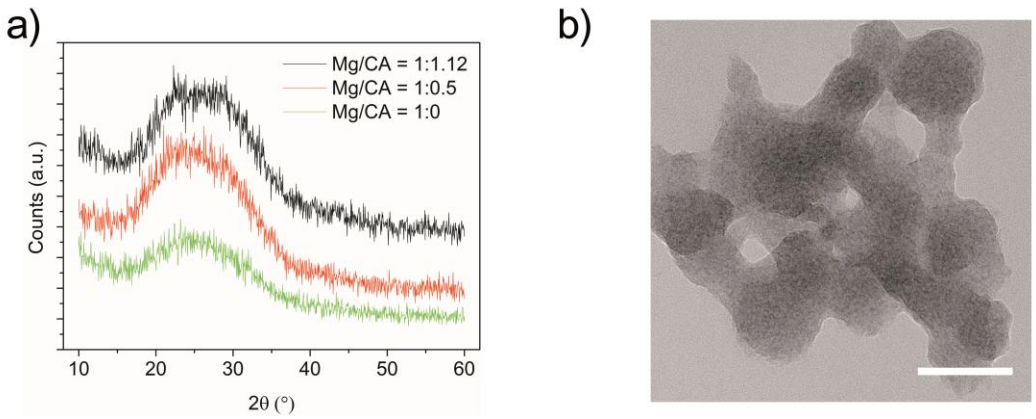

Figure 7.4: **a,** X-ray diffraction of the amorphous MPCs with a molar ratio of Mg/CA = 1:1.12 (black line), 1:0.5 (red line), and 1:0 (green line). **b,** Transmission electron microscopy image of MPCs with a molar ratio of Mg/CA = 1:1.12. Scale bar: 100 nm.

The initial concentration of citric acid in the range of molar ratios of Mg/CA = 1:0, 1:0.5, and 1:1.12 makes a great difference in the resulting material. Hence, we have successfully introduced a synthesis route that leads to small magnesium phosphate-citrate nanoparticles. Additionally, we demonstrate the incorporation of citrate into the structure of magnesium phosphate-citrate, which leads to stable colloidal particles.

Because of its colloidal stability, the large BET surface area, and the highly mesoporous structure, we continued with the sample Mg/CA = 1:1.12 concerning investigations for drug delivery applications.

First, we established a method for the stable and impermeable coating of the MPCs with a supported lipid bilayer. For this purpose, we loaded the particles in a solution of calcein serving as fluorescent model drug and a small amount of

cetyltrimethylammonium chloride (CTAC) as endosomal escape agent[32] for subsequent cell experiments. For the coating we used the solvent exchange method[44] with a mixture of 1,2-dioleoyl-3-trimethylammonium-propane (DOTAP) and 1,2-dioleoyl-sn-glycero-3-phosphocholine (DOPC). This procedure leads to the loaded magnesium phosphate-citrate nanoparticles with a supported lipid bilayer (lipid@MPCs).

The lipid@MPCs were transferred into a special measuring cell for fluorescence detection of release kinetics. The lipid@MPCs were separated from the measuring compartment with a dialysis membrane with a molecular-weight cutoff at 14,000 Da. This setup only allows for the penetration of released fluorescent dye through the membrane into the measuring compartment (see Figure 5.6a). The release of calcein from the lipid@MPCs was measured once for the as-prepared sample (Figure 7.5a, red line) and second for a sample where the lipid@MPCs particles were acidified (Figure 7.5a, green line). The acidification leads to the dissolution of the MPCs, destabilization of the lipid membrane, and therefore release of the fluorescent dye into the measuring compartment mimicking the endosomal escape in cells. This is depicted by the increase in fluorescent counts with respect to the as-prepared closed sample, which reveals only 15 % premature release of the model drug.

In vitro cell experiments were carried out to investigate the uptake behavior of lipid@MPCs with HeLa cells. After an incubation of 24 hours with lipid@MPCs, the cells were investigated with a confocal fluorescence microscope, showing efficient particle uptake (Figure 7.5b). The green fluorescent particles are localized inside the cell, which is clearly visible with the red labeled cell membrane.

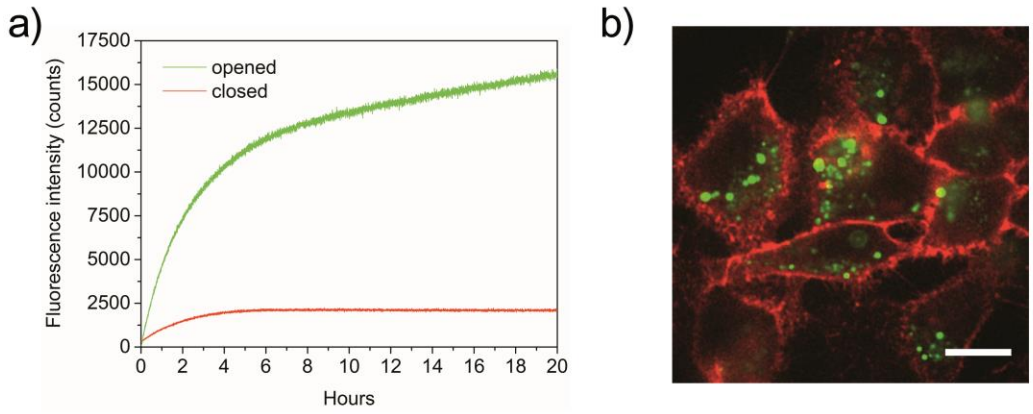

Figure 7.5: **a,** Fluorescence release measurement over 20 hours showing the premature release behavior (red line) and a strong increase upon triggered release by acidification (green line). **b,** Confocal microscopy image of HeLa cells with lipid@MPCs (in green) internalized in the WGA-stained cell membrane in red (incubation for 24 h). Scale bar: 50 µm.

Further, *in vitro* experiments were carried out to investigate the toxicity of magnesium phosphate-citrate particles to cells. Three different kinds of particles were incubated for 72 hours on HeLa cells and analyzed with MTT-assay (Figure 7.6). The sample MPCs@plain (green line) represents the bare magnesium phosphate-citrate particles without any further modification. The sample MPCs@control (black line) was modified in the same way as the sample lipid@MPCs (red line) but without the addition of the endosomal escape agent CTAC. The samples MPCs@plain and MPCs@control show no cytotoxicity up to particle concentrations of 100 µg/mL. For the sample lipid@MPCs a drop in cell viability at a particle concentration of 100 µg/mL was obtained. We calculated an IC_{50} value of 77 µg/mL. Thus, MPCs are quite biocompatible with respect to the investigated samples. MPCs appear to be promising candidates for advanced drug delivery applications.

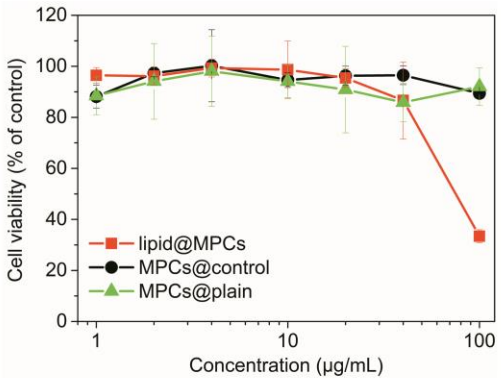

Figure 7.6: Cell viability of HeLa cells with respect to lipid@MPCs that escape from the endosome (red line). The data are compared with those for the particles MPCs@control that do not escape from the endosome (black line), and with particles MPCs@plain without a lipid membrane that are not taken up by cells (green line).

Moreover, we investigated the loading capacity of the newly developed MPCs for methotrexate (MTX, a hydrophobic anti-cancer drug[45]), its release behavior, and its efficiency in cell experiments. MPCs were loaded for 30 min in an MTX-containing solution with small amounts of the endosomal escape agent CTAC. After centrifugation of MPCs containing the membrane-impermeable MTX, the particles were enclosed with a supported lipid bilayer to yield MPCs@MTX. After further washing steps by centrifugation, the maximum loading capacity and the release kinetics of MPCs@MTX were investigated with UV-Vis measurements at a wavelength of 303 nm[46] (Figure 7.7). The spectrum of methotrexate is depicted in Figure 7.7d, showing an absorption maximum at 303 nm measured in simulated body fluid.

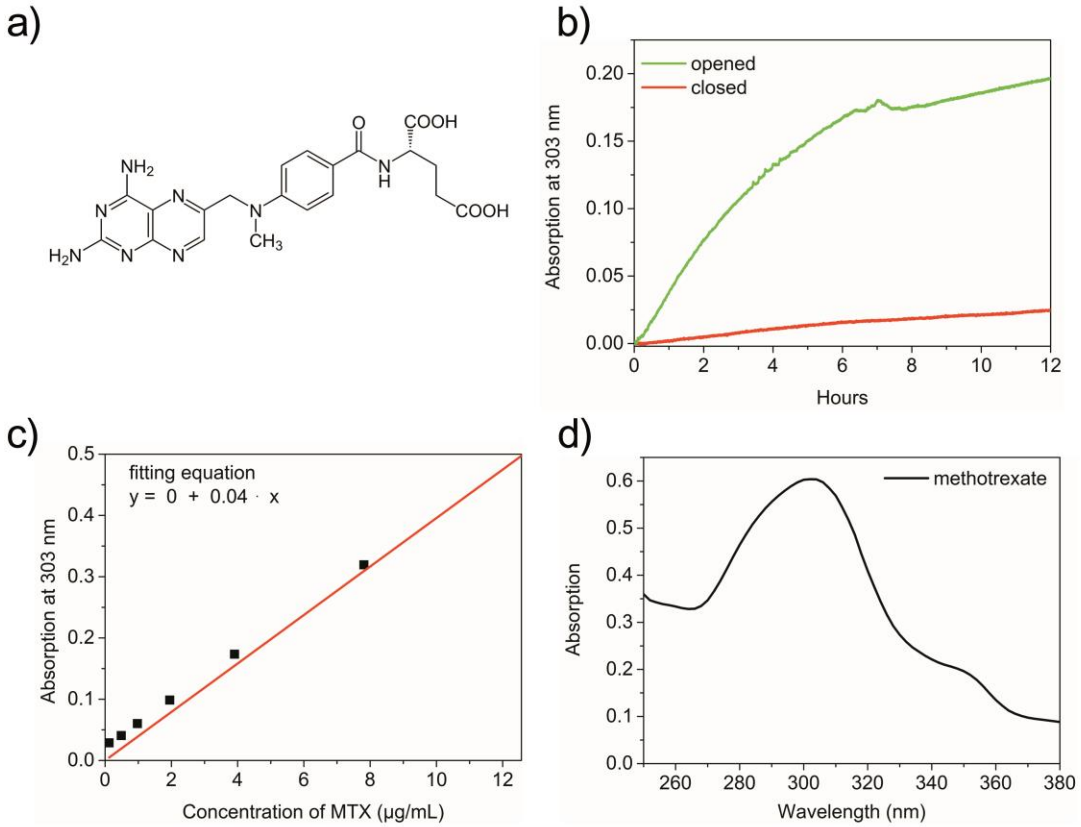

Figure 7.7: **a,** Structure of hydrophobic methotrexate. **b,** UV-Vis release measurement over 12 hours showing only premature release (red line) and a strong increase upon triggered release by acidification (green line). **c,** Absorption fitting curve of methotrexate with different concentrations measured at 303 nm. **d,** UV-Vis absorption spectrum of methotrexate in the range between 250 nm and 380 nm with a concentration of 15.6 µg/mL.

The same measurement cuvette as that for fluorescence release measurements was used and two different samples were analyzed. MPCs@MTX was measured without further purification (Figure 7.7b, closed, red line). The endosomal escape of MTX was mimicked by acidification, and MTX was able to penetrate through the dialysis membrane (the absorption was detected at 303 nm; Figure 7.7b, opened, green line). The premature release of MTX from MPCs@MTX is as low as 13 % with respect to the opened sample, which reached an optical absorption of 0.19 after 12 h. This absorption value corresponds to a total release of 5 µg/mL. The volume of the measurement cuvette is 4 mL, leading to a total mass of 0.02 mg MTX released from an initial 0.5 mg of MPCs@MTX. With these results, a release capacity of 4 wt%

was established after 12 h for the anti-cancer drug MTX. The MPCs@MTX were then incubated for 72 hours on HeLa cells and a viability assay was performed (Figure 7.8, black line). The delivery of MTX into HeLa cells results in an efficient cytotoxicity with an IC_{50} = 1.1 µg/mL for MPCs@MTX particles. This refers to an estimated 0.044 µg/mL free MTX delivered directly to the cytosol of the cells (under the assumption that the particles release 4 wt% MTX from MPCs@MTX after 72 h incubation). Furthermore, the supernatant of MPCs@MTX was analyzed to verify the safe MTX delivery without premature release. Here, we did observe minor changes in cell viability above 20 µg/mL (Figure 7.8, green line).

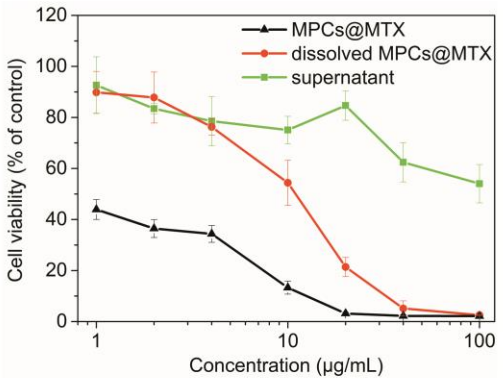

Figure 7.8: HeLa cell viability measured with MTT-assay. MPCs@MTX (black line) with an IC_{50} = 1.1 µg/mL, dissolved MPCs@MTX (red line) with an IC_{50} = 9.3 µg/mL, and the supernatant of MPCs@MTX (green line) with no IC_{50} obtained.

Additionally, we dissolved MPCs@MTX before the incubation with HeLa cells. Thus, the approximately same amount of free MTX that was previously loaded into the particles becomes available to the cells. Thereby, the effect of free undelivered MTX can be obtained, to compare it to the delivery efficacy with MPCs@MTX. Dissolved MPCs@MTX (Figure 7.8, red line) increase the IC_{50} to a value of 9.3 µg/mL. The experiment with the dissolved MPCs is also a good control yielding the amount of MTX that is remaining in adjacent tissue after dissolution of the MPCs

in the target cells. Comparing the above results, the efficacy of our delivery system enhances the activity of MTX by a factor of ~ 9.

7.3 Conclusion

Here, we have presented a novel approach for the synthesis of colloidal mesoporous magnesium phosphate-citrate nanoparticles by investigating the influence of the chelating agent citric acid in a modified Pechini process. The level of citric acid incorporated into the structure of magnesium phosphate-citrate has an influence on the colloidal stability of MPCs in solution. Additionally, incorporated citric acid impacts the mesoporosity in the MPCs. A maximum BET surface area of 560 m^2/g with a pore size of about 6.3 nm and a corresponding pore volume of 0.8 cm^3/g was reached. With the fluorescent model drug calcein, the release kinetics of MPCs closed with a supported lipid bilayer were investigated. Here, we established a synthesis method for a rather tight closure and entrapment of drugs with only 15 % premature release within 12 h. In subsequent cell experiments we observed very good biocompatibility for MPCs. This enables them to become a promising new platform for drug delivery applications. To explore this potential, we loaded the anti-cancer drug methotrexate into MPCs and used the loaded MPCs as delivery vehicle for HeLa cells, reaching high cell toxicity with an IC_{50} value of 1.1 µg/mL. In conclusion, we have developed an efficient drug delivery vehicle synthesized from biocompatible precursors that are neither toxic by themselves nor in the form of nanoparticles. The MPCs furnished with these features may have the potential to reduce the side effects of current chemotherapies.

7.4 Experimental

Chemicals for Nanoparticle Synthesis:

Magnesium nitrate hexahydrate (Sigma, 99 %), ammonium dihydrogenphosphate (Alfa Aeser, 99 %), citric acid (Aldrich, 99.5 %), cetyltrimethylammonium chloride (CTAC, Fluka, 25 wt% in H_2O), ethylene glycol (Aldrich, 99.8 %), ethanolamine (Fluka, >99 %), triethanolamine (TEA, Aldrich, 98%), ethanol (EtOH, Aldrich, >99.5 %), ammonium nitrate (Sigma, 99 %), calcein (Sigma), simulated body fluid (SBF, prepared as written elsewhere[47], contains: Na^+, K^+, Mg^{2+}, Ca^{2+}, Cl^-, CO_3^{2-}, SO_4^{2-}, PO_4^{3-}, and tris(hydroxymethyl) aminomethane, Sigma, >99 %), methotrexate (Sigma, >99 %), hydrochloric acid (Sigma, 2 M), 1,2-dioleoyl-3-trimethylammonium-propane (DOTAP, Avanti Polar Lipids), 1,2-dioleoyl-sn-glycero-3-phosphocholine (DOPC, Avanti Polar Lipids), sodium hydroxide (Aldrich, 0.1 M).

All chemicals were used as received without further purification. Doubly distilled water from a Millipore system (Milli-Q Academic A10) was used for all synthesis steps.

Synthesis of Magnesium Phosphate-Citrate Nanoparticles (MPCs):

The synthesis of MPCs was carried out following a modified Pechini sol-gel process.[35,36] In a 50 mL polypropylene reactor magnesium nitrate hexahydrate (320 mg, 1.25 mmol) and different amounts of citric acid (0 mg/ 120 mg/ 270 mg; 0 mmol/ 0.625 mmol/ 1.41 mmol) were dissolved in water (17 mL, 0.94 mmol). This leads to solutions with a molar ratio of Mg/CA = 1:0, 1:0.5, and 1:1.12. Then, ammonium dihydrogenphosphate (142 mg, 1.25 mmol) was added to the solution and stirred until complete dissolution. Then, cetyltrimethylammonium chloride

(622 mg, 1.94 mmol) and ethylene glycol (7.15 g, 115 mmol) were added and the synthesis mixture was stirred at 500 rpm at room temperature. Thereafter, the clear solution was combined with triethanolamine (7.15 g, 48 mmol) and ethanolamine (3.00 g, 49.1 mmol) under vigorous stirring for three minutes. The suspension was diluted approximately 1:1 with ethanol. The particles were separated by centrifugation at 7,830 rpm (7,197 rcf) for 5 minutes and redispersed in NH_4NO_3/EtOH (2 wt%, 80 mL). To extract the template, the suspension was heated under reflux conditions at 90 °C for 30 minutes. Then the particles were again separated by centrifugation at 7,830 rpm (7,197 rcf) for 5 minutes and redispersed in 80 mL ethanol. The mixture was again heated under reflux conditions at 90 °C for 30 minutes, and the particles were separated by centrifugation at 7,830 rpm (7,197 rcf) for 5 minutes and redispersed in 20 mL ethanol.

Preparation of Magnesium Phosphate-Citrate Nanoparticles for Release and Cell Experiments with the Model Drug Calcein:

The amount of 0.5 mg of magnesium phosphate-citrate nanoparticles was loaded in 1 mL aqueous calcein solution (0.62 mg, 1 mmol, pH 9.4) and, if needed, cetyltrimethylammonium chloride (6.25 µg, 19.5 nmol) for 30 minutes. The particles were separated by centrifugation at 14,000 rpm (16,873 rcf) for 3 minutes. The loaded particles were redispersed in a lipid solution of 1,2-dioleoyl-3-trimethylammonium-propane (DOTAP, 75 µL of a solution with 12.5 mg/mL 60/40 vol% H_2O/EtOH) and 1,2-dioleoyl-sn-glycero-3-phosphocholine (DOPC, 25 µL of a solution with 12.5 mg/mL 60/40 vol% H_2O/EtOH) under sonication conditions, and bi-distilled water (900 µL, pH adjusted to 9.4 with NaOH) was added. Then, the particles were separated by centrifugation at 14,000 rpm (16,873 rcf) for 5 minutes. The lipid-coated magnesium phosphate-citrate

nanoparticles were washed twice by centrifugation at 12,000 rpm (12,396 rcf, 13 °C) for 5 minutes with SBF (500 µL, pH 7.4).

Preparation of Magnesium Phosphate-Citrate Particles for Release and Cell Experiments with the Anti-Cancer Drug Methotrexate:

The amount of 0.5 mg of methotrexate was dissolved in 50 µL of sodium hydroxide solution (0.1 M) and cetyltrimethylammonium chloride (6.25 µg, 19.5 nmol) was added. Then 500 µL of bi-distilled water and 0.5 mg of magnesium phosphate-citrate particles were added. The particles were loaded for 30 minutes and then separated by centrifugation at 14,000 rpm (16,873 rcf) for 3 minutes. The loaded particles were redispersed in a lipid solution of 1,2-dioleoyl-3-trimethylammonium-propane (DOTAP, 75 µL of a solution with 12.5 mg/mL 60/40 vol% H_2O/EtOH) and 1,2-dioleoyl-sn-glycero-3-phosphocholine (DOPC, 25 µL of a solution with 12.5 mg/mL 60/40 vol% H_2O/EtOH) under sonication conditions and 900 µL bi-distilled water was added. Then, the particles were separated by centrifugation at 14,000 rpm (16,873 rcf) for 5 minutes. The lipid-coated magnesium phosphate-citrate nanoparticles were washed twice by centrifugation at 12,000 rpm (12,396 rcf, 13 °C) for 5 minutes with SBF (500 µL, pH 7.4).

***In vitro* Release Fluorescence and UV-Vis Measurements:**

Lipid-coated magnesium phosphate-citrate particles were transferred into the cap of a homebuilt fluorescence and UV-Vis setup (0.5 mg particles in 200 µL SBF) and separated by a cellulose membrane from the measuring cell, which is filled with SBF. Dye or drug that is released from the particles diffuses through the membrane and can be detected in the measuring cell (Figure 5.6b). While detecting the fluorescence of calcein with a fluorescence spectrometer at 512 nm (excitation at

495 nm) as a function of time, the stimulated release can be observed. While detecting the absorbance of methotrexate with a UV-Vis spectrometer at 303 nm as a function of time, the stimulated release can be observed. All experiments were carried out at least twice on different days to evaluate the reproducibility of the tight supported lipid bilayer.

Cell Line and Culture:

HeLa human cervical cancer cells were purchased from and cultured according to American Type Culture Collection (ATCC). HeLa cells were grown in DMEM medium low glucose (Sigma Aldrich) supplemented with 10 % FCS (Gibco) and 2 mM L-glutamine (Gibco) at 37 °C and 5 % CO_2. Cells were routinely tested and confirmed as mycoplasma free.

Cell Viability:

Cell viability assays (MTT) were carried out on HeLa cell line for particles MPCs@MTX, its supernatant, dissolved MPCs@MTX, MPCs@control, MPCs@plain, and lipid@MPCs. As a reference experiment, we dissolved 1 mg of MPCs@MTX that was loaded with MTX and CTAC with 0.1 mL of 0.1 M HCl and added then 0.9 mL of SBF to yield a final concentration of 1 mg/mL with a pH value of 7.4. Therefore, this test solution had the same ingredients as MPCs@MTX except the delivery feature. HeLa cells were treated with this solution that exhibited the same concentrations as the particle solution that contained MPCs@MTX. We enhanced the efficiency of free MTX by a factor of ~ 9 when using MPCs as delivery system. The supernatant of MPCs@MTX was recovered 12 h after preparation of the particles and applied to HeLa cells with the same concentration as the particle solution.

7.5 Characterization

Characterization of Nanoparticles:

Nitrogen sorption analysis was performed on a Quantachrome Instrument Nova 4000e at 77 K. Samples (25 mg) were outgassed at 120 °C for 12 h *in vacuo* (10 mTorr). Pore size and pore volume were calculated by a QSDFT equilibrium model of N_2 on carbon, based on the desorption branch of the isotherms. The QSDFT method takes into account the effects of surface roughness and heterogeneity.[48] Cumulative pore volumes were evaluated up to a pore size of 12 nm, in order to remove the contribution of inter-particle textural porosity. Surface areas were calculated with the BET model in the range $p/p_0 = 0.05–0.2$. Thermogravimetric analysis of the samples was performed on a Netzsch STA 440 C TG/DSC in a stream of synthetic air with a flow rate of 25 mL/min and a heating rate of 10 K/min. Dynamic light scattering measurements were performed on a Malvern Zetasizer-Nano instrument with a 4 mW He-Ne laser (633 nm) in ethanolic suspension with a concentration of 0.5 mg/mL. Scanning electron microscopy (SEM) images were obtained on a JEOL JSM-6400F. For sample preparation a droplet of the ethanolic colloidal suspension was placed on a 60 °C preheated carbon pad. Samples were sputtered with carbon before measurement. Transmission electron microscopy (TEM) was performed on a FEI TECNAI G2 at an acceleration voltage of 200 kV. For sample preparation, a droplet of a diluted ethanolic colloidal suspension was deposited on a carbon-coated copper grid and the solvent was allowed to evaporate. Infrared spectra were measured with a Thermo Scientific Nicolet iN 10 infrared microscope. XRD patterns were obtained with a Bruker D8 Discover X-ray diffractometer using Cu-K_α radiation (1.5406 Å). UV/Vis measurements were performed on a Perkin Elmer Lambda 1050 UV-Vis/NIR spectrophotometer with a

deuterium arc lamp and a tungsten filament equipped with a 150 mm integrating sphere and an InGaAs detector.

MTT-Assay:

For MTT-assays we treated 5000 cells per well containing 100 µL of the respective medium with MPCs@MTX, its supernatant, dissolved MPCs@MTX, MPCs@control, MPCs@plain, or lipid@MPCs. After 72 h incubation 10 µL 3-(4,5-dimethylthiazol-2-yl)-2,5-diphenyltetrazolium bromide (MTT) was added to the magnesium phosphate-citrate treated cells and incubated for further 2 h. Unreacted MTT and medium were removed and the 96-well plates were stored at -80 °C for at least 1 h. Then, 100 µL DMSO was added to each well. The absorbance was read out by a Tecan plate reader. All studies were performed in triplicates. IC_{50} values were calculated with OriginPro 9.

Live-Cell Fluorescence Microscopy:

To visualize nanoparticle internalization by cells, live-cell imaging was performed on a spinning disc microscope based on the Zeiss Cell Observer SD utilizing a Yokogawa spinning disk unit CSU-X1. The system was equipped with a 1.40 NA 63x Plan apochromat oil immersion objective from Zeiss. For all experiments the exposure time was 0.1 s and z-stacks were recorded. Calcein-loaded MPCs were imaged with approximately 0.4 W/mm^2 of 488 nm excitation light. Atto647 was excited with approximately 11 mW/mm^2 of 639 nm. In the excitation path a quad-edge dichroic beamsplitter (FF410/504/582/669-Di01-25x36, Semrock) was used. For two-color detection of calcein and Atto647, a dichroic mirror (560 nm, Semrock) and band-pass filters 525/50 and 690/60 (both Semrock) were used in the detection path. Separate images for each fluorescence channel were acquired using two

separate electron multiplier charge coupled device (EMCCD) cameras (PhotometricsEvolve^{TM}). Immediately before imaging, cell membranes were stained using wheat germ agglutinin Alexa Fluor 647 conjugate at a final concentration of 5 µg/mL. After application of the dye, cells were washed twice.

7.6 References

1 C. Argyo, V. Weiss, C. Bräuchle & T. Bein. Multifunctional mesoporous silica nanoparticles as a universal platform for drug delivery. *Chemistry of Materials* **26,** 435-451, (2014).

2 J. Kecht, A. Schlossbauer & T. Bein. Selective functionalization of the outer and inner surfaces in mesoporous silica nanoparticles. *Chemistry of Materials* **20,** 7207-7214, (2008).

3 V. Cauda, A. Schlossbauer, J. Kecht, A. Zürner & T. Bein. Multiple core−shell functionalized colloidal mesoporous silica nanoparticles. *Journal of the American Chemical Society* **131,** 11361-11370, (2009).

4 S. A. Mackowiak *et al.* Targeted drug delivery in cancer cells with red-light photoactivated mesoporous silica nanoparticles. *Nano Letters* **13,** 2576-2583, (2013).

5 A. Bianco, K. Kostarelos & M. Prato. Applications of carbon nanotubes in drug delivery. *Current Opinion in Chemical Biology* **9,** 674-679, (2005).

6 Z. Liu *et al.* Drug delivery with carbon nanotubes for *in vivo* cancer treatment. *Cancer Research* **68,** 6652-6660, (2008).

7 J.-H. Choy, S.-Y. Kwak, Y.-J. Jeong & J.-S. Park. Inorganic layered double hydroxides as nonviral vectors. *Angewandte Chemie* **39,** 4041-4045, (2000).

8 K. Ladewig, Z. P. Xu & G. Q. Lu. Layered double hydroxide nanoparticles in gene and drug delivery. *Expert Opinion on Drug Delivery* **6,** 907-922, (2009).

9 A. Sharma & U. S. Sharma. Liposomes in drug delivery: progress and limitations. *International Journal of Pharmaceutics* **154,** 123-140, (1997).

10 G. Gregoriadis & A. T. Florence. Liposomes in drug delivery. *Drugs* **45,** 15-28, (1993).

11 E. Wagner. Programmed drug delivery: nanosystems for tumor targeting. *Expert Opinion on Biological Therapy* **7,** 587-593, (2007).

12 R. Duncan. The dawning era of polymer therapeutics. *Nature Reviews: Drug Discovery* **2,** 347-360, (2003).

13 R. Duncan. Drug-polymer conjugates: potential for improved chemotherapy. *Anti-Cancer Drugs* **3,** 175-210, (1992).

14 Q. Zhang *et al.* DNA origami as an *in vivo* drug delivery vehicle for cancer therapy. *ACS Nano* **8,** 6633-6643, (2014).

15 S. Wang. Ordered mesoporous materials for drug delivery. *Microporous and Mesoporous Materials* **117,** 1-9, (2009).

16 D. Peer *et al.* Nanocarriers as an emerging platform for cancer therapy. *Nature Nanotechnology* **2,** 751-760, (2007).

17 A. S. Hoffman. The origins and evolution of "controlled" drug delivery systems. *Journal of Controlled Release* **132,** 153-163, (2008).

18 S. D. Caruthers, S. A. Wickline & G. M. Lanza. Nanotechnological applications in medicine. *Current Opinion in Biotechnology* **18,** 26-30, (2007).

19 T. M. Allen. Ligand-targeted therapeutics in anticancer therapy. *Nature Reviews: Cancer* **2,** 750-763, (2002).

20 M. Ferrari. Cancer nanotechnology: opportunities and challenges. *Nature Reviews: Cancer* **5,** 161-171, (2005).

21 P. Pamies & A. Stoddart. Materials for drug delivery. *Nature Materials* **12,** 957-957, (2013).

22 H. Zhou, T. J. F. Luchini & S. B. Bhaduri. Microwave assisted synthesis of amorphous magnesium phosphate nanospheres. *Journal of Materials Science: Materials in Medicine* **23,** 2831-2837, (2012).

23 M. P. Staiger, A. M. Pietak, J. Huadmai & G. Dias. Magnesium and its alloys as orthopedic biomaterials: a review. *Biomaterials* **27,** 1728-1734, (2006).

24 F. Tamimi *et al.* Biocompatibility of magnesium phosphate minerals and their stability under physiological conditions. *Acta Biomaterialia* **7,** 2678-2685, (2011).

25 W. Xue, K. Dahlquist, A. Banerjee, A. Bandyopadhyay & S. Bose. Synthesis and characterization of tricalcium phosphate with Zn and Mg based dopants. *Journal of Materials Science: Materials in Medicine* **19,** 2669-2677, (2008).

26 G. Bhakta, S. Mitra & A. Maitra. DNA encapsulated magnesium and manganous phosphate nanoparticles: potential non-viral vectors for gene delivery. *Biomaterials* **26,** 2157-2163, (2005).

27 G. Bhakta, A. Shrivastava & A. Maitra. Magnesium phosphate nanoparticles can be efficiently used *in vitro* and *in vivo* as non-viral vectors for targeted gene delivery. *Journal of biomedical nanotechnology* **5,** 106-114, (2009).

28 Y. H. Bae & K. Park. Targeted drug delivery to tumors: myths, reality and possibility. *Journal of Controlled Release* **153,** 198-205, (2011).

29 I. I. Slowing, J. L. Vivero-Escoto, C.-W. Wu & V. S.-Y. Lin. Mesoporous silica nanoparticles as controlled release drug delivery and gene transfection carriers. *Advanced Drug Delivery Reviews* **60,** 1278-1288, (2008).

30 T. M. Allen & P. R. Cullis. Drug delivery systems: entering the mainstream. *Science* **303,** 1818-1822, (2004).

31 S. Wang *et al.* Fabrication of mesoporous magnesium substituted β-tricalcium phosphate nanospheres by self-transformation and assembly involving EDTA ions. *Microporous and Mesoporous Materials* **179,** 172-181, (2013).

32 T. Bein, H. Engelke, H. Feckl & C. von Schirnding. Mesoporous calcium phosphate-citrate nanoparticles and uses thereof. PCT/EP2016/068231 (2015).

33 Z. Wu *et al. In vitro* degradability, bioactivity and cell responses to mesoporous magnesium silicate for the induction of bone regeneration. *Colloids and Surfaces B: Biointerfaces* **120,** 38-46, (2014).

34 J. Roggenbuck & M. Tiemann. Ordered mesoporous magnesium oxide with high thermal stability synthesized by exotemplating using CMK-3 carbon. *Journal of the American Chemical Society* **127,** 1096-1097, (2005).

35 M. P. Pechini. Method of preparing lead and alkaline earth titanates and niobates and coating method using the same to form a capacitor. US3330697 (1967).

36 P. Yang, P. Yang, X. Teng, J. Lin & L. Huang. A novel luminescent mesoporous silica/apatite composite for controlled drug release. *Journal of Materials Chemistry* **21,** 5505-5510, (2011).

37 W. Weng, Z. Ding, Y. Mao & F. Zhang. The gelation behaviour of copper ethoxide. *Journal of Non-Crystalline Solids* **147–148,** 102-105, (1992).

38 K. Möller, J. Kobler & T. Bein. Colloidal suspensions of nanometer-sized mesoporous silica. *Advanced Functional Materials* **17,** 605-612, (2007).

39 K. Nakamoto. *Infrared and Raman Spectra of Inorganic and Coordination Compounds, Applications in Coordination, Organometallic, and Bioinorganic Chemistry*. (Wiley, 2009).

40 M. A. Aramendia, V. Borau, C. Jimenez, J. M. Marinas & F. J. Romero. The selectivity of sodium carbonate-doped zinc phosphate in the gas-phase dehydrogenation-dehydration of cyclohexanol. *Journal of Catalysis* **151,** 44-49, (1995).

41 V. Koleva & V. Stefov. Phosphate ion vibrations in dihydrogen phosphate salts of the type $M(H_2PO_4)_2 \cdot 2H_2O$ (M = Mg, Mn, Co, Ni, Zn, Cd): spectra–structure correlations. *Vibrational Spectroscopy* **64,** 89-100, (2013).

42 S. Mousa. Study on synthesis of magnesium phosphate materials. *Phosphorus Research Bulletin* **24,** 16-21, (2010).

43 H. Assaaoudi, Z. Fang, I. S. Butler, D. H. Ryan & J. A. Kozinski. Characterization of a new magnesium hydrogen orthophosphate salt, $Mg_{3.5}H_2(PO_4)_3$, synthesized in supercritical water. *Solid State Sciences* **9,** 385-393, (2007).

44 V. Cauda *et al.* Colchicine-loaded lipid bilayer-coated 50 nm mesoporous nanoparticles efficiently induce microtubule depolymerization upon cell uptake. *Nano Letters* **10,** 2484-2492, (2010).

45 J. Jingou *et al.* Preparation, characterization of hydrophilic and hydrophobic drug in combine loaded chitosan/cyclodextrin nanoparticles and *in vitro* release study. *Colloids and Surfaces B: Biointerfaces* **83,** 103-107, (2011).

46 Y. Zhang, T. Jin & R.-X. Zhuo. Methotrexate-loaded biodegradable polymeric micelles: preparation, physicochemical properties and *in vitro* drug release. *Colloids and Surfaces B: Biointerfaces* **44,** 104-109, (2005).

47 M. R. Marques, R. Loebenberg & M. Almukainzi. Simulated biological fluids with possible application in dissolution testing. *Dissolution Technologies* **18,** 15-28, (2011).

48 Quantachrome. *Application of QSDFT (quenched solid density functional theory) - a Novel Density Functional Theory for an Accurate Pore Size Analysis of Disordered Porous Carbons*. Volume 40 (Quantachrome Instruments USA).

CHAPTER 8

CONCLUSION AND OUTLOOK

In this work, the results of the research performed during my PhD thesis concerning the synthesis of mesoporous (alkaline earth) metal phosphate-citrate nanoparticles as nano-agents against cancer were presented.

In chapter 3, a novel synthesis strategy for amorphous mesoporous calcium phosphate-citrate nanoparticles (CPCs) was reported. Using a soft templating method in combination with a modified Pechini method, we developed a process to yield mesoporosity. We investigated the influence of the complexing agent, citric acid, on the formation of the mesopores. The amount of citrate incorporated into the structure correlated strongly with the degree of mesoporosity. The incorporation of citrate into the structure of CPCs was verified using IR spectroscopy and thermogravimetric analysis. By optimizing the reaction conditions, CPCs were synthesized with diameters of around 200 nm (confirmed with dynamic light scattering and electron microscopy) and a BET surface area of about 575 m^2/g. The pore size is about 5 nm with a corresponding pore volume of 0.6 cm^3/g. CPCs are of amorphous nature with the ability to crystallize over time in aqueous media. The transition of the amorphous phase into the crystalline phase was followed by X-ray diffraction. In conclusion, we have synthesized colloidally stable mesoporous calcium phosphate-based nanoparticles, which has been a research goal for almost 30 years. The developed nanoparticles could be applicable in fields such as of drug delivery or regenerating bone cement.

In chapter 4, the synthetic approaches regarding further functionalization of mesoporous CPCs was discussed. Using co-precipitation methods, the incorporation of manganese and strontium ions into the framework of CPCs was achieved. The paramagnetic properties and high radiopacity of the incorporated manganese and strontium ions, respectively, were investigated using magnetic resonance imaging

and computer aided tomography experiments. The results confirmed the potential of these nanoparticles as diagnostic tools or for detection in living matter. Through co-precipitation with fluorescent calcein, we produced self-fluorescent CPCs. These nanoparticles were only taken up by HeLa cells after coating them with a supported lipid membrane, confirmed with fluorescence confocal microscopy. Overall, the different functionalizations did not have a negative influence on the BET surface area, pore volume, and pore size with respect to the unfunctionalized CPCs. In conclusion, we have developed a procedure to functionalize CPCs with different bivalent cations and other agents to yield desired physical properties. We demonstrated that bare CPCs can be upgraded to become a diagnostic tool or a multifunctional drug delivery vehicle with tunable properties permitting the uptake by cells.

In chapter 5, an improved synthesis of CPCs with the addition of Pluronic® F127, which led to a significant increase of porosity was presented. As a result, the nanoparticles feature an extraordinary BET surface area of 900 m^2/g, a narrow pore size distribution with a maximum at 4.8 nm, and a cumulative pore volume of 1.0 cm^3/g. The incorporation of citrate into the CPC structure was demonstrated applying solid-state nuclear magnetic resonance spectroscopy. The loading capacity and release kinetics of CPCs were investigated with calcein as a model drug and ibuprofen and were confirmed by fluorescence and UV-Vis measurements. For lipid-coated CPCs we demonstrated that no significant premature release of calcein or ibuprofen occurs. Furthermore, we carried out cell experiments on fourteen different cell lines. For this purpose seven mesenchymal cancer cell lines, six epithelial cancer cell lines, and one epithelial cell line derived from non-tumorigenic tissue were investigated. The cellular uptake was dependent on the lipid-coating of CPCs; uncoated CPCs were not taken up by the cells. Internalized CPCs dissolved once the

endosomal pH turned acidic. A rapid release of Ca^{2+} ions into the cytosol was induced by small amounts of the amphiphile cetyltrimethylammonium chloride 'on board' of the CPCs. We demonstrated that mesenchymal cancer cell lines were much more strongly affected by the Ca^{2+} shock and induced apoptosis at lower IC_{50} values than epithelial cancer cells. And strikingly, the non-cancerous cell line MCF 10A was not even affected significantly by the CPC particles up to concentrations of 100 µg/mL.

Additionally, the correlation of the Ca^{2+} shock with the endolysosomal escape of CPCs was demonstrated with time-resolved cell experiments. Several hours after particle uptake, the activation of caspase-3/7 was recorded, which was followed by a decrease in NADH and finally by ATP depletion. Additionally, we performed mouse studies with an intrapleural tumor model. Firstly, we revealed a decrease in tumor mass by 40 wt% after one single injection of CPCs and secondly a good biocompatibility of the treatment. In conclusion, we presented a chemotherapeutic agent based on calcium phosphate-citrate nanoparticles with strong selectivity in toxicity towards cancer cells. Therefore, the treatment of cancer with CPCs may lead to significantly reduced side effects due to better selectivity with respect to cell types.

In chapter 6, a systematic study on the exchange of calcium ions against magnesium ions in calcium phosphate-citrate nanoparticles was performed. To this end, we gradually substituted the amount of magnesium with respect to the calcium content of CPCs. At 60 mol% magnesium ions in magnesium-calcium phosphate-citrate, a drastic increase in particle size led to objects with 5 µm in length. We investigated a pH-dependence regarding the formation of colloidal mesoporous magnesium-calcium phosphate-citrate nanoparticles during the precipitation. Accordingly, we

have obtained the first colloidal mesoporous magnesium phosphate-citrate nanoparticles (MPCs). These particles feature a size of 40-60 nm with a large BET surface area of 560 m^2/g. The pore size is about 6.3 nm with a corresponding pore volume of 0.8 cm^3/g. The incorporation of citrate into the structure of MPCs was proven with IR spectroscopy. Additionally, we adapted the synthesis procedure to produce colloidal mesoporous manganese phosphate-citrate nanoparticles. In conclusion, we have developed a general method for the synthesis of mesoporous bivalent metal phosphate-citrate nanoparticles.

In the last chapter 7, the potential of mesoporous magnesium phosphate-citrate nanoparticles (MPCs) as biocompatible drug delivery systems was investigated. We demonstrated the impact of the complexing agent, citric acid, with respect to the formation of mesopores in MPCs. A maximum BET surface area of 560 m^2/g and a pore size of about 6.3 nm with a corresponding pore volume of 0.8 cm^3/g were obtained. The amount of incorporated citrate into the structure was verified with IR spectroscopic methods and thermogravimetric analysis. Furthermore, we coated the MPCs with a lipid membrane to encapsulate fluorescent calcein as model drug and the anti-cancer drug methotrexate (MTX). The lipid membrane prevented the incorporated guests from premature release, which we confirmed using fluorescence measurements and UV-Vis spectroscopy. Cell viability assays revealed low toxicity of unloaded MPCs with an IC_{50} value of 77 µg/mL, compared to MTX-loaded MPCs with an IC_{50} value of 1.1 µg/mL. In conclusion, we designed mesoporous magnesium phosphate-citrate nanoparticles as advanced biodegradable and biocompatible platform that can potentially reduce the side effects of current chemotherapies.

Summing up, we have established a novel method for the synthesis of colloidal mesoporous (alkaline earth) metal phosphate-citrate nanoparticles as nano-agents

against cancer. We have demonstrated that citric acid plays a key role as complexing agent for the metal cations, thus reducing the rate of the precipitation reaction. The newly obtained colloidal mesoporous nanomaterials can either be applied directly as chemotherapeutic agent in the case of calcium phosphate-citrate nanoparticles or as advanced biocompatible drug delivery system in the case of magnesium phosphate-citrate nanoparticles. Additionally, we established the flexible functionalization of the novel nanoparticles for special diagnostic or detection purposes. The adaptation of the developed synthesis approaches also led to the synthesis of new materials such as mesoporous manganese phosphate-citrate nanoparticles.

It is hoped that the insights gained in this work regarding the synthesis of novel mesoporous nanoparticles and their function will result in novel strategies for cancer therapy in the future.

CHAPTER 9

APPENDIX

PUBLICATIONS

Mesoporous calcium phosphate-citrate nanoparticles and uses thereof.

Thomas Bein, Hanna Engelke, Johann Feckl, Constantin von Schirnding.

PCT/EP2016/068231 (2015).

Lipid bilayer-coated curcumin-based mesoporous organosilica nanoparticles for cellular delivery.

Stefan Datz, Hanna Engelke, Constantin von Schirnding, Linh Nguyen, Thomas Bein.

Microporous and Mesoporous Materials **225**, 371-377, (2016).

Genetically designed biomolecular capping system for mesoporous silica nanoparticles enables receptor-mediated cell uptake and controlled drug release.

Stefan Datz, Christian Argyo, Michael Gattner, Veronika Weiss, Korbinian Brunner, Johanna Bretzler, Constantin von Schirnding, Adriano A. Torrano, Fabio Spada, Milan Vrabel, Hanna Engelke, Christoph Bräuchle, Thomas Carell, Thomas Bein.

Nanoscale **8**, 8101-8110, (2016).

Targeted drug delivery in cancer cells with red-light photoactivated mesoporous silica nanoparticles.

Stephan A. Mackowiak, Alexandra Schmidt, Veronika Weiss, Christian Argyo, Constantin von Schirnding, Thomas Bein, Christoph Bräuchle.

Nano Letters **13**, 2576-2583, (2013).

$Sn_6[P_{12}N_{24}]$ - A sodalite-type nitridophosphate.

Florian J. Pucher, Constantin Frhr. von Schirnding, Franziska Hummel, Vinicius R. Celinski, Joern Schmedt auf der Guenne, Birgit Gerke, Rainer Poettgen, Wolfgang Schnick.

European Journal of Inorganic Chemistry **2015**, 382-388, (2015).

PRESENTATIONS

1.) Targeted Drug Delivery in Cancer Cells with Red Light Photoactivated Mesoporous Silica Nanoparticles.

SFB749 Workshop, Dynamics and Inclusion Chemistry in Mesoporous Host Systems, 2013, Wildbad Kreuth, Germany.

2.) Multifunctional mesoporous silica nanoparticles for triggered and targeted drug delivery and for studying cell–receptor interactions.

SFB1032 Workshop, Nanoagents for the spatiotemporal control of molecular and cellular reactions, 2014, Hohenkammer, Germany.

3.) Synthesis Strategy for Amorphous Mesoporous Apatite Nanoparticles.

SFB749 Workshop, Dynamics and Inclusion Chemistry in Mesoporous Host Systems, 2014, Venice, Italy.

4.) Synthesis Strategy for Amorphous Mesoporous Apatite Nanoparticles.

26. Deutsche Zeolith-Tagung, 2014, Paderborn, Germany

5.) Synthesis Strategy for Amorphous Mesoporous Apatite Nanoparticles.

113. Bunsentagung, Physical Chemistry on the Nanometer Scale, 2014, Hamburg, Germany.

6.) Drug Delivery Systems.

60th Birthday Symposium, Prof. Thomas Bein, 2014, München, Germany.

7.) Nano-Roboter zur gezielten Behandlung von Krebs.

NIM NanoDay: Hinter den Kulissen der Nanoforschung - Deutsches Museum, 2014, München, Germany.

8.) Synthesis Strategy for Amorphous Mesoporous Apatite Nanoparticles.

6th International FEZA Conference, Porous Systems: From Novel Materials to Sustainable Solutions, 2014, Leipzig, Germany.

9.) Synthesis Strategy for Amorphous Mesoporous Apatite Nanoparticles.

SFB1032 Workshop, Nanoagents for the spatiotemporal control of molecular and cellular reactions, 2014, Fraueninsel, Germany.

10.) Dynamik der Interaktion von mesoporösen Nanopartikeln mit Zellen; Dynamik in nanoskaligen Kanalsystemen; Synthese und Charakterisierung von mesoporösen Nanopartikeln.

SFB749 Workshop, Dynamics and Inclusion Chemistry in Mesoporous Host Systems, 2015, München, Germany.

11.) Synthesis and Characterization of Mesoporous Nanoconstructs; Mesoporous Nanoconstructs for drug delivery - Cell studies.

SFB1032 Workshop, Nanoagents for the spatiotemporal control of molecular and cellular reactions, 2015, Altötting, Germany.

12.) Genetically designed biomolecular capping system for mesoporous silica nanoparticles enables receptor-mediated cell uptake and controlled drug release.

SFB749 Workshop, Dynamics and Inclusion Chemistry in Mesoporous Host Systems, 2016, Irsee, Germany.

13.) Synthesis Strategy for Amorphous Mesoporous Apatite Nanoparticles.

International Symposium on Nanobiotechnology, NanoMedicine from discovery to clinical reality: therapeutics, delivery and imaging, 2016, California Nanosystems Institute, Los Angeles, USA.

SUPPLEMENTARY DIGITAL DATA